

Electronic Thesis and Dissertation Repository

4-3-2012 12:00 AM

Hydrodynamics and Micro Flow Structure of Gas-Solid Circulating Turbulent Fluidized Beds

Maozhan Qi, *The University of Western Ontario*

Supervisor: Dr. J. Zhu, *The University of Western Ontario*

Joint Supervisor: S. Dr. Barghi, *The University of Western Ontario*

A thesis submitted in partial fulfillment of the requirements for the Doctor of Philosophy degree in Chemical and Biochemical Engineering

© Maozhan Qi 2012

Follow this and additional works at: <https://ir.lib.uwo.ca/etd>



Part of the [Engineering Commons](#)

Recommended Citation

Qi, Maozhan, "Hydrodynamics and Micro Flow Structure of Gas-Solid Circulating Turbulent Fluidized Beds" (2012). *Electronic Thesis and Dissertation Repository*. 420.

<https://ir.lib.uwo.ca/etd/420>

This Dissertation/Thesis is brought to you for free and open access by Scholarship@Western. It has been accepted for inclusion in Electronic Thesis and Dissertation Repository by an authorized administrator of Scholarship@Western. For more information, please contact wlsadmin@uwo.ca.

Hydrodynamics and Micro Flow Structure of Gas-Solid Circulating Turbulent Fluidized Beds

(Spine title: Hydrodynamics of CTFB)
(Thesis format: Integrated Article)

by

Maozhan Qi

Graduate Program in Engineering Science
Department of Chemical and Biochemical Engineering

A thesis submitted in partial fulfillment
of the requirements for the degree of
Doctor of Philosophy

The School of Graduate and Postdoctoral Studies
The University of Western Ontario
London, Ontario, Canada

© Maozhan Qi 2012

THE UNIVERSITY OF WESTERN ONTARIO
SCHOOL OF GRADUATE AND POSTDOCTORAL STUDIES

CERTIFICATE OF EXAMINATION

Supervisor

Dr. Jesse Zhu

Co-Supervisor

Dr. Shahzad Barghi

Examiners

Dr. Hugo de Lasa

Dr. Ronald Breault

Dr. Chao Zhang

Dr. Chunbao Xu

The thesis by

Maozhan Qi

entitled:

**Hydrodynamics and Micro Flow Structure of Gas-Solid Circulating
Turbulent Fluidized Beds**

is accepted in partial fulfilment of the
requirements for the degree of
Doctor of Philosophy

Date _____

Chair of the Thesis Examination Board

Abstract

Circulating Turbulent Fluidized Beds (CTFB) refer to fluidized beds integrated into high density circulating systems to simultaneously achieve highly efficient gas-solid interactions existing in turbulent fluidized beds and low solids backmixing featured by circulating fluidized beds. Hydrodynamics and micro flow structure were experimentally studied in a CTFB (3.6 m high and 0.104 m id) using 76 μm FCC particle with air velocities of 0.5 ~ 5.0 m/s and solids circulation rates of 0 ~ 420 $\text{kg/m}^2\text{s}$. The distributions of solids holdup were acquired using optical fibre probes and pressure transducers at sampling frequencies of 50 $\text{kHz} \times 131 \text{ s}$ and 1 $\text{kHz} \times 400 \text{ s}$ respectively. A Pseudo Bubble-Free Fluidized Bed was developed to dynamically calibrate the optical fibre probes. Based on statistical parameters, a Moment Consistency Data Processing Method (MCDPM) was proposed to calculate solids holdups of the dense and dilute phases from the experimental data. A Divided Phase Cross-Correlation Method (DPCCM) was adopted in cross-correlating the solids holdup signals of the dense and dilute phases to obtain the phase particle velocities.

MCDPM provided average solids holdups of the dense and dilute phases and the phase fractions over bubbling (BFB), turbulent (TFB), circulating turbulent (CTFB), high density circulating (HDCFB) and circulating (CFB) fluidized beds. The flow structure in terms of phase division and the micro flow characteristics were studied across all five regimes from low to high velocities, CTFB was found to have strong similarities with TFB.

Study on the detailed hydrodynamics and transition characteristics of the CTFB demonstrated that solids holdup distribution in CTFB was more homogeneous both axially and radially than that of other regimes, and the local solids flux and the local particle velocity were both proportional to the solids circulation rate. Microscopically, CTFB was characterized by dilute phase dominating flow in the centre and dense phase dominating flow in the annular region. Such flow structure was different from either dense phase dominating flow in BFB or dilute phase dominating flow in CFB. New criteria for the transition air velocities were proposed for CTFB. The results demonstrated that the onset transition velocity from BFB to CTFB remained nearly unchanged, and the ending transition air velocity from CTFB to CFB increased, with increasing solids circulation rate.

Keywords: Circulating turbulent fluidized bed, Fluidization regime, Hydrodynamics, Solids holdup, Transition velocity, Micro flow structure, Divided phase cross-correlation, Dense and dilute phase division, Particle velocity, Slip velocity, Apparent particle velocity

Co-Authorship Statement

Title: Dynamic calibration of optical fibre probes in gas-solid flow systems: low and high solids concentrations (Chapter 3)

Authors: Maozhan Qi, Shahzad Barghi, Jesse Zhu

Maozhan Qi designed and performed the experiment and carried out data analysis under the guidance of Dr. Jesse Zhu. All drafts of this manuscript were written by Maozhan Qi. Modifications were carried out under close supervision of Dr. J. Zhu and Dr. Barghi. The final version is ready to submit for publication. Major results were presented at 60th CShE conference.

Title: Identification of micro flow structures and regime transition in gas-solid fluidized beds through moment analysis (Chapter 4)

Authors: Jesse Zhu, Maozhan Qi, Shahzad Barghi.

Under peer review *AIChE Journal*, 2012

The experimental setup of a gas-solid circulating turbulent fluidized bed was modified by Maozhan Qi under the guidance of Dr. Jesse Zhu and Dr. Barghi. All the experimental work and data analysis were undertaken by Maozhan Qi. The first drafts of this manuscript were written by Maozhan Qi with some major parts rewritten by Dr. Zhu in consultation to Qi. Further modifications were done with constructive advices of Dr.

Barghi. Partial results were also presented at 61st CSChE conference. The final version of this article has been submitted to AIChE Journal.

Title: Transition characteristics of gas-solid flow in circulating turbulent fluidized beds (Chapter 5)

Authors: Maozhan Qi, Jesse Zhu, Shahzad Barghi

Maozhan Qi designed and performed the experiments and carried out data analysis under the guidance of Dr. Jesse Zhu and Dr. Barghi. All drafts of this manuscript were written by Maozhan Qi. Modifications were carried out under close supervision of Dr. J. Zhu and Dr. Barghi. The final version has been submitted to Powder Technology.

Title: Detailed hydrodynamics of high flux gas-solid flow in a circulating turbulent fluidized bed (Chapter 6)

Authors: Maozhan Qi, Shahzad Barghi, Jesse Zhu

Maozhan Qi designed and performed the experiment and carried out data analysis under the guidance of Dr. Jesse Zhu and Dr. Barghi. All drafts of this manuscript were written by Maozhan Qi. Modifications were carried out under close supervision of Dr. J. Zhu and Dr. Barghi. The final version is ready to submit for publication. Some results were presented at 59th CSChE conference.

Title: Particle velocity and flux distribution in a high solids concentration circulating turbulent fluidized bed (Chapter 7)

Authors: Maozhan Qi, Jesse Zhu, Shahzad Barghi

Maozhan Qi designed and performed the experiment and carried out data analysis under the guidance of Dr. Jesse Zhu and Dr. Barghi. All drafts of this manuscript were written by Maozhan Qi. Modifications were carried out under close supervision of Dr. J. Zhu and Dr. Barghi. The final version is ready to submit for publication.

Acknowledgments

I would like to extend my sincerest gratitude and deepest appreciation to my supervisor Prof. Jesse Zhu for his unwavering dedication to this project. His knowledge, patience, continual support and guidance have been the foundations, on which this research has been built. I would also like to express my special thanks to my co-supervisor Dr. Barghi for his advice, helpful suggestions and kind encouragement during the progress of this work, and for his generous timely support.

Special appreciations go to Jiemi Gao and Mohammed Abdelhadi who offered their great help and assistance for the experiments. Thanks are also extended to my friends in the research group, Dongbing Li, Jing Xu, Qi Miao, Long Sang, Tracy Wang, Yuanyuan Shao, Jingsi Yang, and other colleagues who supported me in every respect during the completion of this project. I would like to thank Joanna Blom, April Finkenhoefer, Kristen Hunt, J. Wen, Michael Zhu, Qing Mu, George Zhang, Lisa Desalaiz, Mike Gaylard, Clayton Cook for their timely supports.

I would like to thank Western University, Natural Sciences and Engineering Research Council of Canada (NSERC) for their financial supports toward my studies and research.

I am extremely thankful to my mother, my parents-in-law, my son, my brother Maogong Qi, and my sister-in-law Chrystal Ren who encouraged me throughout this journey.

I would like to express my deepest appreciation to my wife, Alice Ren, for her understanding and love during the past few years. Her support and encouragement were what made this dissertation possible.

Dedication

To

My dear mom and my dear wife

Table of contents

CERTIFICATE OF EXAMINATION	ii
Abstract	iii
Acknowledgments	viii
Dedication	ix
Table of contents	x
List of tables	xv
List of figures	xvi
1 Introduction	1
1.1 Background.....	1
1.2 Available measurement technologies	3
1.3 Hydrodynamics of TFB	6
1.4 Studies on circulating turbulent fluidized bed (CTFB).....	10
1.5 Objectives	11
1.6 Thesis organization.....	12
Reference	14
2 Experimental Apparatus and Measurement Technique	21
2.1 Circulating turbulent fluidized bed.....	21
2.2 Particle Properties	23
2.3 Measurement Techniques	24
2.3.1 Measurement of superficial gas velocity	24
2.3.2 Differential pressure measurement	25
2.3.3 Local solids holdup measurement.....	27

2.3.4	Cross-correlation method of particle velocity.....	29
2.3.5	Solids circulation rate measurement	30
	Nomenclature.....	31
	References	32
3	Dynamic calibration of optical fibre probes in gas-solid flow systems: low and high solids concentrations.....	34
3.1	Introduction.....	34
3.2	Experimental setup and calibration procedure.....	38
3.2.1	Experimental setup.....	38
3.2.2	Probe and calibration procedure	41
3.2.3	Application experiment.....	43
3.3	Results and discussion	44
3.3.1	Dynamic signals.....	44
3.3.2	Uniformity.....	45
3.3.3	Calibration curves	47
3.3.4	Applications of optical fibre probe	53
	Conclusion	59
	Nomenclature.....	59
	References	60
4	Identification of micro flow structures and regime transition in gas-solid fluidized beds through moment analysis	64
4.1	Introduction.....	64
4.2	Experimental setup.....	66
4.3	Moment consistency data processing method.....	70
4.3.1	Parameters of moment consistency.....	70

4.3.2	Division of dense and dilute phases.....	76
4.4	Results and discussion	77
4.4.1	Flow structure across regimes.....	77
4.4.2	Flow regime transition and similarities.....	81
4.4.3	Flow regime differences and similarities.....	86
4.4.4	Micro flow structure analyses.....	89
	Conclusion	93
	Acknowledgement.....	94
	Notation	95
	Literature cited.....	96
5	Transition characteristics of gas-solid flow in circulating turbulent fluidized beds.....	99
5.1	Introduction.....	99
5.2	Experimental setup.....	103
5.3	Results and discussion	107
5.3.1	Transient features of solids holdup signals.....	107
5.3.2	Skewness and kurtosis vs. two phase flow	111
5.3.3	Skewness and kurtosis profiles	116
5.3.4	Transition velocities of CTFB	124
	Conclusions	133
	Acknowledgement.....	134
	Nomenclature.....	134
	References	135
6	Detailed hydrodynamics of high flux gas-solid flow in a circulating turbulent fluidized bed	141

6.1	Introduction.....	141
6.2	Experimental setup and methods	144
6.2.1	Experimental setup.....	144
6.2.2	Parameters of dense and dilute phases.....	149
6.2.3	Phase particle velocity computation	150
6.3	Results and discussion	151
6.3.1	Macro flow structure of CTFB	151
6.3.2	Micro flow structure of CTFB	157
6.3.3	Solids circulation effect on CTFB	164
6.3.4	Typical characteristics of CTFB	170
	Conclusion	175
	Acknowledgement.....	175
	Nomenclature.....	176
	References	177
7	Particle velocity and flux distribution in a high solids concentration circulating turbulent fluidized bed.....	180
7.1	Introduction.....	180
7.2	Experimental setup and methods	184
7.2.1	Experimental setup.....	184
7.2.2	Divided phase cross-correlation method.....	188
7.2.3	Apparent particle velocity and phase slip particle velocity	193
7.3	Results and discussion	194
7.3.1	Particle velocities of dilute and dense phases	194
7.3.2	Phase slip particle velocity.....	201
7.3.3	Solids flux of dilute and dense phases	204

7.3.4	Apparent particle velocity and cross-correlation methods.....	210
	Conclusion	212
	Acknowledgement.....	213
	Nomenclature.....	213
	References	215
8	Conclusions and recommendations	220
8.1	Conclusions.....	220
8.2	Assessment on CTFB.....	222
8.3	Recommendations.....	226
Appendix A.1	Derivation of MCDPM (Chapter 4)	228
Appendix A.2	Calculation of coefficient of determination in Chapter 3	232
Appendix A.3	List of equations in Chapter 4	233
Appendix A.4	List of equations in Chapter 5	235
Appendix A.5	List of equations in Chapter 7	236
Appendix B.1	Matlab code for MCDPM and phase division	237
Appendix B.2	MatLab code for DPCCM	239
Appendix C.1	Velocity chart for the primary air supply	242
Appendix C.1	Velocity chart for the secondary air supply	243
Appendix D.1	Pressure chart for transducer	244
Appendix D.2	Pressure chart for transducer	245
Appendix D.3	Error analysis of solids holdup measurements using optical fibre probes	246
	Curriculum vitae	252

List of tables

Table 2.1 FCC particle size distributions	23
Table 2.2 Locations of pressure transducers	26
Table 3.1 Particle properties	41
Table 3.2 Coefficients of determination R^2 at different positions	46
Table 4.1 Operating conditions of experiments	68
Table 4.2 Radial Non-uniformity Index (RNI) and average value for the dilute and dense phase solids holdups and the dense phase volume fraction	87
Table 5.1 A summary of transition air velocities of TFB in previous studies, using FCC as solid particle	102
Table 5.2 Operating conditions of experiments	105
Table 5.3 Local flow structure features of flow regimes vs. moment values	132
Table 6.1 Major advantages and disadvantages of CFB and TFB	143
Table A.1 Error Analysis of probe #1 (at $z = 0.8$ m)	248
Table A.2 Error Analysis of probe #2 (at $z = 1.5$ m)	249
Table A.3 Error Analysis of probe #3 (at $z = 2.2$ m)	250
Table A.4 Error Analysis of probe #4 (at $z = 3.0$ m)	251

List of figures

Figure 2.1 Schematic drawing of experimental apparatus	22
Figure 2.2 Setup of optical fibre probes and pressure transducers	29
Figure 3.1 Pseudo bubble-free fluidized bed and calibration system	40
Figure 3.2 Probe signals of PBFFB with GB #2 at different bed heights	45
Figure 3.3 Time average response voltage vs. solids holdup of sand at different radial and axial positions.....	46
Figure 3.4 Calibration curves with PBFFB and downer calibration procedures:..	49
Figure 3.5 Calibrations of the optical probe in different particles	51
Figure 3.6 Probe responses to different FCC particle size distributions	52
Figure 3.7 Probe responses to different glass bead particle size distributions	53
Figure 3.8 Axial profiles of cross-sectional averaged solids holdup in CTFB obtained by optical fibre probes and differential pressure transducers	54
Figure 3.9 Radial profiles of time-average solids holdup in different regimes obtained by optical fibre probes	55
Figure 3.10 Solids holdup profiles of the dense phase in CTFB	56
Figure 3.11 Solids holdup profiles of the dilute phase in CTFB.....	57
Figure 3.12 Profiles of the dense phase fraction in CTFB.....	58
Figure 4.1 Experimental apparatus and optical fibre probe setup.....	69

Figure 4.2 Segment of (a) measured solids holdup signals of CTFB vs. (b) the solids holdup signals from the corresponding ideal two phase flow	72
Figure 4.3 Relative moment errors of MCDPM with respect to (a) skewness or (b) kurtosis of local solids holdup signals	75
Figure 4.4 Relationship of skewness and kurtosis for all solids holdup signals...	76
Figure 4.5 Radial solids holdup profiles of the dilute phase of BFB, TFB, CTFB, HDCFB and CFB, (data for HDCFB and CFB from Yan and Zhu, 2004).....	79
Figure 4.6 Solids holdup profiles of dense phase of BFB, TFB, CTFB, HDCFB and CFB, (data for HDCFB and CFB from Yan and Zhu, 2004).....	80
Figure 4.7 Profiles of dense phase fraction of BFB, TFB, CTFB, HDCFB and CFB, (data for HDCFB and CFB from Yan and Zhu, 2004).....	81
Figure 4.8 Variation of average values of ϵ_{sb} , ϵ_{sd} and f_d across the fluidization regimes, BFB, TFB, CTFB, HDCFB and CFB, (data for HDCFB and CFB from Yan and Zhu, 2004)	83
Figure 4.9 Radial Nonuniformity Index (RNI) of ϵ_{sb} , ϵ_{sd} and f_d for 5 fluidization regimes, BFB, TFB, CTFB, HDCFB and CFB, (data for HDCFB and CFB from Yan and Zhu, 2004)	85
Figure 4.10 PDF profiles of BFB, TFB, CTFB, HDCFB and CFB, (data for HDCFB and CFB from Yan and Zhu, 2004).....	91
Figure 4.11 Radial skewness profiles for BFB, TFB, CTFB, HDCFB and CFB, (data for HDCFB and CFB from Yan and Zhu, 2004).....	92
Figure 4.12 Profiles of dense phase fraction of BFB, TFB, CTFB, HDCFB and CFB, (data for HDCFB and CFB from Yan and Zhu, 2004).....	93
Figure 5.1 Experimental apparatus and optical fibre probe setup.....	106

Figure 5.2 Evolution of solids concentration traces in BFB, CTFB, and the bottom zone of CFB ($z = 1.5$ m)	108
Figure 5.3 Comparison of solids concentration traces in TFB and CTFB regimes under similar air velocities and different solids circulation rates	110
Figure 5.4 Moments vs. local solids holdup fluctuations in (a) BFB and (b) CFB fluidization regimes	114
Figure 5.5 Skewness profiles of solids holdup under different air velocities and different solids circulation rates in BFB, CTFB and the bottom zone of CFB.....	117
Figure 5.6 Skewness profiles of solids holdup under different solids circulation rates in TFB and CTFB	118
Figure 5.7 Standard kurtosis profiles of solids holdup under different air velocities and different solids circulation rates in BFB, CTFB and the bottom zone of CFB.....	120
Figure 5.8 Standard kurtosis profiles of solids holdup under different solids circulation rates in TFB and CTFB	121
Figure 5.9 Probability Density Function (PDF) of local solids holdup at $r/R = 0$ for CTFB, noted with kurtosis and bi-peak parameter	124
Figure 5.10 Skewness variation of gas-solid flow and the transition velocities..	126
Figure 5.11 Standard deviation, skewness and kurtosis of solids holdup signals in a conventional turbulent fluidized bed (data from Zhu and Zhu, 2008).....	127
Figure 5.12 β values vs. air velocity and ending transition air velocity of CTFB	129
Figure 5.13 Ending transition air velocities of CTFB regime against solids circulation rates	130

Figure 6.1 Experimental apparatus and optical fibre probe setup.....	148
Figure 6.2 Axial profiles of cross-sectional average solids holdup obtained from pressure gradients, (a) at different air velocities, and (b) with and without solids circulation, and (c) from optical probe measurement	153
Figure 6.3 Radial profiles of local average solids holdup against air velocity	155
Figure 6.4 Annular average solids holdup with respect to air velocity and solids circulation rate	156
Figure 6.5 Annular average solids holdups of the dilute phase with respect to air velocity and solids circulation rate	158
Figure 6.6 Annular average solids holdups of the dense phase with respect to air velocity and solids circulation rate	160
Figure 6.7 Annular average values of the dense phase fraction with respect to air velocity and solids circulation rate	162
Figure 6.8 Comparison of probability density function of solids holdup over transition, and over effects of superficial air velocity and effects of the solids circulation rate	164
Figure 6.9 Profiles of the reduced net solids flux at different air velocities: in entrance, fully developed and exit sections	167
Figure 6.10 Profiles of the reduced net solids flux at different solids circulation rates: in entrance, fully developed and exit sections.....	168
Figure 6.11 Profiles of the apparent particle velocity at different air velocities: in entrance, fully developed and exit sections.....	169
Figure 6.12 Profiles of the apparent particle velocity at different solids circulation rates: in entrance, fully developed and exit sections.....	170

Figure 7.1 Experimental apparatus and optical fibre probe setup.....	187
Figure 7.2 Signal decomposition of DPCCM: (a) original signal segment of solids holdup, (b) sub-signals of dense phase, (c) sub-signals of dilute phase. 189	
Figure 7.3 Profiles of upward radial particle velocity of dilute and dense phases.....	195
Figure 7.4 Profiles of downward radial particle velocity of dilute and dense phases.....	197
Figure 7.5 Annular average of upward particle velocities of dilute and dense phases with respect to air velocity, $z = 1.5\text{m}$	198
Figure 7.6 Annular average of upward particle velocities of dilute and dense phases with respect to solids circulation rate, $z = 1.5\text{ m}$	199
Figure 7.7 Profiles of upward and downward time fractions of dilute and dense phases, $u_g = 2.90\text{ m/s}$, $G_s = 145\text{ kg/m}^2\text{s}$	201
Figure 7.8 Profiles of phase slip particle velocity between dilute and dense phases.....	202
Figure 7.9 Phase slip particle velocity between dilute and dense phases	204
Figure 7.10 Profiles of upward solids flux profiles of dilute and dense phases..	205
Figure 7.11 Profiles of downward solids flux profiles of dilute and dense phases.....	206
Figure 7.12 Profiles of apparent particle velocity at different air velocities and solids circulation rates	210
Figure 7.13 Apparent particle velocity and comparison between CCM and DPCCM, $u_g = 2.99\text{ m/s}$, $G_s = 379\text{ kg/m}^2\text{s}$, $z = 1.5\text{ m}$	212

Figure A1 Velocity chart for the primary air supply.....	242
Figure A2 Velocity chart for the secondary air supply.....	243
Figure A3 Pressure chart for transducer of PX163-120D5V.....	244
Figure A4 Pressure chart for transducer of PX162-027D5V.....	245
Figure A5 Solids holdup profiles and error bars of optical fibre probe data...	247

1 Introduction

1.1 Background

Flow of a gas through a bed of solid particles can result in suspension of the particles due to the imposed drag force on them. Particles in suspension move randomly and offer maximum contact area, which is critical in heat and mass transfer processes. Winkler introduced such gas-solid system for coal gasification in 1920s, as regarded as the first fluidized bed reactor. The fluidization technology has drawn much attention ever since due to its unique features, and a wide range of industrial application have been developed, such as catalytic cracking of crude oil in the 1940s (Jahnig et al, 1980; Squires, 1986). At early stages (1970s), the main research focus was on bubbling fluidized beds. The concept of circulating fluidized bed or fast fluidized bed was first proposed by Yerushalmi (1976), where solids must be fed continuously into the bed and entrained upward in a riser, then collected/separated at the riser top, and re-circulated through a particle storage vessel or stand pipe back to the bottom of the riser. Due to excellent heat and mass transfer efficiencies, uniform temperature distribution and easy addition and withdrawal of solids, circulating fluidized bed (CFB) has been applied to chemical processing, mineral processing, pharmaceutical production and energy-related process, etc. (Grace, 1990). The turbulent fluidization flow regime is commonly considered to lie between bubbling fluidization and the fast fluidization regimes. It has been characterized by lower amplitude of pressure fluctuations, resulting from the

disappearance of large bubbles/voids. The first photo graph of a turbulent fluidized bed, distinctly different from bubbling fluidization, was published by Matheson et al (1949). A turbulent fluidization regime was introduced in the flow regime diagram of Zenz (1949). The first quantitative study seems to have been performed by Lanneau (1960) who measured local voidage fluctuations and pierced void lengths in a 76 mmID fluidized bed with fine catalyst particles at high gas velocities, although the transition from bubbling/slugging to the turbulent regime was not quantified. Kehoe and Davidson (1970) extended their work on slugging to higher velocity operation and identified the transition from bubbling to turbulent fluidization based on visualization of a 2-D bed and bubble rise velocity and capacitance traces in a 3-D column. Later the turbulent fluidization regime was reported by Massimilla (1978), Thiel and Potter (1977) and Crescitelli et al (1978).

There are some inherent characteristics of CFB and TFB which limit the performance of these reactors. The relatively low solid concentration and the non-uniform axial and radial flow structure in CFBs cause many disadvantages. For instance, their serious gas by-passing through the core dilute region and extensive backmixing of solids in the wall region, consequently, led to reduced overall gas-solid contact efficiency (Perales et al, 1990). As TFB is concerned, serious backmixing of the solids phases responds to a broad residence time-distribution of the solids and poor chemical reaction selectivity (Zhu and Zhu, 2008a). Low gas passing through is another shortcoming of TFB. In view of CFB making up most of TFB shortcomings, a new concept of circulating turbulent fluidized bed (CTFB) reactor was proposed by Zhu and Zhu (2008), integrating conventional

circulating and turbulent fluidized beds into a unique high-density fluidization system, to simultaneously achieve efficient gas-solid contact and low solids back-mixing. Their results demonstrated that CTFB operation may be attributed to a new flow regime, the circulating turbulent fluidization regime, independent of turbulent fluidization, fast fluidization and dense suspension upflow (Qi and Zhu, 2009)..

1.2 Available measurement technologies

Many techniques based on a variety of principles have been developed to study hydrodynamics in fluidized beds and other gas–solids systems (Yates et al, 1994; Bachalo, 1994). These methods can be broadly classified as: impact, isokinetic, flow visualization, laser Doppler and cross-correlation techniques. The impact method is based on measuring the force exerted on a small obstacle inserted in the flow path. The particle velocity can then be related to the measured impact force (Heertjes, 1970). However, calibration in this method is difficult, limiting its application (Massimilla, 1978; and Donsi et al, 1980). Using an isokinetic sampling probe set along the flow direction to collect particles can measure the mass flux and velocity of solid particles in the riser of circulating fluidized beds. Dividing the amount of solids collected by the time of collection and the open area of the sampling tube gives the mass flux of solid particles. The isokinetic conditions are usually obtained by balancing the static pressure difference inside and outside the sampling probe. However, to obtain particle velocity, it is necessary to measure the solids concentration simultaneously (Monceaux et al, 1986; Bader et al, 1988; Rhodes et al, 1988; Herb et al, 1992). Both impact and isokinetic sampling methods are indirect measurement methods, which need only simple equipment

and often make continuous measurement possible (Donadono et al, 1978; Donsi et al, 1980). However, these devices tend to interfere with the flow system being investigated and often require other parameters, such as the solids concentration, to be determined simultaneously, thus increasing the complexity and reducing the accuracy. Direct visual techniques have also been employed to measure particle velocity. These include high-speed photography for dilute systems (Donadono et al, 1978; Donsi et al, 1980), periodically excited fluorescent particles, other tracer techniques, and particle imaging velocimetry PIV. These methods tend to be accurate and are usually non-intrusive. Another advantage is that the whole pattern of particle movement may be obtained instantly. However, analyses of the results tend to be very time-consuming and often require a high-speed computation system. Another disadvantage is that the associated equipment is generally expensive. Laser Doppler Velocimetry LDV is another powerful instrument in fluid dynamics research, which is reliable, accurate and easy to use (Bachalo, 1994; Adrian, 1991). The basis of this technique is that the frequency of light scattered by a moving particle is subject to a Doppler shift and the particle velocity can be determined by measuring the shift. This method has been demonstrated as being able to accurately measure gas–solids velocities in gas–solid suspensions, with very small seed particles added in the flow for gas velocity, over a velocity range from creeping to hypersonic flow. The measurements are made in situ and non-intrusively in the flow fields that range in size from less than a millimeter to many meters in cross-section. Levy and Lockwood (1983), Kale and Eaton (1985), Hamdullahpur and Mackay (1986) and Berkelmann and Renz (1989) have used LDV to measure particle and gas velocities in the freeboard region of a fluidized bed. However, LDV can only be applied when an

optic path is available to the measurement site so that it is only suitable for dilute suspensions. In addition, LDV instruments are costly. Cross-correlation technique has been widely used in determining particle velocity. The principle is that individual or groups of particles in the flow are detected at two locations aligned in the direction of particle flow. The velocity can then be determined by computing the cross-correlation function. A common technique is to cross-correlate capacitance signals from two nearby needle probes. Mathur and Klinzing (1984) applied the cross-correlation method for measuring the average particle velocity using signals from two commercial dielectric-property measuring devices in pneumatic transport. Euzen et al (1993) used a capacitive sensor to measure the particle velocity in a gas–solids reactor. The capacitive measurement is based on variations in dielectric capacitance caused by the change in solids concentration in a measuring volume. If the capacitance variations are measured at two points fairly close to each other in the main particle flow direction, the solids velocity can be obtained from cross-correlation of the two signals. Such capacitive measurements are sensitive to electrostatic effects, so that good grounding is needed to decrease the interference.

Cross-correlation technique is applicable to optic fiber probes containing light-emitting and light-receiving fibers to detect reflected light from particles in their vicinity. Measurements of particle velocity and concentration have been reported using optic fiber probes in conventional low-velocity fluidized beds and pneumatic transport systems (Oki et al, 1975; Shirai et al, 1977; Horio et al, 1980; Ishida et al, 1980; Patrose, 1982; Rathbone, 1989; Zhou et al, 1991). A significant disadvantage of the cross-correlation

method is the preferential detection of the velocity of particle clusters over individually flowing particles, especially when the gas–solids suspension is not very dilute. For both the capacitance and light reflection signals, the passage of particles closely grouped together in the form of clusters or agglomerates tends to cause much larger peaks than individual particles. During cross-correlation, it is the large peaks in the signals which dominate in determining the maximum of the cross-correlation function. On the other hand, individual particles tend to travel at higher velocities in most gas–solids upflow given their reduced slip velocities. As a result, the cross-correlation method tends to underestimate the actual particle velocity in up-flow, while overestimating the magnitude of the velocity for downflow systems. Another disadvantage of the cross-correlation method is that it gives only an average value over extended periods. It provides no information on the velocity distribution or the instantaneous velocity.

1.3 Hydrodynamics of TFB

Compared with other fluidization regimes, studies on hydrodynamics of turbulent fluidized beds (TFB) are relatively scarce and mainly focusing on the macro structures, such as dilute phase volume fraction and dense phase void. Knowledge of the local flow structures of TFB had been started from the investigation on the properties of bubbles (Lanneau, 1960). Assuming two distinct phases as in (TFB), dilute phase volume fraction was obtained. Local void fractions were also roughly been deduced using gas tracer (Lee and Kim, 1989), and from solids holdup signals measured by optical probes (Nieuwland et al,1996; Farag et al, 1997; Zhang et al, 1997). However, it is questionable how to define the void with these measurements (Bi et al, 2001). Investigations on dense phase

seemed to reach similar conclusions: the dense phase void increased with increasing air velocity in TFB (Werther and Wein 1994; Yamazaki et al, 1991). Relatively, only a few studies focused on the macro structures of TFB. The radial non-uniformity decreased for the higher static bed height due to smaller voids near the wall at higher axial positions. Farag et al (1997) found two circulation cells in a column of diameter 0.3 m, and a more homogeneous flow structure for a 0.5 m diameter column in the turbulent regime. The greater homogeneity for the larger column could result from a lesser wall effect and turbulent eddies disrupting gulf streaming (Ege, 1996). Core-annular structure was observed in a FCC TFB by Zhu and Zhu (2008c). Obviously, studies on the flow structures are not adequate to understand TFB regimes, possibly due to its transition characteristics and lack of knowledge of TFB (Zhou et al, 2000).

TFB has not been always recognized as an actual fluidization regime (Bi et al, 2000). It behaves like a continuous phase, where intermittent and interspersing voids and dense pockets alternating. However, Rhodes (1996) did not considered turbulent regime as a separate regime of dense fluidization. He equated this regime to dilute flow regime at different suspension densities in the freeboard of a bubbling bed, to dilute region of a CFB or even to pneumatic transport under certain conditions. Such a flow regime was related to the variation of the solids inventory in the bed (Rhode, 1996). While Rhode did not refer to the same flow as other researchers, he emphasized the importance of solids circulation to correctly study TFB.

There are also uncertainties about transition critical velocity determination. Yerushalmi and Cankurt (1979) divided the transition flow regime between bubbling and fast fluidization regimes into turbulent transition and turbulent fluidization regimes using transient velocity u_c , onset velocity u_k and ending velocity u_{tr} . Using pressure drop signals with pressure transducers along the bed, u_c and u_k were defined at the specific air velocities corresponding to the maximum standard deviation and to the levelling off of standard deviation of the pressure signals respectively. However, other authors found no such a u_k to mark the beginning of TFB (Kashkin et al, 2003). It is now widely considered that TFB extends from u_c to the onset of fast fluidization, u_{tr} (Bi et al, 2000). This confusion resulted from the fact that pressure fluctuations of a gas-solid system and flow regime transition are two different hydrodynamic phenomena. They may or may not coincide in the same pace or pattern (Horio et al, 1992). Therefore, it might be a proper way to relate the critical air velocity of TFB to the standard deviation of the local solids holdup, one property parameter of local flow structures of TFB (Zhu and Zhu, 2008).

The confusion on the ending air velocity of TFB or onset air velocity of CFB, u_{tr} was attributed to the lack of knowledge about how the flow structure of a gas-solid system transited from TFB to CFB (Kashkin et al, 2003). TFB can operate at much higher than particles terminal velocity and at higher density than dilute transport as there exist plenty of high density clusters (Guilherme et al, 2009) and different flow structures compared to BFB and CFB (He et al, 2009). As the ending of TFB responds just to the onset of CFB, the high density flow structure and solids circulation are two important factors influencing the transition from TFB to CFB. Yerushalmi and Cankurt (1979) defined u_{tr}

as the transport air velocity close to terminal velocity of median particle using pressure diagram. The transport velocity, corresponding to the saturation carrying capability of the gas-solid system, is used in defining the regime transition between the dilute transport suspension flow and fast fluidization (Xu et al, 2001; Yang, 2004). Schnitzlein et al (1988) also found such a velocity did not mark any observable changes of flow structure. Related to choking velocity and solids circulation rate, a significant entrainment velocity in the fluidized bed was defined as the transition point from TFB to CFB (Bi, 1994), while high solids circulation of $50\text{kg/m}^2\text{s}$ was obtained in an FCC particle CTFB at 0.70 m/s air velocity equal to u_c (Zhu and Zhu, 2008b).

There were also debates on the void velocity in TFB. Pointing at studies on void rising being analogous to the bubbling regime (Lanneau, 1960; Yamazaki et al, 1991; Lu et al, 1997; Farag et al, 1997; Taxil et al, 1998), other researchers found that voids in turbulent fluidized beds tend to be small and transient, with indistinct or irregular boundaries (Rowe & MacGillivray, 1980; Lee & Kim, 1989). As $u_g > 0.6\text{m/s}$, it was very hard to identify the voids in TFB due to their rapid rising (Lanneau, 1960). Negative rise velocities in the centre of TFB of diameter 0.3 m were observed by Farag et al (1997), indicating a circulation pattern where gas travels downwards near the axis and upwards near the wall. Taxil et al (1998) found a correlation between the void chord length and rise velocity, which was widely used in measuring the bubble rising velocity in bubbling fluidized bed. Using cross-correlation method on solids holdup signals measured by dual channel optical fibre probes, Zhu and Zhu (2008a) obtained the profiles of the upward

and downward particle velocities, indicating potential applications of cross-correlation methods in studies on TFB.

1.4 Studies on circulating turbulent fluidized bed (CTFB)

CFB and TFB can mostly make up their shortcomings one another (Zhu and Zhu, 2008a). This raises a question how to combine them together without losing their merits and to make the fluidization reactors more efficient (Zhu and Bi, 1995). Zhu and Zhu (2008a) integrated a conventional turbulent fluidized bed into a high-density circulating system to simultaneously achieve high efficient gas-solid contact and low solids backmixing. Their investigations proved the benefits of such a combination. The results at $u_g = 1.0, 2.0$ m/s and $G_s = 50, 150$ kg/m²s demonstrated that the CTFB is capable of: (1) recycling particles and maintaining a high solids concentration and gas-solid reaction intensity; (2) handling high particle capacity with low gas by-passing; (3) exhibiting no net downflow of solids over the whole section; (4) providing axial homogenous flow and enforced radial homogeneity of the solids suspension (Zhu and Zhu, 2008a and c). Their results demonstrated that the CTFB operation is achievable and its flow structure can be attributed to a new flow regime, the circulating turbulent fluidization regime, independent of turbulent fluidization, fast fluidization and dense suspension upflow (Zhu, 2010; Qi and Zhu, 2009). Obviously, reported investigation results on CTFB are not adequate in understanding the new fluidization regime and designing CTFB reactors. Experiments should be conducted at a wide range of air velocities and high solids circulation rates to

depict CTFB macroscopically and microscopically, especially on the transition mechanism and detailed hydrodynamics of CTFB.

1.5 Objectives

The objectives in this thesis are composed of the following five parts:

1) Study hydrodynamics and detailed flow structures of BFB, TFB, CTFB, CFB and HDCFB to explore the transition, the differences and similarities across the regimes and to further distinguish the new fluidization regime, CTFB, from the other regimes;

2) Study the transient mechanism and characteristics spanning from BFB to HDCFB to define the criteria for determining the transient critical air velocities demarcating the novel circulating turbulent fluidized bed;

3) Investigate properties of the dense and dilute phases in the various fluidized beds to further characterize the heterogeneous flow structures observed at high density and high solids flux;

4) Analyze dynamic behaviors of the dense and dilute phases in CTFB, such as, phase particle velocities in upward and downward directions, slip velocity, apparent particle velocity and local solids flux, etc. to understand hydrodynamics in CTFB;

5) Establish new data processing methods to divide the dense and dilute phases and to compute the phase particle velocities.

1.6 Thesis organization

Following the introductory, a comprehensive literature review on hydrodynamics of gas-solid fluidization is presented in chapter 1.

Chapter 2 provides the details about the experimental apparatus, the measurement techniques and experimental procedures in this study.

Chapter 3 presents the calibration procedure of optical fibre probes at low and high solids concentrations. A novel technique is developed for this calibration, with which significant improvements are made on high solids concentration over previous reported investigations. Using this technique, the probes are uniquely calibrated in a downer and in a pseudo bubble-free fluidized bed for FCC powders to obtain the calibration curves.

In Chapter 4, a Moment Consistency Data Processing Method (MCDPM) is proposed based on statistical parameters of the experimental data. From microscopic point, three parameters, the solids holdups of the dense and dilute phases and the relative phase fraction, are obtained using MCDPM in bubbling (BFB), turbulent (TFB), circulating turbulent (CTFB), circulating (CFB) and high density circulating (HDCFB), displaying the different flow structures in the 5 regimes. Using the 3 parameters, the average values and the non-uniformity indices are discussed to explore the flow transition, differences and similarities across the 5 regimes. The micro flow structures in the 5 regimes are also discussed through the probability density function (PDF), skewness and kurtosis of the solids holdup data.

In Chapters 5, the transition mechanism of a circulating turbulent fluidized bed is analyzed through the solids holdup fluctuation, the profiles of the skewness and kurtosis of the solids holdup data, and variation of PDF. The determination criteria for two transition air velocities of CTFB are proposed, corresponding to the transitions from BFB to CTFB and from CTFB to CFB.

In Chapter 6, the detailed hydrodynamics of CTFB are analyzed through the axial and radial profiles of solids holdup, and variation of the annular average solids holdups of the dense and dilute phase and relative phase fraction, suggesting the different flow structure in CTFB from that in other fluidization regimes. The solids circulation effect on the flow is also explored, suggesting the interior solids circulation structure in CTFB is different from that in conventional TFB. Typical characteristics of CTFB are also discussed.

In Chapter 7, based on the phase division procedure proposed with MCDPM, a Divided Phase Cross-Correlation Method (DPCCM) for studying the particle movements in the dense and dilute phases is established by cross-correlating the solids holdup signals of the dense and dilute phases. Using DPCCM, phase particle movement is studied, and phase particle slip velocity, apparent particle velocity, and net local solids flux are defined and discussed to explore the effects of solids circulation on the flow in CTFB.

Chapter 8 summarizes the major findings of this study with recommendations for continuous improvement on this novel fluidized bed reactor.

Reference

Adrian R.J., (1991), *Rev. Fluid Mech.*, 23, 261

Bachalo W.D., (1994), *Int. J. Multiphase Flow*, 20, 261, (suppl.)

Bader R., J. Findley and T.M. Knowlton, (1988), *Circulating Fluidized Technology II*, Pergamon, Toronto, pp. 123–137.

Berkelmann K.G. and Renz U., (1989), *Fluidization VI*, Engineering Foundation, New York, pp. 105–112.

Bi X., (1994), *Flow regime transitions in gas-solid fluidization and transport*, Ph.D. dissertation, University of British Columbia, Vancouver, Canada

Bi H. T., Ellis N., Abba I. A. and Grace J. R., (2000), Review: A state-of-the-art review of gas-solid turbulent fluidization, *Chemical Engineering Science* 55 4789-4825

Bi H. T. and Su P., (2001), Local Phase Holdups in Gas-Solids fluidization and Transport, *AIChE Journal*, Vol. 47(9), 2025

Crescitelli S., Donsi G., Russo G., and Clift R., (1978), High velocity behaviour of fluidized beds: Slugs and turbulent flow. In S. Schlosser, *Selected papers presented at the sixth international congress CHISA '78*, Prague (pp. 1-11).

Donadono S. and L. Massimilla, (1978), Cambridge Univ. Press, UK, pp.375–381

Donsi G., L. Massimilla and L. Colantuoni, (1980), *Fluidization*, Plenum, New York, pp. 295–304.

Ege P., Grislinga A. and deLasa H. I., (1996), Modelling turbulent fluidized bed reactors: Tracer and "bre optic probe studies. *Chemical Engineering Journal*, 61, 179-190

Euzen J.P., P. Trambouze and J.P. Wauquier, (1993), Eds., Scale-up Methodology for Chemical Processes, Gulf Publishing, Houston, Chap. 4

Farag H. I., Ege P. E., Grislinga A. and deLasa H. I., (1997), Flow patterns in a pilot plant-scale turbulent fluidized bed reactor: Concurrent application of tracers and fiber optic sensors. *Canadian Journal of Chemical Engineering*, 75, 851-860

Guilherme J. Castilho and Marco A. Cremasco, (2009), Experimental Study In A Short Circulating Fluidized Bed Riser, *Particulate Science And Technology*, 27: 210–221

Grace J. R., (1990), High Velocity Fluidized Bed Reactors, *Chem. Eng. Sci.*, 45, 1953-1966,

Hamdullahpur F. and Mackay G.D.W., (1986), *AIChE J*, 32, 2047.

He Y., Deen N. G., van Sint Annal and M. Kuipers J. A. M., (2009), Gas Solid Turbulent flow in a Circulating fluidized Bed Riser: Experimental and Numerical Study of Mono-disperse Particle Systems, *Ind. Eng. Chem. Res.*, 48, 8091–8097

Heertjes P.W., J. Verloop and R. Willems, (1970), *Powder Technol.*, 4, 38

Herb B., Dou S., Tuzla K. and Chen, J.C., (1992), "Solid mass fluxes in circulating fluidized beds", *Powder Technology*, 70, 197-205

Horio M., A. Taki, Y.S. Hsieh and I. Muchi, (1980), *Fluidization*, Plenum, New York, pp. 509–518

Horio M., Ishii H. and Nishimuro M., (1992), "On the nature of turbulent and fast fluidized beds", *Powder Technology*, 70, 229-236

Ishida M. and T. Shirai, (1980), *Powder Technol.*, 27, 1

Jahnig C.E., Campbell D.L. and Martin H.A., (1980), "History of Fluidized Solids Development at EXXON", *Fluidization*, (eds. J.R. Grace and J.M. Matsen), Plenum Press, New York, 3-24

Kale S.R. and J.K. Eaton, (1985), *Int. J. Multiphase Flow*, 11, 659.

Kashkin V. N. and Lakhmostov V. S., (2003), Studies on the onset velocity of turbulent fluidization for alpha-alumina particles, *Chemical Engineering Journal*, 91, 215–218

Kehoe P.W.K. and Davidson J.F., (1970), "Continuously slugging fluidized beds", *Chemeca '70*, Institution of Chemical Engineers Symposium Series, Australia: Butterworths, 33, 97-116

Lanneau K. P., (1960), "Gas-solids contacting in fluidized beds", *Transactions of the Institution of Chemical Engineers*, 38, 125-137

Lee G. S. and Kim S. D., (1989), Gas mixing in slugging and turbulent fluidized beds, *Chemical Engineering Communications*, 86, 91-111

Levy Y. and F.C. Lockwood, *AIChE J.*, 29, 1983, 889

Lu C., Xu Y., Shi M. and Shen F., (1997), Two-area model for bubble distribution in a turbulent fluidized bed of fine particles, *Chinese Journal of Chemical Engineering*, 5(4), 287-295

Massimilla L. and Donadono S., (1978), Cambridge Univ. Press, UK, pp. 375–381.

Matheson G.L., W.A. Herbst and P.R. Holt, (1949), "Characteristics of fluid-solid systems," *Ind. Eng. Chem.*, 41, 1099-1104

Mathur M.P. and G. Klinzing, (1984), Part. Sci. Technol, 2, 223

Monceaux L., M. Azzi, Y. Molodtof and J.F. Large, (1986), Fluidization V, Engineering Foundation, New York, pp. 337–344

Nieuwland, J. J. etc., (1996), Measurement of solid concentration and axial solids velocity in gas-solid two phase flow, Powder Technology, 87, 127 – 139

Oki K., T. Akehata and T. Shirai, (1975), Powder Technol., 11, 51

Patrose B. and H.S. Caram, (1982), AIChE J, 28, 604

Perales J. F., T. Coll, M. F. Llop, L.,Puigjaner, J. Arnaldos and J. Casal, (1990), On the Transition from Bubbling to Fast Fluidization Regimes, Circulating Fluidized Bed Technology, Vol. 111, p.73, P. Basu, M. Horio, and M. Hasatani, eds., Pergamon Press, Oxford.

Qi X., Zhu H. and Zhu J., (2009), Demarcation of a New Circulating Turbulent fluidization Regime, AIChE Journal Vol. 55, No. 3, 595

Rathbone R.R., M. Ghadiri and R. Clift, (1989), Fluidization VI, Engineering Foundation, New York, pp. 629–635

Rhodes M.J., P. Laussmann, F. Villain and D. Geldart, (1988), Circulating Fluidized Technology II, Pergamon, Toronto, pp. 155–164.

Rhodes M., (1996), What is turbulent fluidization, Powder Technology, 88, 3-14

Rowe P. N. and MacGillivray H. J. (1980), The structure of a 15 cm diameter gas fluidized bed operated at up to 1 m/s and seen by X-rays. In J. R. Grace, & J. M. Matsen, *Fluidization* (pp. 545-553), New York: Plenum Press

Schnitzlein M. G. and Weinstein H., (1988), Flow characterization in high-velocity fluidized beds using pressure fluctuations. *Chemical Engineering Science*, 43, 2605-2614

Shirai T., M. Ishida and Y. Tto, N. Inoue and S. Kobayashi, (1977), *J. Chem. Eng. Jpn.*, 10, 40.

Squires A.M. (1986), "The story of fluid catalytic cracking: The first circulating fluid bed", *Circulating Fluidized Bed Technology*, (eds. P. Basu), Pergamon Press, Toronto, 1-19

Taxil I., Guigon P., Archimbault F. and Gauthier T. A., (1998), Gas flow characterization in turbulent fluidization for FCC catalyst. In L. S. Fan, & T.M. Knowlton, *Fluidization IX* (pp. 69-76). New York: Engineering Foundation

Thiel W. J. and O. E. Potter, (1977), "Slugging in Fluidized Beds," *Ind. Eng. Chem. Fund.*, 16, 242

Wang J., (2010), Flow structures inside a large-scale turbulent fluidized bed of FCC particles: Eulerian simulation with an EMMS-based sub-grid scale model, *Particuology*, 8, 176–185

Werther J. and Wein J., (1994), Expansion behavior of gas fluidized bed in the turbulent regime. *A.I.Ch.E. Symposium Series*, 90(301), 31-44

Xu G., Nomura K., Gao S. and Kato, K., (2001), More Fundamentals of Dilute Suspension Collapse and Choking for Vertical Conveying Systems, Vol. 47, No. 10, AIChE Journal, 2177

Yamazaki R., Asai M., Nakajima M. and Jimbo G. (1991), Characteristics of transition regime in a turbulent fluidized bed, *Proceedings of the forth China-Japan fluidization conference* (pp. 720-725), Beijing: Science Press

Yang W., (2004), "Choking" Revisited, *Ind. Eng. Chem. Res.*, 43, 5496-5506

Yates J. G. and J.R. Simons, (1994), *Int. J. Multiphase Flow*, 20, 297, (suppl.)

Yerushalmi J., Turner D.H. and Squires A.M., (1976), "The fast fluidized bed", *Ind. Engrng. Chem., Proc. Des. Dev.*, 15, 47-57

Yerushalmi J. and N. T. Cankurt, (1979), Further Studies of the Regimes of Fluidization, *Powder Technology*, 24 187 - 205

Zenz F.A., (1949), "Two-phase fluidized-solid flow", *Ind. Engrng Chem.*, 41, 2801-2806

Zhang X. and Qian Y., (1997), Mass transfer between the bubble and emulsion phase in a turbulent fluidized bed with FCC particles. In Q. Yu & C. Huanqin, *Advances in environmental engineering and chemical engineering* (pp. 190}193). Guangzhou, China: South China University of Technology Press

Zhou C., M.C. Slaughter and S.L. Soo, (1991), *Rev. Sci. Instrum.*, 62, 2036

Zhou H., Lu J. and Lin L., (2000), Turbulence structure of the solid phase in transition region of a circulating fluidized bed, *Chemical Engineering Science*, 55, 839-847

Zhu J. (2010), Circulating turbulent fluidization—A new fluidization regime or just a transitional phenomenon, *Particuology*, 8, Pages 640-644

Zhu J. and Bi H., (1995), Distinctions between Low Density and High Density Circulating Fluidized Beds, *The Canadian Journal of Chemical Engineering*, Volume 73, 644

Zhu Haiyan and Jesse Zhu, (2008a), Gas-Solids Flow Structures in a Novel Circulating-Turbulent Fluidized Bed, *AIChE Journal*, Vol. 54, No. 5, 1213

Zhu Haiyan and Jesse Zhu, (2008b), New Investigation in Regime Transition from Bubbling to Turbulent Fluidization, *The Canadian Journal of Chemical Engineering*, Vol. 86(6), 553

Zhu Haiyan and Jesse Zhu, (2008c), Comparative study of flow structures in a circulating-turbulent fluidized bed, *Chemical Engineering Science*, 63, 2920-2927

Zhang H. and Zhu J.-X., (1998), A novel calibration procedure for a fiber optic solids concentration probe, *Powder Technology*, 100, 260-272

2 Experimental Apparatus and Measurement Technique

2.1 Circulating turbulent fluidized bed

To conduct the experiments on the detailed hydrodynamics of CTFB, a solids circulating loop was setup, where two parallel columns (riser and downcomer) connected with a bottom inclined tube and a smooth top bent as shown in Fig. 1. The riser column i.d. is 0.101 m and its height is 3.6m at lower part and an upper quick discharging section with a diameter of 0.203 m and a total height of 6.4 m. At the bottom of the riser a disk type air distributor was also installed, and an annular air distributor was installed between the CTFB column and the upper discharge section, both being perforated with 12.6% free area. The smooth bent on the top of quick discharging section was connected to a primary cyclone at the inner top of a down comer, the other column (i.d. 0.305 m) in the loop. A solid control valve was installed in the inclined tube and a solids circulation rate measurement device with two flapper valves in the top section of the downcomer just below the primary cyclone to measure the solids flow rate. Before air discharge, two other standard cyclones and a bag filter house were linked between the exit of the primary cyclone and the air discharge line in series, where fine particle was captured and returned to a seal tank connected the downcomer below the solid circulation flow rate control device.

Two streams of metered air were supplied through two orifice plates, regarded as primary and secondary air. The primary air fluidized the particles coming from the downcomer at a desired rate where the gas-solid flow was in steady status. To maintain the requested fluidization regimes in CTFB, the secondary air through the annular distributor at a

proper flow rate was able to quickly discharge the particles out of CTFB to maximum particle delivery capacity by relatively increasing the backpressure of the downcomer and dragging force of the primary air. Most of the entrained particles in gas-solid stream from the quick discharge section were separated in the primary cyclone and back to the circulating process with or without being measured according to the experiment requirements, while the clean air was discharged downstream at the filter. The special design of the quick discharge section made it possible for CTFB to operate at high solids circulation rates and high suspension density at superficial gas velocity of 1–5 m/s. FCC particles with a particle density of 1780 kg/m³ and a Sauter mean diameter of 76 μm was used in the experiments, and air was at the relative humidity of 70 and 80% maintained using steam supply to minimize the electrostatic effects.

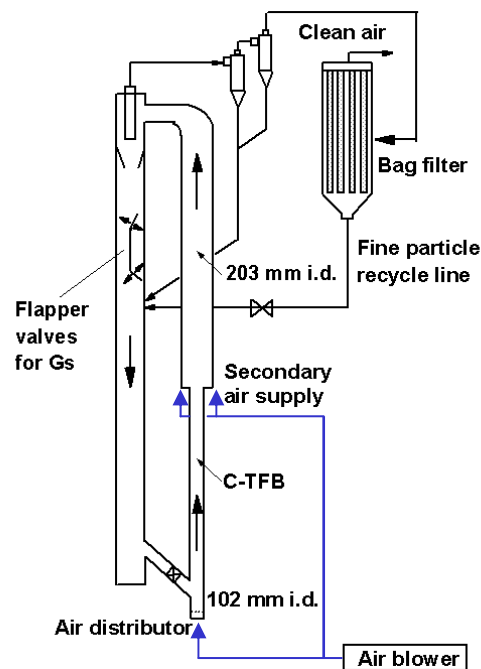


Figure 2.1 Schematic drawing of experimental apparatus

2.2 Particle Properties

Spent fluid catalytic cracking (FCC) catalyst with a particle density of 1780 kg/m³ and a Sauter mean diameter of 65 μm was used as solid phase. The particle size distribution is summarized in Table 2.1.

Table 2.1 FCC particle size distributions

Particle Size (μm)	Volume in %
<28.222	0.61
32.015	1.66
36.319	3.10
41.2	4.96
46.738	6.97
53.02	8.90
60.147	10.45
68.231	11.35
77.403	11.45
87.807	10.75
99.609	9.37
112.998	7.55
128.286	5.57
145.416	3.71
164.962	2.16
187.135	1.06
212.288	0.33
>240.822	0.05

2.3 Measurement Techniques

Experimental studies conducted in this research include the following parameters measurements: superficial gas velocity, u_g ; pressure gradient along the column, $\Delta P/\Delta H$; local solids holdup, ϵ_s ; solids circulation rate, G_s ; and local particle velocity, v_p .

2.3.1 Measurement of superficial gas velocity

Superficial gas velocity in the three fluidized beds was measured by a sharp-edged orifice meter on which vena-contracta taps had been installed. The orifice meter was designed following the ASME standards (American Society of Mechanical Engineers, New York, 1959) so that the performance of the orifice meter could be predicted accurately without calibration (McCabe et al, 1993). Eq. 2.1 is used in this study to calculate the air flow-rate:

$$Q = \frac{C_0 Y S_0}{\sqrt{1 - \beta^4}} \sqrt{\frac{2g\Delta h(\rho_{H_2O} - \rho_g)}{\rho_g}} \quad (2.1)$$

Where Q is the volume flow-rate of air through the orifice (m^3/s); C_0 is the orifice coefficient and it is taken as 0.609 for vena-contracta taps; β is the ratio of orifice diameter to tube diameter; S_0 is the cross-sectional area of the orifice; Δh is the pressure drop reading, which shows the pressure drop across the orifice, mH_2O ; ρ_g is the air density when flowing through the orifice; and Y is an expansion factor, which provides modification of the equation when the fluid is not incompressible. An empirical equation for Y of a standard sharp edged orifice is available (Fluid Meters: The theory and application, 5thed., American Society of Mechanical Engineers, New York, 1959):

$$Y = 1 - \frac{0.41 + 0.35\beta^4}{\gamma} \left(1 - \frac{p_1}{p_2}\right) \quad (2.2)$$

where p_1 and p_2 are the pressures at stations 1 and 2, which are positioned before and after the orifice plate; γ is the isentropic exponent and it is taken as 1.40 when the gas is considered ideal.

The superficial gas velocity in a fluidized bed is dependent upon both volumetric flow-rate at the orifice meter and the pressure ratio P_c/P_m , where P_c is the pressure at the inlets of the bed; P_m is the pressure at the upstream of the orifice meter. The superficial gas velocity can be calculated using Eq. 2.3. S is the cross-sectional area of the bed.

$$u_g = \frac{Q}{S} \frac{P_c}{P_m} \quad (2.3)$$

2.3.2 Differential pressure measurement

To obtain pressure drops along the bed, 10 pieces of differential pressure transducers from Omega Engineering (PX163-120D5V and PX162-027D5V) were installed along the riser. Excitation voltage supplying to these pressure transducers was 8 VDC (at 20 mA each), giving a voltage output of 1 to 5 VDC over its pressure ranges. Manometers were used to calibrate the pressure transducers: Air source of 20 psig was connected to one end of the meter and the high-pressure pin of the unidirectional differential pressure transducer. The other end of the U-tube and the other pin of the pressure transducer were open to room air. The typical calibration data were well agreeable with a linear calibration curve. Differential pressure data were acquired with an on-line personal computer via a 16-bits A/D converter. The transducer output signals were linearly

proportional to the pressure drop in the range of 0 to 10 kPa. For all experiments, the signals of the differential pressure fluctuations were sampled with a frequency of 1000 Hz and stored on a hard disk of a computer. The total acquisition time was 40s and thus the maximum length of the time series was 40,000 points. The locations of pressure taps along the fluidized bed are shown in Table 2.2. It can be seen that the lowest position is 0.3 m higher than the gas distributor, which is above the primary bubble formation and coalescence controlled region.

Table 2.2 Locations of pressure transducers

Section: range (m)	Mid-elevation (m)
0.244-0.515	379.5
0.515-0.812	663.5
0.812-1.095	953.5
1.095-1.478	1286.52
1.478-1.819	1648.62
1.819-2.209	2014.38
2.209-2.697	2453.4
2.697-3.005	2851.32
3.005-3.427	3216.5
3.427-3.794	3611.06

2.3.3 Local solids holdup measurement

Experimental data were acquired using four multi-fibre optical reflective probes of model PV-6, developed by the Institute of Process Engineering, Chinese Academy of Sciences, Beijing, China. Each of the four probes consists of two fibre bundles located on the same vertical line. Each bundle is composed of both light-emitting and receiving quartz fibres arranged in an alternating array, corresponding to emitting and receiving layers of fibres. The diameter of each fibre was 25 μm . Light from a light emitting diode (LED) transmits through the emitting half of the fibres to the tip, where upon hitting particle(s) in the riser, will be reflected back to the probe. The intensity of the reflected light depends on the concentration, size distribution, composition, and shape of the particles. The received light reflected by the particles was converted by a photo-multiplier into voltage signals. The voltage signals were further amplified and fed into a PC. The sampling rate was 50 kHz and data were collected for 131 sec. A special calibration procedure in high particle density environment had been carried out and the calibration curves had been obtained to convert the voltage data to solids holdups, following the procedure proposed by Zhang et al (1998).

The probes were setup at four separate axial elevations and traversed horizontally to measure local solids holdups at eleven radial positions (Fig. 2.2). The four axial locations were chosen in an effort to characterize the acceleration zone (0.8m) and the fully developed zone (1.5, 2.2 and 3.0m). Radial positions were chosen at the midpoints of eleven equal area circles ($r/R = 0.0, 0.16, 0.38, 0.5, 0.59, 0.67, 0.74, 0.81, 0.87, 0.92$, and

0.98) at each axial level within the risers. There were two PV6 units used in the experiments: a master and a slave. A special setup procedure was carried out for the two units to control four probes and a special data processing method was implemented with normalized calibration curves and different unit gains and offsets to obtain consistent experimental results throughout the bed. At one radial location two adjacent probes were connected to the units and then switched to the other two. To ensure the consistency of the data at one specific operating condition, the data at all anticipated locations were collected within one run by the four probes.

From the solids holdup signals, the heterogeneous flow structures in a fluidized bed can be studied macroscopically and microscopically by signal moment estimations, such as mean solids holdup, $\bar{\varepsilon}_s$, standard deviation σ , skewness S and kurtosis K (Eqs. 2.2-2.5).

$$\bar{\varepsilon}_s = \frac{1}{N} \sum_{i=1}^N \varepsilon_i \quad (2.4)$$

$$\sigma = \left[\frac{1}{N-1} \sum_{i=1}^N (\varepsilon_i - \bar{\varepsilon}_s)^2 \right]^{1/2} \quad (2.5)$$

$$S = \frac{\sum_{i=1}^N (\varepsilon_i - \bar{\varepsilon}_s)^3}{(N-1)\sigma^3} \quad (2.6)$$

$$K = \frac{\sum_{i=1}^N (\varepsilon_i - \bar{\varepsilon}_s)^4}{(N-1)\sigma^4} \quad (2.7)$$

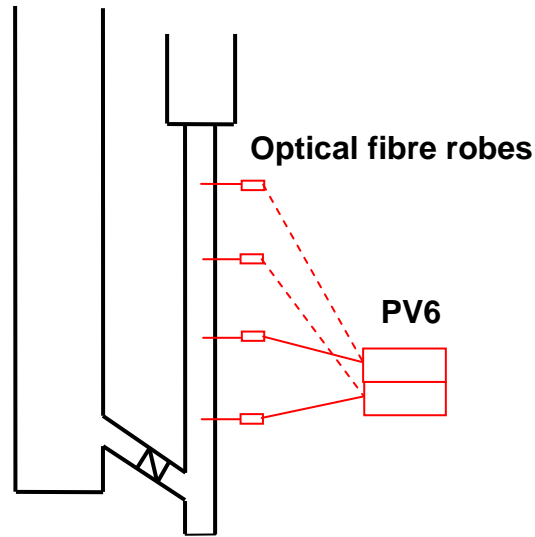


Figure 2.2 Setup of optical fibre probes and pressure transducers

2.3.4 Cross-correlation method of particle velocity

In addition to being converted to the local solids holdup, the dual signals of solids holdup acquired by a two-channel optical fibre probe can be used in computing the particle velocity. To measure the solids holdup fluctuations, the two channels of the probe are aligned vertically, and they respond to upward or down ward movements of the particle in front of the probe. If a particle or a cluster velocity is v_s , there is a time delay τ for both of the channel detecting the same particle or cluster, as shown Eq. 2.8.

$$v_s = \frac{d}{\tau} \quad (2.8)$$

where d is the distance between the two channels. The time delay can be calculated using cross-correlation method, as shown by Eq. 2.9. For different time delay, τ , Eq. 2.9 gives different cross-correlation coefficient and only the time delay corresponding to the maximum coefficients are used in producing instantaneous particle velocity solutions over a given tiny time period using Eq. 2.8. For dual solids holdup signals, $\varepsilon_{s1}(t)$ and $\varepsilon_{s2}(t)$, the cross-correlation can be expressed as

$$\phi(\tau) = \frac{\sum_{N_t} [(\varepsilon_{s,1}(n) - \overline{\varepsilon_{s,1}})(\varepsilon_{s,2}(n - \tau) - \overline{\varepsilon_{s,2}})]}{\sqrt{\sum_{N_t} (\varepsilon_{s,1}(n) - \overline{\varepsilon_{s,1}})^2} \sqrt{\sum_{N_t} (\varepsilon_{s,2}(n - \tau) - \overline{\varepsilon_{s,2}})^2}} \quad (2.9)$$

Using instantaneous particle velocity and solids holdup, other local parameters can be derived, such as local flux, local net flux, average particle velocity and solids circulation rate, etc, as shown in Eqs. 2.10-2.13.

$$F_{s,i,j} = \frac{\rho_p}{T_{i,j}} \int_{T_i} v_{s,i,j}(t) \varepsilon_{s,i,j}(t) dt, \quad (2.10)$$

$$G_{s,l} = \sum F_{s,i,j} \quad (2.11)$$

$$V_{s,i,j} = \frac{1}{T_{i,j}} \int_{T_i} v_{s,i,j}(t) dt \quad (2.12)$$

$$G_s = \frac{2}{R} \int_{T_i} G_{s,l} dr \quad (2.13)$$

2.3.5 Solids circulation rate measurement

The measuring device of solids circulation rate is located at the top of the downcomer. Two half butterfly valves and the vertical separate board conduct and collect the particles from the primary cyclone in a measureable space. By appropriately flipping over the two

valves from one side to the other, solids circulated through the system can be accumulated in one side of the measuring section for a given time period to provide the solids circulation rate:

$$G_s = \frac{V\rho_b}{S\Delta t} \quad (2.14)$$

where V is the volume of the half section during time period (Δt), m^3 ;

Nomenclature

d , distance between the emitting and receiving optical fibre bundles of the probe, m

F_p , phase solids flux, kg/m^2s

G_s , cross-sectional average net solids flux or solids circulation rate, kg/m^2s

G_{sl} , local net solids flux, kg/m^2s

K , standard kurtosis of local solids holdup fluctuations

N , population of a time series

R , radius of the column, m

S , skewness of local solids holdup fluctuations

T , time, s

V , local average particle velocity, m/s

\bar{V}_s , apparent particle velocity, m/s

r , radial position, m

u_g , superficial air velocity, m/s

v_s , instantaneous particle velocity, m/s

z , elevation from the air distributor, m

ρ_p , particle density, kg/m³

ϵ_s , local time-averaged solids holdup

τ , delay time, s

σ , standard deviation of local solids holdup fluctuations

σ_p , standard deviation of differential pressure drop

ρ_b is the bulk density of the particles, kg/m³ ;

Δt is the time period when the particles accumulated in one side of the measuring section, s.

References

ASME (1959), "Fluid Meters: Their theory and applications", 5th ed., American Society of Mechanical Engineers, New York, 50-72

Bai D. and Kato K., (1995), "Saturation carrying capacity of gas and flow regimes in CFB", Journal of Chemical Engineering of Japan, 28(2), pp.179-185

Cui H., Mostoufi N. and Chaouki J. (2001), Comparison of measurement techniques of local particle concentration for gas-solid fluidization, In: Fluidization X (eds. M. Kwauk J., Li and W.C. Yang, United Engineering Foundation, Beijing, 779-786

Johnsson H, and Johnsson F., (2001), Measurements of local solids volume fraction in fluidized bed boilers. Powder Technol.;115:13–26.

Liu JZ, Grace JG and Bi HT., (2003), Novel multifunctional optical-fibre probe: development and validation. AIChE J.;49(6):1405–1420.

Liu JZ, Grace JG and Bi HT., (2003), Novel multifunctional optical-fibre probe: high-density CFB measurements. *AIChE J.*, 49(6):1421–1432.

Mastellone M.L. and Arena U., (1999), “The effect of particle size and density on solids distribution along the riser of a circulating fluidized bed”, *Chemical Engineering Science*, 54, 5383-5391

McCabe, (1976), “Unit operations of chemical engineering”, 3rd ed., McGraw-Hill, New York, 172-220

Park A, Bi HT and Grace JR., (2002), Reduction of electrostatic charges in fluidized beds. *Chem Eng Sci.* 2002;57:153–162.

van Ommen JR and Mudde RF., (2007), Measuring the gas-solids distribution in Fluidized beds - a review. in: Bi HT, Berruti F, Pugsley T, eds. *Fluidization XII*. Vancouver: Engineering Foundation, 31–46.

Werther J., (1999), Measurement techniques in fluidized beds. *Powder Technol.*, 102:15–36.

Zhang H, Johnston PM, Zhu JX, de Lasa HI and Bergougnou MA., (1998), A novel calibration procedure for a fibre optic solids concentration probe. *Powder Technol.*, 100:260–272.

Zhu HY and Zhu JX., (2008), Comparative study of flow structures in a circulating-turbulent fluidized bed. *Chem Eng Sci.*, 63:2920–2927.

Zhu HY. and Zhu JX., (2008), Gas-solids flow structures in a novel circulating turbulent fluidized bed. *AIChE J.*, 54(5):1212–1223.

3 Dynamic calibration of optical fibre probes in gas-solid flow systems: low and high solids concentrations

3.1 Introduction

Reflective optical fibre probes have found extensive applications in the study of multi-phase flow systems due to their relatively simple structure and small size. These probes do not disturb the overall flow structure and allow existing pressure taps along the reactor wall to be used as insert locations for the rapid and sensitive measurement of the radial and axial particle concentrations. They measure solids concentrations under very dilute to very dense conditions in gas or liquid media. Furthermore, they are almost independent of temperature, humidity and electromagnetic fields. For local measurements, the optical fibre probes are very effective because of their small proliferative angle and small effective responding distance (Liu, et al, 2003; Amos, et al, 1996). Due to these advantages, reflective optical probes have become increasingly popular for the characterization of the particulate phase behaviour in gas-solid flow systems (Zhang et al, 1998).

The optical fiber probe measurement techniques are based on the modulation of the incident radiation caused by the particles in a fluidized bed. These methods rely on the absorption, scattering and reflection of the incident light by the particles, and generally the intensity of the reflected light is measured and converted to electrical signals/voltages.

The change in voltages of an optical probe is proportional to the variation of the solids concentrations in a gas-solid fluidized bed. However the quantitative analysis of the relationships between them is unfruitful without calibrating the probe. By definition, calibration of a probe is referred to finding a mapping function or calibration curve with specific experiments and computations that convert the voltage time series into solids concentration time series from point to point and vice versa.

In contrast to all researches on gas-solid flow, more challenges are presented on optical probe calibration, not only from the heterogeneity of gas-solid phases and particle size distribution, but also from instability of the two phase flow. That is the reason for limited publications on the optical probe calibration compared to other measurement methods in gas-solid flow systems. Moreover, nearly all investigations performed on probe calibration are focused on obtaining relatively homogeneous solids mixture or flow at low solids concentrations (Zhang et al, 1998; Amos et al, 1996; Song et al, 2004; Cutolo et al, 1990; Wiesendorf and Werther, 2000; Matsuno et al, 1983), probably due to the difficulty on maintaining a homogeneous flow condition at high solids concentrations.

There are two kinds of optical probe calibration methods: indirect and direct. Song et al (2004) used mixtures with different ratios of FCC to black coke particles to indirectly simulate a wide range of the solids holdups in bubbling and turbulent fluidization regimes. An optical probe to be calibrated was submerged into the mixture and fed back signals to produce the mapping function through a deliberate procedure. The calibration curve was confirmed with the data computed from the pressure drops across the

measurement interval. Obviously in this technique only the first layer of particles facing the probe had been considered. Theoretical analysis (Liu et al, 2003; Amos, 1996; Rundqvist et al, 2003) had shown that the response of the optical probe was also influenced by other layers of particles in the bed. In addition, Herberta (1994) considered that a calibration technique based on the comparison of the signals with voidages calculated from the pressure profile was invalid since the reference volume pertinent to the pressure difference was completely different from the local measurement. Rundqvist et al (2003) proposed another indirect calibration procedure, in which the signals from an optical probe were assumed to be proportional to the intensity of the reflected light. They derived a complicated formula using Mont Carlo simulation technique to relate the optical probe responses to solids holdup. The obvious common limitation of all indirect calibration procedures is the effects of the glare points of particles, especially of rough particles (Magnusson et al, 2005). The indirect procedures also do not address the differences between the unique state of the calibration data and the time average of dynamic signals of the probe.

One of the direct calibration methods allowed particles to fall through a series of nets, which acted as a solids distributor to create a solids suspension. Matsuno et al (1983) used particle terminal velocity to evaluate the solids fraction in this method and calibrated the probe up to 1% solids holdup. To increase the solids holdup for calibration, Cutolo et al (1990) put the sieves in a pipe below a hopper and measured the solids rate with a switch tube at the pipe exit. Later, downers were used for optical probe calibrations (Herbert et al, 1994; Zhang et al, 1998; Saberi et al, 1998) due to their relatively uniform radial profiles of solids concentration in the fully developed section

(Zhang et al, 1999). Although the solids concentration in the downer method was higher than free falling particle method, the reported calibration range of solids holdup with the downer calibration technique did not cover solids concentrations in high density fluidized beds, such as turbulent fluidized beds and high density circulating fluidized beds (Zhang et al., 1998; Herbert et al, 1994). By way of exception Saberi et al (1998) proposed a calibration technique combining the downer and circulating fluidized bed (CFB) procedures and reported more than 30% solids holdup of FCC powder. The downer procedure corresponded to high solids concentration flow and CFB to dilute calibration procedure. They used velocity probe to measure the particle velocities and evaluated the solids holdups based on solids flow rates. In order to use the downer calibration in higher solids concentration system, Zhang et al (1998) proposed a back pressure control method to reduce particle falling velocity.

In addition to the calibration procedures and models, signal/voltage oscillation of the probe responses is also an important factor in the dynamic calibration techniques, which has been rarely explored. The signal oscillation in dynamic calibration is caused by both hydrodynamics of the gas-solid flow and particle properties. The dynamic calibration of the optical probe is currently limited to low solids concentrations due to the lack of proper qualitative and quantitative analysis of the relationships between the signal oscillation and the calibration data. Zhang et al (1998) proposed an iteration computational method to modify the effects of the signal fluctuation on the calibration results. It is a powerful tool to help understand the dynamic calibration and to analyze the oscillation effects of dynamic signals on the probe calibration. On the other hand, the

investigation on the linear characteristic of probe response to solids holdup (Liu et al, 2003) is also helpful to this issue, because theoretically there is no difference between average of the converted signals with a linear calibration curve and true mean solids holdups.

To the best of our knowledge there is no robust calibration method for optical fibre probe, which covers a wide range of solids concentrations and therefore it is crucial to develop a new feasible and simple technique for such a purpose in gas-solid flow systems. In this study a pseudo bubble-free fluidized bed was employed to investigate optical fibre probe calibration and its characteristics at high solids concentrations. A novel optical probe calibration procedure, combining with downer calibration method proposed by Zhang et al (1998) was developed to calibrate optical fibre probe at nearly full range of the solids concentrations. Using calibrated optical fibre probes, the detail flow structure in a circulating turbulent fluidized bed (CTFB) was studied.

3.2 Experimental setup and calibration procedure

3.2.1 Experimental setup

The experiments on optical probe calibration procedure were carried out on two experimental rigs: a downer and a Pseudo Bubble-Free Fluidized Bed (PBFFB) for low and high low solids concentrations respectively, of which the experimental setup for the downer can be found in Zhang et al (1998). PBFFB (Fig. 3.1) was composed of a calibration column and particle separation section, two Plexiglas cylinders with the same i.d. of 38mm and different heights of 440 and 200mm. In calibration column, bubble

suppressors were installed, which were composed of a set of metal mesh assembly with 5.88 mm axial pitches and take 3.01% of the volume. Each assembly consists of two layers of rigid steel mesh and one middle layer of aluminum mesh. The opening of steel mesh was 2.83 X 2.77mm with 0.39 mm steel wire, and the aluminum mesh was 1.37 X 1.4 mm with 0.2 mm aluminum wire. These metal layers were staggered over each other to reduce the mean opening size of the assembly to about 0.95 mm. The bubble suppressors were connected and grounded to remove static electricity. In the separator section, a #325 stainless steel mesh cylinder with a closed top end was installed to collect the small quantity of the elutriated particles and maintain constant particle storage in the calibration section. A bag filter was also used to separate fine particles before air discharge.

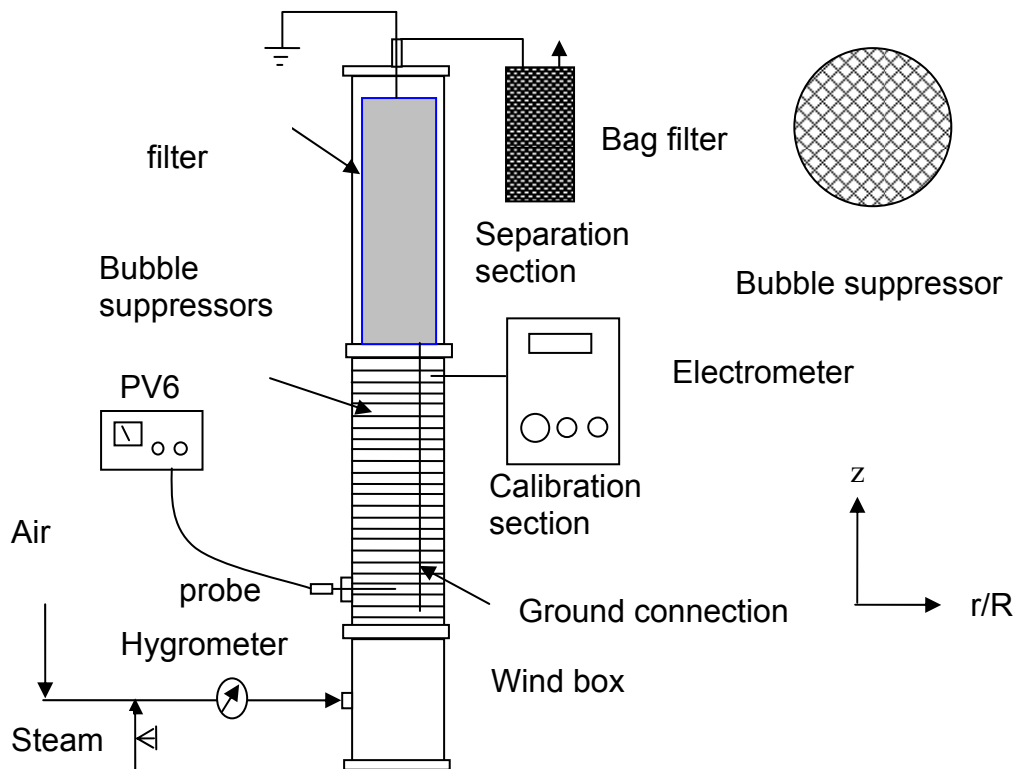


Figure 3.1 Pseudo bubble-free fluidized bed and calibration system

The optical probe, used in this study, was model PV6 produced by the Institute of Process Engineering, Chinese Academy of Sciences, Beijing, China. The probe is composed of two optical fibre bundles located on the same vertical line. Each bundle consists of both light-emitting and receiving quartz fibres arranged in an alternating array, corresponding to emitting and receiving layers of fibres. The diameter of each fibre is 25 μ m. Light from a light emitting diode (LED) transmits through the emitting half of the fibres to the tip, where hitting upon particle(s) in the riser, is reflected back to the probe. The intensity of the reflected light depends on the concentration, size distribution, composition, and shape of the particles. The received light reflected by the particles is converted by a photomultiplier into voltage signals. The voltage signals are further amplified and fed into a computer. Such probe, with proliferative angle of less than 30° and 2mm effective measurement distance (Liu, 2003; Amos, 1996), was inserted between the bubble suppressors with 5.88 mm pitches to acquire the solids concentration data in PBFFB (Fig. 3.1).

FCC, glass beads and quartz sand were used (shown in Table 3.1) to investigate the particle properties effects. The FCC particles and glass beads were also screened into two narrow distribution parts of big and small sizes to study the size and size distribution effects. Before filled into the bed, aerosol particles were removed by air drifting to prevent them from sticking on the column wall.

Table 3.1 Particle properties

particles		color	Size (μm)	bulk density (kg/m ³)	particle density (kg/m ³)
FCC	FCC #1	brown	72.3	880	1600
	FCC #2		65.8	860	
	FCC #3		103.8	850	
Quartz Sand	S #1	light brown	330	1330	2610
Glass beads	GB #2	grey	138	1520	2350
	GB #3	light grey	76	1430	2410
	GB #4	white	65	1340	2410
	GB #1	grey	288	1520	2460
	GB #5		296	1510	
	GB #6		267	1510	

3.2.2 Probe and calibration procedure

The calibration under high solids concentration was completed in PBFFB. With inserting the optical fibre probe to the column center between two successive bubble suppressor plates, the calibration section of PBFFB was filled with a given quantity of particles just covering the probe. The particles were fluidized by air conducted through a bottom air distributor and were homogeneously distributed throughout the volume within a steady bed height with the assistance of bubble suppressors installed in the calibration column. The fluidized bed operated under the ratio of H/H_{mf} up to 6.0, where H_{mf} and H are the bed height at minimum fluidization state and other air supplies respectively. To obtain different steady bed heights, the air flow was controlled by a needle valve and a rotary flow meter to provide a wide range of high solids concentrations for the probe calibration. The metered air was maintained under the specific humidity (70 ~ 80%). The solids holdups were computed using Eq. 3.1.

$$\frac{\varepsilon_s}{\varepsilon_{s,mf}} = \frac{H_{mf}}{H} \quad (3.1)$$

The offsets of PV6 were set at zero with empty black box and the gains roughly at 4.5v with packed box (less than the full range of 5v of PV6), making the calibration procedure respond to most of possible particle concentrations. The values of offset and gain were checked and determined with the dilute and dense phases in another bubbling fluidized bed. For a different probe set up and synchronization of the multi-channel probe, the signals are proportionally modified by;

$$V = \frac{V_{mf}}{V'_{mf}} V' \quad (3.2)$$

where, V' is the measured voltage, and V'_{mf} is the response voltage at the incipient fluidization with a typical setting up of the instrument, considered as the peak value of the signal. V_{mf} is the normal voltage at incipient fluidization, equal to the upper limit of the measurement range of 0 ~ 5 voltage optical probe system. Generally, it is hard to set the system to an identical condition between calibrations and applications. Eq. 3.2 also provides a scale up or down criteria to the same conditions. Especially for the multi-channel probes, it is necessary to synchronize the channel measurements using Eq. 3.2 for other purposes from the experimental signals.

Experimental data were acquired by PV6, which had two options: single or multiple continuous sampling. At single sampling option, at least two samples should be taken at a steady experimental condition and only the second one was taken as the correct result due to the possibility of overlapping with existing data from previous experiments. At

continuous sampling option, the first set of data was always disregarded when being processed because of the same reason.

Experiments demonstrated that PBFFB was capable of providing steady homogeneous solids concentrations. It was found that PBFFB operated steadily with stable bed surface on low air velocity or high bed solids concentrations. Although the period of steady operation states decreased with increasing air velocities due to particle elutriation, it still remained more than four seconds until $H/H_{mf} = 6.0$, in which an optical fibre probe is able to respond to valid solids holdup signals for calibration. With a Keithley Electrometer, comparisons between the results, bubble suppressors grounded and not grounded, demonstrated PBFFB operation without any accumulation of static electricity, even under very dry air supply condition.

The low solids concentration calibration data was obtained in a stable gas-solid downer system with a small enough diameter (0.013 m) so that a local measurement could yield a cross-sectional averaged value (H. Zhang, 1999; W. Liu et al, 2001). Details of the experimental rig and the calibration method had been described by Zhang et al (1998). After a series of steady experiments, average solids holdups were determined using Eq. 3.1 and the response voltages were mapped to the full range of 5v using Eq. 3.2. The results were fitted to a proper curve, calibration curve, using specially developed Matlab code.

3.2.3 Application experiment

Experiments for application were carried out in a circulating turbulent fluidized bed and a

twin riser fluidized bed, covering bubbling fluidization (BFB), turbulent fluidization (TFB), circulating turbulent fluidization (CTFB), and bottom zone of circulating fluidization (CFB). The experimental detail description can be found in Chapter 6. The particles used for the experiments were FCC catalyst with a Sauter mean diameter of 76 μm and a particle density of 1780 kg/m^3 . Air velocity range was 0.5 ~ 5.0 m/s and solids circulation rates were 0 ~ 420 $\text{kg}/\text{m}^2\text{s}$, covering bubbling, circulating turbulent and circulating fluidization regimes.

3.3 Results and discussion

3.3.1 Dynamic signals

Fig. 3.2 shows the optical probe signals of PBFFB at different bed heights. The relative bed heights (H/H_{mf}), varying from 1.1 to 6.0, are corresponding to the relative solids holdup ($\varepsilon_s / \varepsilon_{smf}$) from 0.91 to 0.17 respectively. The peaks of the signals respond to high solids holdups, and the valleys responds to low particle concentration or dilute phase. The peaks of the signals decrease with increasing relative bed heights, corresponding to the decreasing average bed solids holdup. The maximum peak value of the signals corresponds to the solids concentration at incipient fluidization. The valleys also decrease and then remain at a value much higher than the instrument offset, which shows that there are no large bubbles developed at all conditions in PBFFB as bubble suppressors efficiently distribute particles and prevent fine bubbles from growing.

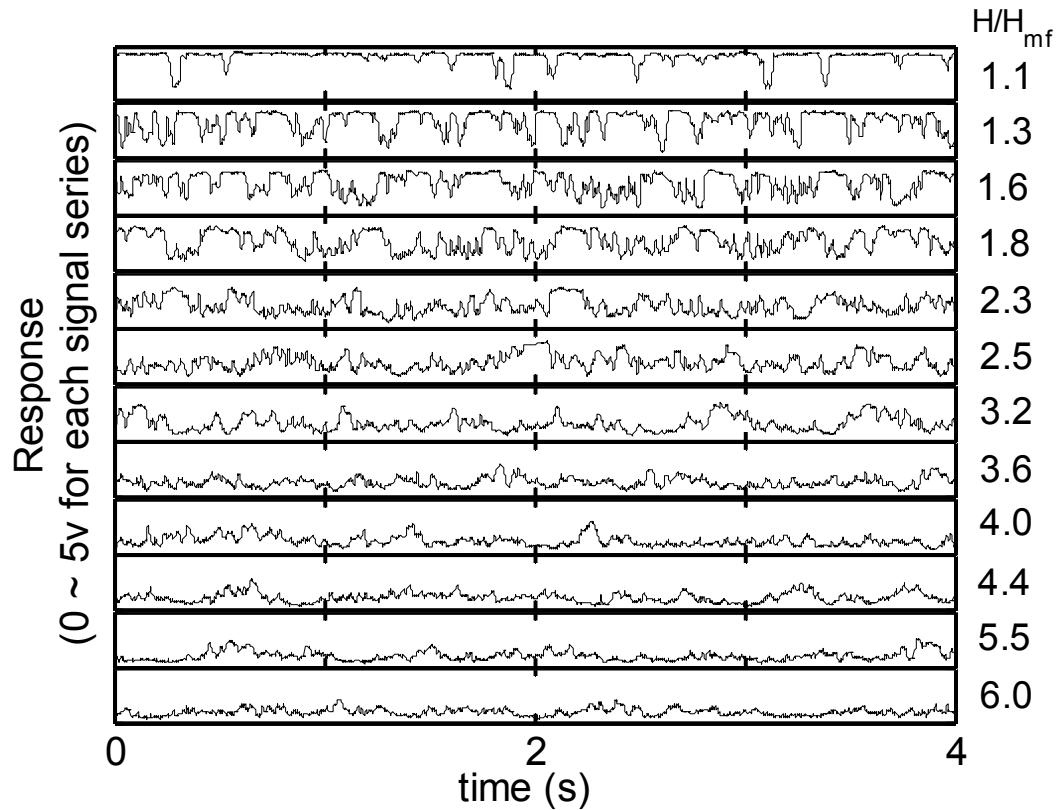


Figure 3.2 Probe signals of PBFFB with GB #2 at different bed heights

3.3.2 Uniformity

To evaluate the reliability of the PBFFB calibration technique, nine sets of calibration data were obtained at different radial and axial positions, as shown in Fig. 3.3. Solid line plotted in the graph is the regression model based on the experimental data at different positions. Slight deviations were observed for locations near the wall ($r/R = 0.75$ at $z = 75$ mm) which was most probably due to wall effect. All other points are well fitted to the model. Coefficients of determination, R^2 at different positions are listed in Table 3.2, which confirmed the uniformity of the PBFFB for optical fibre probe calibration.

Table 3.2 Coefficients of determination R^2 at different positions

Z (mm)	r/R*	R^{2**}
75	0.25	0.9944
	0.50	0.9831
	0.75	0.9714
	-0.25	0.9882
	-0.50	0.9956
	0.00	0.9808
125	0.00	0.9921

Note: * R is the radius of the column.

** R^2 is coefficient of determination.

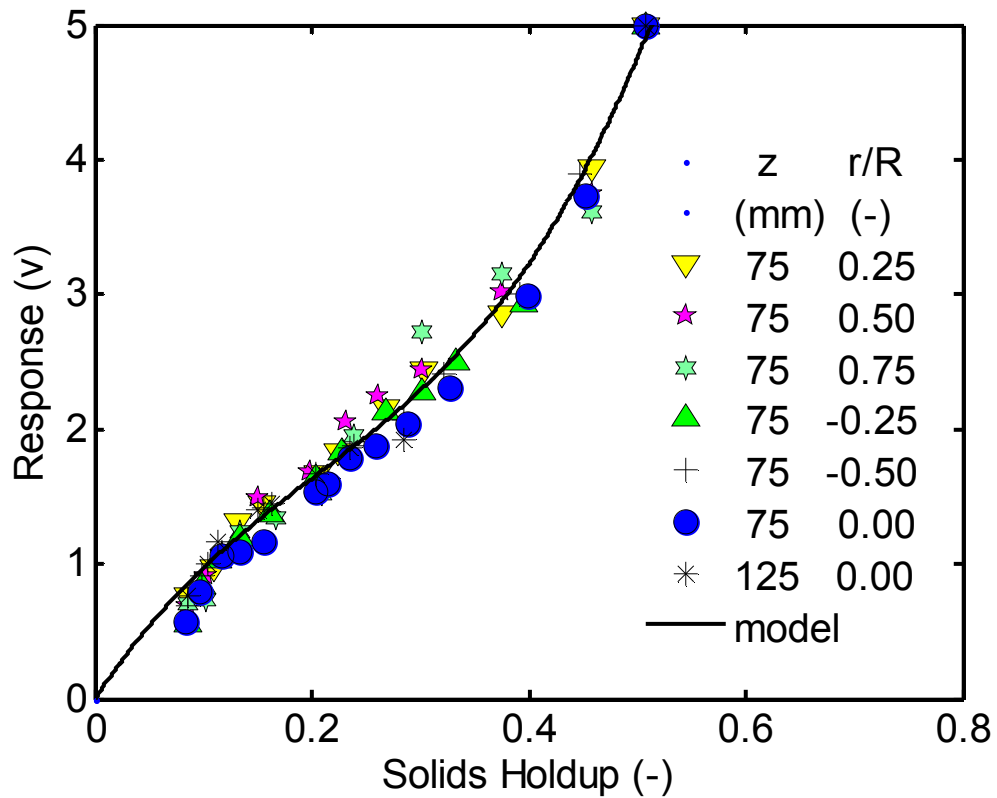
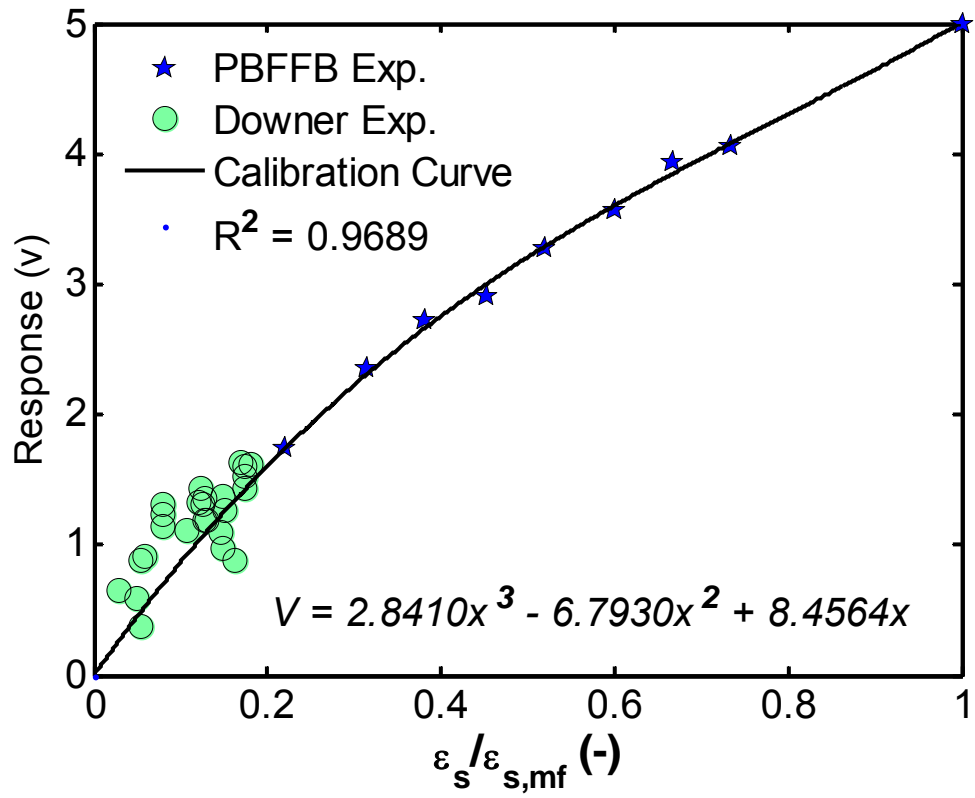


Figure 3.3 Time average response voltage vs. solids holdup of sand ($d_p = 330 \mu\text{m}$, $\rho_p = 2610 \text{ kg/m}^3$) at different radial and axial positions

3.3.3 Calibration curves

Calibration curves of an optical probe using FCC and quartz sand particles have been obtained by the downer and PBFFB procedures, which correspond to low and high solids concentrations respectively, as shown in Fig. 3.4 (a) and (b). For FCC particles, the downer procedure calibrates the probe from 0.03 to 0.20 of solids concentration, being somehow over-responding to the particle concentration from the fitness to the cubic-polynomial model (Zhu and Zhu, 2008a), while the PBFFB procedure works from 0.25 to 0.78, agreeable well with the model. For quartz sand the downer procedure works at the solids concentration from 0.05 to 0.25, while PBFFB works at 0.25-0.95 of solids concentration, both well agreeable with the fitting model. With $R^2 > 0.97$, the downer and PBFFB calibration procedures together are capable of providing the much wider scope of solids holdups for optical fibre probe calibrations.



(a)

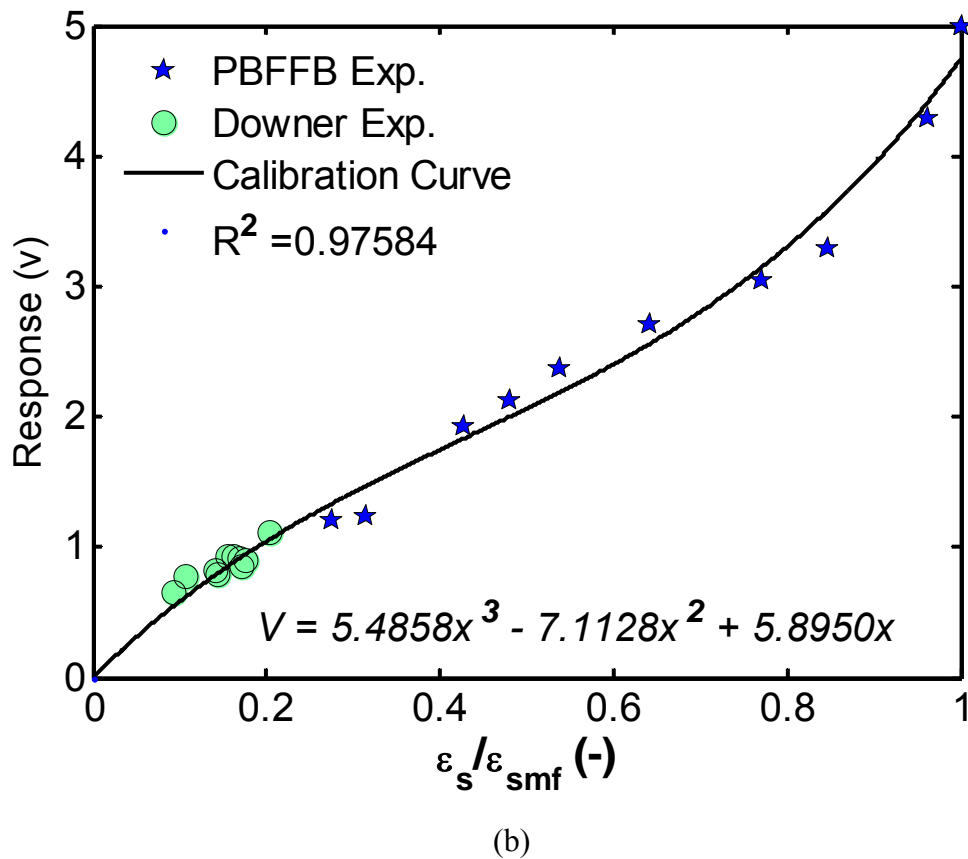


Figure 3.4 Calibration curves with PBFFB and downer calibration procedures:
 (a) using FCC #1 particles and (b) using quartz sand

To study the effects of particle properties on the calibration, such as particle size, sphericity, color, size and surface roughness etc., six kinds of particles (Table 3.1) were experimented through the PBFFB calibration procedure, as shown in Fig. 3.5. The calibration curves appear to be linear, C- and S-shapes, depending on particle properties which are similar to the reported results by Magnusson et al (2005). As the size effect is concerned, the shapes of the calibration curves of GB #1, 2, and 4 vary from the concave, linear and then to the convex when the particle size increased. GB #3 and 4 are close in size and density but different in color, hence the difference of the calibration curves

indicates the effect of color predominating the particle size and density. Light gray glass beads (GB #3) has more tendency to absorb light compared to white glass beads, and its calibration curve is below the curve of the white glass beads. The effect of sphericity on the probe response voltages can be observed from the results of GB #1 and Sand #1. Although both of particles had different particle properties (shown in Table 3.1), their calibration curves were very close, and overlapped at less than 0.6 of relative solids holdup, showing the significant effect of sphericity on the dilute particle concentration. Moreover, the notable difference of the curve shapes, linear vs. s-shape, is also attributed to their surface roughness. Light casts on non-spherical moving particles and rough particle surfaces and is reflected non-uniformly at one view point, while it is reflected relatively uniform on smooth and round solids. With respect to the time average value, this kind of non-uniform light reflection becomes significant and influences the probe response because particles move less at low air velocity or high solids concentration of PBFFB, so that the calibration curve of sand is like s-shape instead of linear. This explanation can be extended to the results of GB #3 and FCC #1 (in Fig. 3.4). That is why the inflection points of calibration curves to GB #1, 2 and 4 are very vague. Of all six kinds of particles, as FCC particles have darkest color and lowest bulk density and roughest surface except for similar size to GB #3 and 4, the probe response to FCC is obviously different from to other particles. This result demonstrated that particle properties can significantly influence the probe response and calibration curve shape.

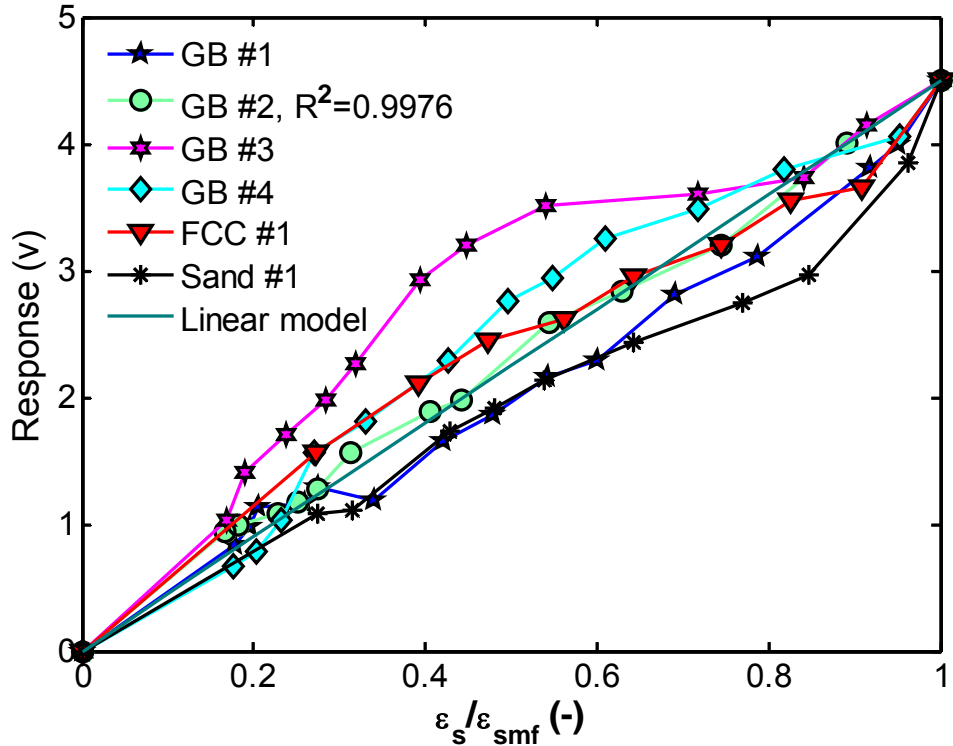


Figure 3.5 Calibrations of the optical probe in different particles

Due to attrition and elutriation, the size of the particles used in gas-solid flow systems may be different from the size of the particles for calibration. This might bring errors to the final solids concentration results converted from voltage signals and the given calibration curve to specific particles. To investigate the effect of size distribution change, FCC #1 and GB #1 were screened into two narrow sizes, FCC #2 and 3, and GB #5 and 6 respectively. They are the identical material with different size distributions: The average size of screened FCC #3 is 1.43 time as big as the original FCC #1, and screened FCC #2 is 0.91 time (Table 3.1). The calibration results on the three FCC particles demonstrate that the changes of particle size and distribution due to operation might not bring notable errors through the solids holdup interpretation from a specific calibration curve, as shown in Fig. 3.6. The similar calibration results of three sizes of glass beads confirm this conclusion, as shown in Fig. 3.7.

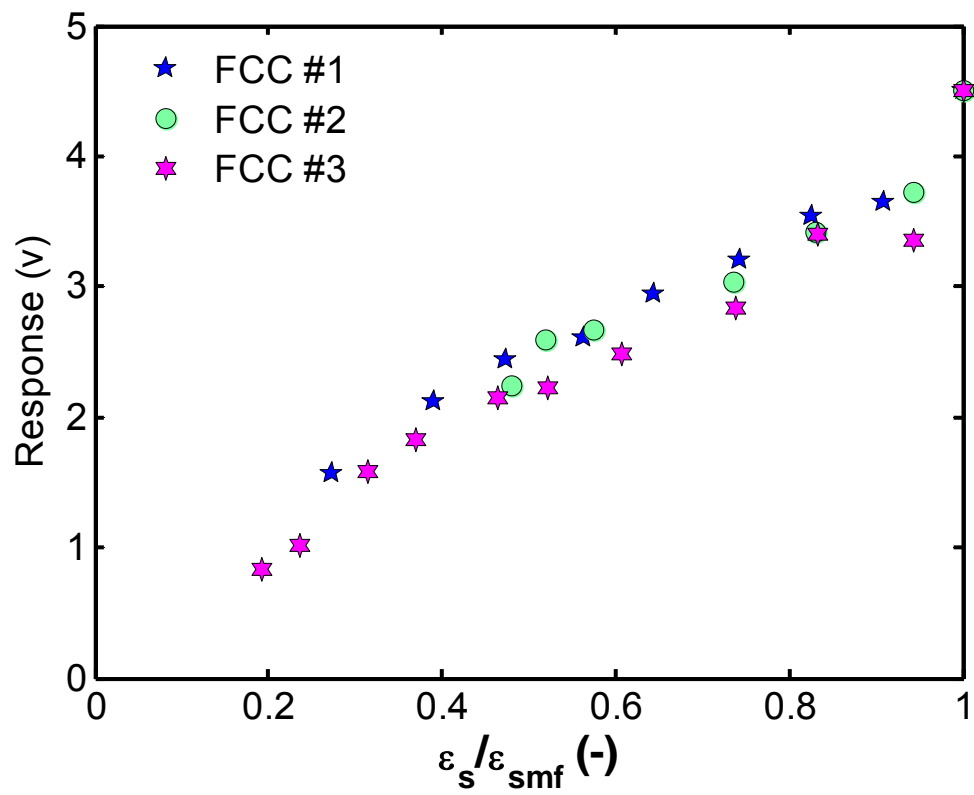


Figure 3.6 Probe responses to different FCC particle size distributions

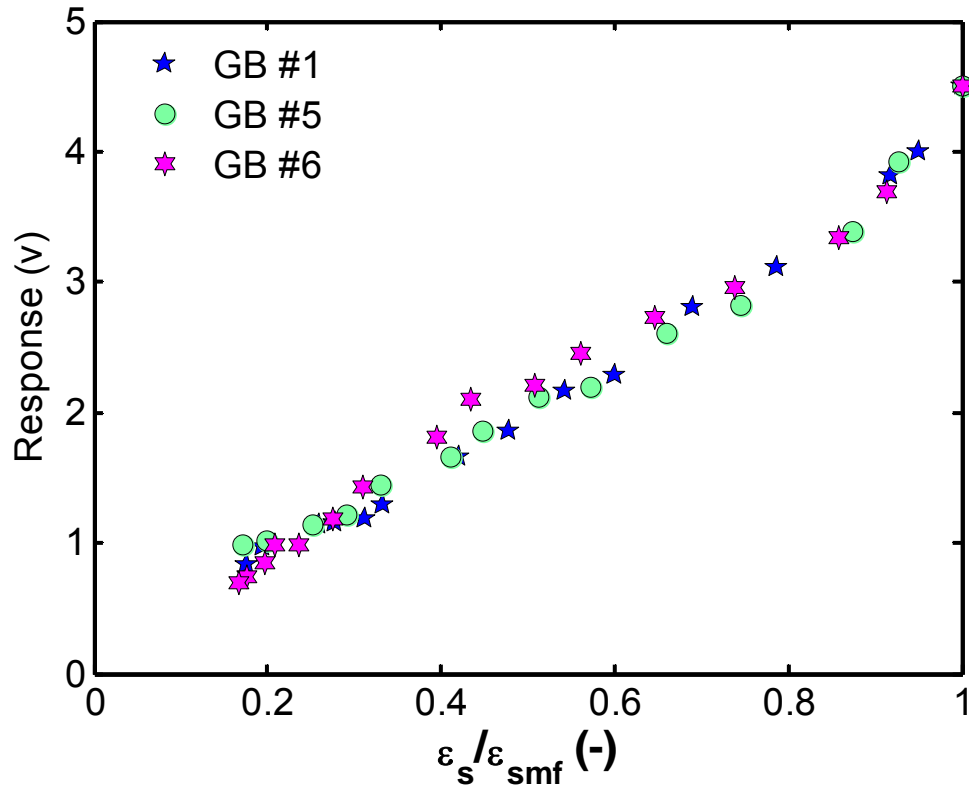


Figure 3.7 Probe responses to different glass bead particle size distributions

3.3.4 Applications of optical fibre probe

Through the calibration procedure proposed in this study, four optical fibre probes were calibrated. Using the probes, the holdup distributions of FCC particles were obtained in a high solids flux circulation system at relatively low air velocities. The experimental details can be found in Chapter 6. Fig. 3.8 provides the axial solids holdup profile, referring to the axial distribution of the cross-sectional average solids concentrations of CTFB. The axial profiles demonstrated that the results obtained through the local solids holdup measurement by optical fibre probes are agreeable well with the ones from the pressure drop signals measured by differential pressure transducers.

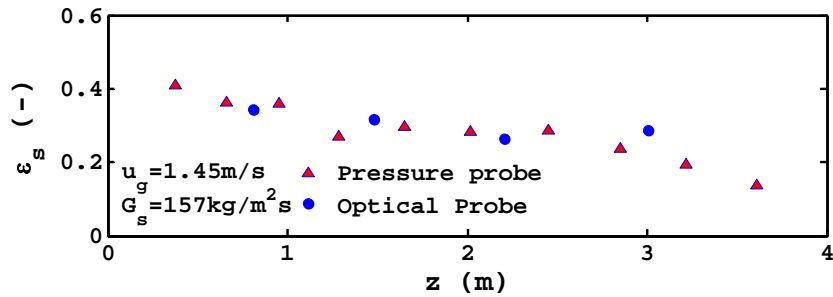


Figure 3.8 Axial profiles of cross-sectional averaged solids holdup in CTFB obtained by optical fibre probes and differential pressure transducers

Fig. 3.9 provides the radial profiles of the local time-average solids holdup in bubbling (BFB), circulating bubbling (CBFB), turbulent (TFB), circulating turbulent (CTFB), and circulating (CFB) fluidized beds. Those radial profiles of local average solids holdup cover very different solids holdup distributions of four fluidization regimes. For BFB (including CBFB), the solids holdup is high and uniform across most of the bed and slightly increases near the wall. On the other hand, the solids holdup in the bottom zone of CFB steadily increases toward the wall in a parabolic shape. Such variations of the solids holdup in BFB and CFB correspond to the flow structures of the dense phase dominating flow in BFB and of the dilute phase dominating flow in CFB, as widely accepted. Between BFB and CFB, the radial solids holdup profile of CTFB/TFB is characterized in core and annular regions. In the core region, the solids holdup profile is flat and between the radial solids holdup distributions in the BFB and CFB regimes, and it increases in a mediate rate in the annular region. The profile variation of the solids holdup in CTFB corresponds to the dilute phase dominating flow in the centre and of the

dense phase dominating flow in the annular regions (Chapter 6), a different flow structure from BFB and CFB.

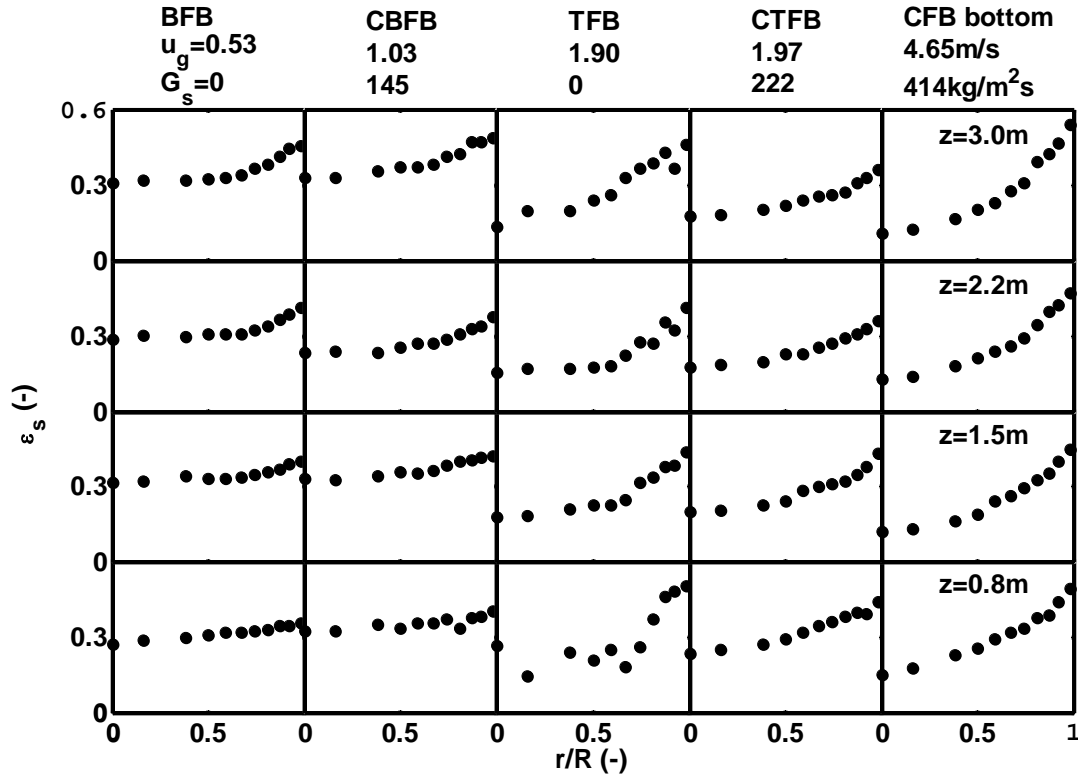


Figure 3.9 Radial profiles of time-average solids holdup in different regimes obtained by optical fibre probes

To further study the flow structure in CTFB, the mean solids holdups of the dense and dilute phases and relative phase fractions were obtained from the measured signals using Moment Consistency Data Processing Method (MCDPM) proposed by Zhu et al (2012, Chapter 4). The profiles of the dense phase (Fig. 3.10) demonstrate that the solids holdup is uniform across the bed over a wider range of air velocities. At the end of the CTFB regime ($u_{tc} = 2.5$ m/s at $G_s = 220$ kg/m²s), the solids holdup in the core region is somehow lower than the one in the annulus, corresponding to dense phase expansion (Bi and Su, 2001) and implying the beginning of CFB regime (Qi et al, 2012, Chapter 5). On

the other hand, the variation of the dilute phase solids holdup is a little more complicated than the one of the dense phase, characterized in core and annular regions, as shown in Fig. 3.11. In the core region, the solids holdup does not change appreciably with increasing air velocity. However, the solids holdup in the annulus varies in different ways with increasing air velocity. At lower air velocity, the annulus is wide and the variation range of the solids holdup is high. With increasing air velocity, the annulus becomes narrower and the variation range is lower until $u_g = 2.0$ m/s, as regarded as an optimal air velocity of CTFB in view of the maximum operation states (Chapter 6). Such a profile variation of the dilute phase solids holdup echoes the development of the turbulent fluidization regime from the centre to the wall (Zhu and Zhu, 2008). Further increasing air velocity, the annulus range and the difference of solids holdup between the centre and wall both increase, indicating the advent of core-annular flow structure in CFB regime (Chapter 6).

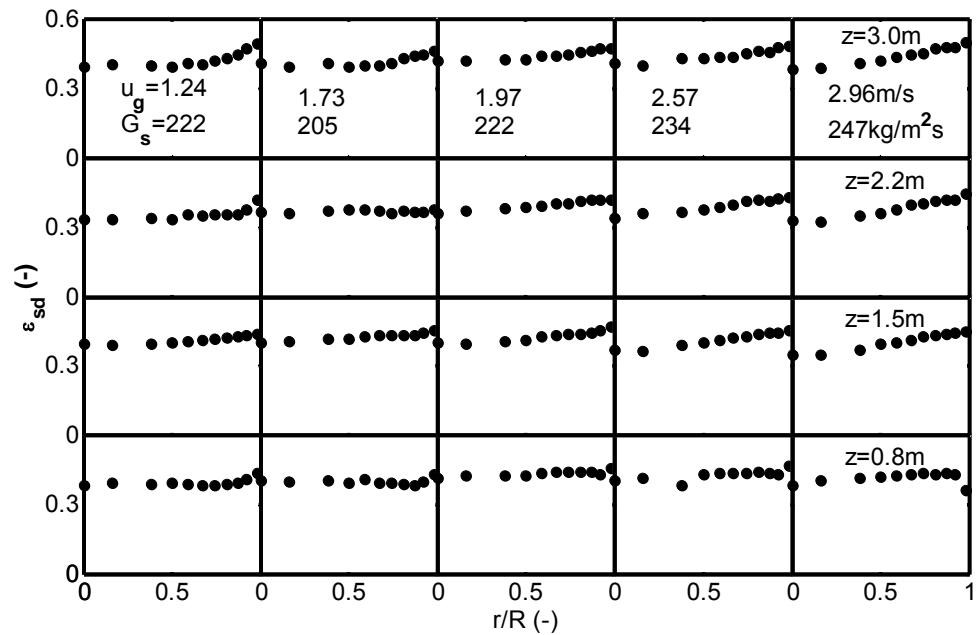


Figure 3.10 Solids holdup profiles of the dense phase in CTFB

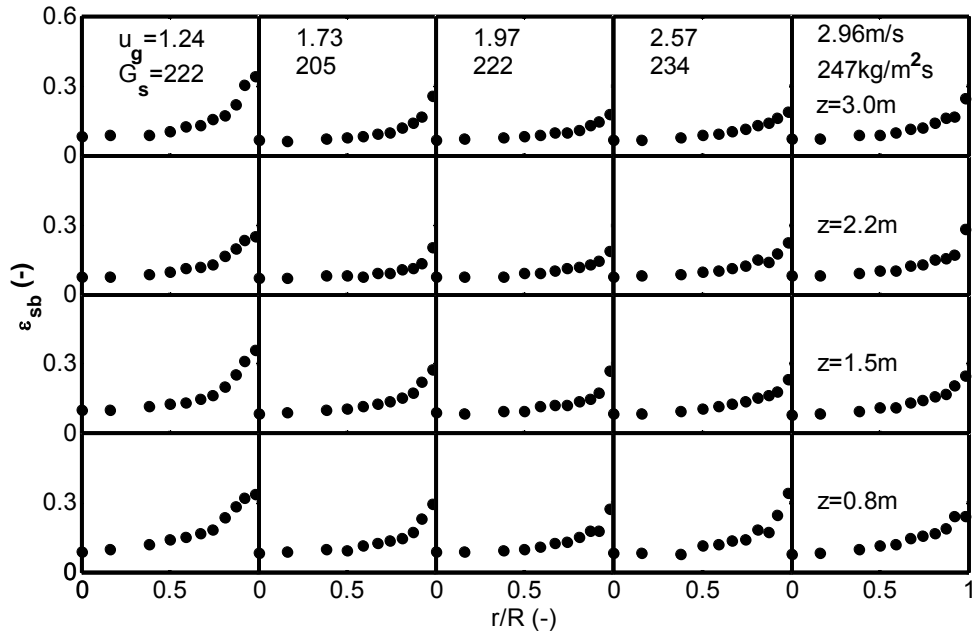


Figure 3.11 Solids holdup profiles of the dilute phase in CTFB

Reasonably, as the solids holdups of the dense and dilute phases hardly change, the dense phase fraction has to be subject to the variation of the radial solids holdup profiles (Fig. 3.9) with respect to air velocity at similar solids circulation rates. Generally, the profile varies from the flat parabolic shape at lower air velocity to the steep shape at higher air velocity, as shown in Fig. 3.12. Postulating that turbulent fluidization regime starts at the phase inversion point (the dense and dilute phases predominating alternatively) (Qi et al, 2012, Chapter 5), one can observe the development of the flow structure in CTFB from profile variation of the dense phase fraction. The dense phase fraction greater than 0.5 corresponds to the dense phase dominating flow in the core region, while the fraction less than 0.5 indicates the dilute phase dominating flow in the annular region. At low air velocity ($u_g = 1.24$ m/s), the profile variation displays that the turbulent flow takes place first at the centre of the top and then develops toward the wall and the bottom in view of the region of less than 0.5 of the dense phase fraction. With increasing air velocity, the

range of the dilute phase dominating flow is enlarged across the bed. At the ending transition air velocity ($u_{tc} = 2.5$ m/s), the dilute phase dominating flow prevails within the core region of $r/R = 0.6$ against the dense phase dominating flow in the annulus. Such results obtained from the solids holdup measurements by optical fibre probes directly confirm that CTFB/TFB is a transition regime between the bubbling and circulating fluidization regimes (Bi et al, 2000) because BFB is of dilute phase dominating flow while HDCFB/CFB is of dilute phase dominating flow (Zhu et al, 2012, Chapter 4).

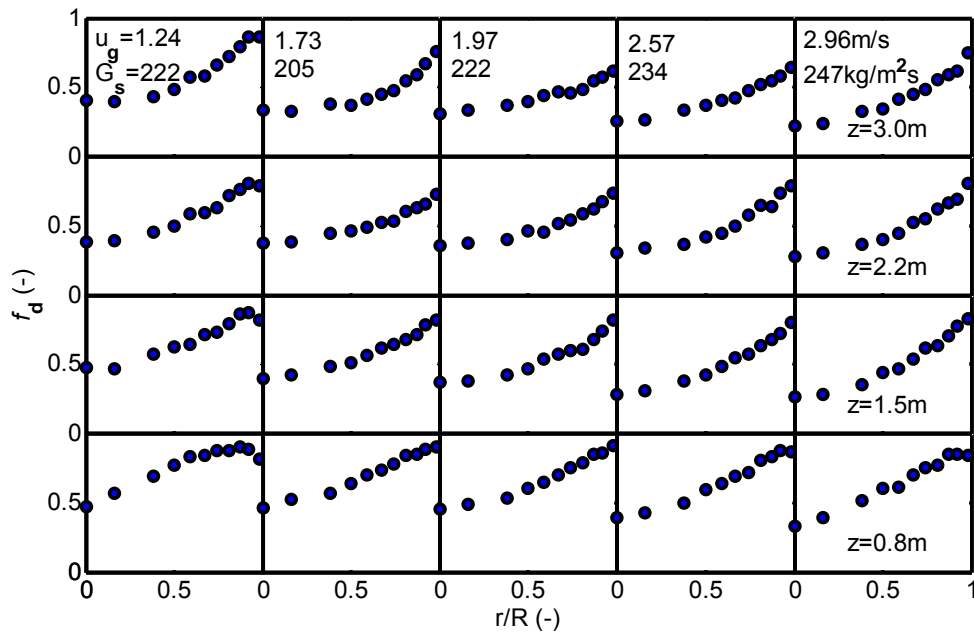


Figure 3.12 Profiles of the dense phase fraction in CTFB

Quantitatively, the local time average solids holdup of the dense phase is about 0.4, while the dense phase fraction is about 0.44 in the centre, which are quite consistent with the results obtained using ECT method at similar experimental conditions (Du et al, 2003). Using FCC particles ($d_p = 60 \mu\text{m}$, $\rho_p = 1400 \text{ kg/m}^3$), Du et al reported that the mean solids holdup of the dense phase was about 0.42 and the dense phase fraction was about 0.45 in the center of a 0.1m column at $u_g = 0.74$ m/s.

Conclusion

A novel pseudo bubble-free fluidized bed (PBFFB) was developed to calibrate optical fibre probe at high solids concentrations. The PBFFB plus downer calibration procedures are capable of providing stable and relatively uniform gas-solid flow in a quite wide range of mean solids concentrations. PBFFB is electrostatic-free and of simple operation, which make it possible to calibrate optical probes easily and precisely. The influences of particle properties on optical fibre probe response were studied. Particle size, color, sphericity, and surface roughness notably affected probe response and the shape of calibration curves, corresponding to linear, C- and S-type calibration curves. Particle size and distribution changes due to operation did not influence the probe response significantly.

From the solids holdup measurements using optical fibre probes, the flow structure in different fluidization regimes was explored. The results demonstrated that CTFB/TFB regime was of the dilute phase dominating flow in the core region and of the dense phase dominating flow in the annular region, different from the flow structures in bubbling and circulating fluidization regimes.

Nomenclature

f_d	dense phase fraction
H, H_{mf}	dynamic and incipient fluidized bed heights (m)
R^2	coefficient of determination

u_g ,	superficial air velocity, m/s
u_{tc} ,	ending transition air velocity of CTFB, m/s
V	optical probe response (v)
$\varepsilon_s, \varepsilon_{s,mf}$	solids volume fraction (-),

subscript

mf	incipient fluidization
b	dilute phase
d	dense phase
s	particle

References

Amos G., M.J. Rhodes and H. Benkreira, Calculation of optic fibres calibration curves for the measurement of solids volume fractions in multiphase flows, Powder Technology 88 (1996) 107-121

Bi H. T. and Su P., (2001), Local Phase Holdups in Gas-Solids fluidization and Transport, AIChE Journal, Vol. 47(9), 2025

Bi H. T., Ellis N., Abba I. A. and Grace J. R.; (2000); Review: A state-of-the-art review of gas-solid turbulent fluidization; Chemical Engineering Science, 55, 4789-4825

Du B., Warsito W. and Fan L., (2003), Bed Nonhomogeneity in Turbulent Gas-Solid Fluidization, Vol. 49, No. 5, AIChE Journal, 1109

Cutolo A., I. Rendina U. Arena A. Marzocchella, and L. Massimilla, (1990), Optoelectronic technique for the characterization of high concentration gas-solid suspension, APPLIED OPTIC, Vol. 29, No. 9, 1317

Herberta P.M., T.A. Gauthierb, C.L. Briema and M.A. Bergougnou, Application of fiber optic reflection probes to the measurement of local particle velocity and concentration in

gas-solid flow, Powder Technology, 80 (1994), 243-252

Hartge E.-U., D. Rensner and J. Werther, (1989), Faseroptisches Messsystem zur Erfassung lokaler Feststoffkonzentrationen und -geschwindigkeiten in höher konzentrierten Gas-/Feststoffströmungen, Chem.-Ing.-Tech., 1, 744–745.

Link J.M., W. Godlieb, P. Tripp, N.G. Deen, S. Heinrich, J.A.M. Kuipers, M. Schönherr and M. Peglow, (2009), Comparison of fibre optical measurements and discrete element simulations for the study of granulation in a spout fluidized bed, Powder Technology, 189, 202-217

Liu, Jinzhong, John R. Grace, and Xiaotao Bi, (June 2003), Novel Multifunctional Optical-Fiber Probe: I Development and Validation, Vol. 49, No. 6 AIChE Journal 1405

Liu, W., K.-B. Luo, J. -X. Zhu and J.M. Beeckmans, (2001), Characterization of high-density gas–solids downward fluidized flow, Powder Technology, 115, 27–35

Louge, M., in: J.R. Grace, A.A. Avidan, T. Knowlton (Eds.), Circulating Fluidized Beds, Blackie Academic and Professional, London, 1997, p. 312.

Matsuno Y., H. Yahiaguchi, T. Oka, H. Kage and K. Higashitanp, (1983), The Use of Optic Fiber Probes for the Measurement of Dilute Particle Concentrations: Calibration and Application to Gas-Fluidized Bed Carryover, Powder Technology., 36, 215 – 221

Magnusson A., R. Rundqvist, A.E. Almstedt and F. Johnsson, (2005), Dual fibre optical probe measurements of solids volume fraction in a circulating fluidized bed, Powder Technology 151, 19– 26

Qi M., Zhu. J. and Barghi S., (2012), Transition characteristics of gas-solid flow in circulating turbulent fluidized beds, Powder Technology, submitted, Chapter 5 in this thesis

Rensner D. and J. Werther, in: A. Dybbs and B. Ghorashi (Eds.), Proc. of the Fourth International Conference on Laser Anemometrie, Cleveland, OH, Vol. 2, ASME, New York, 1991, p. 753.

Rundqvist R., A. Magnusson, B.G.M. van Wachem and A.E. Almstedt, (2003), Dual optical fibre measurements of the particle concentration in gas/solid flows, *Experiments in Fluids*, 35, 572–579

Saberi, B., K. Shakourzadeh and P. Guigon, (September 1998), Local Solid Concentration Measurement by Fibre Optics: Application to Circulating Fluidized Beds, *Trans IChemE*, Vol 76, Part A, 748

Song X., H. Bi, C. J. Lima, J. R. Grace, E. Chanb, B. Knapper and C. McKnight, (2004), Hydrodynamics of the reactor section in fluid cokers, *Powder Technology*, 147, 126–136

Wiesendorf V. and J. Werther, (2000), Capacitance probes for solids volume concentration and velocity measurements in industrial fluidized bed reactors, *Powder Technology*, 110, 143–157

Yan A. and Zhu J., (2004), Scale-Up Effect of Riser Reactors (1): Axial and Radial Solids Concentration Distribution and flow Development, *Ind. Eng. Chem. Res.*, 43, 5810 - 5819

Zhang H., P. M. Johnston, J. Zhu, H. I. de Lasa and M. A. Bergougnou, (1998), A novel calibration procedure for a fiber optic solids concentration probe, *Powder Technology*, 100, 260-272

Zhang H., J. Zhu and M. A. Bergougnou, (1999), Hydrodynamics in downflow fluidized beds (1): solids concentration profiles and pressure gradient distributions, *Chemical Engineering Science*, 54, 5461-5470

Zhu J, Qi M. and Baighi S., (2012), Identification of Micro Flow Structures and Regime Transition in Gas-Solid Fluidized Beds through Moment Analysis, AIChE Journal, Submitted, Chapter 4 in this thesis

Zhu H. and Zhu J., (2008), New Investigation in Regime Transition from Bubbling to Turbulent Fluidization, The Canadian Journal of Chemical Engineering, Vol. 86(6), 553

Zhu H. and Zhu J. (2008a), Gas-Solids flow Structures in a Novel Circulating Turbulent fluidized Bed, AIChE Journal, Vol. 54 (5), 1213

4 Identification of micro flow structures and regime transition in gas-solid fluidized beds through moment analysis

4.1 Introduction

Many industrial processes have been utilizing gas–solid fluidized bed reactors which may operate in the following flow regimes: particulate fluidization, bubbling fluidization, turbulent fluidization, fast fluidization, and pneumatic transport (Grace, 2000; Zhu, 2010). Among the industrial applications of these fluidized beds, most key commercial gas–solid fluidized bed reactors behave in the flow regimes of turbulent fluidization (TFB) and fast (circulating) fluidization (CFB) due to their favorable gas–solid contacting, mixing and transfer characteristics. They include not only catalytic cracking, partial oxidation reactions, chlorination, etc., but also some important non-catalytic processes, such as roasting of various ores and drying (Grace, 2000; Zhu and Cheng, 2005). Among these fluidized bed reactors, typical FCC units are operated under high density circulating fluidization (HDCFB) conditions, at high gas velocities from 6 to 28 m/s and high solids circulation rates from 400 to 1200 kg/m²s with high solids holdups of typically 10-20% (Zhu and Bi, 1995). Fischer-Tropsch synthesis and acrylonitrile production routinely operate in the turbulent regime of fluidization, for which heat and mass transfer tend to reach a maximum (Grace, 1990). For these operations, fluidized beds are able to operate with small catalyst particles and hence high effectiveness factors, favourable bed-to-immersed-surface heat transfer coefficients in CFB and TFB reactors. They are also capable of withdrawing and adding particulate solids continuously, and operating on a

very large scale (Zhu and Zhu, 2008).

Fluidized beds have been characterized by their heterogeneous two-phase flow structures. The flow structures may be characterized mathematically through some or all of the four moments of local solids holdup signals. The first moment (mean value) corresponds to the local time average solids holdup and the second moment (standard deviation) relates to the fluctuations of the solids holdup around the mean value (Abbas et al, 2009; Song and Bi et al, 2004; Yang et al, 2004, Wang et al, 2005; Zhu and Zhu, 2008b; Yan and Zhu, 2004), reflecting the heterogeneity of a gas-solid flow. The third moment (skewness) is a measure of the lack of symmetry in the probability density function (PDF) of the solids holdup around the mean. The fourth moment (kurtosis) is a measure of the peakedness or flatness of PDF of the solids holdup compared to a normal distribution (Abbasi, 2010; Taylor, 2008; Briens and Bojarra, 2010; Lee and Kim, 1988). Despite their importance, skewness and kurtosis have not been very often used in analyzing the hydrodynamics of fluidization systems. Using the skewness of local solids signals, Manyele and Zhu (2003) analyzed the hydrodynamics of a downer reactor and concluded that skewness provides more information that could not be identified directly from PDF. Using the all four moments, Bi and Su (2001) proposed a two-phase structural model to predict the average solids holdups and phase volume fractions of dense and dilute phases in some gas-solids fluidization and transport systems. Breault et al (2012; Talor et al, 2008) investigated the hydrodynamics of upflow in a riser using direct wavelet transformation, skewness and kurtosis.

The objective of this study is to apply a new moment analysis method, the moment consistency data processing method (MCDPM), to study the micro-flow structure on various flow regimes and to identify distinct changes along with regime transition in gas-solid fluidization systems. Additionally, this method is used to further confirm the existence of a circulating turbulent fluidization regime with regard to its microscopic flow structure. Such a circulating turbulent fluidized bed (CTFB) reactor was proposed by Zhu and Zhu (2008a), integrating conventional circulating and turbulent fluidized beds into a distinguished dense fluidization system with external solids circulation, to simultaneously achieve efficient gas-solid contact similar to TFB and low solids back-mixing similar to HDCFB. Their results demonstrated that the CTFB operation is achievable and its flow structure can be attributed to a new flow regime, the circulating turbulent fluidization regime, different from turbulent fluidization, fast fluidization and dense suspension upflow (Zhu, 2010; Qi and Zhu, 2009). Although our earlier studies (Zhu and Zhu, 2008a, 2008c; Qi and Zhu, 2009) have utilized the first and second moments to distinguish and characterize the various fluidization regimes, more details of the dynamic flow structure, such as the division of the dense and dilute phases, may be further revealed through the additional application of the third and fourth moments.

4.2 Experimental setup

Experiments were carried out in a circulating turbulent fluidized bed and a twin riser fluidized bed, covering bubbling fluidization (BFB), turbulent fluidization (TFB), circulating turbulent fluidization (CTFB), fast fluidization (CFB) and high density circulating fluidization regimes (HDCFB). The schematic diagram of the first

experimental unit is shown in Fig. 4.1, whose detail description can be found in Zhu and Zhu (2008a). Steady flow of different fluidization regimes at low air velocities, namely, BFB, TFB, CTFB regimes and bottom zone of CFB, were obtained through controlling the solids circulation rate and adjusting the air flow. Air velocities and solids circulation rates are listed in Table 4.1, corresponding to bubbling, circulating turbulent and fast fluidization regimes at low air velocities.

Experimental data were acquired using four multi-fiber optical reflective probes of model PV-6, developed by the Institute of Process Engineering, Chinese Academy of Sciences, Beijing, China. The probes were setup at four separate axial elevations and traversed horizontally to measure local solids holdups at eleven radial positions (Fig. 4.1b). The four axial locations were chosen in an effort to characterize the acceleration zone (0.8m) and the fully developed zone (1.5, 2.2 and 3.0m). Radial positions were chosen at the midpoints of eleven equal area circles ($r/R = 0.0, 0.16, 0.38, 0.5, 0.59, 0.67, 0.74, 0.81, 0.87, 0.92, \text{ and } 0.98$) at each axial level within the risers. There were two PV6 units used in the experiments: a master and a slave. A special setup procedure was carried out for the two units to control four probes and a special data processing method was implemented with normalized calibration curves and different unit gains and offsets to obtain consistent experimental results. At one radial location, the units were connected to two adjacent probes for a measurement and then switched to the other two. To ensure the consistency of the data at one specific operating condition, the data at all locations were collected within one run by the four probes. The sampling rate was 50 kHz and data were collected for 131 sec for each measurement.

The second unit was a twin riser circulating fluidized bed, with two risers of 76 and 203 mm in diameter, sharing a 300 mm diameter common downcomer (Yan and Zhu, 2004), where experiments on CFB and HDCFB at high air velocities (over 5.0 m/s) were carried out. For all experiments, different solids circulation rates were maintained through adjusting the total solids inventory in the downcomer and the solids control valve. For CFB regime, the system operated at air velocities of 5.5 and 8.0 m/s and at the solids circulation rates of 50, 70 and 100 kg/m²s, while for HDCFB regime it operated at air velocities of 5.0, 8.0 and 10 m/s and at solids circulation rates of 300, 400 and 550 kg/m²s. The solids holdup distributions were acquired with optical fibre probes at eleven equal area circles ($r/R = 0.0, 0.16, 0.38, 0.5, 0.59, 0.67, 0.74, 0.81, 0.87, 0.92, \text{ and } 0.98$) at eight axial levels within the risers. Two samples were taken at each location, and the total sampling time was 60 s.

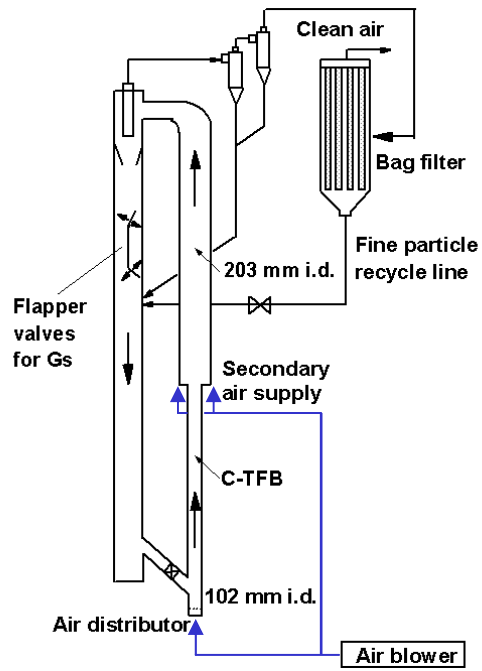
The particles used in these units were FCC catalyst with a Sauter mean diameter of 60 ~ 76 μm and a particle density of 1500 ~ 1780 kg/m³. The relative humidity was kept between 70 and 80% by the addition of steam to minimize the electrostatic effects.

Table 4.1 Operating conditions of experiments

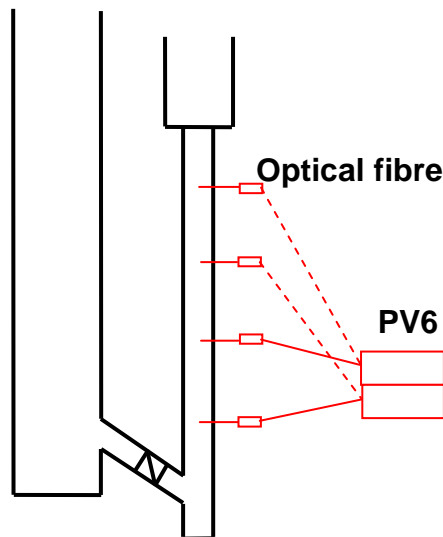
Regime	BFB*	TFB*	CTFB	HDCFB**	CFB**
D (mm)	101	101	101	76	203
height (m)	3.6	3.6	3.6	10	10
d_p (μm)	76	76	76	67	67
ρ_p (kg/m ³)	1780	1780	1780	1500	1500
u_g (m/s)	0.53~0.74	1.6	0.74~3.0	5.5~10	5.5~8.0
G_s (kg/m ² s)	0	0	150~420	300~550	50~100

Note: * dynamic bed height of 3.6m.

** Data from Yan and Zhu (2004)



(a)



(b)

Figure 4.1 Experimental apparatus and optical fibre probe setup

4.3 Moment consistency data processing method

4.3.1 Parameters of moment consistency

The heterogeneous flow structures in a fluidized bed can be studied macroscopically and microscopically. Using measured solids holdup signals with the population N represented by Eq. 4.1, the overall flow structures may be characterized by signal moment estimations, such as mean solids holdup $\bar{\varepsilon}_s$, standard deviation σ , skewness S and kurtosis K (Eqs. 4.2-4.5).

$$\{\varepsilon_i\}, i \in N \quad (4.1)$$

$$\bar{\varepsilon}_s = \frac{1}{N} \sum_{i=1}^N \varepsilon_i \quad (4.2)$$

$$\sigma = \left[\frac{1}{N-1} \sum_{i=1}^N (\varepsilon_i - \bar{\varepsilon}_s)^2 \right]^{1/2} \quad (4.3)$$

$$S = \frac{\sum_{i=1}^N (\varepsilon_i - \bar{\varepsilon}_s)^3}{(N-1)\sigma^3} \quad (4.4)$$

$$K = \frac{\sum_{i=1}^N (\varepsilon_i - \bar{\varepsilon}_s)^4}{(N-1)\sigma^4} \quad (4.5)$$

For an ideal completely segregated two-phase flow system, where exist only two values of solids holdups, namely, a high solids holdup representing the dense phase, ε_{sd} , and a low solids holdup representing the dilute phase, ε_{sb} , with f_d being the fraction of the dense phase, as represented by Eq. 4.6.

$$\{\varepsilon_{id} = \varepsilon_{sd}, \varepsilon_{ib} = \varepsilon_{sb}\}, \quad id \in N \text{ and } ib \in N \quad (4.6)$$

where the number of the elements in dense phase is $n(\varepsilon_{sd}) = f_d N$, and the number of the elements in dilute phase is $n(\varepsilon_{sb}) = (1 - f_d) N$.

For such an ideal case, Eqs. 4.2-4.5 can be simplified to Eqs. 4.7-4.10:

$$\bar{\varepsilon}_s = f_d \varepsilon_{sd} + (1 - f_d) \varepsilon_{sb} \quad (4.7)$$

$$\sigma = \sqrt{(\varepsilon_{sd} - \bar{\varepsilon}_s)^2 f_d + (\varepsilon_{sb} - \bar{\varepsilon}_s)^2 (1 - f_d)} \quad (4.8)$$

$$S = \frac{1}{\sigma^3} [(\varepsilon_{sd} - \bar{\varepsilon}_s)^3 f_d + (\varepsilon_{sb} - \bar{\varepsilon}_s)^3 (1 - f_d)] \quad (4.9)$$

$$K = \frac{1}{\sigma^4} [(\varepsilon_{sd} - \bar{\varepsilon}_s)^4 f_d + (\varepsilon_{sb} - \bar{\varepsilon}_s)^4 (1 - f_d)] \quad (4.10)$$

A typical data series (series 1) for Eq. 4.1 from a circulating turbulent fluidized bed is shown in Fig. 4.2(a), where a two-phase structure is clearly observed. A new series (series 6, as represented by Eq. 4.6) may be generated as shown in Fig. 4.2(b) to follow the trend of series 1 as represented by Eq. 4.1. Comparing the two series shown in Fig. 4.2, by adjusting the values ε_{sd} and ε_{sb} and their respective fractions f_d and $f_b (= 1 - f_d)$ in series 4.6, it is possible to have at least 3 or 4 moments as calculated by Eqs. 4.7-4.10 to be equal to those obtained through series 4.1 based on an experimental measurement. Therefore the two series are considered to have the same sets of moments. Under such circumstances, it is hereby postulated that if the above two series (Eqs. 4.1 and 4.6) have the same sets of moments, the average values of the two phases and their respective fractions must be the same between the two series. In other words, ε_{sd} , ε_{sb} and f_d ($f_b = 1 - f_d$) from series 4.6 can be taken as (or at least be used to estimate) $\bar{\varepsilon}_{sd}$, $\bar{\varepsilon}_{sb}$ and f_d from

series 4.1 and then be used to analyze time series 4.1. Such an approach is proposed here as a Moment Consistency Data Processing Method (MCDPM).

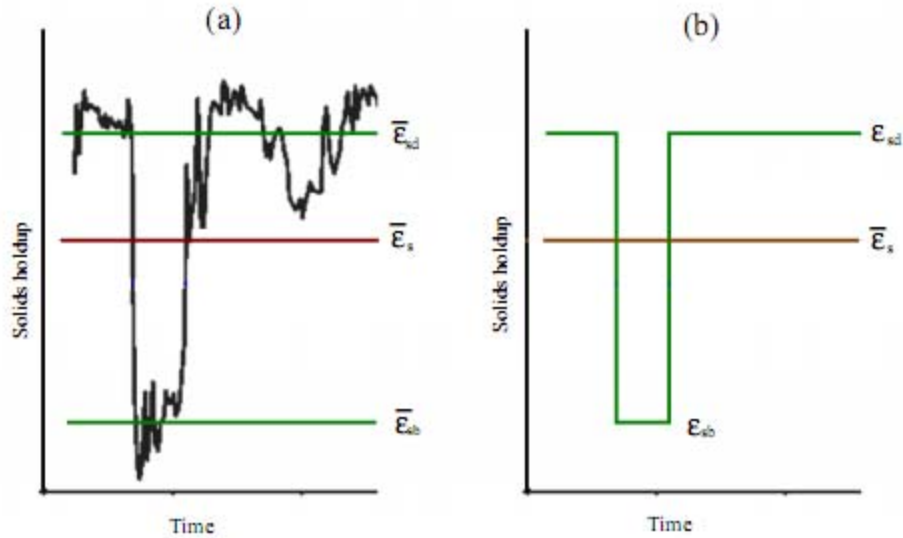


Figure 4.2 Segment of (a) measured solids holdup signals of CTFB vs. (b) the solids holdup signals from the corresponding ideal two phase flow

For analysis, the 4 moments will first be calculated from the experimental series Eq. 4.1. Then, the 4 moment values will be applied in Eqs. 4.7-4.10 to back calculate the 3 key parameters ϵ_{sd} , ϵ_{sb} and f_d . However, as there are 3 unknowns and 4 equations, it is necessary to make a proper combination of three equations out of the four equations (Eqs. 4.7-4.10) to produce the most pertinent results. As the two most important characteristics of the two phase flow, the mean and standard deviation should remain consistent between the two series and therefore always be included in the calculation. The next moment equation to be included can be chosen from the skewness and the kurtosis, each referring to equal important properties of a series, depending on what parameters are being examined. Thus, there are two combinations or two methods, Eqs. 4.7-4.9 or Eqs. 4.7, 4.8 and 4.10, to process the data into the parameters of the dense and dilute phases. As a first

approach, the combination of Eqs. 4.7-4.9, including skewness, can be rearranged in the following explicit expressions (Eqs. 4.11-4.13), with detailed derivations given in Appendix A.1.

Method one (M1)

$$f_d = \frac{1}{2}(1 - S\sqrt{\frac{1}{4 + S^2}}) \quad (4.11)$$

$$\varepsilon_{sd} = \bar{\varepsilon}_s + \frac{\sigma}{2}[\sqrt{4 + S^2} + S] \quad (4.12)$$

$$\varepsilon_{sb} = \bar{\varepsilon}_s - \frac{\sigma}{2}[\sqrt{4 + S^2} - S] \quad (4.13)$$

Similarly, a second approach is to include kurtosis, using the combination of Eqs. 4.7, 4.8 and 4.10, leading to the following explicit expressions (Eqs. 4.14-4.16), with detailed derivation shown in Appendix A.1.

Method Two (M2)

$$f_d = \frac{1}{2}(1 \pm \sqrt{\frac{K-1}{3+K}}) \quad (4.14)$$

$$\bar{\varepsilon}_{sd} = \bar{\varepsilon}_s + \frac{\sigma}{2}(\sqrt{K+3} \mp \sqrt{K-1}) \quad (4.15)$$

$$\bar{\varepsilon}_{sb} = \bar{\varepsilon}_s - \frac{\sigma}{2}(\sqrt{K+3} \pm \sqrt{K-1}) \quad (4.16)$$

To evaluate the proper applicable conditions of these two methods for the desirable results, the relative errors of the other moment, not included in the data processing through either M1 or M2, reduced to the same dimension as the experimental data, can be estimated by Eqs. 4.17 and 4.18. When using Method 1, the relative errors on kurtosis between the series 4.1 and 4.6 is

$$E_K = \frac{|K^{1/4} - K_{th}^{1/4}|}{K^{1/4}} \quad (M1) \quad (4.17)$$

Similarly, the relative moment error on skewness with Method 2 is

$$E_S = \frac{|S^{1/3} - S_{th}^{1/3}|}{S^{1/3}} \quad (M2) \quad (4.18)$$

where S_{th} and K_{th} , the theoretical skewness and kurtosis are calculated using Eqs. 4.9 and 4.10 respectively from the known values of ε_{sd} , ε_{sb} , f_d , and $\bar{\varepsilon}_s$, and S and K , the actual skewness and kurtosis are obtained from Eqs. 4.4 and 4.5.

For a given solids holdup distribution, relative large moment errors may occur due to the skewness or kurtosis not being included, depending on what method is selected. Fig. 4.3 displays the relative errors of Method 1 and Method 2 for solids holdup distributions at 11 radial positions at 4 elevations under 56 experimental conditions of high density gas-solids flow. The results demonstrate that Method 1 predicts the solids holdups of the dense and dilute phases and the dense phase volume fraction with small moment errors in kurtosis at small absolute skewness values, and large kurtosis error happens at the large absolute skewness values (Fig. 4.3a). On the other hand, Method 2 computes the parameters with small moment errors in skewness at large kurtosis values, and the error in skewness increases as the value of kurtosis decreases toward zero. The results demonstrate that the selection for most pertinent results between Method 1 and Method 2 might be made through evaluating the magnitudes of the skewness or kurtosis, corresponding to the minimum moment error defined by Eqs. 4.17 and 4.18.

Plotting all skewness and kurtosis calculated through Eqs. 4.4 and 4.5 for all

experimental data listed in Table 4.1 gives rise to a parabolic strap on the K - S plane, as shown in Fig. 4.4. Checking the values of the errors in skewness, E_s , and kurtosis, E_k , as computed by Eqs. 4.17 and 4.18 and plotted in Fig. 4.3, corresponding to the S - K values plotted in Fig. 4.4, the method that results in lesser errors is marked out in Fig. 4.4. Interestingly, the regimes where Method 2 is applicable are clearly separated from that of Method 1, with Method 2 in the two tailing straps and Method 1 in the nose region. With such a clear mapping, the selection of the methods of MCDPM for a specific solids holdup distribution is now made easier, as it can be determined directly using the skewness or kurtosis values as expressed in Eq. 4.19.

$$\text{Method 1 for } |S| < 1.5 \text{ or } K < 4.5 \quad (4.19a)$$

and

$$\text{Method 2 for } |S| > 1.5 \text{ or } K > 4.5 \quad (4.19b)$$

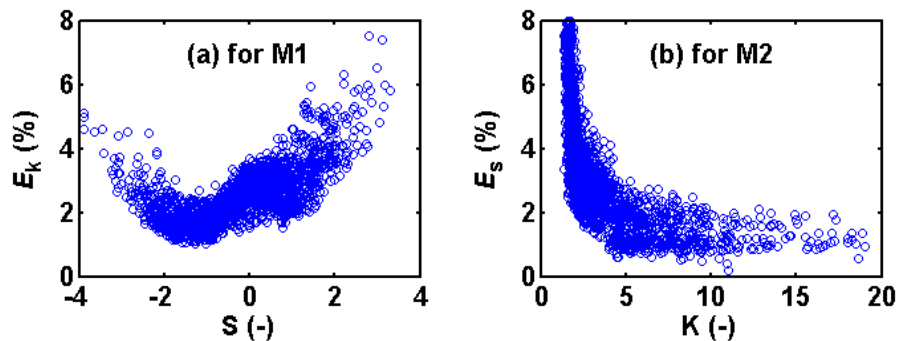


Figure 4.3 Relative moment errors of MCDPM with respect to (a) skewness or (b) kurtosis of local solids holdup signals

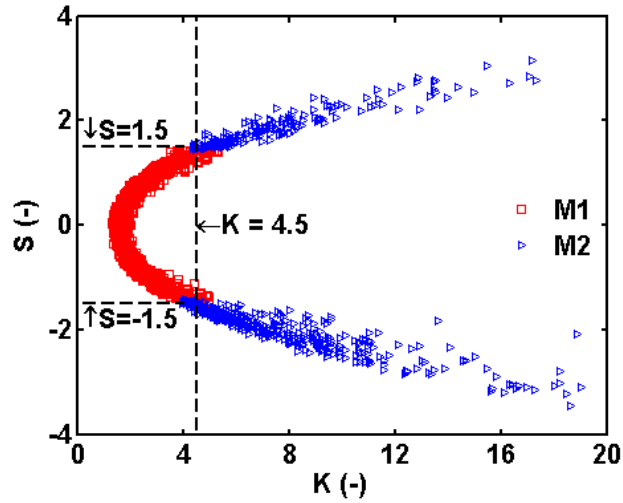


Figure 4.4 Relationship of skewness and kurtosis for all solids holdup signals

4.3.2 Division of dense and dilute phases

Dividing the dense and dilute phases from a solids holdup time series requires finding a division value, a special solids holdup, to identify the transition between the two phases. Using the dense phase fraction, f_d , a number n can be obtained by Eq. 4.20, from a solids holdup time series with population N , e.g. series 1 from Eq. 4.1.

$$n = f_d N \quad (4.20)$$

If the time series is sorted in a descending order, the n th solids holdup value in the sorted series, $\varepsilon_s(n)$, will be the division value. Thus, the subset of the solids holdup numbered up to n in the sorted series includes all members of the dense phase and the rest includes all members of the dilute phase in the measured time series. As a result, the dense and

dilute phases can be divided from the measured time series using the determined value $\varepsilon_s(n)$.

Considering that time series 4.1 represents a series of solids holdup values over time at a given location inside the fluidized bed, the dense phase time fraction in the time series actually also represents the volume fraction of the dense phase at that given location. As well, the average dense and dilute phase holdups in the time series would represent the dense and dilute phase holdups at the given location.

4.4 Results and discussion

4.4.1 Flow structure across regimes

Figs. 4.5 to 4.7 provide the profiles of the solids holdups of the dense and dilute phases and the dense phase volume fraction of BFB, TFB, CTFB, HDCFB and CFB obtained by MCDPM, whose operating conditions are listed in Table 4.1. The profiles demonstrate that different fluidization regimes have different flow structures. For the dilute phase, BFB, TFB and CTFB share similar solids holdup profiles, which do not change appreciably (around 0.06) in the core region but increase quickly toward the wall to up to about 0.20. Further increasing the air velocity to enter HDCFB and CFB regimes, the profiles of the dilute phase solids holdups, although still in parabolic shape, are seen to have much smaller magnitudes than those in BFB, TFB and CTFB, both in the centre and at the wall (Fig. 4.5). However, the profile of the dilute phase solids holdup for CTFB is seen to have a more gradual increase toward the wall than all other 4 regimes and a lower

value at the wall than BFB and TFB. For the dense phase, BFB, TFB and CTFB have same uniform profiles of the dense phase solids holdups across the bed except that CTFB has a slight but steady increase from the centre toward the wall, corresponding to the values from 0.45 at the centre to 0.50 at the wall. Much different from the uniform radial distribution of BFB, TFB and CTFB, the dense phase solids holdup profiles of HDCFB and CFB are characterized by the typical core-annular structure, with the solids holdups in the core region of HDCFB and CFB much less than those of BFB, TFB and CTFB and increasing quickly in the annular region (Fig. 4.6). Despite similarities between HDCFB and CFB profiles, significant differences are observed in the magnitudes of the solids holdups of the dense phase, with HDCFB varying from ~ 0.05 to ~ 0.5 , while CFB from ~ 0.03 to ~ 0.20 . Further examining the dilute phase profiles for HDCFB and CFB can also reveal some differences between the two regimes, although on a much smaller scale, with HDCFB varying from ~ 0.01 to ~ 0.15 and while CFB from ~ 0.01 to ~ 0.10 .

Compared to the solids holdup profiles of the dense and dilute phases, the profiles of the dense phase volume fraction vary differently across the fluidization regimes, as shown in Fig. 4.7: BFB regime is dominated by dense phase with dense phase volume fractions of 0.6 or greater throughout the bed, while HDCFB and CFB regimes are clearly dominated by dilute phase with dense phase volume fractions mostly lower than 0.2 except near the wall area. Unlike the phase holdup profiles for both dense and dilute phases, the radial profiles of the dense phase volume fraction for both TFB and CTFB is completely different from that of BFB, increasing steadily from the centre to the wall. Additionally, the volume fraction profiles for TFB and CTFB appear to be nearly indistinguishable,

suggesting that CTFB is clearly a turbulent fluidization regime although significant external solids circulation has been introduced. Likewise, the volume fraction profiles for CFB and HDCFB are also extremely similar, both having typical clear core-annulus structure, suggesting a possible common root for those two regimes.

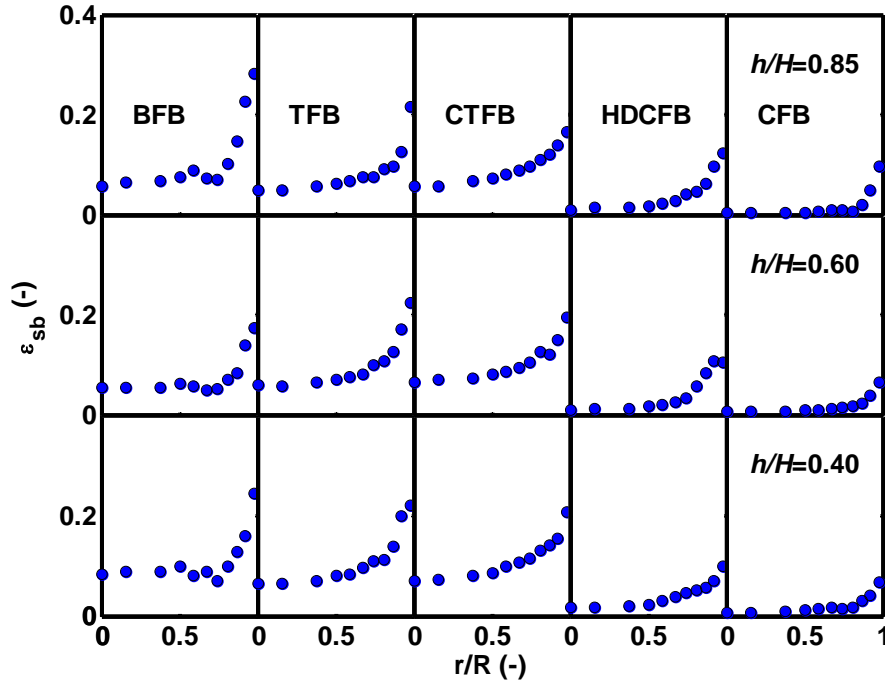


Figure 4.5 Radial solids holdup profiles of the dilute phase of BFB ($u_g = 0.53\text{m/s}$), TFB ($u_g = 1.6\text{m/s}$), CTFB ($u_g = 2.57\text{m/s}$, $G_s = 234\text{kg/m}^2\text{s}$), HDCFB ($u_g = 8\text{m/s}$, $G_s = 550\text{kg/m}^2\text{s}$) and CFB ($u_g = 8\text{m/s}$, $G_s = 100\text{kg/m}^2\text{s}$), (data for HDCFB and CFB from Yan and Zhu, 2004)

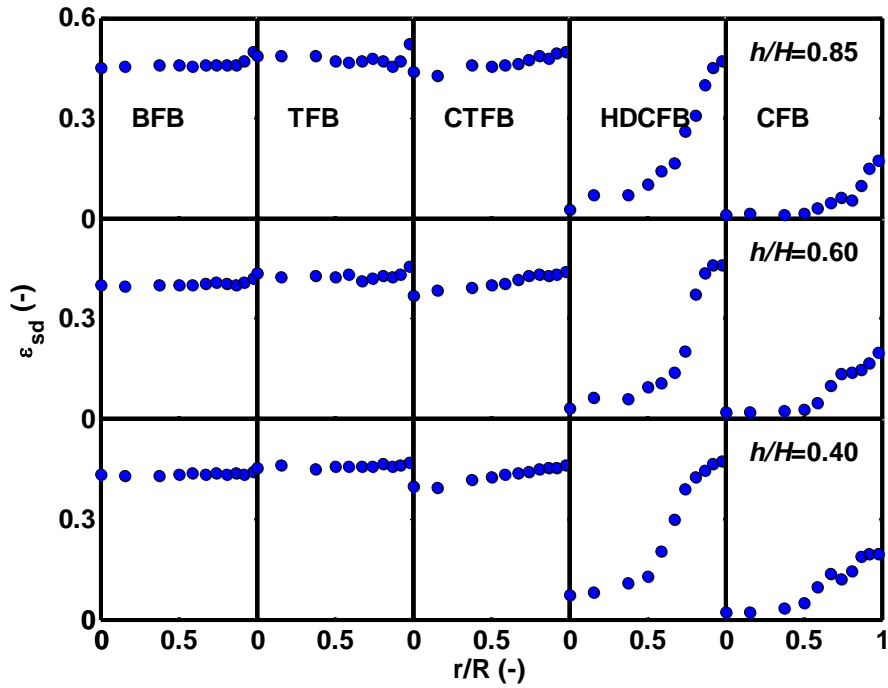


Figure 4.6 Solids holdup profiles of dense phase of BFB ($u_g = 0.53\text{m/s}$), TFB ($u_g = 1.6\text{m/s}$), CTFB ($u_g = 2.57\text{m/s}$, $G_s = 234\text{kg/m}^2\text{s}$), HDCFB ($u_g = 8\text{m/s}$, $G_s = 550\text{kg/m}^2\text{s}$) and CFB ($u_g = 8\text{m/s}$, $G_s = 100\text{kg/m}^2\text{s}$), (data for HDCFB and CFB from Yan and Zhu, 2004)

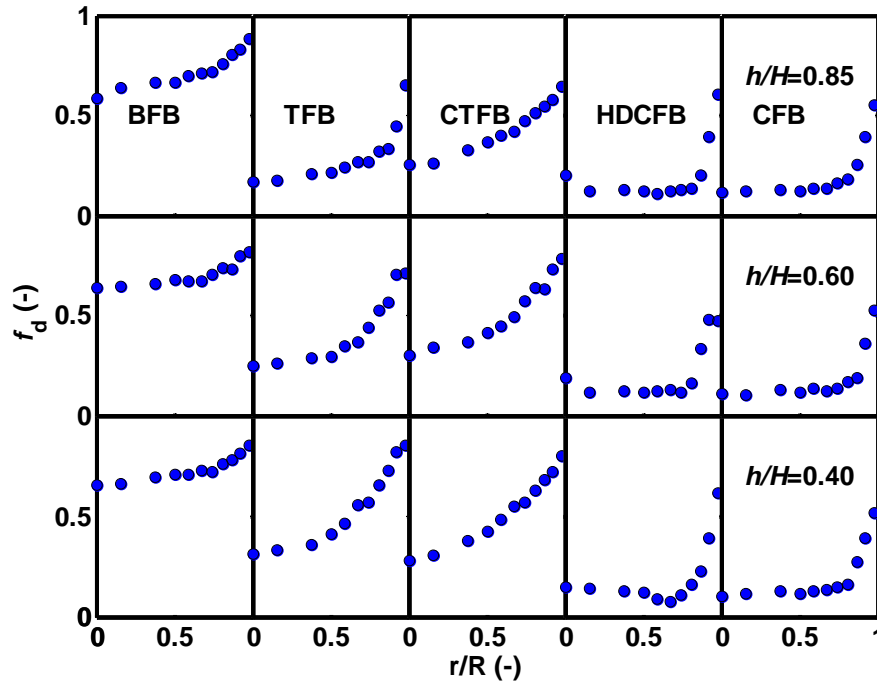


Figure 4.7 Profiles of dense phase fraction of BFB ($u_g = 0.53\text{m/s}$), TFB ($u_g = 1.6\text{m/s}$), CTFB ($u_g = 2.57\text{m/s}$, $G_s = 234\text{kg/m}^2\text{s}$), HDCFB ($u_g = 8\text{m/s}$, $G_s = 550\text{kg/m}^2\text{s}$) and CFB ($u_g = 8\text{m/s}$, $G_s = 100\text{kg/m}^2\text{s}$), (data for HDCFB and CFB from Yan and Zhu, 2004)

4.4.2 Flow regime transition and similarities

Comprehensively examining all results, shown in Figs. 4.5-4.7, can also help to reveal the mechanism of the regime transitions through the various fluidization regimes. The overall average values of ε_{sb} , ε_{sd} and f_d are plotted against the fluidization regimes in Fig. 4.8, from low-velocity fluidization regimes (BFB, TFB and CTFB) to high-velocity fluidization regimes (HDCFB and CFB). For the dense phase, its average values stay relatively constant in the low-velocity regimes, but decreases with increasing gas velocity in the high-velocity regimes. For the dilute phase, the situation is similar, although

somewhat less significant than the dense phase. On the other hand, the dense phase fraction, f_d , decreases dramatically with increasing velocity, through bubbling, turbulent (TFB and CTFB) and high-velocity regimes (HDCFB and CFB). From those trends, it can be postulated that from low velocity up, the regime transition starts with the increase of the dilute phase fraction, while the magnitudes of both dense phase and dilute phase holdups remain constant, within the 3 low-velocity fluidization regimes. In other words, within low-velocity regimes, the values of the solids holdups in both the dilute and dense phases do not change much, but the relative volume (fraction) of the dense phase shrinks with increasing velocity. A most significant change in the flow structure, i.e. regime transition, happens between CTEB and HDCFB, where the dense phase holdups, as well as but to a smaller extent the dilute phase holdups, begin to decrease, while the dense phase fraction continues to decrease, with increasing gas velocity. Therefore, one may say that this transition has a more profound change in the flow structure, or the transition between CTEB and HDCFB represents a more dramatic regime transition than those within each one of the low-velocity and high-velocity regimes. In the high-velocity regimes, the phase holdups begin to have more changes, while the phase fractions experience little change, and the transition between HDCFB and CFB is more signified by values of the phase holdups rather than their relative phase fractions.

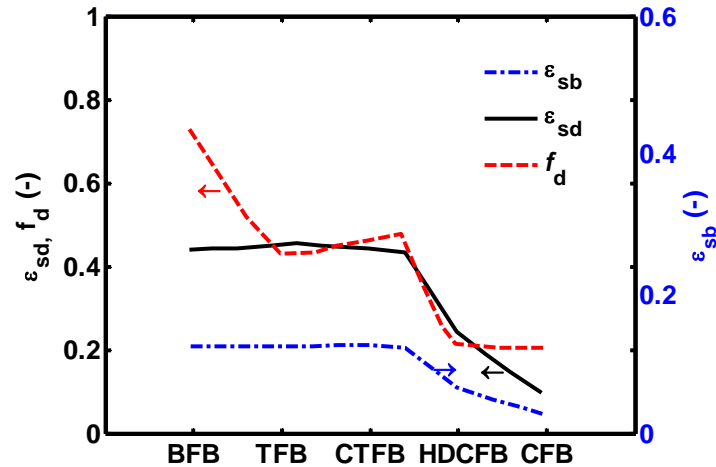


Figure 4.8 Variation of average values of ϵ_{sb} , ϵ_{sd} and f_d across the fluidization regimes, BFB ($u_g = 0.53\text{m/s}$), TFB ($u_g = 1.6\text{m/s}$), CTFB ($u_g = 2.57\text{m/s}$, $G_s = 234\text{kg/m}^2\text{s}$), HDCFB ($u_g = 8\text{m/s}$, $G_s = 550\text{kg/m}^2\text{s}$) and CFB ($u_g = 8\text{m/s}$, $G_s = 100\text{kg/m}^2\text{s}$), (data for HDCFB and CFB from Yan and Zhu, 2004)

Further examining Fig. 4.8, one should be able to notice that TFB and CTFB have almost the same flow structures in term of solids holdup, and therefore may be considered being operated under very similar regimes. Noting that the particle velocity in CTFB would not be zero given the external solids recirculation, the difference between the TFB and CTFB regimes would be mostly on that CTFB has a net particle upflow (Zhu and Zhu 2008b). Such net upwards solids flow also seems to yield a slightly more obvious variation in radial solids holdup in the CTFB regime than in the TFB regime. On the contrary, the differences between the flow structures in the HDCFB and CFB are more significant, than those between TFB and CTFB. This transition (between HDCFB and CFB) may be similar in magnitude as the transition between BFB and TFB, but with the changes both in “quantity” (the relative division of the phases) and “quality” (the phase holdup values). On the other hand, the transition between the low-velocity and high-velocity regime

groups, as represented by the transition between CTFB and HDCFB, is more on the change in the phase holdup values (“quality”) rather than the division of the two phases (“quantity”).

Such a change first in the reduction of dense phase fraction and then the reduction of the solids holdup values of the two phases, in the regime transitions with increasing gas velocity and as discussed above with respect to Fig. 4.8, can also be observed with increasing radial distances from the centre towards the wall. As reported by Zhu and Zhu (2008), regime transition can happen gradually with respect to the locations inside a fluidized bed. Careful analyses over Figs. 4.5-4.7 suggest that the regime transition starts from the centre of the bed and then propagates towards the wall. For example, Fig. 4.7 shows that the reduction in dense phase fraction first starts from the bed centre with increasing gas velocity, while Fig. 4.6. shows little change in dense phase holdups in the low-velocity regimes. When the dense phase holdup does begin to change, its change also starts from the centre, gradually towards the wall, as shown by the radial profiles of the dense phase holdup in HDCFB and CFB in Fig. 4.6. For the dilute phase holdup shown in Fig. 4.5, there is also a clear trend that reduction in phase holdups starts from the centre towards the wall and only propagates to the wall region under the high-velocity regimes. Experimentally, the above postulation has been verified by the results of Qi et al (2009).

To further evaluate transitions among the 5 fluidization regimes, the Radial Nonuniformity Index (RNI) for ε_{sb} , ε_{sd} and f_d , as proposed by Zhu and Manyele (2001), are plotted in Fig. 4.9 for the various regimes. This radial uniformity index has a value

between 0 and 1 and represents the relative uniformity in the radial profiles with 0 indicating a flat and uniform profile. As such, the RNI values may be used to illustrate the flow development in the radial direction for the various regimes. Within the low velocity fluidization regimes, $RNI(\varepsilon_{sb})$ and $RNI(\varepsilon_{sd})$ remain relatively constant, suggesting more uniform fluidization and less variation in special regime transition. Into the high-velocity regimes, $RNI(\varepsilon_{sb})$, $RNI(\varepsilon_{sd})$ both have an obvious increase in HDCFB and then drop off into CFB, with the effect being very dramatic for the dense phase. $RNI(f_d)$ shows a similar trend but has a clear dip for CFB, suggesting that the division between the dense and dilute phases is more uniform across the bed than TFB/CTFB. The above mentioned phenomena echo at least partially the trends shown in Fig. 4.8 and certainly illustrate the differences and transitions between the various fluidization regimes.

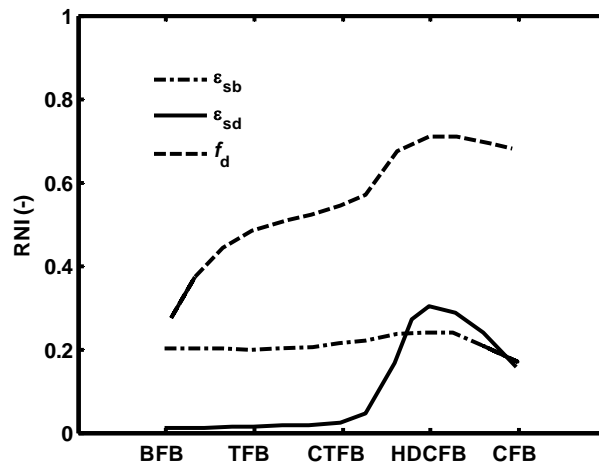


Figure 4.9 Radial Nonuniformity Index (RNI) of ε_{sb} , ε_{sd} and f_d at $h/H = 0.60$ for 5 fluidization regimes, BFB ($u_g = 0.53\text{m/s}$), TFB ($u_g = 1.6\text{m/s}$), CTFB ($u_g = 2.57\text{m/s}$, $G_s = 234\text{kg/m}^2\text{s}$), HDCFB ($u_g = 8\text{m/s}$, $G_s = 550\text{kg/m}^2\text{s}$) and CFB ($u_g = 8\text{m/s}$, $G_s = 100\text{kg/m}^2\text{s}$), (data for HDCFB and CFB from Yan and Zhu, 2004)

4.4.3 Flow regime differences and similarities

From the above analyses, it can be seen that the differences between each pair of neighbouring regimes and therefore the transition in between are not always the same and as a matter of fact can be dramatically different. Table 4.2 summarizes the values of the averages and Radial Non-uniformity Indices (RNIs) of ε_{sb} , ε_{sd} and f_d as used in Figs. 4.8 and 4.9. Following the same trend of Figs. 4.8 and 4.9, one can see that these parameters do not change much in the low-velocity regimes, but have a large jump crossing into HDCFB regime, and then “moderate” to a smaller change going into CFB regime. The extent of the above changes may be used to explore similarities among the various regimes.

As discussed above, TFB and CTFB have almost the same characteristics with minor differences so that they may be considered as a single regime. Between TFB (as well as CTFB) and BFB, the only difference seems to be the relative fractions of the dense and dilute phases, so that the difference is small and quantitative. In general, BFB is characterized by large bubbles going through the central areas of the bed, while TFB by

Table 4.2 Radial Non-uniformity Index (RNI) and average value for the dilute and dense phase solids holdups and the dense phase volume fraction

		BEB	TEB	CTEB	HDCFB	CFB
Dense Phase Fraction	Average Value	0.72	0.43	0.49	0.21	0.20
	Uniformity Index	0.02	0.03	0.04	0.60	0.31
Dense Phase Holdups	Average Value	0.43	0.45	0.44	0.24	0.08
	Uniformity Index	0.20	0.20	0.21	0.24	0.17
Dilute Phase Holdups	Average Value	0.10	0.10	0.11	0.04	0.02
	Uniformity Index	0.13	0.24	0.27	0.35	0.34

smaller voids more uniformly distributed across the bed. In other words, the transition is more on the changes in the size of the voids, while the dense phase remains the continuous phase. Therefore, TFB (including CTFB) still share many similarities with BFB and should be still grouped with BFB and considered a low-velocity fluidization, rather than high-velocity fluidization. Entering into the high-velocity regimes, the flow is more characterized with a continuous dilute phase and dispersed dense phase aggregates. Such a dramatic change is clearly exhibited in Table 4.2 on all the parameters presented, reflecting the fact that this is a more fundamental change (regime transition) in the flow structure, where the two phases inverse their role as the dominant phase. Furthering into CFB regime, the relative changes in the parameters become smaller again, indicating a smaller change or a milder transition from HDCFB. However, the relative changes between HDCFB and CFB are still larger than those between BFB and TFB/CTFB.

From the above discussion and based on a wide span of the gas-solids multiphase flow systems in all fluidized beds, one can conclude:

- (1) TFB and CTFB may be considered a similar regime.
- (2) The differences between TFB/CTFB and BFB are relatively small.
- (3) CTFB, although having net external solids circulation like HDCFB/CFB, is essentially still a turbulent regime, similar to TFB.
- (4) The transition between TFB/CTFB and HDCFB is much more significant than any other transitions.
- (5) There is a clear difference between HDCFB and CFB and such difference is larger than the difference between BFB and TFB.

4.4.4 Micro flow structure analyses

The differences between BFB, TFB, CTFB, HDCFB and CFB regimes can be further studied by the natures of probability density function (PDF) of the solids holdups and moment features, such as skewness and kurtosis, as shown in Figs. 4.10-4.12. The results demonstrate that the fluidization regimes can be classified into two groups: flow dominated by high solids holdup peak and flow dominated by the dilute phase peak (Fig. 4.10), corresponding to the low-velocity and high-velocity fluidization regime groups discussed earlier. In the first group, BFB, TFB and CTFB have a clear peak in their PDF graphs around the dense phase solids holdup, and a more scattered dilute phase distribution. The dense phase peak also increases from the centre toward the wall, while the magnitude of the dilute phase reduces from the centre to the wall, implying more dense phase dominating toward the wall. In the second group, HDCFB and CFB only display a dilute phase peak on the left side in their PDF graphs, implying dilute phase dominating. From the centre to the wall, the dilute phase peak widens and shifts right, responding to the weakened dilute phase structure. The lack of high density peak for HDCFB and CFB regimes echoes the low density fraction as shown in Fig. 4.8.

The differences between the fluidization regimes displayed by PDF can be exhibited through the skewness and kurtosis features of the solids holdups, as shown in Figs. 4.11 and 4.12. Typically, skewness is a measure of the lack of symmetry in the probability density function (PDF) of the solids holdup signals around the mean value and reflects the predominance between the dense and dilute phases in the gas-solid phase flow, negative skewness reflecting dense phase dominating flow and positive skewness

reflecting dilute phase dominating flow. The negative skewness in BFB and most of TFB and CTFB confirms the dense phase dominated flow, while the high skewness in HDCFB and CFB confirms the dilute phase dominated flow. For CTFB and to a lesser extent also for TFB, the skewness is close to zero in the centre, suggesting a beginning of the transition of the flow from dense phase dominating to dilute phase dominating. On the other hand, kurtosis is a measure of the peakedness of the PDF and quantifies the magnitude of the variation of solids holdup distribution of the dispersive phase (bubbles in BFB and clusters in CFB). Therefore, the long and sharp tails in the PDF in Fig. 4.10 lead to higher kurtosis values, corresponding to the solids distribution in the core region of HDCFB and CFB and in the wall region of BFB, TFB and CTFB. On the other hand, a narrow phase distribution on the PDF in Fig. 4.10 corresponds to lower kurtosis values, representing the solids holdup distributions in the core region of BFB, TFB and CTFB and in the wall region of HDCFB and CFB.

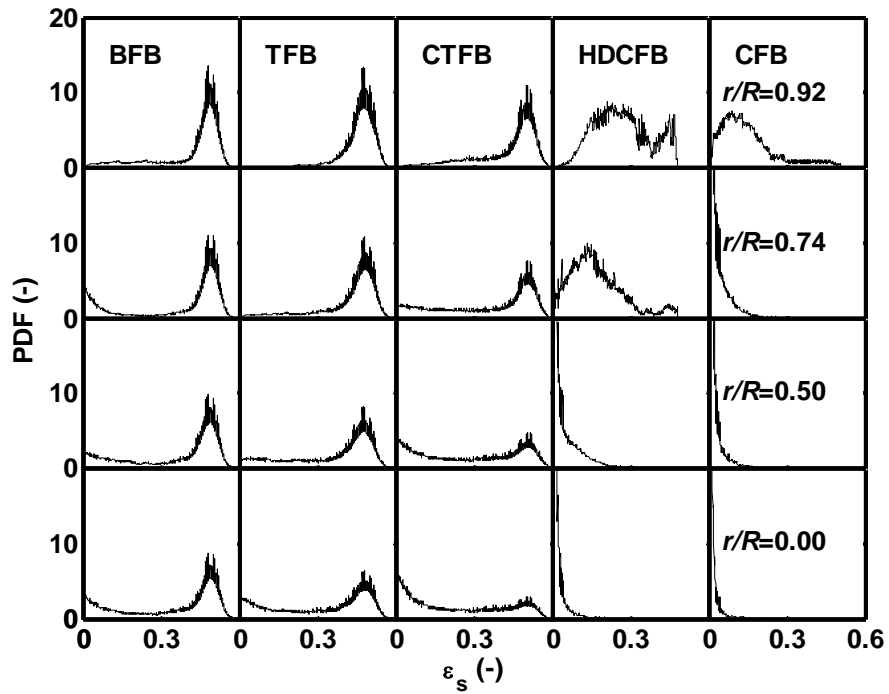


Figure 4.10 PDF profiles of BFB ($u_g = 0.53\text{m/s}$), TFB ($u_g = 1.6\text{ m/s}$), CTFB ($u_g = 2.57\text{m/s}$, $G_s = 234\text{kg/m}^2\text{s}$), HDCFB ($u_g = 8\text{m/s}$, $G_s = 550\text{kg/m}^2\text{s}$) and CFB ($u_g = 8\text{m/s}$, $G_s = 100\text{kg/m}^2\text{s}$), corresponding to the data at $h/H = 0.60$ in Fig. 4.11 and 12, (data for HDCFB and CFB from Yan and Zhu, 2004)

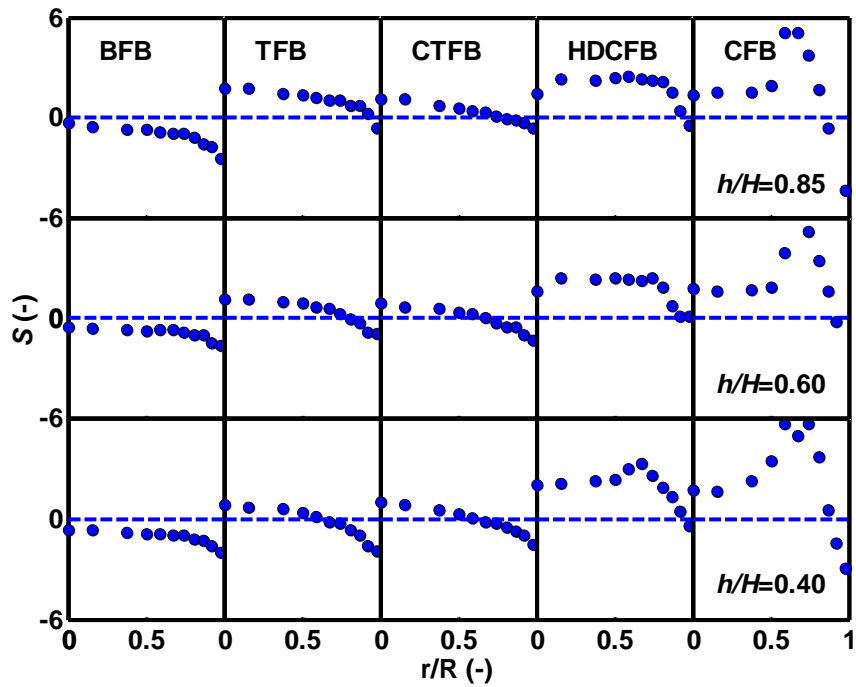


Figure 4.11 Radial skewness profiles for BFB ($u_g = 0.53\text{m/s}$), TFB ($u_g = 1.6 \text{ m/s}$), CTFB ($u_g = 2.57\text{m/s}$, $G_s = 234\text{kg/m}^2\text{s}$), HDCFB ($u_g = 8\text{m/s}$, $G_s = 550\text{kg/m}^2\text{s}$) and CFB ($u_g = 8\text{m/s}$, $G_s = 100\text{kg/m}^2\text{s}$), (data for HDCFB and CFB from Yan and Zhu, 2004)

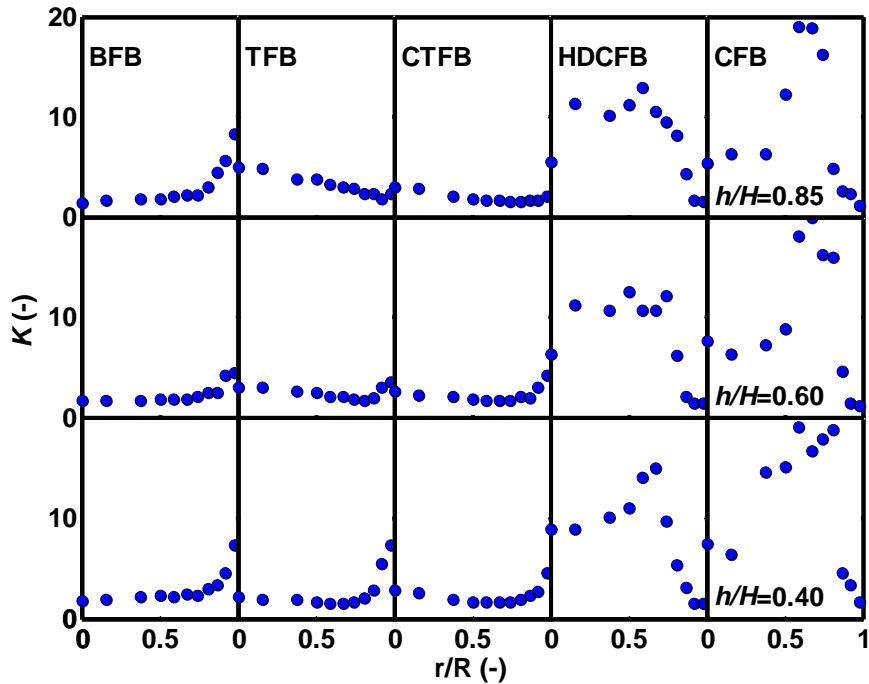


Figure 4.12 Profiles of dense phase fraction of BFB ($u_g = 0.53\text{m/s}$), TFB ($u_g = 1.6\text{ m/s}$), CTFB ($u_g = 2.57\text{m/s}$, $G_s = 234\text{kg/m}^2\text{s}$), HDCFB ($u_g = 8\text{m/s}$, $G_s = 550\text{kg/m}^2\text{s}$) and CFB ($u_g = 8\text{m/s}$, $G_s = 100\text{kg/m}^2\text{s}$), (data for HDCFB and CFB from Yan and Zhu, 2004)

Conclusion

Experiments with FCC particles were carried out in two fluidized beds under five different fluidization regimes, bubbling (BFB), turbulent (TFB), circulating turbulent (CTFB), high density circulating (HDCFB) and circulating fluidized beds (CFB). Solids holdup signals were obtained with optical fibre probes at eleven radial positions at four elevations. The moments (mean, standard deviation, skewness and kurtosis) from the experimentally measured solids holdup signals were compared with those of equivalent ideal two phase flow systems and a Moment Consistency Data Processing Method

(MCDPM) was proposed to estimate the solids holdups and volume fractions of the dense and dilute phases at each measured location. These key parameters and their radial and axial distributions were used to study the detailed flow structures inside the various fluidized beds and the regime transitions among them. The results showed great similarities between the turbulent (TFB) and circulating turbulent (CTFB) fluidized beds but less similarities between the high-density circulating fluidized bed (HDCFB) and the circulating fluidized bed (CFB), with a more significant regime transition from TFB/CTFB to HDCFB. In the low-velocity regimes of BFB, TFB and CTFB, increasing gas velocity leads only to the decreasing of dense phase fraction but not the average dilute and dense phase holdups, while in the high-velocity regimes from HDCFB to CFB, it is the solids holdups of the dense phase that undergoes the most change. From the low-velocity to the high-velocity regimes, both the solids holdup and the fraction of the dense phase experience a drastic decrease, suggesting that this transition has a more profound change in the flow structure and further suggesting that CTFB is in reality still a turbulent fluidized bed although external solids recirculation has been imposed. Across the bed, the regime transition starts from the centre of the bed and then propagates towards the wall.

Acknowledgement

The authors are grateful to the Natural Sciences and Engineering Research Council of Canada for supporting this work.

Notation

D = bed diameter, m

E_k = relative kurtosis error

E_s = relative skewness error

f_d = volume fraction of dense phase

G_s = circulation rates, kg/m²s

K = kurtosis of local solids holdup fluctuations

K_{th} = theoretical kurtosis value

N = sampling population

r = radial position, m

R = radius of the column, m

S = skewness of local solids holdup fluctuations

S_{th} = theoretical skewness value

u_g = superficial air velocity, m/s

v_p = instantaneous particle velocity, m/s

V_p = particle velocity, m/s

Z = elevation from the air distributor, m

Greek letters

ε = Instantaneous solids holdup

$\bar{\varepsilon}_s$ = local time-averaged solids holdup

ε_{sb} = local time-averaged solids holdup of dilute phase

ε_{sd} = local time-averaged solids holdup of dense phase

ρ_p = particle density, kg/m³

σ = standard deviation of local solids holdup fluctuations

Subscripts

c = phase

b = Dilute phase

g = gas

P = particle

s = solids

Literature cited

Abbasi, M., Sotudeh-Gharebagh, R., Mostoufi, N. and Zarghami, R., (2009), Nonintrusive characterization of fluidized bed hydrodynamics using vibration signature analysis, *AIChE Journal*, Volume 56, Issue 3, 597-603

Bi, H. T., Su, P., (2001), Local Phase Holdups in Gas-Solids fluidization and Transport, *AIChE Journal*, Vol. 47(9), 2025.

Briens L. and Bojarra, M., (2010), Monitoring Fluidized Bed Drying of Pharmaceutical Granules, *AAPS PHARMSCITECH*, Volume 11, Number 4, 1612-1618

Breault R. W., Emily M. Casleton, Christopher P. Guenther, "Chaotic and statistical tests on fiber optic dynamic data taken from the riser section of a circulating fluidized bed, *Powder Technology*, Volume 220, April 2012, Pages 151-163

Grace, J. R., (1990), High-Velocity Fluidized Bed Reactors, *Chemical Engineering Science*, Vol. 45, No. 8, pp. 1953-1966

- Grace, J. R., (2000), Reflections on turbulent fluidization and dense suspension upflow, Powder Technology, 113, 242–248
- Lee, G. and Kim, S., (1988), Pressure Fluctuations in Turbulent Fluidized Beds, Journal of Chemical Engineering of Japan, Vol.21 (5), 515-521
- Manyele, S. V., Zhu, J.-X., Zhang, H., (2003), Analysis of the Microscopic Flow Structure of a CFB Downer Reactor Using Solids Concentration Signals, International Journal of Chemical Reactor Engineering Volume 1 Article A55.
- Qi, X., Zhu, H., Zhu, J., (2009), Demarcation of a New Circulating Turbulent fluidization Regime, AIChE Journal Vol. 55, No. 3, 595
- Song, X., et al, (2004), Hydrodynamics of the reactor section in fluid cokers, Powder Technology, 147, 126–136.
- Taylor, E.M., Guenther, C.P., Breault, R. W., (2008), Dynamical Tests on Fiber Optic Data Taken from the Riser Section of a Circulating Fluidized Bed, DOE/NETL-2008/1927
- Yang, J, L Wang, L Tong, H Li, Modeling of radiative heat transfer between high-temperature fluidized beds and immersed walls, Chemical engineering science, Volume 59, Issue 15, August 2004, Pages 3195-3199
- Wang, L., Wu, P., Xuezh Ni, Surface-particle-emulsion model of heat transfer between a fluidized bed and an immersed surface, Powder technology, Volume 149, Issues 2-3, 3 January 2005, Pages 127-138
- Yan, A., Zhu, J.-X, (2004), Scale-Up Effect of Riser Reactors (1): Axial and Radial Solids Concentration Distribution and flow Development, Ind. Eng. Chem. Res., 43, 5810-5819.
- Zhu, J., Bi, H., (1995), Distinctions Between Low Density and High Density Circulating fluidized Beds, The Canadian Journal Of Chemical Engineering, Volume 73, 644

- Zhu, J., Manyele, S. V., (2001), Radial Nonuniformity Index (RNI) in fluidized Beds and Other Multiphase flow Systems, *The Canadian Journal of Chemical Engineering*, Vol. 79, 203
- Zhang, H., Zhu, J.-X, (1998), A novel calibration procedure for a fiber optic solids concentration probe, *Powder Technology*, 100, 260-272.
- Zhu, H., Zhu, J.-X, (2008a), Gas-Solids flow Structures in a Novel Circulating-Turbulent fluidized Bed, *AIChE Journal*, Vol. 54 (5), 1213.
- Zhu, H., Zhu, J.-X, (2008b), Comparative study of flow structures in a circulating-turbulent fluidized bed, *Chemical Engineering Science*, 63, 2920-2927.
- Zhu, H., Zhu, J., (2008c), Characterization of fluidization behavior in the bottom region of CFB risers, *Chemical Engineering Journal*, 141, 169–179.
- Zhu, H., Zhu, J., (2008), New Investigation in Regime Transition from Bubbling to Turbulent Fluidization, *The Canadian Journal of Chemical Engineering*, Vol. 86(6), 553
- Zhu J-X and Cheng Yi, “Fluidized-Bed Reactors and Applications”, Chapter 5.3 in *Multiphase Flow Handbook*, ed. Clayton Crowe, CRC Press, New York, 2005, pp 5.55-5.93.
- Zhu, J. (2010), Circulating turbulent fluidization—A new fluidization regime or just a transitional phenomenon, *Particuology*, 8, Pages 640-644

5 Transition characteristics of gas-solid flow in circulating turbulent fluidized beds

5.1 Introduction

Most of the solid materials in industry are used as particles or powders. As particulate solid materials are fed in a column and air is supplied to the bottom of the column in a proper way, the gas-solid system experiences in different dynamic regimes at different air velocities, such as packed bed, fluidized bed and pneumatic transport. The fluidized bed can be further divided into bubbling, turbulent and fast fluidization regimes. The knowledge on the transition of fluidized beds from one regime to another is very helpful in designing fluidized bed reactors and operating them properly. For example, typical FCC units operate under circulating fluidized bed conditions at high gas velocities and high solids circulation rates. The turbulent fluidized bed reactors operating at lower gas velocities are widely used in Fischer-Tropsch synthesis and acrylonitrile production due to high heat and mass transfer efficiencies (Grace, 1990).

Turbulent fluidization regime (TFB) is between the bubbling fluidization (BFB) and fast fluidization (CFB) regimes. There are controversial debates on transition from BFB to CFB due to the complexity of such transition in high density gas-solid flow systems. One controversy on TFB is related to the confusion about transition velocity determination. Yerushalmi and Cankurt (1979) divided the transition flow regime between bubbling and

fast fluidization regimes into transient turbulent and turbulent fluidization regimes using transition velocity, u_c , onset velocity, u_k , and ending velocity, u_{tr} . Using pressure drop signals with pressure transducers along the bed, u_c , and, u_k , were defined at the specific air velocities corresponding to the maximum standard deviation and to the levelling off standard deviation of the signals respectively. However, other authors found no such u_k to mark the beginning of TFB. Although it is now widely considered that TFB extends from u_c to the onset of fast fluidization, u_{tr} (Bi et al, 2000), this confusion is not clarified as pressure fluctuations of a gas-solid system, on average across the bed, can be related to many factors, such as bed geometry, pressure probe installation, and the flow, leading to inconsistent results (Bi et al, 1995). On the other hand, as the flow regime transition corresponds to the change of the flow structure, it might be a proper way to determine the onset transition air velocity of TFB using the standard deviation of the local solids holdup, one property parameter of local flow structures of TFB (Zhu and Zhu, 2008).

Another controversy is on the ending transition air velocity of TFB or onset transition air velocity of CFB, u_{tr} , due to the lack of correctly understanding as how the flow structure of TFB develops to the one of CFB. Although attributed to dilute phase dominating flow (Zhu et al, 2012), CFB can operate at much higher than particles terminal velocity and at higher density than dilute transport as there exist plenty of high density clusters and different flow structures from BFB. The ending of TFB responds just to the onset of CFB, so the high density flow structure and solids circulation have to be two important factors influencing the transition from TFB to CFB. However, Yerushalmi and Cankurt (1979) defined u_{tr} as the transport air velocity close to terminal velocity of median particle size

using pressure diagram. On the other hand, the transport velocity, corresponding to the saturation carrying capability of the gas-solid system, was used in defining the regime transition between fast fluidization and the dilute transport suspension flow (Xu et al, 2006; Yang, 2004). In fact, Schnitzlein et al (1998) did not find such a velocity making any observable changes in flow structure. Related to the choking velocity and solids circulation rate, a significant entrainment velocity of the fluidized bed was defined as the transition point from TFB to CFB (Bi, 1994), while significant solids circulation at a rate of $100\text{kg/m}^2\text{s}$ was achieved in CTFB with FCC particles at 1.0 m/s of air velocity close to u_c (Zhu and Zhu, 2008a). The other experimental results on the transition velocities were summarized in Table 5.1.

Inadequate study on the transient nature of flow structure of the TFB regime and insufficient consideration on the solids circulation effect on flow regime development are two key aspects to characterize the transient flow regime. Recently, Zhu and Zhu (2008a, b) proposed a novel circulating fluidized bed (CTFB) reactor, integrating conventional turbulent fluidized beds into a unique high-density circulating system, having provided a proper platform to investigate the said issues in depth. In this study, experiments on CTFB were carried out using FCC particles. Solids holdup signals were then processed using moment analysis method to explore the transition characteristics of the flow structure in CTFB and determine the corresponding transition air velocities.

Table 5.1 A summary of transition air velocities of TFB in previous studies, using FCC as solid particle

Author	$d_p(\mu\text{m})$	$\rho_p(\text{kg/m}^3)$	$D_b(\text{mm})$	$u_c(\text{m/s})$	$u_k(\text{m/s})$	$u_{tr}(\text{m/s})$
Kwauk et al (1986)	58	1780	300			1.85
Le Palud & Zenz (1989)	35-90	1250	102			0.61-0.91
Li et al (1988)	54	930	90			2.5
Horio et al (1989)	60	1000	50			0.92
Yang et al (1990)	67	1700	224			1.5
Perales et al (1990)	80	1715	92	0.76	1.15	1.6
Theil & Potter (1977)	60	930	51 102 218		0.41 0.22 0.0225	
Yerushalmi & Cankurt (1979)	49	1070	152		0.61	1.37
Jin et al (1986)	52.7 65.3	1667 1172	280	0.55 0.42		
Mori et al (1988)	56	729	50	0.44	1.26	
Horio et al (1992) FCC	60	1000	50	0.5	0.6	0.95
Tsukada et al (1993)	46.4	1780	50	0.3	0.65	
Chehbouni et al (1994)	78	1450	82	0.26		1.0-1.2
Bi and Grace (1995)	60	1580	102	0.7		
Cui et al (2000)	70	1673	152	0.77		
Shou and Leu (2005a)	71	1800	108	1	1.65	

5.2 Experimental setup

The experimental unit was a cold model circulating turbulent fluidized bed (CTFB), which consisted of six parts (Fig. a): (1) a CTFB column, with i.d. of 0.101m and height of 3.6m between gas distributor (a perforated-plate with open area ratio 14%) and column top; (2) a quick discharging section on the top of the CTFB column with a diameter of 0.203m and a total height of 6.4m; (3) a downcomer (i.d. 0.305m) with a solids level of 4.85m where all solids were stored; (4) a solids circulation rate measurement device with two flapper valves in the upper section of the downcomer (Pärssinen and Zhu, 2001); (5) a recycle loop including a primary inner cyclone, secondary and tertiary standard cyclones, and a bag filter to capture the entrained particles and return them to the downcomer; (6) an inclined solids return tube at the bottom with a solid circulation rate control device.

After passing the solids control valve in the inclined tube, the particles coming from the downcomer entered the CTFB bottom at a height of 0.2 m above the gas distributor, and were accelerated by air at ambient conditions. Secondary air supply was distributed via an annular perforated plate with 12.6% free area at the bottom of the upper discharging section to lift the particles upwards and to entrain particles out of the column as quickly as possible to minimize the pressure drop in the upper section. Therefore, this unique

design enabled high solids circulation rates and high suspension density in the CTFB with relatively low superficial gas velocity (0.5–5 m/s). In the present study, the secondary air velocity was kept at 6 m/s. The particles used in this study were FCC catalyst with a Sauter mean diameter of 76 μm and a particle density of 1780 kg/m^3 . The relative humidity was kept between 70 and 80% to minimize the electrostatic effects.

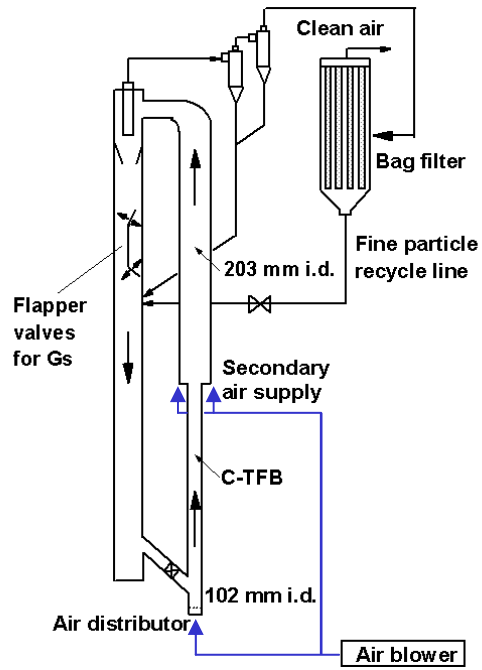
Experimental data were acquired using 4 multi-fibre optical reflective probes of model PV-6, developed by the Institute of Process Engineering, Chinese Academy of Sciences, Beijing, China. Each of 4 probes is composed of two optical fibre bundles located on the same vertical line. Each bundle consists of both light-emitting and receiving quartz fibres arranged in an alternating array, corresponding to emitting and receiving layers of fibres. The diameter of each fibre is 25 μm . Light from a light emitting diode (LED) transmits through the emitting half of the fibres to the tip, where hitting upon particle(s) in the riser, is reflected back to the probe. The intensity of the reflected light depends on the concentration, size distribution, composition, and shape of the particles. The received light reflected by the particles is converted by a photo-multiplier into voltage signals. The voltage signals are further amplified and fed into a computer. A special calibration procedure in high particle density environment was carried out and the calibration curves were obtained to convert the voltage data to solids holdups, following the procedure proposed by Zhang et al (1998).

The probes were setup at four separate axial elevations, and traversed horizontally to measure local solids holdups at eleven radial positions (Fig. 5.1b). The 4 axial locations

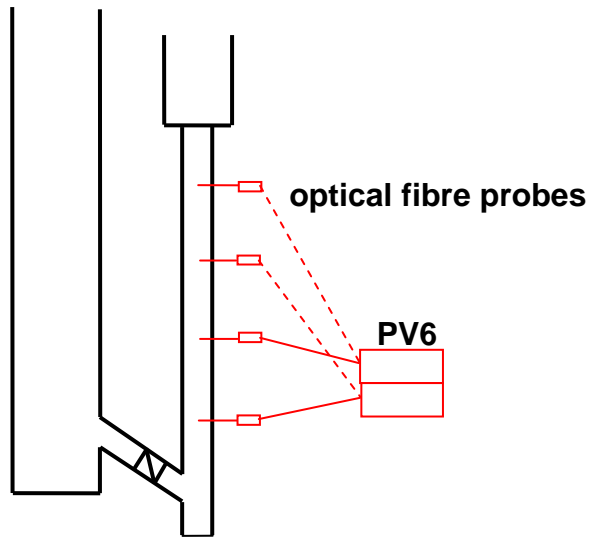
were chosen in an effort to characterize the acceleration zone (0.8 m) and the fully developed zone (1.5, 2.2 and 3.0 m). Radial positions were chosen at the midpoints of eleven equal distributed areas ($r/R = 0.0, 0.16, 0.38, 0.5, 0.59, 0.67, 0.74, 0.81, 0.87, 0.92,$ and 0.98) at each axial level within the risers. There were two PV6 units used in the experiments: a master and a slave. A special setup procedure was implemented for the two units to control four probes and a special data processing method was carried out with normalized calibration curves and different unit gains and offsets to obtain consistent experimental results throughout the bed. At one radial location the units were connected to two adjacent probes and then switched to the other two. To ensure the consistency of the data at one specific operating condition, the data at all locations were acquired within one run by the four probes. The sampling rate was 50 kHz and data were collected for 131 sec. In addition, 10 Ω -type differential pressure transducers of PX163-120D5V and PX162-027D5V were installed at median positions of $z = 0.38, 0.66, 0.95, 1.29, 1.65, 2.01, 2.45, 2.85, 3.22, 3.61$ m along the column, sampling 400 s at 1000 Hz. The pressure probes were made of brass tubes with Taylor #500 screen end and the link plastic tubes were not longer than 25 cm. Air velocities and solids circulation rates are listed in Table 5.2, corresponding to bubbling, circulating turbulent and fast fluidization regimes.

Table 5.2 Operating conditions of experiments

Regime	u_g (m/s)	G_s (kg/m ² s)
Bubbling	0.53	0
Circulating Turbulent	0.74-3.0	0-330
Fast	3.0 - 4.87	150-420



(a)



(b)

Figure 5.1 Experimental apparatus and optical fibre probe setup

5.3 Results and discussion

5.3.1 Transient features of solids holdup signals

Local solids concentration signals are the record of solids holdup fluctuations of the gas-solid flow. Such fluctuations reflect the transient behavior of the gas-solid flow (Cui et al, 2000). Fig. 5.2 shows some typical signals of solids holdup in bubbling fluidized bed (BFB), circulating turbulent fluidized bed (CTFB) and the bottom zone of circulating fluidized bed (CFB) at three radial positions, where peaks represent dense phase and valleys represent dilute phase. For BFB regime ($u_g = 0.53$ m/s and $G_s = 0$ kg/m²s), the signals are characterized by large square peaks around a constant height of 0.4, equivalent to the dense phase solids holdup. From the centre to the wall, the shapes and the heights of the peaks and valleys do not change appreciably. Maximum solids fluctuations and clear differences in solids holdup difference between the dense and dilute phases are observed across the bed, implying no obvious difference in the flow structure between the center and the wall. Examining the signal fluctuation, a higher fraction of the dense phase than the dilute phase can be seen.

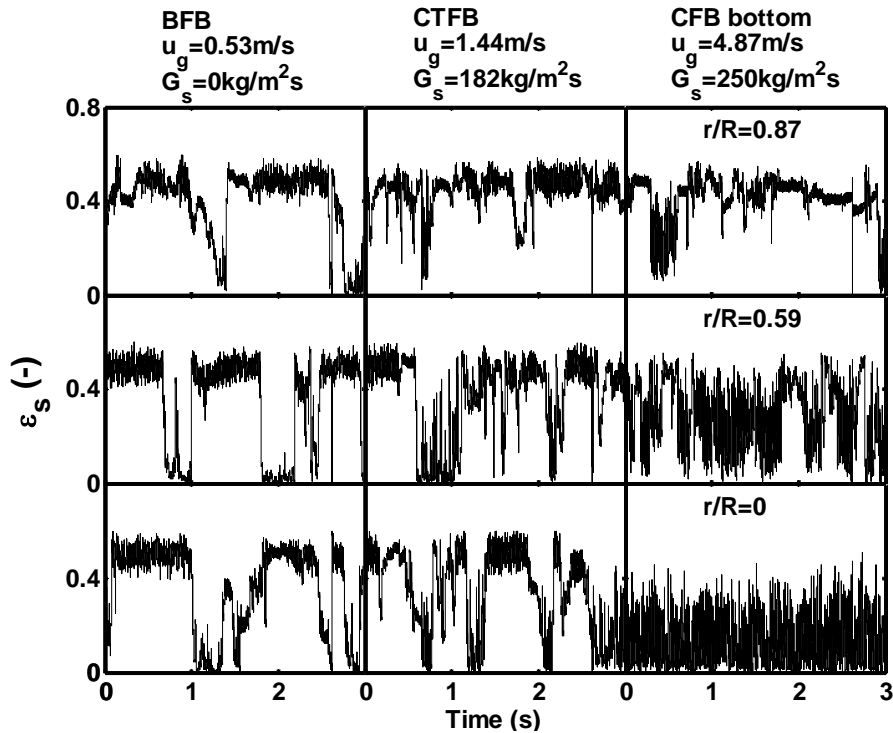


Figure 5.2 Evolution of solids concentration traces in BFB, CTFB, and the bottom zone of CFB ($z = 1.5$ m)

CTFB operating at higher air velocity ($u_g = 1.44$ m/s and $G_s = 182$ kg/m²s) appears to have similar maximum solids holdup fluctuations at the central and the middle positions as BFB, but the widths of each of the peaks and the valleys in the signals become narrower. Compared to those from the BFB regime, solids holdup signals from the CTFB regime start to have vague dense and dilute phases, with a good fraction of the recorded solids holdup having intermediate values between the two. In other words, there are narrow deep valleys splitting the dense phase peaks and there are narrow high peaks appearing in the dilute phase valleys. From the center to the wall, the depths of the valleys reduce to half, leading to large square peaks appearing at the wall. With regard to the fraction, while the wall region still has clear dense phase domination, a nearly equal fraction appears in the center. Further increasing air velocity ($u_g = 1.94$ m/s in Fig. 5.3),

the signals still appear to have maximum solids holdup fluctuations throughout the bed, but the dense phase fraction reduces clearly to less than 0.5 in the central region, and the average value of the fluctuating signal becomes less than the maximum value occurring in BFB. On the other hand, the fluctuation pattern does not seem to change much with increasing solids circulation rate as shown in Fig. 5.3. However, the signals of TFB regime (graphs at $G_s = 0 \text{ kg/m}^2\text{s}$ in Fig. 5.3) differ somewhat from the ones of CTFB, with the much narrower peaks in central and middle regions. In other words, TFB seems to have less uniform solids holdup distribution across the bed than CTFB, which may distinguish TFB from CTFB. With increasing solids circulation rate in CTFB, however, wider square peaks in the dense phase and more small clusters with intermediate density are observed (Fig. 5.3), implying that solids circulation may delay the transition from the CTFB regime to the flow in the bottom zone of CFB.

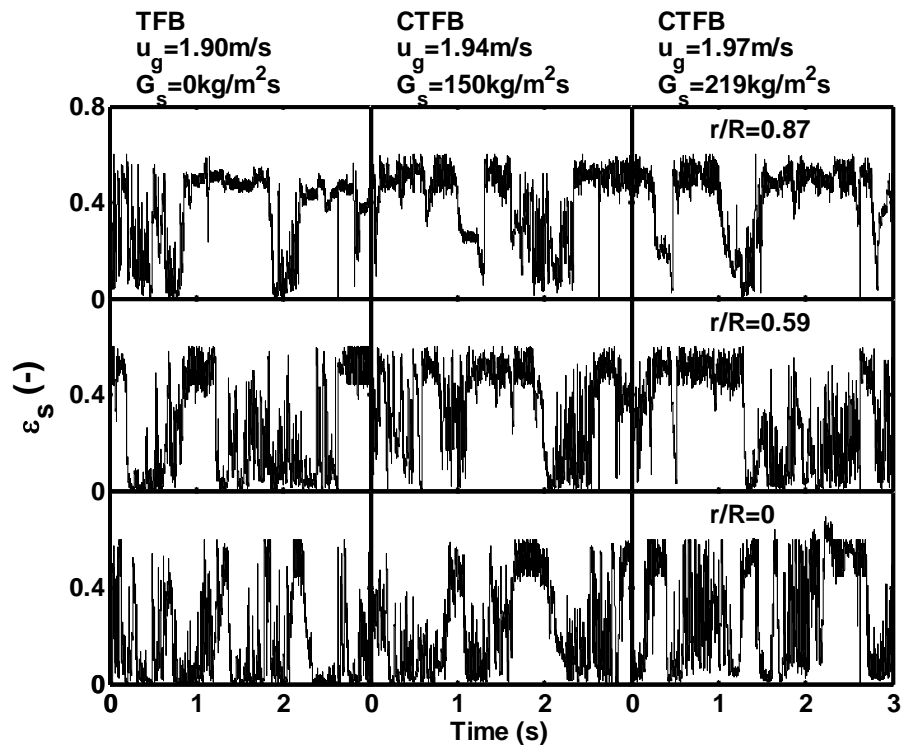


Figure 5.3 Comparison of solids concentration traces in TFB and CTFB regimes under similar air velocities and different solids circulation rates ($z = 1.5$ m)

Totally different from signals of BFB and CTFB, the signals at the bottom zone of CFB ($u_g = 4.87$ m/s in Fig. 5.2) does not display square peaks and valleys, but many sharp peaks with much lower height in the centre and to a lesser extent in the middle region. Near the wall, the signal peaks become very wide and slightly lower. Obviously, the dense phase fraction is low at the central and middle positions, corresponding to dilute phase dominating flow in CFB. Further studying the graphs of CFB, the different fluctuation patterns of the solids holdups between the core region (central and middle positions) and the wall region echo the core-annular structure widely accepted by other researchers (Issangya et al, 2000; Pärssinen et al, 2001). Most importantly, a broader solids holdup distribution (in various peak heights) of the dense phase is observed at the

central position, clearly distinguishing the CFB regime from the BFB, TFB and CTFB regimes.

From the above analyses, the transition characteristics between BFB and CTFB and between CTFB and CFB may be summarized in view of the differences between these regimes shown in the graphs at the central and middle positions in Figs. 5.2 and 5.3. (1) BFB regime has dense phase dominating flow with the maximum solids holdup fluctuations throughout the bed. CTFB (including TFB) has nearly equal dense and dilute phase fractions with stronger solids holdup fluctuation at the central and middle positions. With increasing air velocity, CTFB regime no longer has the maximum solids holdup fluctuation near the wall. The dense phase fraction in the centre also becomes less than 0.5. Therefore, the transition from BFB to CTFB can be characterized by the equal phase fraction, as to be discussed further in later sections. (2) Further increasing air velocity within the CTFB regime, the solids holdup fluctuation experiences a broader distribution of the solids holdup peaks (shown at the central position of the middle column in Fig. 5.3). On the other hand, CFB (bottom zone flow) is of dilute phase dominating flow and has even broader distributions of the dense phase solids holdup (referring to various heights of the peaks). Therefore, the transition between CTFB and CFB can be described by the change of the dense phase solids holdup distribution.

5.3.2 Skewness and kurtosis vs. two phase flow

The transition features of the signals may be quantitatively analyzed using statistic moments, such as skewness and kurtosis, to characterize the flow regimes. In statistics, skewness is a measure of the lack of symmetry in the probability density function (PDF)

of the solids holdup distribution around the mean, while kurtosis is a measure of the peakedness or flatness of PDF of the solids holdup compared to a normal distribution, reflecting the uniformity of the solids distribution in a flow. Mathematically, the skewness, S , and standard kurtosis, K , of solids holdup signals are presented as

$$S = \frac{\sum_{i=1}^N (\varepsilon_{si} - \bar{\varepsilon}_s)^3}{(N-1)\sigma^3} \quad (5.1)$$

$$K = \frac{\sum_{i=1}^N (\varepsilon_{si} - \bar{\varepsilon}_s)^4}{(N-1)\sigma^4} \quad (5.2)$$

where ε_{si} is instantaneous local solids holdup, σ is the standard deviation of the solids holdup, N is the population of signals.

Practically, the variation of the skewness and the kurtosis of the solids holdup signals may be used to elucidate the regime transition characteristics of the gas-solid flow, as schematically shown in Fig. 5.4. Eq. 5.1 indicates that the sign and the magnitude of the skewness is more sensitive to the variances, $(\varepsilon_{si} - \bar{\varepsilon}_s)$, of a few of large peaks/valleys, than to that of a large number of small peaks/valleys due to the cubic order. In other word, a few of large peaks can result in large change of the skewness. Signals of BFB (Fig. 5.4a) are characterized by less symmetry to the mean (very close to solids holdup value of the dense phase), and small variances of dense phase at large population, and large variances of the valleys at small population, so its skewness is negative ($S < 0$). On the contrary, signals from CFB regime (Fig. 5.4b) are characterized by less symmetry (the mean close to the dilute phase), large variances of dense phase at small population, and small

variances of the dilute phase at large population, so its skewness is positive. CTFB lies between BFB and CFB and has small skewness being close to zero due to the close-to-even number of the high and low solids holdup peaks. As a result, the skewness would respond to the flow transition state of CTFB (including TFB), indicating the predominance of the dense and dilute phases in flow.

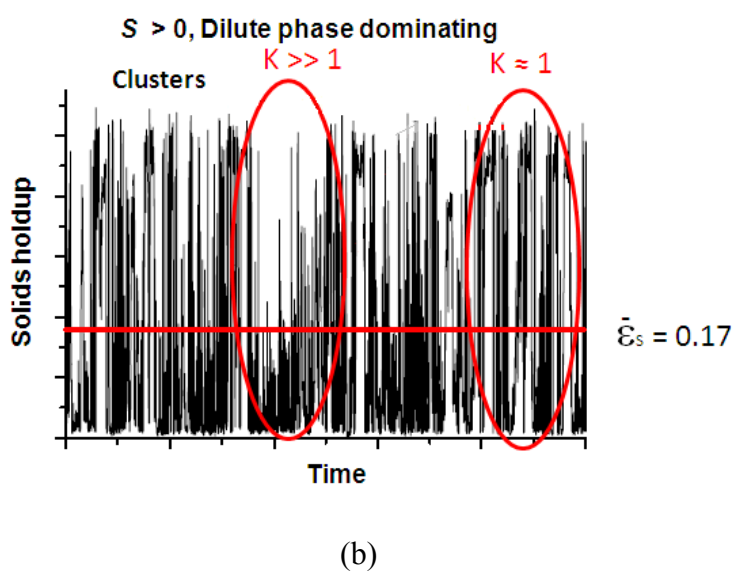
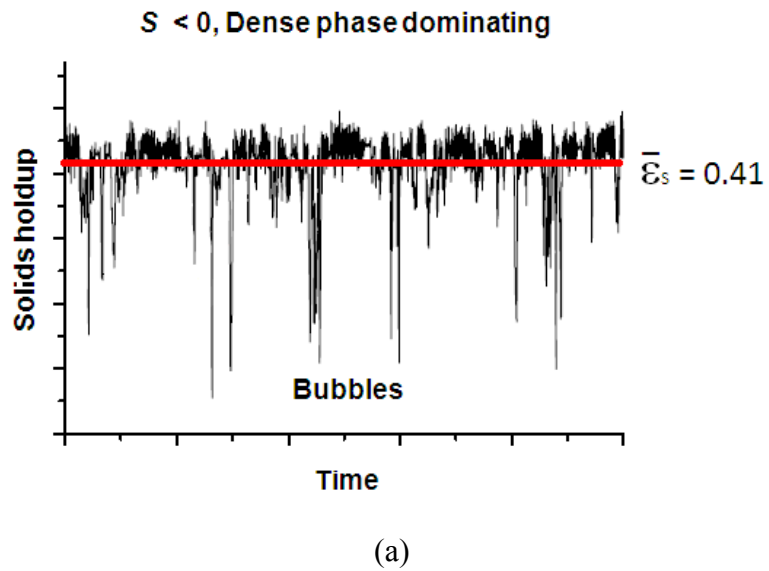


Figure 5.4 Moments vs. local solids holdup fluctuations in (a) BFB and (b) CFB fluidization regimes

Eq. 5.2 suggests that the kurtosis is a function of the solids holdup variances related to the ratio of the forth and second order of the variances at the same dimension. The magnitude of the kurtosis depends on how the solids holdups of the dense and dilute phases appear in the flow. For the dilute phase dominating flow, Fig. 5.4b provides signals from CFB

regime with two circled segments, illustrating two kinds of solids distributions of the dense phase: Non-uniform solids holdup of the dense phase peaks corresponds to large kurtosis value, while uniform solids holdup of the dense phase peaks gives rise to small kurtosis value. Theoretically, the distribution variation of the solids holdups of both dense and dilute phases could change the value of the kurtosis. However, the dense phase has more effect on the kurtosis than the dilute phase in dilute phase dominating flow, as the overall mean value is close to the mean dilute phase solids holdup. As a result, the flow with the broader solids holdup distribution of the dense phase gives rise to large kurtosis values. For the dense phase dominating and the transition flow, the flow usually has small kurtosis value in the bed's central region, as BFB (at relative high velocity) and CTFB/TFB regimes have the clear two phase feature and relative uniform phase solids holdup distribution, and the overall mean value is nearly in the middle of the mean solids holdups of the dense and dilute phases. In the wall region of BFB, TFB, CTFB and to some extent CFB, the solids holdup distribution of the dilute phase is much broader than the one of the dilute phase in the core region, leading to large kurtosis value. For the flow in the annulus region of CFB, the situation is usually similar to the flow of TFB and gives rise to small kurtosis value.

As a transient flow regime between BFB and CFB, CTFB (including TFB) need to undergo through the change of the flow structure from the dense phase dominating to the dilute phase dominating, including phase inversion, the change of size and shape of the phase aggregations, and phase expansion/contraction, etc. The phase inversion refers to a transition point or an air velocity where the dilute and dense phases alternately

predominate in the gas-solid flow (Zhu et al, Chapter 4, 2012; Bi and Su, 2001). The dense phase expansion is corresponding to the decreasing of the mean solids holdup of the dense phase (Bi and Su, 2001; Chapter 6), while the dilute phase contraction is corresponding to the disintegration of large bubbles into small voids in TFB (Du et al, 2003). With increasing air velocity, the experimental results in this study demonstrate that phase inversion happens first, and then followed by the dilute phase contract and the dense phase expansion (2012, Chapter 6).

5.3.3 Skewness and kurtosis profiles

Figs. 5.5-5.6 provide the skewness profiles obtained from the experimental data of solids holdup at a wide range of air velocities and solids circulation rates in both core and annular regions. Within the core region, the skewness profiles do not appreciably change, which are rather uniform radially and axially. However, they vary with increasing air velocity or with changing flow regimes: negative skewness in BFB, positive skewness in the bottom zone of CFB, and close or equal to zero skewness in CTFB/TFB. Related to the flow structure in different fluidization regimes, the skewness variations suggest that the negative skewness refers to the dense phase as the dominating phase in the flow (BFB regime), and the positive skewness refers to the dilute phase as the dominating phase in the flow (CFB regime). Lying between BFB and CFB, CTFB/TFB has the skewness close to zero responding to the phase inversion of the gas-solid flow.

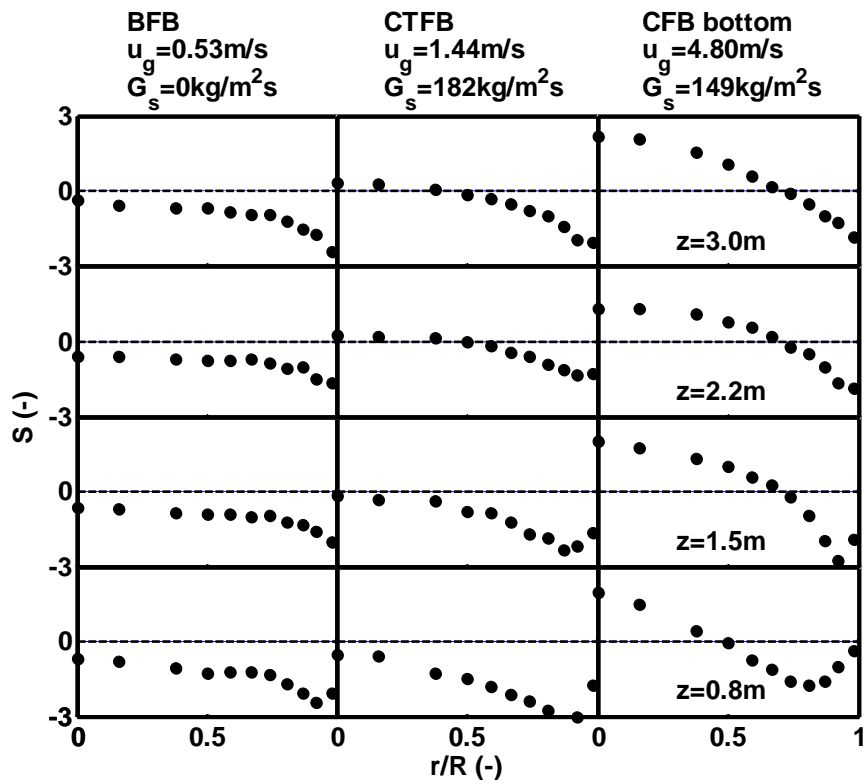


Figure 5.5 Skewness profiles of solids holdup under different air velocities and different solids circulation rates in BFB, CTFB and the bottom zone of CFB

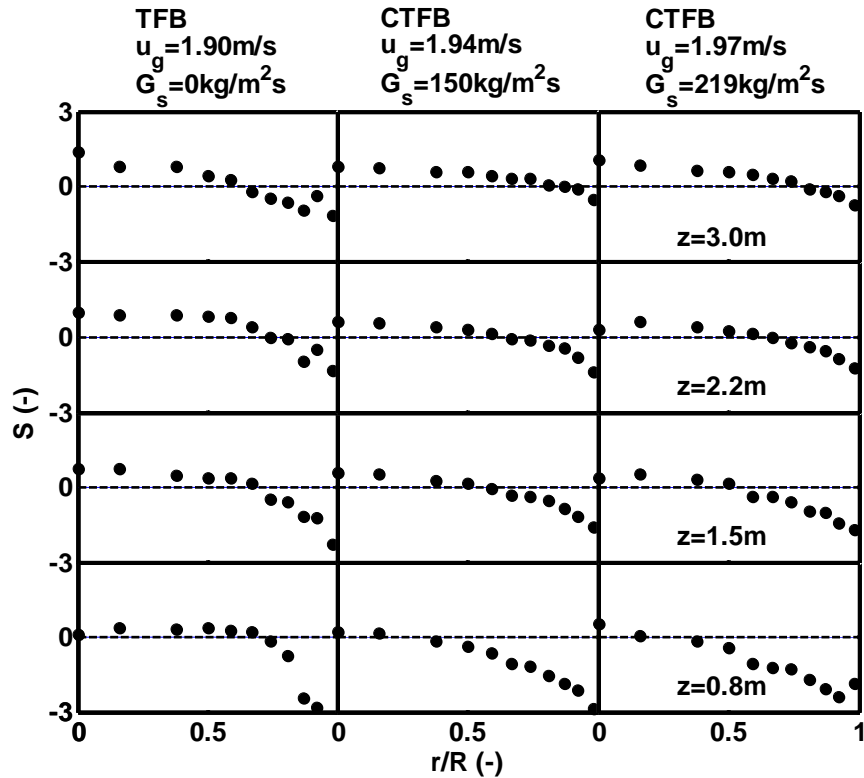


Figure 5.6 Skewness profiles of solids holdup under different solids circulation rates in TFB and CTFB

If one postulates that skewness equal to zero is at the transition point of the phase inversion and the flow with small positive skewness values is attributed to turbulent fluidization regime, Figs. 5.5 and 5.6 clearly suggest that the regime transition from BFB to CTFB/TFB first starts at the bed centre surface and develops toward the wall and then down to the bottom of the bed with increasing air velocity, as reported by Zhu and Zhu (2008). For example, the middle column graphs in Fig. 5.5 show that the skewness approaches to zero at the centre with increasing gas velocity, while graphs in Fig. 5.6 show the positive range (core region) increases gradually from the bottom to the top of the bed. The graphs also clearly show the difference in the turbulent zone in the bed with and without solids circulation, which suggests CTFB somehow differs from TFB.

However, the solids circulation rate is not a critical issue as long as the system operates under significant solids circulation rates.

On the other hand, the transition features of solids holdup distribution in CTFB can be represented by the kurtosis profiles in the core region but not in the annular region, as shown in Figs. 5.7 and 5.8. Within the core region, BFB and CTFB have similar flat kurtosis profiles ($K \approx 1.5$), implying their similar solids holdup distributions of the dense phase (Zhu et al, 2012), while the kurtosis of bottom zone of CFB decreases from greater than 6 at centre to about 1 at $r/R = 0.75$, indicating the different flow structure of CTFB from the one at the bottom zone of CFB within the core region. In annulus region, however, all three regimes have similar kurtosis profiles, quickly increasing toward the wall, implying no obvious transition features between BFB and CTFB or CTFB and CFB in annular region. In fact, such annulus kurtosis profiles, although also very steep, differ from the steep core profiles in the bottom zone of CFB, referring to dense phase predominating flow for the former and dilute phase predominating flow for the latter.

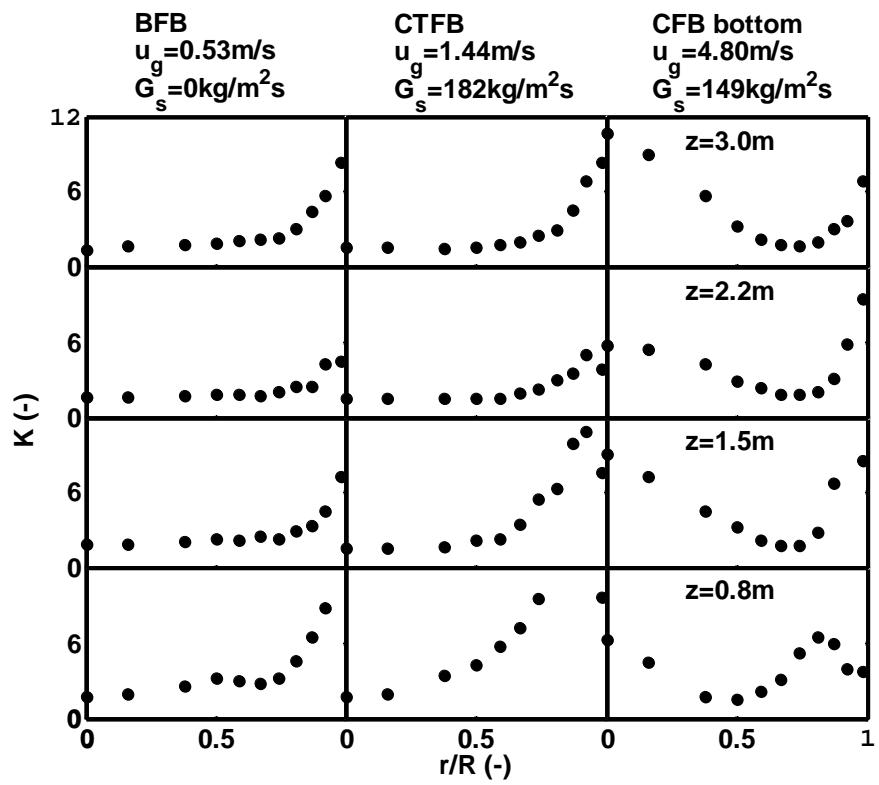


Figure 5.7 Standard kurtosis profiles of solids holdup under different air velocities and different solids circulation rates in BFB, CTFB and the bottom zone of CFB

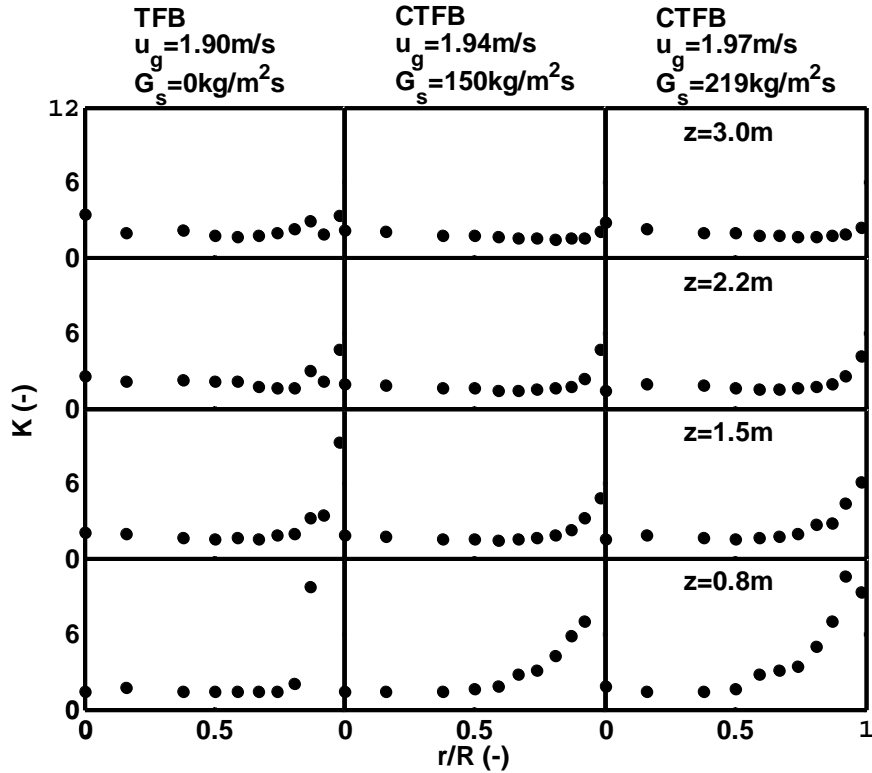


Figure 5.8 Standard kurtosis profiles of solids holdup under different solids circulation rates in TFB and CTFB

Further exploring the variation of the kurtosis profiles at different air velocities and solids circulation rates, one can observe the development of the transient flow in CTFB. In the core region, the constant kurtosis values mean that BFB and CTFB have similar and consistent solids holdup distribution in the core region. In the annular region, the kurtosis increase toward the wall and with increasing air velocity, indicating the variation of the dilute phase solids distribution in dense phase dominating flow. On the contrary, further increasing air velocity to some extent, the kurtosis in the annular region decreases, leading to uniform kurtosis distribution across the bed, implying the fully development of the turbulent regime in CTFB (Fig. 5.8). From CTFB to CFB, the increase of the kurtosis

in the centre and near the wall indicates the start of the new flow structure across the bed or the onset of the typical core-annular flow structure in CFB, a broader solids distribution both in the centre and near the wall. In other words, BFB and CTFB share very similar solids distribution, while the flow transition from CTFB to CFB undergoes the profound change of the flow structure and solids distribution.

Comprehensively examining Figs. 5.5-5.8, one might postulate that the flow structure in core region of the bed undergoes all transient states with increasing air velocity, while the variation of the flow structure in annular region always fails to keep pace with the one in the centre and sometimes is even totally different due to the wall effect and gas preference to flow in the centre. Therefore, any result based on the cross-sectional average data in small bed cannot be applied to a large scale. That is why \underline{u}_c determined using the standard deviation of differential pressure drop decreased with increasing column diameter for small columns and became insensitive to column diameter greater than 0.2 m (Cai, 1989; Zhao and Yang, 1991). On the other hand, the results at the centre or averaged in the core region might be more applicable for any column size. Similarly, Breault et al (2012) investigated the transition of gas-solid flow with small particle density and large particle size from core-annular to fast fluidization regimes at higher air velocities. They found that the solids holdup fluctuations and fit Gaussian distribution in the centre and no-Gauss distribution in the annular region in terms of skewness and kurtosis, which is opposite to the results in this study due to differences between low- and high-velocity regimes.

The transition of the flow structure of the gas-solids flow from BFB to CFB can be further examined through the Probability Density Function (PDF) of the local solids holdup in the centre, as shown in Fig. 5.9 with corresponding kurtosis values. The PDF profile is divided into two parts by a division value (a special solids holdup, its determination to be discussed in Zhu et al (2012, Chapter 4): dilute phase on the left and dense phase on the right. One can observe that CTFB have narrower peaked probability density distribution of the dense phase which gives rise to a small kurtosis value. With increasing air velocity, the probability peak of the dense phase diminishes and the distribution of the dilute phase becomes narrower and the distribution the dense phase becomes broader, displaying the typical transient characteristics from CTFB to CFB. In view of the various heights in much lower mean value of the dense phase of CFB than other regimes (shown the right column in Fig. 5.2), the broader solids holdup distribution is regarded as dense phase expansion (Bi et al, 2000).

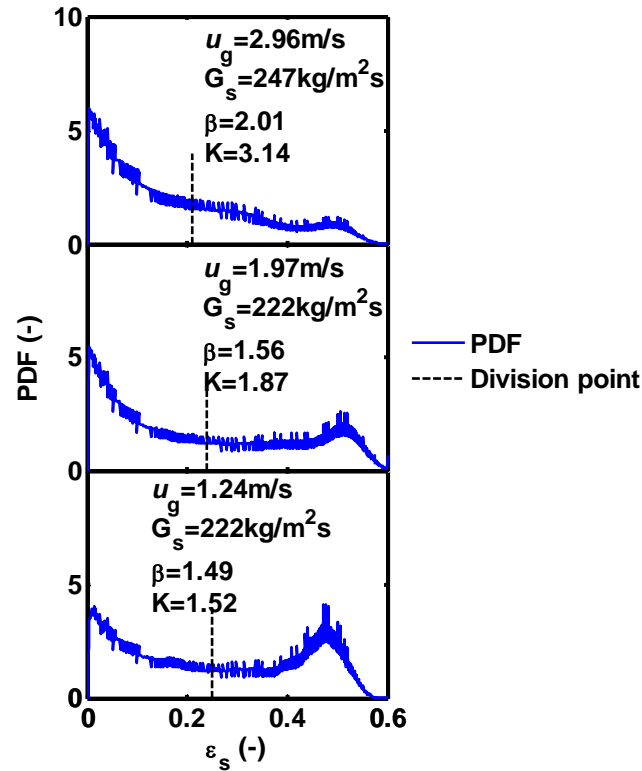


Figure 5.9 Probability Density Function (PDF) of local solids holdup at $r/R = 0$ for CTFB, noted with kurtosis and bi-peak parameter

5.3.4 Transition velocities of CTFB

To determine the onset transition air velocity, u_c , from bubbling to transient turbulent fluidization regime, differential and absolute pressure drop (Cai et al, 1989; Lee & Kim, 1988; Brereton & Grace, 1992), local void fluctuations (Kehoe and Davidson, 1970; Crescitelli et al, 1978; Chehbouni et al, 1994, Zhu and Zhu, 2008), bed expansion (Avidan and Yerushalmi, 1982; Grace & Sun, 1991; Bi & Grace, 1995), etc. were proposed, following the definition by Yerushalmi and Cankurt (1979). However, Bi and Grace (1995) found that the transition velocity u_c depended on the interpretation method. For

differential pressure fluctuations, a higher transition velocity was obtained from the normalized standard deviation. Skewness of absolute or differential pressure fluctuations did not appear to be a reliable indicator of flow regime transition. It was also difficult to determine a transition point based on the standard deviation of local voidage fluctuations (Bi et al, 1995). The results in this study also found that the maximum standard deviation of differential pressure took place in bubbling fluidization regime and was far away from the transition state. The major controversy on those methods is that the definition on turbulent fluidization regime is too vague to set a criterion for the transition velocity. The pressure and bed expansion methods also comprise too much effects of the bed geometry and particle return to correctly reflect the variation of flow structure.

The experimental results in this study demonstrate the transition characteristics of the flow structure from BFB to CTFB regime. By definition, the gas-solid system from bubbling to fast fluidization regimes undergoes transient flow structure states: firstly phase inversion and then dense phase expansion. To avoid the wall effect, the transition air velocities of CTFB from BFB can be easily determined using the skewness of local solids holdup in the centre, represented by u_{bt} . Fig. 5.10 provides the variation of skewness of the solids holdup in the central region against air velocity at $G_s = 150 \text{ kg/m}^2\text{s}$. The curve is divided into two sections by $S = 0$ at $u_g = 1.15 \text{ m/s}$. For $u_g < 1.15 \text{ m/s}$, $S < 0$ and the flow is under bubbling fluidization regime, corresponding to the dense phase dominating flow in the centre of bed reflected in the left column of Figs. 5.2 and 5.6. For $u_g > 1.15 \text{ m/s}$ and to some extent, $S > 0$ and the flow is under turbulent fluidization regime, corresponding to the dilute phase dominating flow in the centre of CTFB reflected in the

middle column of Figs. 5.2 and 5.6. For $S = 0$ at $u_g = 1.15\text{m/s}$, the flow is at the transition point where the dilute phase and dense phase intermittently and alternately predominate. Thus, the air velocity corresponding to $S = 0$ is proposed here as the turbulent onset transition velocity of CTFB, u_{bt} , a transition point from BFB to CTFB.

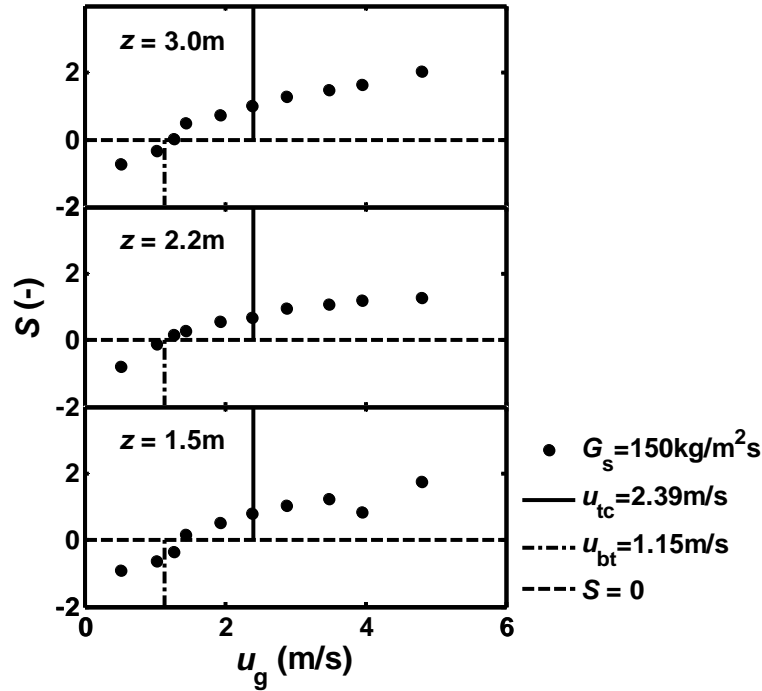


Figure 5.10 Skewness variation of gas-solid flow and the transition velocities

The prediction using skewness method is well agreeable with “determining transition velocity” of conventional turbulent fluidized bed (TFB) using maximum standard deviation of the local solids holdup. Zhu and Zhu (2008) reported $u_{bt} = 0.7\text{m/s}$ for a TFB bed using $67\mu\text{m}$ FCC particles, corresponding to the maximum standard deviation. This velocity is very close to skewness equal to zero and the minimum kurtosis of the solids holdup obtained from their data, as shown in Fig. 5.11. In other words, the transition air

velocities from BFB to TFB are consistent from the maximum standard deviation and from the phase inversion point. However, $u_{bt} = 1.15\text{m/s}$ as the transition air velocity of CTFB from BFB in this study seems slightly higher than the first velocity value but equal to the second one in Table 5.1 at the similar experimental conditions but no solids circulation (Perales et al, 1990). That would suggest that the transition air velocity, u_{bt} , does not change appreciably with the solids circulation rates.

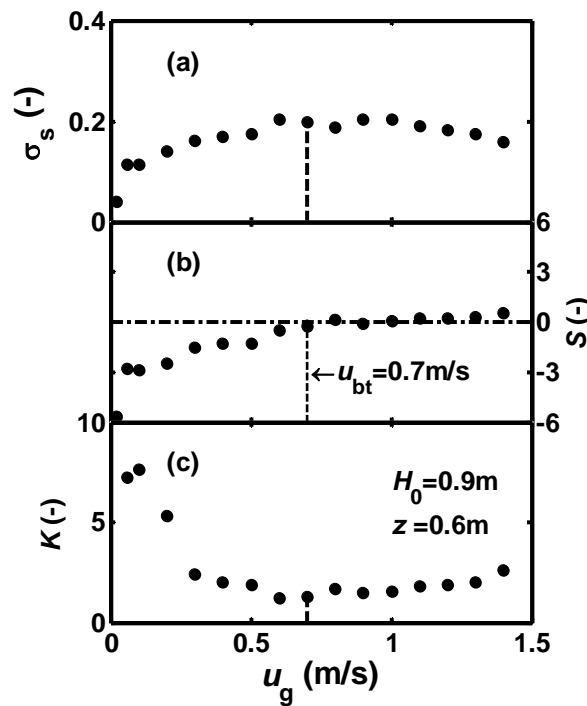


Figure 5.11 Standard deviation, skewness and kurtosis of solids holdup signals in a conventional turbulent fluidized bed obtained by an optical fibre probe at $z = 0.6$ m, static bed height: 0.9 m, FCC particles of $67\ \mu\text{m}$ (data from Zhu and Zhu, 2008)

Conventionally, the transition from turbulent fluidization to fast fluidization was characterized by significant entrainment of particles, setting an upper limit on the gas

velocity for batch operation, and a lower limit for the disappearance of the upper dense-dilute interface (Bi et al, 2000). There were two types of transition criteria, one based on solids entrainment behaviour (Han et al, 1985; Schnitzlein and Weinstein, 1988; Le Palud and Zenz, 1989; Bi et al, 1995) and the other on solids concentration profiles (Schnitzlein and Weinstein, 1988; Bi et al, 1991; Chen et al, 1980; Leu et al, 1990). These criteria coped with the issue on average across the bed. However, the flow transition from turbulent to fast fluidization regimes is fundamentally characterized by the variation of the flow structure, mostly in the centre of the bed. Differently from TFB, CTFB operates under the condition of significant solids circulation over the entire operation range of air velocities and it does not have the varied upper dense-dilute interface from the beginning to the end.

With respect to the variation of flow structure in CTFB, the results in this study demonstrate that the solids holdup PDF of the dense phase changes from a narrower peaked distribution to a broader linear distribution (Fig. 5.9), corresponding to the start of dense phase expansion (Chapter 6). Such PDF change and the dense phase expansion correspond to obvious increase of the kurtosis of the solids holdup in the centre of the bed (Fig. 5.7). Thus, Eq. 5.3 is constructed to quantitatively depict such a regime transition.

$$\beta = K - S^{4/3} \quad (5.3)$$

Fig. 5.12 shows that the β profiles, obtained from the data in the central region of CTFB, does not vary appreciably within lower air velocity range and then increases at a greater gradient after air velocity of 3.0m/s, an inflection point of the curve, where the broader

linear probability density distribution of the dense phase coincides. In fact, the first term of Eq. 5.3, kurtosis, comprises the effects of the dense phase expansion and asymmetry of probability density distribution, while the second term in skewness reflects the effect of asymmetry of probability density distribution, so the equation might totally represent the net variation of the solids holdup of the dense phase. As a result, the ending transition air velocity of CTFB or the onset transition air velocity of CFB can be determined by the inflection point of the curve obtained using Eq. 5.3. If BFB and CTFB regimes are considered as two-peak PDF system, one could regard β as the two-peak parameter of the gas-solid flow.

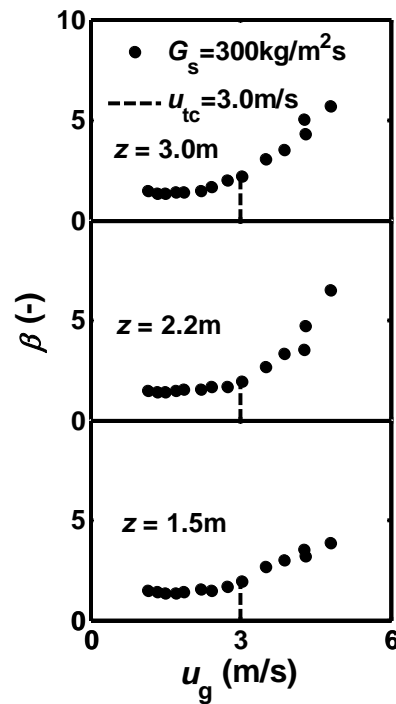


Figure 5.12 β values vs. air velocity and ending transition air velocity of CTFB

Different from u_{bt} , the ending transition air velocity, u_{tc} , obtained by β value steadily and

constantly increases with increasing solids circulation rate, as shown in Fig. 5.13. The trend of the ending velocity follows the regressive formula as Eq. 5.4,

$$u_{tc} = 0.0041G_s + 1.78 \quad (5.4)$$

which extrapolates $u_{tc} = 1.78$ m/s at $G_s = 0$ kg/m²s, slightly higher than the value obtained by Perales et al (1990) at the similar conditions (in Table 5.1). In view of the same u_{bt} as Perales et al', one can postulate that S - and β -method can predict the transition air velocities well. As a result, the onset transition air velocity of CTFB hardly changes, while the ending transition air velocity increases with increasing solids circulation rate. The results seem to further suggest that regular TFB is a special case of CTFB.

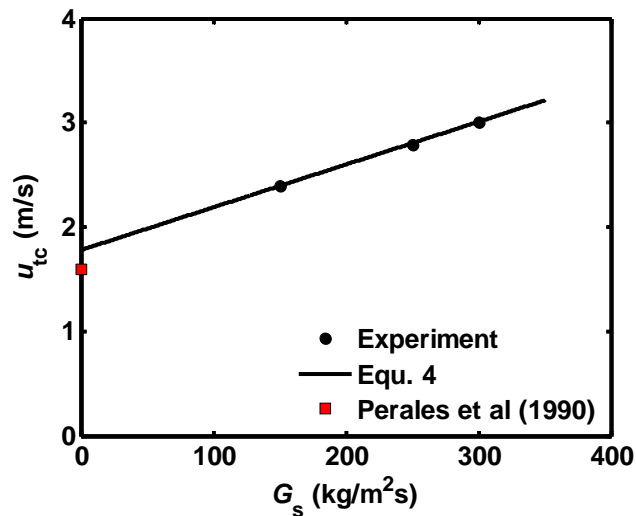


Figure 5.13 Ending transition air velocities of CTFB regime against solids circulation rates

From the results, the transition characteristics of CTFB regime can be summarized. For

BFB regime ($u_g < u_{bt}$), the gas-solid flow is characterized by dense phase dominating due to $S < 0$, and it has bi-peak solids holdup probability density distribution with peaked dense phase in PDF distribution (small kurtosis value). With increasing air velocity, the flow enters the turbulent fluidization regime ($u_{bt} < u_g < u_{tc}$) and it starts to have less fraction of the dense phase than the dilute phase in the centre (corresponding to small positive skewness value), leading to dilute phase dominating flow. To some extent of the air velocity, however, the dense phase of the regime is still characterized by the right peak in PDF (Fig. 5.9) and small kurtosis value (Figs. 5.7 and 5.8). On the other hand, CFB regimes is of dilute phase dominating flow ($S > 0$, shown in Figs. 5.7 and 5.13), and its dense phase has a broader solids hold up distribution. Compared to CFB, although the dilute phase dominates the flow, the turbulent fluidization regime differs from the characteristics of CFB until the ending transition air velocity, where the dense phase peak diminishing and kurtosis value increasing with increasing air velocity. The transition structure characteristics of the high density flow are summarized in Table 5.3.

Table 5.3 Local flow structure features of flow regimes vs. moment values

Regime	U_g	Moments	Comments
BFB	$U_g < U_{bt}$	$S < 0, K > 2.0$	Bubble as disperse phase, dense phase as continuous phase, Unstable bubbles and pressure drop reaching a maximum with increasing air velocity
CTFB	$U_g = U_{bt}$	$S = 0, K \sim 1$	Phase inversion point in the centre
	$U_{bt} < U_g < U_{tc}$	$S > 0, K \sim 1-2.0$	Bi-peak probability density distribution of solids holdup, prevailing dilute phase in the centre
	$U_g = U_{tc}$	$S > 0,$ inflection of β function	Onset of fast fluidized bed, changing solids holdup distribution of dense phase
CFB	$U_g > U_{tc}$	$S > 0, K > 2.0$	Broader solids holdup distribution of dense phase, prevailing dilute phase nearly across the bed

Conclusions

Experiments were carried out in a Circulating Turbulent Fluidized Bed (CTFB) using FCC particles in a wide range of air velocities and high solids circulation rates. Skewness, kurtosis and the Probability Density Function (PDF) of the solids holdup signals were analyzed and the transition features of the CTFB were explored. From the unique transition characteristics of the flow structure in BFB and CTFB/TFB, it was postulated that the onset transition from bubbling to turbulent fluidization regimes took place at the phase inversion point where the flow transits from the dense phase dominating flow in the bubbling fluidization regime to the dilute phase dominating flow in the centre region of the turbulent fluidization regime. It was also proposed that the ending transition air velocity from the turbulent to circulating fluidization regimes occurred at transition state where the dense phase starts to expand, corresponding to bi-peak PDF transiting to the triangular PDF. The experimental results demonstrated that the onset transition velocity hardly changed, while the ending transition velocity increased with increasing solids circulation rate, implying that the air velocity range of CTFB regime significantly increased with increasing solids circulation rates. They further suggest that regular TFB is a special case of CTFB.

Acknowledgement

The authors are grateful to the Natural Sciences and Engineering Research Council of Canada for supporting this work.

Nomenclature

G_s , solids circulation rates, kg/m²s

K , standard kurtosis of local solids holdup fluctuations

r , radial position, m

R , radius of the column, m

S , skewness of local solids holdup fluctuations

u_g , superficial air velocity, m/s

u_c , onset transition air velocity of TFB, defined by the maximum standard deviation of differential pressure drop, m/s

u_k , transition air velocity of TFB, defined by the levelling off maximum standard deviation of differential pressure drop, m/s

u_{tr} , transition air velocity of TFB, defined by pressure diagram, m/s

u_{bt} , onset transition air velocity of CTFB, defined by $S = 0$, m/s

u_{tc} , ending transition air velocity of CTFB, defined by the inflection point of β -parameter curve, m/s

Z , elevation from the air distributor, m

β , parameter for solids holdup distribution of dense phase

ϵ_s , local instantaneous solids holdup

$\bar{\epsilon}_s$, local time-averaged solids holdup

σ , standard deviation of local solids holdup fluctuations

References

Avidan A.A. and J. Yerushalmi, *Powder Technology*, 32 (1982), 223.

Bi H. T., Ellis N., Abba I. A. and Grace J. R., (2000), Review: A state-of-the-art review of gas-solid turbulent fluidization, *Chemical Engineering Science* 55 4789-4825

Bi H. T. and Su P., (2001), Local Phase Holdups in Gas-Solids fluidization and Transport, *AIChE Journal*, Vol. 47(9), 2025.

Bi H. T. and Grace J. R., (1995), Effect of measurement method on the velocities used to demarcate the onset of turbulent fluidization, *Chemical Engineering Journal*, 57, 261-271

Bi H. T., Grace J. R. and Lim K. S., (1995), Transition from Bubbling to Turbulent fluidization, *Ind. Eng. Chem. Res.*, 34, 4003-4008

Bi H. T., Jiang P. J., and Fan, L.S., (1991), Hydrodynamic behaviour of the circulating fluidized bed with low density polymer particles, *AIChE, annual meeting*, Los Angeles, November, 1991, #101d

Bi H. T., Ph. D thesis, The University of British Columbia, 1994

Breault R. W., Emily M. Casleton, Christopher P. Guenther, "Chaotic and statistical tests

on fiber optic dynamic data taken from the riser section of a circulating fluidized bed, *Powder Technology*, Volume 220, April 2012, Pages 151-163

Brereton C.M.H. and J.R. Grace, (1992), *Chem. Eng. Res. Des.*, 70, 246

Cai P., Chen S. P., Jin Z. Q. and Wang Z. W., (1989), Effect of Operating Temperature and Pressure on the Transition from Bubbling to Turbulent Fluidization, *AIChE Symposium Series*, 85(270), 37-43.

Chen B. Y., Li Y., Wang F., Wang Y. and Kwauk M., (1980), Studies on fast fluidization. *Chemical Metallurgy*, 5, 30-38 (in Chinese)

Chehbouni A., Chaouki J., Guy C., and Klvana D., (1994), Characterization of the flow transition between bubbling and turbulent fluidization, *Industrial and Engineering Chemistry Research*, 33, 1889-1898

Crescitelli S., Donsi G., Russo G., and Clift R., (1978), High velocity behaviour of fluidized beds: Slugs and turbulent flow. In S. Schlosser, *Selected papers presented at the sixth international congress CHISA '78*, Prague (pp. 1-11)

Cui H., Mostoufi N. and Chaouki J., (2000), Characterization of dynamic gas–solid distribution in fluidized beds, *Chemical Engineering Journal*, 79, 134–143

Du B., Warsito W. and Fan L., (2003), Bed Nonhomogeneity in Turbulent Gas-Solid Fluidization, Vol. 49, No. 5, *AIChE Journal*, 1109

Grace J. R., (1990), High-Velocity Fluidized Bed Reactors, *Chemical Engineering Science*, Vol. 45, No. 8, pp. 1953-1966

Grace J. R. and Sun G., (1991), Influence of particle size distribution on the performance of fluidized bed reactors, *Canadian Journal of Chemical Engineering*, 69, 1126-1134

Han G. Y., Lee G. S. and Kim S. D., (1985), Hydrodynamics of a circulating fluidized bed, *Korean Journal of Chemical Engineering*, 2, 141-147

Horio M., Ishill H. and Nishimuro M., (1992), On the nature of turbulent and fast fluidized beds, *Powder Technology*, 70, 239–246

Horio M., M. Nishimura and H. Ishii, (1989), “On the Nature of Turbulent and Fast Fluidized Beds,” Proc. of SOC. of Chem. Eng. of Japan Symp, in *Circulating Fluidized Beds*, Tokyo, 54

Issangya A. S., Grace J. R. Bai D. and Zhu J., (2000), Further measurements of flow dynamics in a high-density circulating fluidized bed riser, *Powder Technology* 111, 104–113

Jin Y., Yu Z.Q., Wang, Z. and Cai P., (1986), A criterion for transition from bubbling to turbulent fluidization, In: Ostergaard, K., Sorensen, A. (Eds.), *Fluidization*, vol. V. Engineering Foundation, New York, pp. 289–296

Kehoe P.W.K. and J.F. Davidson, *Inst. Chem. Eng. Symp., Ser.*, 33 (1970) 97

Kwauk M., N. Wang, Y. Li, B. Chen, and Z. Shen, (1986), “Fast Fluidization at ICM,” *Circulating Fluidized Bed Technology*, Vol. I, p.33, P. Basu, ed., Pergamon Press, Toronto

Le Palud T., and F. A. Zenz, (1989), “Supercritical Phase Behavior of Fluid particle Systems,” *Fluidization*, Vol. VI, p.121, J. R. Grace, L. W. Shemilt, and M. A. Bergougnou, eds., Engineering Foundation, New York

Lee G. and S. Kim, (1988), Pressure Fluctuations in Turbulent Fluidized Beds, *Journal of Chemical Engineering of Japan*, Vol21(5),515

Leu L.-P., Huang J.-W. and Gua B.-B., (1990), Axial pressure distribution in turbulent fluidized beds, *Proceedings of the second Asian conference on fluidized-bed and three-phase reactors*, pp. 71-79.

Li J., Y. Li and M. Kwauk, (1988), "Energy Transport and Regime Transition in Particle-Fluid Two-Phase Flow," *Circulating Fluidized Bed Technology*, Vol.11, p.75, Pergamon Press, Toronto

Mori S., Hashimoto O., Haruta T., Mochizuki K., Matsutani W., Hiraoka S., Yamada I., Kojima T. and Tuji K., (1988), Turbulent fluidization phenomena, In: Basu, P., Large, J.F. (Eds.), *Circulating Fluidized Beds Technology*, vol. II. Pergamon Press, Oxford, pp. 105–112

Pärssinen JH and Zhu JX, (2001), Axial and radial solids distribution in a long and high-flux CFB riser, *AIChE J.*, 47, 2197–2205

Perales J. F., T. Coll, M. F. Llop, L. Puigjaner, J. Arnaldos and J. Casal, (1990), "On the Transition from Bubbling to Fast Fluidization Regimes," *Circulating Fluidized Bed Technology*, Vol. 111, p.73, P. Basu, M. Horio, and M. Hasatani, eds., Pergamon Press, Oxford.

Schnitzlein, Michael G. and Herbert Weinstein, (1988), Flow characterization in high-velocity fluidized beds using pressure fluctuations, *Chemical Engineering Science* (January 1988), 43 (10), pg. 2605-2614

Shou M.C. and Leu L.P., (2005), Energy of power spectral density function and wavelet analysis of absolute pressure fluctuation measurements in fluidized beds, *Trans IChemE, Part A, Chemical Engineering Research and Design* 83 (A5), 478–491

Tsukada M., Nakanishi D. and Horio M., (1993), The effect of pressure on the phase transition from bubbling to turbulent fluidization, *International Journal of Multiphase*

Flow 19, 27–34

Thiel W. J. and O. E. Potter, (1977), “Slugging in Fluidized Beds,” *Ind. Eng. Chem. Fund.*, 16, 242

Xu G., (2006), Saturation carrying capacity at high Archimedes number of vertical concurrent gas–particle flow, *Chemical Engineering Science*, 61, 7115, – 7124

Yang Y. R., S. X. Rong, G. T. Chen and B. C. Chen, (1990), “Flow Regimes and Regime Transitions in Turbulent Fluidized Beds,” *Chem. Reaction Eng. and Technol.*, 6, 9

Yang W., (2004), “Choking” Revisited, *Ind. Eng. Chem. Res.*, 43, 5496-5506

Yerushalmi J., and N. T. Cankurt, (1979), “Further Studies of the Regimes of Fluidization,” *Powder Technol.*, 24, 187

Zhang H. and Zhu J.-X, (1998), A novel calibration procedure for a fiber optic solids concentration probe, *Powder Technology*, 100, 260-272

Zhao X. and Yang G. L. (1991), Critical turbulent velocity for fluidized beds with baffles, In M. Kwauk, & M. Hasatani, *Proceedings of the fourth China-Japan fluidization conference* (pp. 196-201), Beijing: Science Press

Zhu J, Qi M., Baighi S., (2012), Identification of Micro Flow Structures and Regime Transition in Gas-Solid Fluidized Beds through Moment Analysis, *AIChE Journal*, Submitted, Chapter 4 in this thesis

Zhu H. and Zhu J., (2008), New Investigation in Regime Transition from Bubbling to Turbulent Fluidization, *The Canadian Journal of Chemical Engineering*, Vol. 86(6), 553

Zhu H. and Zhu J. X, (2008a), Gas-Solids flow Structures in a Novel Circulating-Turbulent fluidized Bed, AIChE Journal, Vol. 54 (5), 1213

Zhu H. and Zhu J. X, (2008b), Comparative study of flow structures in a circulating-turbulent fluidized bed, Chemical Engineering Science, 63, 2920-2927

6 Detailed hydrodynamics of high flux gas-solid flow in a circulating turbulent fluidized bed

6.1 Introduction

The favourable hydrodynamic properties of fluidized bed reactors have found their specific applications in many industrial processes. Increasing air velocity, the fluidized beds operate in bubbling, turbulent and circulating (fast) fluidization regimes. Circulating fluidized beds (CFB) operating under relatively low gas velocity (3 ~ 10 m/s) and low solids circulation rate ($< 200 \text{ kg/m}^2\text{s}$) are mostly applicable to gas-solid reactions such as combustion in CFB. They have advantages of favourable bed-to-immersed-surface heat transfer rates, the ability to withdraw and add particulate solids continuously, applicability for a wide range of fuels, and the possibility of operating in a very large scale (Grace, 1990). Differently, the typical FCC industry circulating fluidized bed operates at a gas velocity ranging from 6 to 28 m/s and solids circulation rates from 400 to 1200 $\text{kg/m}^2\text{s}$. This is regarded as high-density circulating fluidized-beds (HDCFB), providing increased capacity and more desired product due to the increased gas throughput and higher solids concentration without serious backmixing (Zhu and Bi, 1995). On the other hand, turbulent fluidized bed regime (TFB), operating at less than 2.0 m/s and without solids circulation, has found its applications in a number of commercial fluid bed reactors, such as sulphide ore roasting, Fischer-Tropsch synthesis and acrylonitrile manufacture. This regime offers a number of advantages over the well-

known lower velocity bubbling fluidization regime, such as higher heat transfer efficiency between the bed and immersed surfaces. Rapid exchange of gas between the dilute and dense phases also results in a very low gas bypassing and promotes intimate gas-solid contact. The temperature uniformity makes TFB in a very attractive choice to applications at lower gas velocities (Grace, 1990).

However, there are some inherent unfavorable characteristics of CFB and TFB which limit or hinder further improvement on their performances. The relatively low solids concentration and the non-uniform axial and radial flow structure in CFBs cause some major disadvantages. For instance, their serious gas by-passing through the core dilute region and extensive backmixing of solids in the wall region, consequently, lead to reduced overall gas-solid contact efficiency (Perales et al, 1990). On the other hand, serious back-mixing of the solids phase in TFBs causes a broad residence time-distribution of the solids and poor chemical reaction selectivity (Zhu and Zhu, 2008; Zhu, 2010). Low gas throughput is another shortcoming of TFB. The major advantages and disadvantages of both TFB and CFB are listed in Table 6.1.

Table 6.1 Major advantages and disadvantages of CFB and TFB

	Advantages	Disadvantages
TFB	<ul style="list-style-type: none"> - High solids concentrations - Low and mediate fluid flux - Vigorous gas-solids contacting - High heat transfer in the bed - Simple separation system 	<ul style="list-style-type: none"> - Serious gas and solids back-mixing - Larger gradient axial solids distribution - Relatively low gas production
CFB	<ul style="list-style-type: none"> - Reduced gas and solids backmixing - High gas and solids flux - Higher gas production capacity - Short solids regeneration cycle - Easy for product selection and control 	<ul style="list-style-type: none"> - Lower solids holdup - Significant non-uniformity in axial and radial flow structure - Complicated separation system or loop

As shown in Table 6.1, CFB and TFB can mostly make up their shortcomings on one another. This raises a question on how to combine them together without losing their merits while making the fluidization reactors more efficient. Zhu and Zhu (2008a and b) integrated a conventional turbulent fluidized bed into a high-density circulating system to simultaneously achieve high efficient gas-solid contact and low solids backmixing. Their investigations proved the benefits of such a combination. The results at $u_g = 1.0, 2.0$ m/s and $G_s = 50, 150$ kg/m²s demonstrated that the CTFB is capable of: (1) maintaining a high solids concentration and gas-solid contact efficiency over a wide range of air velocity and solids circulation rates; (2) having high particle handling capacity with low gas by-passing; (3) operating without downflow of solids across the bed; (4) providing axial homogenous flow and enforced radial homogeneity of the solids suspension. To explore the detailed flow structure of the new fluidization regime and to further assess it, experiments on CTFB were carried out over a wide range of air velocities and high solids circulation rates using FCC particles in this study.

6.2 Experimental setup and methods

6.2.1 Experimental setup

The experimental unit was a cold model circulating turbulent fluidized bed, which

consisted of six parts (Fig. 6.1a): (1) a CTFB column, with i.d. of 0.101 m and height of 3.6 m between gas distributor (a perforated-plate with open area ratio 14%) and column top; (2) a quick discharging section at the top of the CTFB column with a diameter of 0.203 m and a height of 6.4 m; (3) a downcomer (i.d. 0.305 m) with a solids level of up to 4.95 m when all solids were stored; (4) a solids circulation rate measurement device with two flapper valves in the upper section of the downcomer (Pärssinen and Zhu, 2001); (5) a recycle loop including a primary inner cyclone, secondary and tertiary standard cyclones, and a bag filter to capture the entrained particles and return them to the downcomer; (6) an inclined solids return pipe at the bottom with a solids circulation flow rate control device.

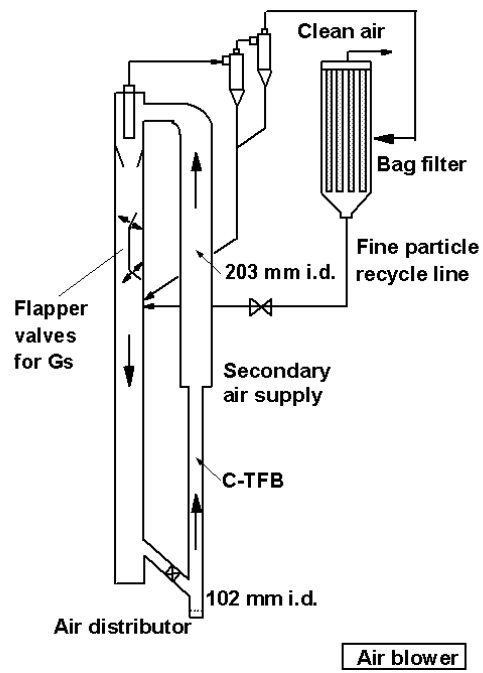
After passing the solids control valve in the inclined pipe, the particles coming from the downcomer entered the CTFB bottom at a height of 0.2 m above the gas distributor, and were accelerated by air at ambient conditions. Secondary air supply was distributed via an annular perforated plate with 12.6% free area at the bottom of the upper discharging section to lift the particles upwards and to entrain particles out of the column as quickly as possible to minimize the pressure drop in the upper section. Therefore, this unique design enabled high solids circulation rates and high suspension density in the CTFB with relatively low superficial gas velocity (1–5 m/s). The particles used in this study were FCC catalyst with a Sauter mean diameter of 76 μm and a particle density of 1780 kg/m^3 . The relative humidity was kept between 70 and 80% to minimize the electrostatic effects.

Experimental data were acquired using 4 multi-fiber optical reflective probes of model PV-6, developed by the Institute of Process Engineering, Chinese Academy of Sciences, Beijing, China. Each of the four probes consists of two fiber bundles located on the same vertical line. Each bundle is composed of both light-emitting and receiving quartz fibers arranged in an alternating array, corresponding to emitting and receiving layers of fibers. The diameter of each fiber is 25 μm . Light from a light emitting diode (LED) transmits through the emitting half of the fibers to the tip, where hitting upon particle(s) in the riser, will be reflected back to the probe. The intensity of the reflected light depends on the concentration, size distribution, composition, and shape of the particles. The received light reflected by the particles was converted by a photo-multiplier into voltage signals. The voltage signals were further amplified and fed into a computer. A special calibration procedure in high particle density environment had been carried out and the calibration curves had been obtained to convert the voltage data to solids holdups (Zhang et al, 1998).

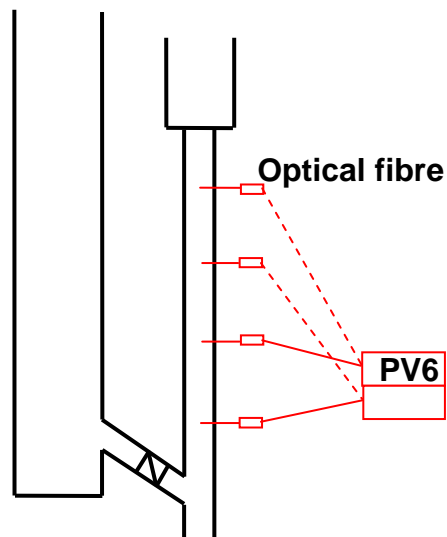
The probes were setup at four separate axial elevations, and traversed horizontally to measure local solids holdup at eleven radial positions (Fig. 6.1b). The four axial locations were chosen in an effort to characterize the acceleration section (0.8m) and the fully developed section (1.5, 2.2 and 3.0m). Radial positions were chosen at the midpoints of eleven equal area circles ($r/R = 0.0, 0.16, 0.38, 0.5, 0.59, 0.67, 0.74, 0.81, 0.87, 0.92, \text{ and } 0.98$) at each axial level within the risers. There were two PV6 units used in the experiments: a master and a slave. A special setup procedure was carried out for the two units to control four probes and a special data processing method was implemented with normalized calibration curves and different unit gains and offsets to obtain consistent

experimental results. At one radial location the units were connected to two adjacent probes and then switched to the other two. To ensure the consistency of the data at one specific operating condition, the experimental data at all locations were collected within one run by the four probes. The sampling rate was 50 kHz and data were collected for 131 sec. 10 Ω -type differential pressure transducers of model PX163-120D5V and PX162-027D5V were installed at median positions of $z = 0.38, 0.66, 0.95, 1.29, 1.65, 2.01, 2.45, 2.85, 3.22, 3.61$ m along the column, sampling for 400 s at 1000 Hz. The pressure probes were made of brass tubes with Taylor #500 screen end and the link plastic tubes were not longer than 25 cm.

Experimental air velocities varied from 0.5 to 5.0 m/s, more than covering the whole range from onset air velocity u_{bt} and ending air velocity u_{tc} of FCC particle CTFB regime, and solids circulation rates from 0 to 420 kg/m²s. There were two particle inventory cases to be implemented for the experiments: static downcomer bed height of 3.85 m for solids circulation rates of up to 250 kg/m²s and less, 4.95 m for solids circulation rates of up to 420 kg/m²s. The experimental air velocities and corresponding solids circulation rates were obtained through adjusting the opening of the solids control valve and the pressure of primary air supply, in the condition that there was no apparent dense phase appearing in the delivery section over CTFB.



(a)



(b)

Figure 6.1 Experimental apparatus and optical fibre probe setup

6.2.2 Parameters of dense and dilute phases

The heterogeneous flow structures of a fluidized bed may be macroscopically characterized by moment estimation of experimental series, such as mean solids holdup $\bar{\varepsilon}_s$, standard deviation σ_s , skewness S and kurtosis K (Eqs. 6.1-6.4).

$$\bar{\varepsilon}_s = \frac{1}{N} \sum_{i=1}^N \varepsilon_{si} \quad (6.1)$$

$$\sigma_s = \left[\frac{1}{N-1} \sum_{i=1}^N (\varepsilon_{si} - \bar{\varepsilon}_s)^2 \right]^{1/2} \quad (6.2)$$

$$S = \frac{\sum_{i=1}^N (\varepsilon_{si} - \bar{\varepsilon}_s)^3}{(N-1)\sigma_s^3} \quad (6.3)$$

$$K = \frac{\sum_{i=1}^N (\varepsilon_{si} - \bar{\varepsilon}_s)^4}{(N-1)\sigma_s^4} \quad (6.4)$$

Based on these moments, a Moment Consistency Data Processing method (MCDPM) had been proposed to further investigate the detailed flow structure in fluidized beds in dense and dilute phases, the details of which can be found in Zhu et al (2012, Chapter 4). In MCDPM, the detail hydrodynamics of the dense and dilute phases are represented by three average phase parameters, a high solids holdup representing the dense phase, ε_{sd} , and a low solids holdup representing the dilute phase, ε_{sb} , with f_d being the fraction of the dense phase. With these parameters, Eqs. 6.1-6.4 can be simplified to Eqs. 6.5-6.8 for an ideal two phase flow:

$$\bar{\varepsilon}_s = f_d \varepsilon_{sd} + (1 - f_d) \varepsilon_{sb} \quad (6.5)$$

$$\sigma_s = \sqrt{(\varepsilon_{sd} - \bar{\varepsilon}_s)^2 f_d + (\varepsilon_{sb} - \bar{\varepsilon}_s)^2 (1 - f_d)} \quad (6.6)$$

$$S = \frac{1}{\sigma_s^3} [(\varepsilon_{sd} - \bar{\varepsilon}_s)^3 f_d + (\varepsilon_{sb} - \bar{\varepsilon}_s)^3 (1 - f_d)] \quad (6.7)$$

$$K = \frac{1}{\sigma_s^4} [(\varepsilon_{sd} - \bar{\varepsilon}_s)^4 f_d + (\varepsilon_{sb} - \bar{\varepsilon}_s)^4 (1 - f_d)] \quad (6.8)$$

For analysis, the 4 moments will first be calculated from the experimental data. Then, the 4 moment values will be applied in Eqs. 6.5-6.8 to back calculate the 3 key parameters ε_{sd} , ε_{sb} and f_d . The details for the explicit expressions of these three parameters can be found in Zhu et al (2012, Chapter 4).

6.2.3 Phase particle velocity computation

MCDPM provides a procedure to divide solids holdup series into two sub-series representing the dense and dilute phases. Cross-correlating two series of dense and dilute phase sub series, one can calculate particle velocities of the dense and dilute phases with a Divided Phase Cross-Correlation Method (DPCCM) (Eqs. 6.9 and 6.10), as to be proposed in Chapter 7.

$$\phi_c(\tau) = \frac{\sum_{NC} [(\varepsilon_{s,1}(n) - \overline{\varepsilon_{sc,1}})(\varepsilon_{s,2}(n-\tau) - \overline{\varepsilon_{sc,2}})]}{\sqrt{\sum_{NC} (\varepsilon_{s,1}(n) - \overline{\varepsilon_{sc,1}})^2} \sqrt{\sum_{NC} (\varepsilon_{s,2}(n-\tau) - \overline{\varepsilon_{sc,2}})^2}}, \text{ for dense phase} \quad (6.9)$$

$$\phi_b(\tau) = \frac{\sum_{NB} [(\varepsilon_{s,1}(n) - \overline{\varepsilon_{sb,1}})(\varepsilon_{s,2}(n-\tau) - \overline{\varepsilon_{sb,2}})]}{\sqrt{\sum_{NB} (\varepsilon_{s,1}(n) - \overline{\varepsilon_{sb,1}})^2} \sqrt{\sum_{NB} (\varepsilon_{s,2}(n-\tau) - \overline{\varepsilon_{sb,2}})^2}}, \text{ for dilute phase} \quad (6.10)$$

Correspondingly, averaged local solids flux and net solids flux can be computed by Eqs.

6.11 and 6.12 using the instantaneous particle velocities and solids holdups, while the computation accuracy and convergent condition are assessed by the measured solids circulation rate using Eq. 6.14.

$$F_{s,i,j} = \frac{\rho_p}{T_{i,j}} \int_{T_i} v_{s,i,j}(t) \varepsilon_{s,i,j}(t) dt, \quad (i = b \text{ (dilute)}, c \text{ (dense)} \text{ and } j = \text{up, down}) \quad (6.11)$$

$$G_{s,l} = \sum \frac{T_{i,j}}{T} F_{s,i,j} \quad (6.12)$$

$$G_s = \frac{2}{R} \int_{T_i} G_{s,l} dr \quad (6.13)$$

where $T_{i,j}$ is the incidental time of the dense or dilute phase sweeping an optical fibre probe in upward or downward direction. The apparent particle velocity can then be calculated from the local net solids flux over local mean solids holdup:

$$u_p = \frac{G_{s,l}}{\varepsilon_s} \quad (6.14)$$

6.3 Results and discussion

6.3.1 Macro flow structure of CTFB

Axial solids holdup profile refers to the axial distribution of the cross-sectional average solids holdup, which can be calculated through local solids holdup measurement by optical fibre probes or from the pressure drop signals measured by differential pressure transducers (Chapter3). Figs. 6.2a and 6.2b display the high solids density and the uniform axial solids holdup profiles in CTFB, characterized by entrance, fully developed and exit zones. In the entrance zone (about 15% of the bed height), the solids holdup was high and quickly decreased from the high value to the level of the fully developed section

as particles coming from the downcomer were accumulated and then accelerated. Within the fully developed section, the cross-sectional average solids holdups were over 0.25 up to 3.0 m high, uniform in majority of the CTFB bed. In the exit zone, the particles were accelerated again and the solids holdup quickly decreased to up 10%. One can see that the cross-sectional average solids holdup along the bed decreases with increasing air velocity (Fig. 6.2a) and increases with increasing solids circulation rate (Fig. 6.2b). It is noticeable that solids circulation apparently makes axial solids holdup distributions more uniform, compared to no solids circulation case, as shown in Fig. 6.2b. The above results are agreeable well with the ones obtained using optical fibre probes by Zhu and Zhu (2008a), as shown in Fig. 6.2c. These results show that CTFB can achieve very high and uniform solids holdup varying within 0.25 ~ 0.35 over a wide range of operating air velocities (1.15 ~ 3.0 m/s) and solids circulation rates (0 ~ 420 kg/m²s so far). That also means extremely large solid-to-gas loading ratio, $G_s/(\rho_g u_g)$, reaching more than 350 under certain experimental conditions, in comparison to 10–80 for most CFB operations (Zhu and Zhu, 2008a).

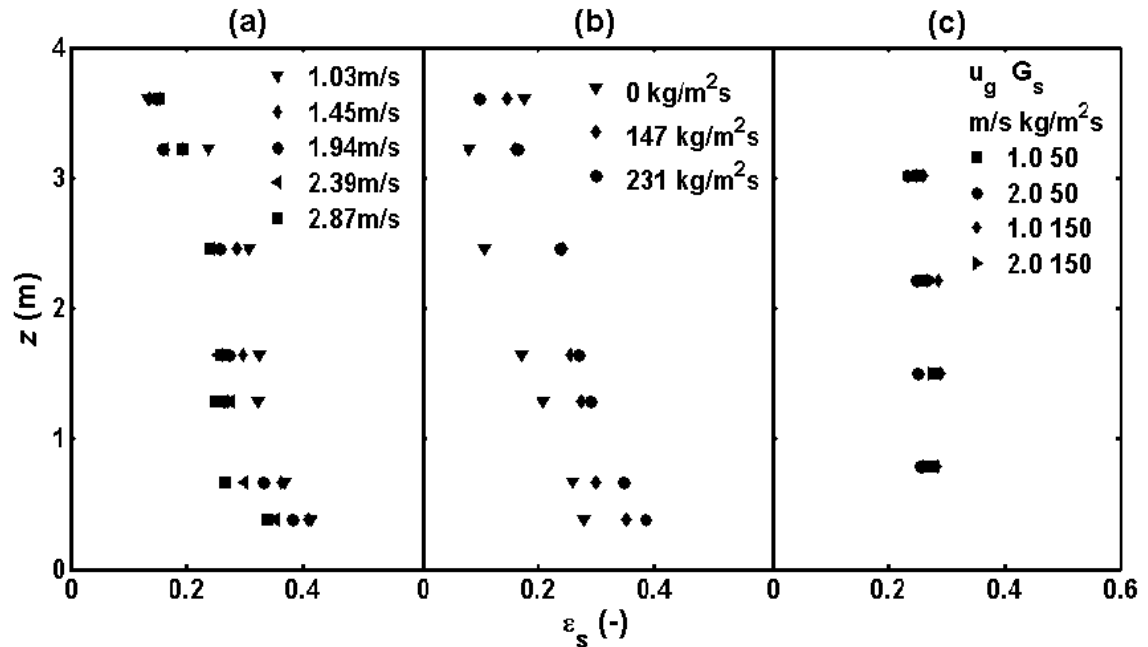


Figure 6.2 Axial profiles of cross-sectional average solids holdup obtained from pressure gradients, (a) at different air velocities, $G_s = 150 \text{ kg/m}^2\text{s}$, and (b) with and without solids circulation, $u_g = 2.4 \text{ m/s}$, and (c) from optical probe measurement (FCC particles, $d_p = 65 \mu\text{m}$, $\rho_p = 1780 \text{ kg/m}^3$, from Zhu and Zhu, 2008)

Comparatively, cross-sectional average solids holdup of more than 0.25 in the major part of the bed is higher than or comparable to that in the bottom dense region of typical CFBs (~ 0.2) and is higher than that in the “DSU” ($0.15 \sim 0.25$) (Issangya et al, 1999; Grace et al, 1999; Pärssinen and Zhu, 2001; Louge and Chang, 1990; Malcus et al 2002). On the other hand, gas-solid interfacial area per unit volume of suspension directly affects gas-solid interaction, which is closely related to the solids concentration. Solids residence time distribution within the fluidized bed and heat transfer between the suspension and the wall are also dependent on the solids concentration. For example, particle convective

heat transfer coefficient increases with the solids suspension density because of higher particle thermal capacity (Reddy and Basu, 2001).

Such macro flow structure of CTFB can be further studied through radial profiles at the different axial positions, as shown in Fig. 6.3. In the fully developed section ($z = 1.5$ and 2.2 m), the solids holdup varies in a parabolic shape across the bed, whose minimum value at the center decreases with increasing air velocity and maximum value at the wall shows little change. In the entrance zone, the solids holdup increases steadily from the center to the wall and has higher values than at higher axial positions due to the effect of air distribution and particle acceleration, somehow different from the fully developed section. On the contrary, the profiles in the exit zone are more curved and have decreased values both at the center and at the wall with increasing air velocity, suggesting that particles are discharged more quickly at higher air velocity. Overall, the values of the solids holdup of $0.15 \sim 0.50$ along the radial direction throughout the bed (Fig. 6.3) echo the holdup values in Figs. 6.2a and 6.2b for the axial profiles.

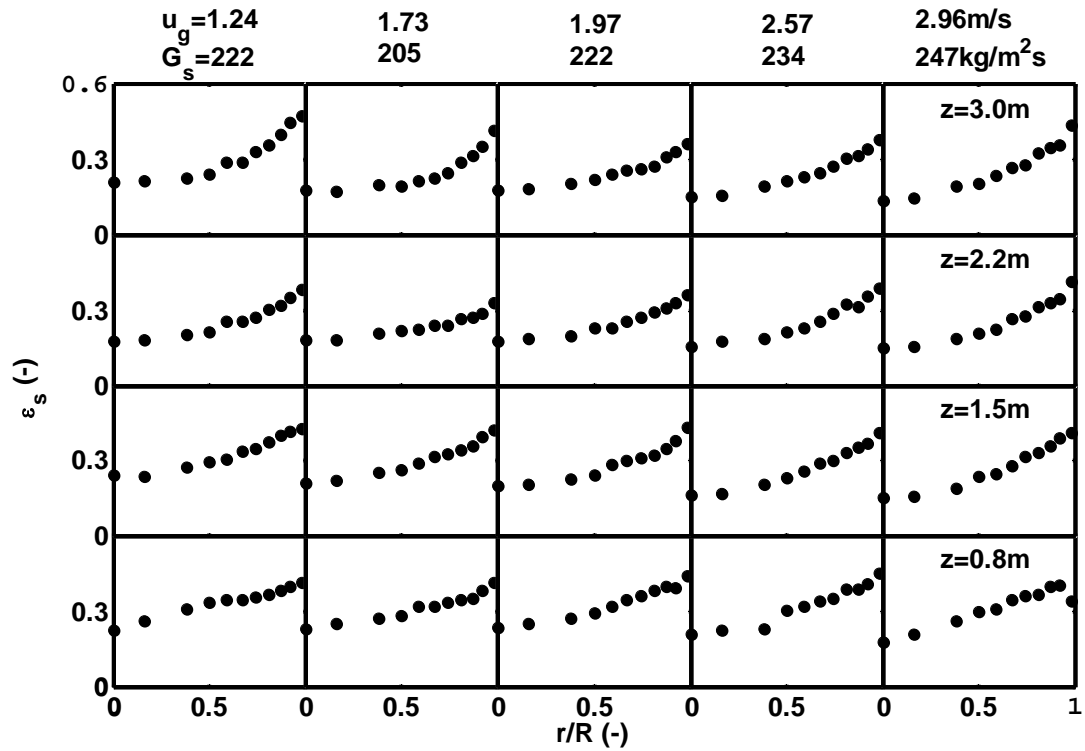


Figure 6.3 Radial profiles of local average solids holdup with varying air velocity

To study the radial profile of the solids holdup and to understand the flow structure in CTFB more clearly, one can examine the variation of annular average solids holdup with respect to air velocities and solids circulation rates, corresponding to the central (40% of the bed), middle annular (40%) and wall annular (20%) regions, as shown in Fig. 6.4. In the centre, the local mean solids holdup decreases quickly from about 0.30 and then levels off at about 0.18 with increasing air velocity. In the middle annular region, the holdup is higher than that in the centre and slightly decreases until $u_g = 2$ m/s, and then slightly increases with increasing air velocity. In the wall annular region, the solids holdup is even higher than that in the middle annulus due to lower gas velocity in the

wall region. It increases with air velocity nearly under all experimental conditions, suggesting more particles are pushed into this region. As a result, increasing air velocity makes the flow more dilute in the center and denser in the middle and annular regions. In other words, the greatest solids holdup variation happens in the center as the gas phase preferably flows in this region, while the highest solids holdup occurs at the wall.

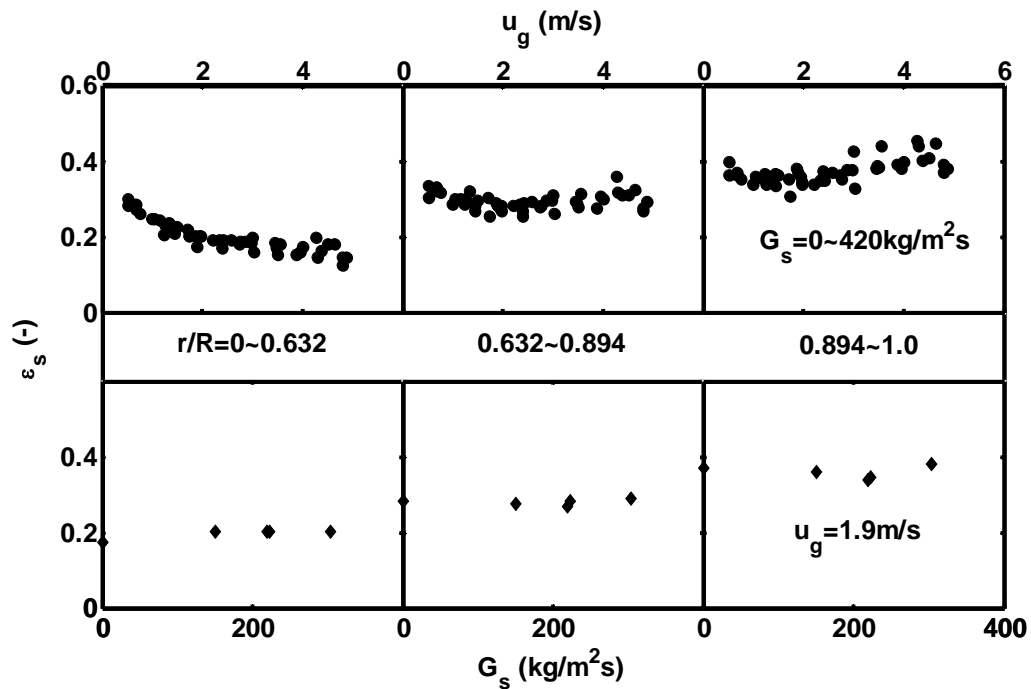


Figure 6.4 Annular average solids holdup with respect to air velocity and solids circulation rate

Relatively, the effect of the solids circulation rate on the flow structure is really small. The annular average solids holdup does not appreciably change with increasing solids circulation rate as long as the system has significant solids circulation. Noticeably, the solids holdup in the central region without solids circulation is lower than other cases

with solids circulation, indicating that solids circulation improves fluidization quality and helps to increase the particle concentration at central region. This phenomenon implies that changes of air velocity mostly influences the flow in the central region in the bed, while variation of another operating condition, solids circulation rate, has no significant influence on the radial solids concentration profiles. This insensitivity to the operating conditions suggests that the two-phase suspension density reached a saturation state in the CTFB (Zhu and Zhu, 2008a).

6.3.2 Micro flow structure of CTFB

The detail information of the flow structure, such as solids holdups of the dense and dilute phases and the dense phase volume fraction, is very helpful in understanding CTFB and modeling heat and mass transfer. Figs. 6.5-6.7 provide the variations of the annular average solids holdups of the dilute and dense phases and dense phase fraction obtained using MCDPM from the measured solids holdup signals at different air velocities and solids circulation rates. For the dilute phase, the holdup value is higher in the wall region than in the centre (shown in Fig. 6.5). The average solids holdup in the central region does not vary appreciably with either the air velocity or the solids circulation rate. Differently, the solids holdup in the middle annular region slightly decreases first from 0.12 at $u_g = 0.5$ m/s to 0.09 at $u_g = 2.0$ m/s and then slightly increases to 0.16 at $u_g = 4.8$ m/s. Although the average solids holdup values near the wall are slightly scattered due to the different wall effects and the different flow structure at different air velocities, they are higher than those in the central and middle regions and do not change appreciably with the air velocity. In all three regions, the annular average solids holdup does not

change significantly with the solids circulation rate. It is worth noting that the solids holdup of the dilute phase is around 0.1 much higher than what is expected in other gas-solids fluidized beds (Zhu et al, 2012, Chapter 4). Much more sharp peaks were observed in the valleys of solids holdup trace in CTFB regimes than BFB regime, leading to higher local mean solids holdup of the dilute phase in CTFB regime (Qi et al, 2012, Chapter 5).

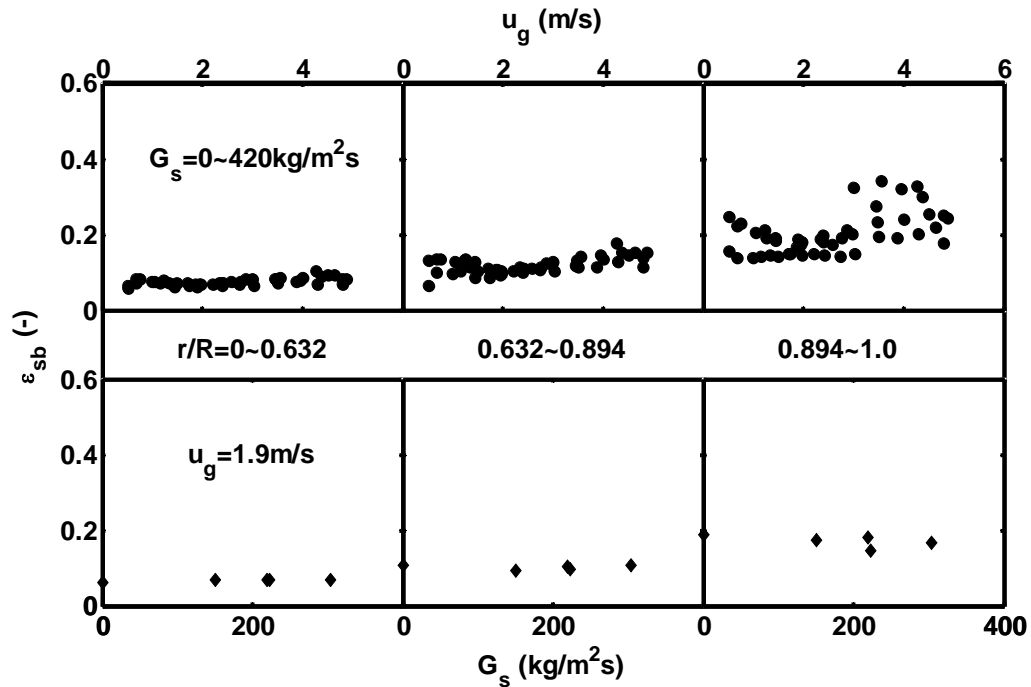


Figure 6.5 Annular average solids holdups of the dilute phase with respect to air velocity and solids circulation rate

Knowing that CTFB starts at $u_{bt} = 1.15$ m/s and ended at $u_{tc} = 3.0$ m/s at solids circulation rate of $330 \text{ kg/m}^2\text{s}$ (Qi et al, 2012, Chapter 5), one can observe the flow structure development. At low air velocity (corresponding to BFB regime at $u_g < 1.15$ m/s), the diffusive data distribution in the middle and wall annular regions reflects somewhat undetermined dilute phase due to air flow mainly in the center. With increasing air velocity,

the turbulent flow develops gradually across the entire bed in view of the experimental data forming a trend line. Such a flow refers to the steady state in CTFB proposed by Qi and Zhu (2009), implying that the dilute phase can be modeled simply across the bed. Further increasing air velocity, the flow enters CFB regime at $u_g > 3.0$ m/s, where the core-annular structure starts to form and the dilute phase flow becomes weakened, leading to diffusive data distribution again. Such flow structure transition is attributed to gas flow preferably in the centre and the wall effect coupling with the help of gravity, which results in remarkable segregation of the solids from the core region to the wall region (Zhu and Zhu, 2008a).

Compared to the dilute phase, the dense phase profile shows a simple feature of the flow structure in CTFB, as shown in Fig. 6.6. At $u_g < 3.0$ m/s, the solids holdup of the dense phase at all three regions does not change with either increasing air velocity or solids circulation rate. At $u_g > 3.0$ m/s, the solids holdup of the dense phase starts to decrease in the centre with increasing air velocity. Such a decrease of the dense phase solids holdup is regarded as dense phase expansion (Bi and Su, 2001) and suggests the beginning of CFB regime (Qi et al, 2012, Chapter 5). The dense phase expansion takes place at the local mean solids holdup of about 0.15 in this study, corresponding to the central region of the profile in the right column graphs in Fig. 6.3. This characteristic solids holdup is different from the result of dense phase expansion at less than 0.3 of the local mean solids holdup suggested by Bi and Su (2001). As to be discussed later, such expansion occurs at the end of CTFB regime instead of the beginning of the regime proposed by earlier researchers (Nakajima et al, 1991; Bi and Grace, 1995). Therefore, dense phase

expansion needs to be further studied in order to properly design and model the CTFB reactor.

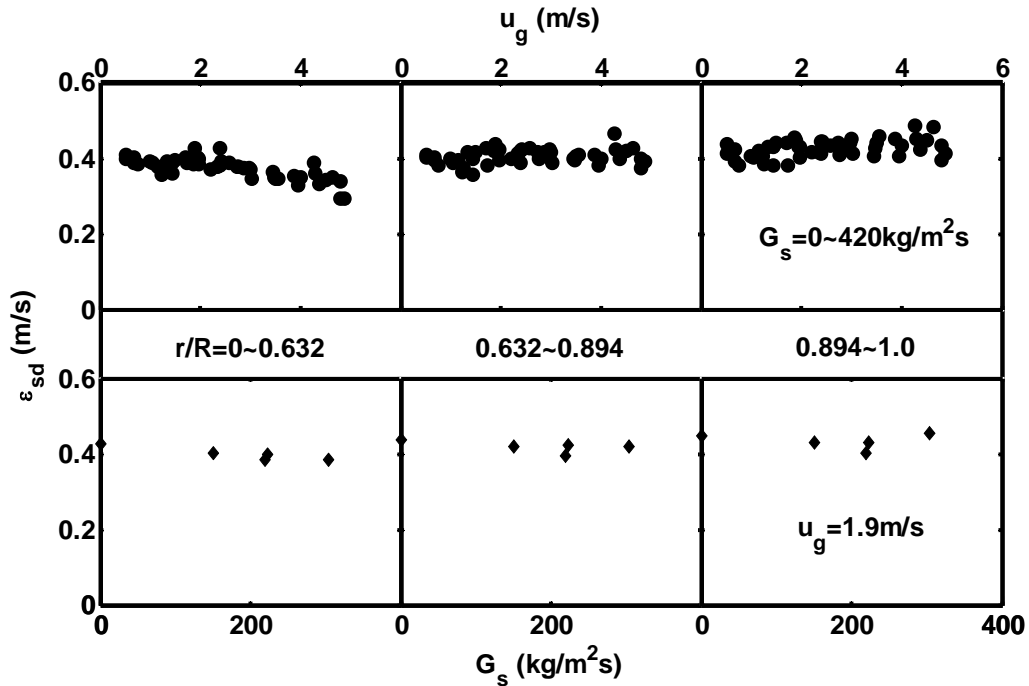


Figure 6.6 Annular average solids holdups of the dense phase with respect to air velocity and solids circulation rate

Reasonably, as the solids holdups of the dense and dilute phases hardly change, the dense phase fraction has to be subject to the variation of the radial solids holdup profiles (Fig. 6.3) with respect to air velocity and solids circulation rate, as shown in Fig. 6.7. Within the central region, the annular average dense phase fraction decreases quickly from 0.59 to 0.50 in BFB regime ($u_g = 0.5 \sim 1.15 \text{ m/s}$) and then it reduces gradually within the turbulent regime to 0.35 at $u_g = 3.0 \text{ m/s}$, suggesting dilute phase dominating flow over the whole operating air velocity range. Differently, in the middle and wall annular regions, there exists a minimum value, suggesting the fully development of the turbulent

fluidization regime across the bed at about $u_g = 2.0$ m/s with data aggregating to a trend line in a maximum extent. The minimum value divides the fraction profiles into two sections. At lower air velocity section, the fraction quickly and constantly decreases with increasing air velocity, suggesting the flow trends to dilute phase. However, before such flow trend fully develops, a new flow structure starts to appear. At the higher air velocity section, the fraction in the middle annular region stops decreasing and remains unchanged until entering CFB regime at $u_g = 3.0$ m/s. On the other hand, the fraction in the wall annular region slightly increases with increasing air velocity, suggesting the flow trends to form core-annular structure near the wall.

Further examining the profiles, one can observe that the dense phase fractions in the middle and wall annular regions are always above 0.5, suggesting a dense phase dominating flow. In other words, CTFB regime is characterized by a core structure of dilute phase dominating flow and an annular structure of dense phase dominating flow. Such flow structure reflects the transition characteristics of CTFB, as BFB is dense phase dominating flow and HDCFB is dilute phase dominating flow (Zhu et al, 2012, Chapter 4). In addition, the dense phase fraction does not change significantly with solids circulation rate but the fraction at the zero solids circulation rate is an exception, similar to the solids holdup of the dense and dilute phases.

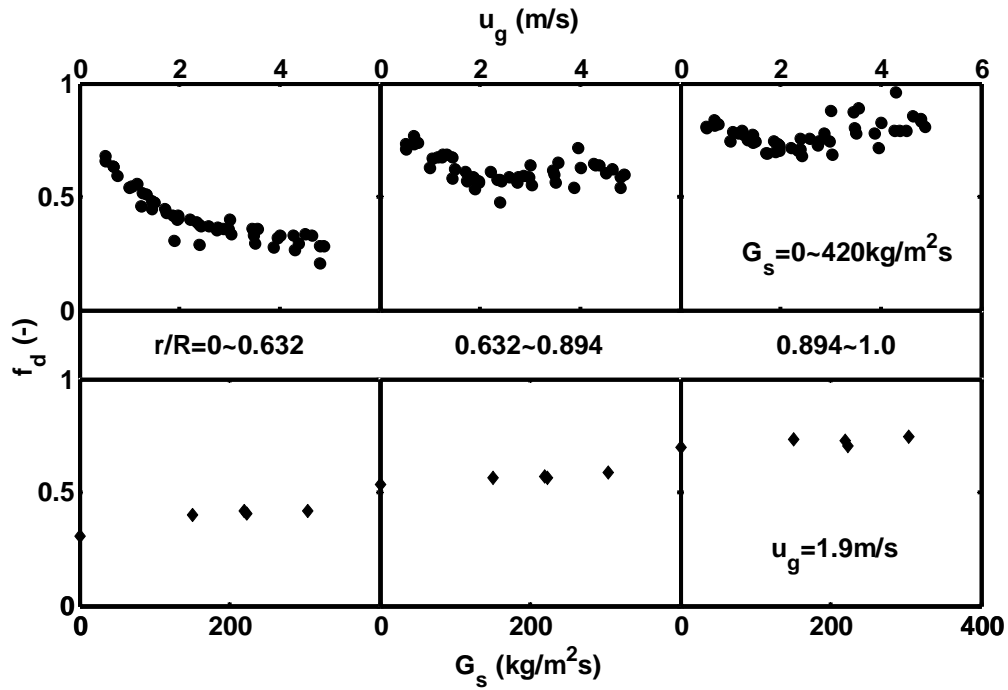


Figure 6.7 Annular average values of the dense phase fraction with respect to air velocity and solids circulation rate

Figs. 6.4, 6.6 and 6.7 show that the flow structure in the central region of CTFB undergoes most changes with respect to air velocity and solids circulation rate. To explore the flow structure variation in the central region of the bed, the Probability Density Functions (PDF) of solids holdup was examined, as shown in Fig. 6.8. Like conventional turbulent fluidization regime (Zhu and Zhu, 2008a), two peak-PDFs were obtained in the centre of CTFB, representing solids holdups of the dilute phase and dense phase respectively. The solids holdup at the dilute phase peak is nearly constant at about 0.026 through air velocities from 0.5 to 3.0m/s. The differences between BFB (Fig. 6.8a), CTFB (Fig. 6.8b) and CFB (Fig. 6.8c) are mainly reflected by the shapes of the dense phase peak. For the BFB regime (Fig. 6.8a), the dense phase peak is narrower and higher

($\varepsilon_s = 0.53$). With increasing air velocity, the peak of the dense phase of the CTFB regime becomes broader and lower but remains at the same position (shown in Fig. 6.8b, d-j). In other words, the maximum probability density of solids holdup of the dense phase decreases, while that of the dilute phase increases with increasing air velocity. Further increasing air velocity up to the ending air velocity of CTFB ($u_{tc} = 3.0\text{m/s}$), the dense phase peak diminishes and PDF curve decays nearly to a triangular distribution, leading to the expansion (reflected by no predominate dense phase peak and smaller average solids holdup) of the dense phase of the CFB regime (Fig. 6.8c, g-j), echoing the decrease of the dense phase solids holdup at the central region (shown in Fig. 6.6). In addition, although there is no apparent evidence that solids circulation would influence the dense phase structure from PDF (Fig. 6.8e-f), the extremely high probability density of the dilute phase of gas-solid flow without particle circulating (Fig. 6.8d) implies that CTFB is different from the conventional TFB, echoing the less dense phase fraction as shown in Fig. 6.7.

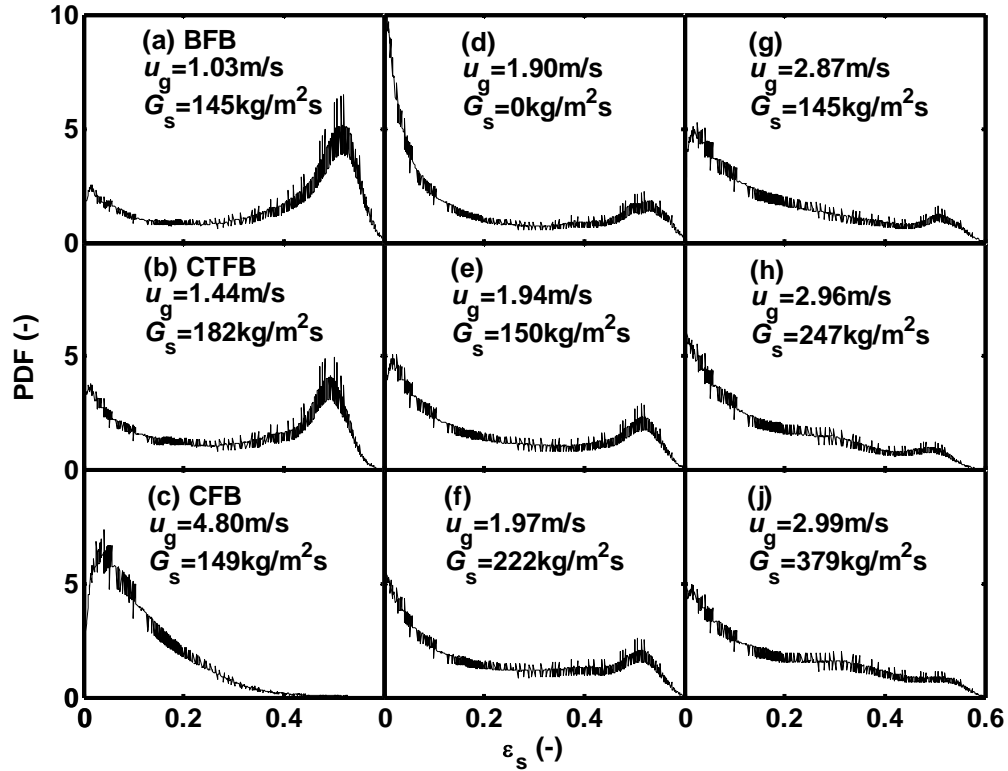


Figure 6.8 Comparison of probability density function of solids holdup (at $z = 1.5$ m, $r/R = 0.0$), over transition (a-c), and over effects of superficial air velocity and effects of the solids circulation rate (d-j)

6.3.3 Solids circulation effect on CTFB

As discussed earlier, as long as there is no significant change in solids circulation rate in CTFB, the probability density function, radial and axial distributions of solids holdup, and the micro flow structure of the dense and dilute phases remain approximately unchanged. However, the results in Figs. 6.2 and 6.8 imply that the flow structure in a gas-solid fluidized bed with and without solids circulation may be attributed to different fluidization features. On the other hand, as CTFB can operate at very high solids circulation rates, from 0 to 420 kg/m²s in this study, there must exist other factors that

influence the flow regime of CTFB, differentiating CTFB from TFB. The local solids fluxes and particle velocities, obtained through the analysis of the solids holdup signals of the dense and dilute phases using PDCCM, demonstrate that the flow in CTFB is different from TFB and obviously related to the solids circulation rates.

Comprehensively taking into account the effects of the dense and dilute phases, the net solids flux is the integration of instantaneous solids holdup and particle velocity in upward and downward directions (Eqs. 6.11 and 6.12). Correspondingly, reduced net solids flux is defined as the local net solids flux over the measured solids circulation rate, and apparent particle velocity is calculated through the cross-sectional average net solids flux and solids holdup using Eqs. 6.12 and 6.14.

$$F_{s,i,j} = \frac{\rho_p}{T_{i,j}} \int_{T_i} v_{s,i,j}(t) \varepsilon_{s,i,j}(t) dt, (i = b \text{ (dilute), } c \text{ (dense) and } j = \text{up, down}) \quad (6.11)$$

$$G_{s,l} = \sum \frac{T_{i,j}}{T} F_{s,i,j} \quad (6.12)$$

$$G_s = \frac{2}{R} \int_{T_i} G_{s,l} dr \quad (6.13)$$

$$u_p = \frac{G_{s,l}}{\varepsilon_s} \quad (6.14)$$

Figs. 6.9 and 6.10 display the radial profiles of the reduced net solids flux in the fully developed section ($z > 1.5$ m), which are characterized by core-annular regions. The solids flux is uniform in the core region, but decreases quickly in the wall region. In the profiles, a maximum net solids flux is observed at the center at low air velocity (< 1.27 m/s) and it shifts to the reduced radius of about 0.61 at high velocity (> 2.34 m/s).

Although similar to the variation at fully developed section, net solids flux distribution at entrance zone ($z = 0.8$ m) has less uniformity than in fully developed section due to the effects of air dispersion and solids acceleration. Apparent fluctuations between net solids flux profiles at entrance zone ($z = 3.0$ m) are observed in Figs. 6.9 and 6.10, which may result from the air supply pressure fluctuations within and between the experiments. The slightly different flow conditions at exit zone of CTFB also affect the local solids flux distributions. In addition, no serious net back mixing is found throughout the bed (referring to the lines in the Figs. 6.9 and 6.10), except for the exit region of CTFB, which echoes the results reported by Zhu and Zhu (2008a). Most importantly, the reduced net solids flux profiles both in Figs. 6.9 and 6.10 are similar, which agrees well with the experimental results obtained in circulating fluidized beds by Rhodes et al (1992) and Wei et al (199). The results demonstrate that the reduced net solids flux does not change appreciably either with air velocity or with measured solids circulation rate. In other word, the net solids flux is proportional to solids circulation rate, implying that particle movements in CTFB are affected by the solids circulation. The local net solids flux is calculated from the integration of the instantaneous particle velocities of the dense and dilute phases by the relative instantaneous solids holdups and time fractions in the upward and downward directions. However, the uniform distribution in the core region mainly reflects the comprehensive effects of the upward particle velocity and solids holdups of the dense and dilute phases on the flow structure (Chapter 7). Toward the wall, the instantaneous solids fluxes appear to decrease in time-mean magnitude but accompanied by more vigorous fluctuations with higher frequency and amplitude, giving rise to similar solids flux to the one at the centre (Qi and Zhu, 2009).

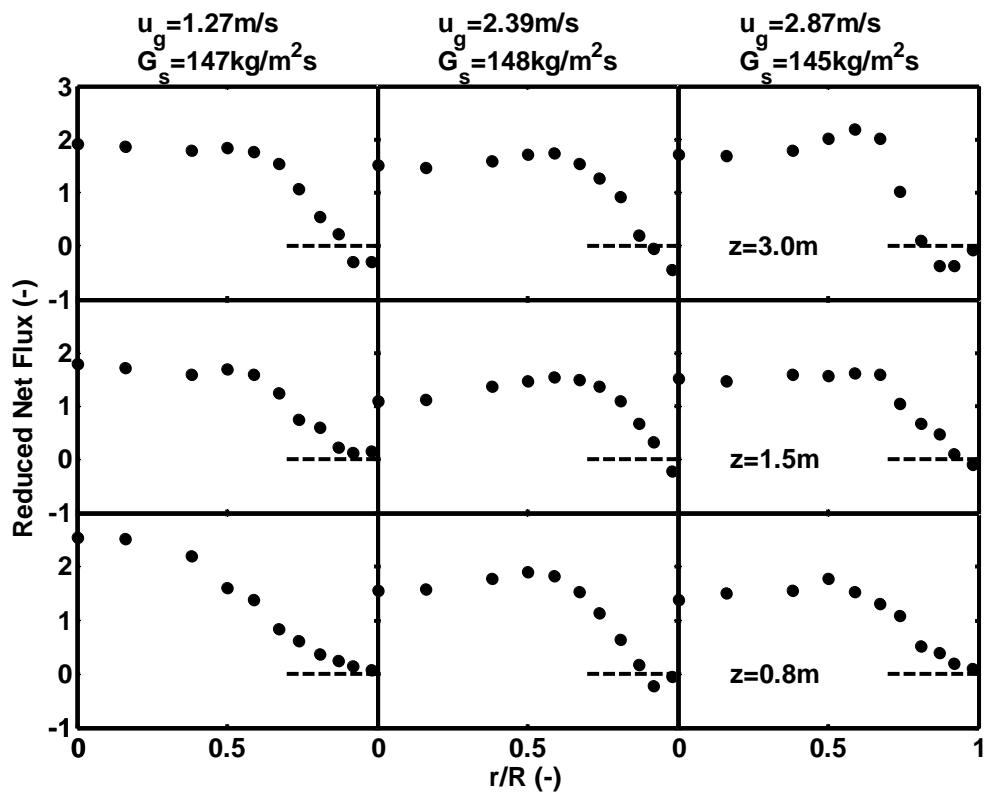


Figure 6.9 Profiles of the reduced net solids flux at different air velocities: in entrance, fully developed and exit sections

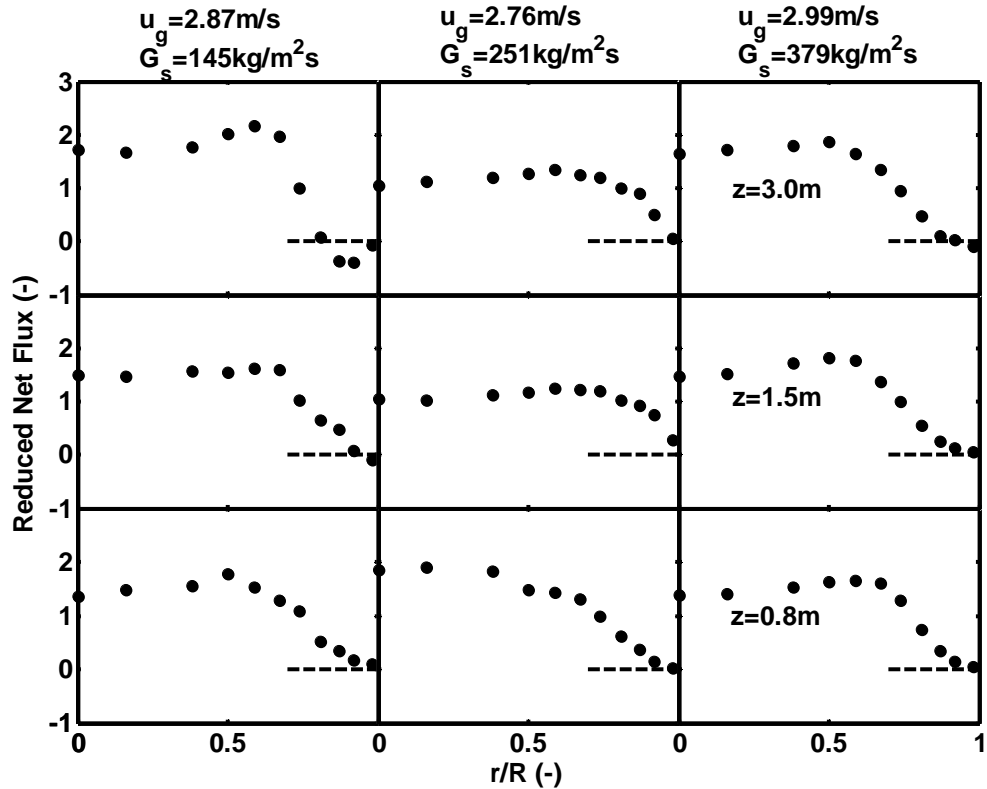


Figure 6.10 Profiles of the reduced net solids flux at different solids circulation rates: in entrance, fully developed and exit sections

The solids circulating effect in CTFB is further confirmed by the local apparent particle velocity distributions, as shown in Figs. 6.11 and 6.12. At a given solids circulation rate, the maximum apparent particle velocity at the center slightly increases and makes the profile a little steeper with increasing air velocity (shown in Fig. 6.11). That means the air preferably flows through central region, which causes higher particle velocity in the central region. At air velocity of about 2.9m/s, obvious increase of the apparent particle velocity is observed with increasing solids circulation rates, from flat parabolic shape at $150 \text{ kg/m}^2\text{s}$ to the steepest triangular shape at $380 \text{ kg/m}^2\text{s}$ (Fig. 6.12), implying that apparent slip velocity between gas and solids decreases with increasing solids circulation rate. However, it seems impossible if ignoring solids circulation effect, as smaller

apparent slip velocity should be corresponding to smaller mean size of dense phase, which requires reducing the solids circulation rate. In fact, higher solids inventory in downcomer and higher primary air pressure make CTFB operating at higher solids circulation rate without changing air velocity. High back pressure at the bottom pushes the particles up as dense phase delivery and leads to the smaller apparent slip velocity without significantly changing the flow structure. In the dense conditions, higher solids holdup might provide more upward momentum to reduce the tendency for the descending particles by particle-particle interactions (collisions). In the CTFB, therefore, most portion of the particle momentum is transferred by interactions (collisions) between particles, but not by drag forces between gas and solid phases, due to the low local gas velocities (Qi and Zhu, 2009).

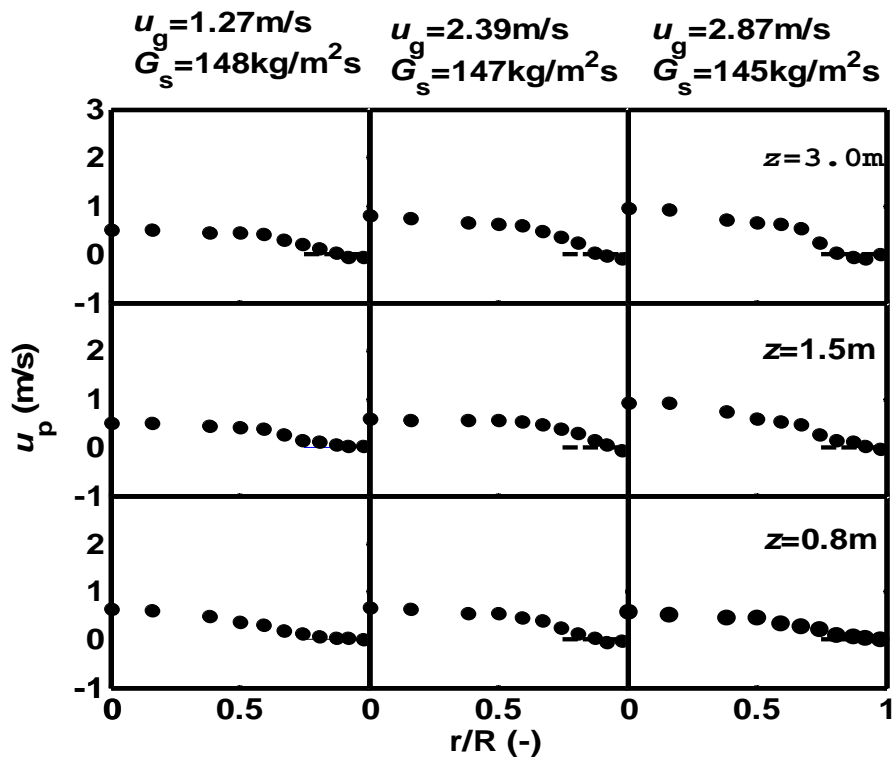


Figure 6.11 Profiles of the apparent particle velocity at different air velocities: in entrance, fully developed and exit sections

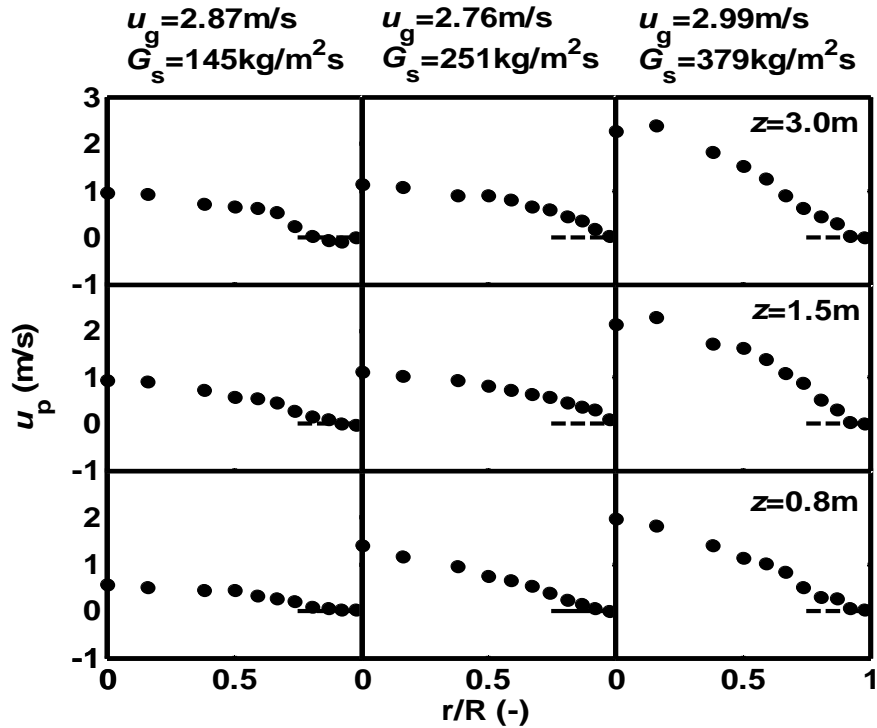


Figure 6.12 Profiles of the apparent particle velocity at different solids circulation rates: in entrance, fully developed and exit sections

6.3.4 Typical characteristics of CTFB

As suggested by Qi and Zhu (2009; Zhu and Zhu, 2008a, b; Zhu, 2010), CTFB runs in a novel gas-solid flow regime, which differed from BFB, HDCFB, CFB in many aspects. Progressively, the results in this study not only confirm their claims but also provide further evidences to conform the new fluidization regime. CTFB combines the benefits of both TFB and CFB, realizing a fluidized bed operating under low superficial gas velocity and high solids circulation rate, giving rise to some noticeable characteristics with respect to hydrodynamics and CTFB reactor application. For flow structure, CTFB is characterized by the following:

(1) Homogeneous axial flow structure with high solids concentration. Under quite wide range of air velocities of 1.0 ~ 3.0 m/s and solids circulation rates of 0 ~ 420 kg/m²s shown in Fig. 6.2, the experimental results confirms the homogeneous axial solids holdup distribution of 0.25 ~ 0.35 within the majority part of the bed, as had also been observed in earlier studies (Zhu and Zhu, 2008a; Qi and Zhu, 2009, Zhu, 2010). Such high solids concentrations vary neither with solids circulation rates nor with air velocities. Although CTFB and TFB are classified into the same regime (Zhu et al, 2012, Chapter 4), the axial profile of CTFB is different from that of TFB but similar to HDCFB (Issangya, 1997).

(2) Optimal radial flow structure. CTFB has quite different radial profile of solids holdup from BFB, TFB, HDCFB and CFB (Grace et al, 1999), which varies from about 0.15 to 0.5 (Fig. 6.3), much higher than the highest value among TFB, HDCFB and CFB regimes (0.06 ~0.3 in HDCFB obtained by Issangya et al, 1997). The results also exhibit that there exists an optimal air velocity, where the solids distribution is not too dilute in the centre and not too dense near the wall (on average over the annular region, shown in Fig. 6.4), for instance, $u_g = 2.0$ m/s in this study. Moreover, such a radial solids distribution is independent of solids circulation rate and reproducible to the maximum extent over the CTFB operation air velocity range ($u_g = 1.15 \sim 3.0$ m/s in Fig. 6.7), as regarded as the steady state of CTFB (Qi and Zhu, 2009; Zhu, 2010), further suggesting the fully developed status of CTFB.

(3) Excellent micro flow structure. CTFB is quite attributed to two-phase flow (Fig. 6.8), as described by Bi and Su (2001). Over the entire operation air velocity range of CTFB,

the dilute phase contains the solids holdup, about 0.08 in the centre, 0.10 in the middle annular region, and 0.15 in the wall annular region, while the dense phase has constant solids holdup of 0.40, as slightly lower than the result obtained using ECT (Du et al, 2003). These solids holdups are quite uniform and high, compared to those of HDCFB and CFB (Zhu et al, 2012, Chapter 4). From the variation of dense phase fraction, on the other hand, CTFB is of a dilute phase dominating flow in the centre and dense phase dominating flow in the annular regions (Fig. 6.9), totally different from the dense phase dominating flow in BFB and dilute phase dominating flow in HDCFB and CFB (Zhu et al, 2012, Chapter 4).

(4) No net downward solids flux. The fairly uniform radial solids flux across the bed in the CTFB increases with solids circulation rate, which makes CTFB distinguished by the lack of significant backmixing of solids from the “regular” TFB and fast fluidization (Zhu and Zhu, 2008b; Qi and Zhu, 2009; Zhu 2010), proportional to the solids circulation rate like a plug flow.

(5) Intensive particle–particle interaction. High solids holdup at relatively low air velocity and high solids circulation rate leads to intensive particle-particle interaction. Qi and Zhu (2009) studied the relationship between instantaneous local particle velocity and solids concentration, and concluded that the particle movements were mainly controlled by gas-particle interaction in the HDCFB, while particle-particle interaction predominated in CTFB and TFB regimes. Such particle-particle interaction is energized by the high back-pressure from downcomer and the pressure of the primary air supply. It can also be

indirectly confirmed by the maximum standard deviation of the local solids holdup in TFB (Grace et al, 1999). In detail, gas-particle interaction dominates in the dilute phase, and particle-particle interaction dominated in the dense phases at low solids circulation rate, and particle-particle and back-pressure interactions dominate in the dense phase at high solids circulation rate (Chapter 7).

(6) Quite wide operation range of air velocity and solids circulation rate. Qi et al (2012, Chapter 5) have reported that the starting air velocity, (u_{bt}), of CTFB is nearly the same as ‘regular’ TFB, while the ending velocity is proportional to the solids circulation rate. In other words, the higher the circulation rate, the wider the operating range of air velocities in CTFB. For instance, ‘regular’ TFB of FCC starts at 1.15 m/s and ends at 1.60 m/s (Perales et al, 1990). Using similar FCC particle, the operation range of CTFB is enlarged as 1.15 ~ 3.0 m/s at solids circulation rate of 330 kg/m²s (Qi et al, 2012, Chapter 5). TFB is a special case of CTFB.

(7) Extremely large solid-to-gas loading ratio, $G_s/(\rho_g u_g)$. Operating at $u_{tc} = 3.0$ m/s at $\rho_g u_g = 0 \sim 380$ kg/m²s, the solid-to-gas loading ratio reaches 0 ~350 under the all experimental operating conditions, in comparison of 10–80 for most CFB operations of Geldart’s Group A particles (Zhu and Zhu, 2008a).

Comprehensively, the above characteristics distinguish CTFB from BFB, conventional TFB, HDCFB and CFB. Correspondingly, such characteristics also make CTFB at a very attractive choice to industrial applications. CTFB is capable of (1) recycling a large

amount of particles, while maintaining a high solids concentration and therefore high gas–solid reaction intensity; (2) having a flexible capacity dealing with solids circulation and gas throughput due to a wide range of operation gas velocities and solids circulation rates with little change of axial and radial solids holdup profiles; (3) having better solids reaction selectivity due to no net downflow solids flux over the entire reactor; (4) operating at good mass and heat transfer efficiencies because of high average solids holdup over the entire reactor, and of high average solids holdup in the dilute phase; (5) Buffering fluctuation of loading and temperature during production to a maximum extent; (6) easily predicting the performance of a CTFB reactor and being simply modeled on hydrodynamics, mass and heat transfer in the reactor in view of the constant solids holdups of the dense and dilute phases across the bed.

In essence, CTFB can maintain a high solids concentration to intensify gas–solids interaction efficiency and to enhance chemical reactions, while suppress axial solids backmixing in order to accommodate reactions where a narrow solids residence time distribution is required for high reaction selectivity. Thus, CTFB is suitable for such processes as FCC process, where the catalyst deactivates quickly and therefore requires continuous regeneration, and the reaction time is short, while the solids backmixing is impeded in favour of high reaction selectivity. However, the construction and operation of CTFB is much simpler than those of CFB (Zhu, 2010).

Conclusion

Hydrodynamics of gas-solid flow were experimentally studied in depth in a Circulating Turbulent Fluidized Bed (CTFB) using FCC particles of 76 μm at air velocities of 0.5 ~ 5.0 m/s and solids circulation rates from 0 to 420 $\text{kg}/\text{m}^2\text{s}$. The experimental results demonstrated the favorable hydrodynamics and high density macro flow structure in CTFB for good mass and heat transfer, and flexible capacities of gas and solids handling. Cross-sectional average solids holdup of higher than 0.25 distributed uniformly along the majority of the bed, with high local average solids holdup radially varying in a parabolic shape of 0.15 ~ 0.50. Using the Moment Consistency Data Processing Method, solids holdups of the dense and dilute phases and dense phase fraction were predicted from the solids holdup signals. The results demonstrated that CTFB was characterized by dilute dominating flow in the centre and dense phase dominating flow in the annular region, different from the dense phase dominating flow of bubbling fluidized bed and the dilute phase dominating flow of circulating fluidized bed. Microscopically, the dense phase had constant solids holdup, and the dilute phase solids holdup hardly changed across the majority part of the bed. Using the Divided Phase Cross-Correlation Method, the net solids flux and apparent particle velocity were also obtained and displayed that the net solids flux and the local apparent particle velocity were proportional to the measured solids circulation rates.

Acknowledgement

The authors are grateful to the Natural Sciences and Engineering Research Council of Canada for supporting this work.

Nomenclature

f_d , dense phase fraction

F_s , local solids flux of the dense and dilute phases, kg/m²s

G_s , measured circulation rates, kg/m²s

$G_{s,l}$, local net solids flux, kg/m²s

H , the bed height of CTFB, m

K , kurtosis of local solids holdup fluctuations

r , radial position, m

R , radius of the column, m

S , skewness of local solids holdup fluctuations

T , time, s

u_g , superficial air velocity, m/s

u_{bt} , onset air velocity of CTFB, m/s

u_{tc} , ending air velocity of CTFB, m/s

u_p , apparent particle velocity, m/s

v_s , instantaneous particle velocity, m/s

Z , elevation from the air distributor, m

ε_s , instantaneous local solids holdup

ε_{sb} , local time-averaged solids holdup of the dilute phase

ε_{sd} , local time-averaged solids holdup of the dense phase

$\bar{\varepsilon}_s$ local time-averaged solids holdup

ρ_g , air density, kg/m³

ρ_p , solids density, kg/m³

σ_s , standard deviation of local solids holdup fluctuations

References

Bi, H.T. and J. R. Grace, (1995), “Effects of Measurements on Transition Velocities Used to Demarcate the Onset of Turbulent Fluidization,” Chem. Eng. J., 57, p261

Bi H. T., Su P., (2001), Local Phase Holdups in Gas-Solids fluidization and Transport, AIChE Journal, Vol. 47(9), 2025

Du B., Warsito W. and Fan, L., (2003), Bed Non-homogeneity in Turbulent Gas-Solid Fluidization, Vol. 49, No. 5, AIChE Journal, 1109

Grace J. R., Issangya A. S, Bai D. R, Bi H. T and Zhu, J. X, (1999), Situating the high density circulating fluidized bed, AIChE J., 45, 2108–2116

Grace J. R., (1990), High-Velocity Fluidized Bed Reactors, Chemical Engineering Science, Vol. 45, No. 8, Pp. 1953-1966

Issangya A. S, Bai D, Bi H. T, Lim K. S, Zhu J and Grace J. R., (1999), Suspension densities in a high-density circulating fluidized bed riser, Chem Eng Sci., 54, 5451–5460

Issangya A. S. and Zhu J., (1997), Flow Behavior in the Riser of a High-Density Circulating fluidized Bed, AIChE Symposium Series, Vol. 93 (317), 27

Louge M and Chang H., (1990), Pressure and voidage gradients in vertical gas solid risers, Powder Technol., 60, 197–201

Malcus S, Cruz E, Rowe C and Pugsley T. S., Radial solid mass flux profiles in a high-suspension density circulating fluidized bed, Powder Technol., 2002, 125, 5–9

Nakajima M., M. Harada, M. Asai, R. Yamazaki and G. Jimbo, (1991), "Bubble Fraction and Voidage in an Emulsion Phase in the Transition to a Turbulent Fluidized Bed," Circulating Fluidized Bed Technology III, P. Basu, M. Horio and M. Hasatani, eds., Pergamon Press, Oxford, p. 79

Perales J. F., T. Coll, M. F. Llop, L. Puigjaner, J. Arnaldos and J. Casal, (1990), On the Transition from Bubbling to Fast Fluidization Regimes, Circulating Fluidized Bed Technology, Vol. 111, p.73, P. Basu, M. Horio, and M. Hasatani, eds., Pergamon Press, Oxford

Pärssinen J. H and Zhu J. X., Axial and radial solids distribution in a long and high-flux CFB riser, AIChE J., 2001, 47, 2197–2205

Qi M, Zhu J. and Barghi S., (2012), Transition characteristics of gas-solid flow in circulating turbulent fluidized beds, Powder Technology, submitted, Chapter 5 in this thesis

Qi X., Zhu H. and Zhu, J., (2009), Demarcation of a New Circulating Turbulent fluidization Regime, AIChE Journal Vol. 55, No. 3, 595

Reddy B.V and Basu P., (2001), Effect of pressure and temperature on cluster and particle heat transfer in a pressurized circulating fluidized bed, Int J Energy Res., 25, 1263–1274

Rhodes M.J., X.S. Wang, H. Cheng, T. HIRAMA and B.M. Gibbs, (1992), Similar profiles of solid flux in circulating fluidized-bed risers, Chemical Engineering Science (May 1992), 47 (7), pg. 1635-1643

Wei Fei, Fangbin Lu, Jin Yong and Yu Zhiqing, (1997), Mass flux profiles in a high density circulating fluidized bed, Powder Technology (May 1997), 91 (3), pg. 189-195

Zhang H. and Zhu J.-X, (1998), A novel calibration procedure for a fiber optic solids concentration probe, *Powder Technology*, 100, 260-272

Zhu J. (2010), Circulating turbulent fluidization—A new fluidization regime or just a transitional phenomenon, *Particuology*, 8, Pages 640-644

Zhu J. and Bi H., (1995), Distinctions between Low Density and High Density Circulating Fluidized Beds, *The Canadian Journal of Chemical Engineering*, Volume 73, 644

Zhu J., Qi M., Baighi S., (2012), Identification of Micro Flow Structures and Regime Transition in Gas-Solid Fluidized Beds through Moment Analysis, *AIChE Journal*, Submitted, Chapter 4 in this thesis

Zhu H. and Zhu J., (2008), New Investigation in Regime Transition from Bubbling to Turbulent Fluidization, *The Canadian Journal of Chemical Engineering*, Vol. 86(6), 553

Zhu H. and Zhu J.-X, (2008a), Gas-Solids flow Structures in a Novel Circulating-Turbulent fluidized Bed, *AIChE Journal*, Vol. 54 (5), 1213.

Zhu H. and Zhu J.-X, (2008b), Comparative study of flow structures in a circulating-turbulent fluidized bed, *Chemical Engineering Science*, 63, 2920-2927

7 Particle velocity and flux distribution in a high solids concentration circulating turbulent fluidized bed

7.1 Introduction

Turbulent fluidized bed (TFB) is a fluidization regime between bubbling and circulating fluidized beds, in which there is no clear continuous phase, but intermittent or interspersing voids and dense pockets (Bi et al, 2000). The TFB regime starts from the equal fraction between the dilute and dense phases (Grace, 1986b; Bi and Su, 2001). As a result, TFB is characterized by different flow structure from the clusters in circulating fluidized beds (CFB) and from the bubbles in bubbling fluidized beds (BFB). On the other hand, TFB has very good gas-solid contact and heat transfer efficiencies, and it has found many applications in industry, such as TFB reactors for Fischer-Tropsch synthesis and acrylonitrile production. Compared to other fluidization regimes, however, TFB has many aspects that have been rarely studied, especially on its flow structure.

Little progress has been made on the properties of flow heterogeneity in TFB due to its unusual flow structure. Recently, however, Bi and Su (2001) proposed a two phase structural model, which was capable of predicting the solids holdups and corresponding volume fractions of the dilute and dense phases in gas-solid systems. Considering little differences in moments between the original signals and the predicted parameters, a Moment Consistency Data Processing Method (MCDPM) was proposed and used in

studying the solids holdups of the dilute and dense phases and the relative phase fractions in a CTFB (Zhu et al, 2012). Based on MCDPM, a division procedure of the dilute and dense phases from local solids holdup signals was proposed, which identified the dilute and dense phases without distinguishing their predominance in the flow. This may make it possible to microscopically study the properties of the flow heterogeneity of high density fluidized beds, such as particle velocities of the dilute and dense phases, slip velocity and local flux etc.

There are many techniques developed on a variety of principles in studying particle movement in fluidized beds or other gas–solids systems (Yates and Simons, 1994; Clift and Grace, 1985; Cheremisinoff, 1986; Bachalo, 1994; Adrian, 1991). These methods can be broadly classified as impact, isokinetic, flow visualization, laser Doppler, and cross-correlation techniques, etc. Both impact and isokinetic sampling methods are indirect measurement methods, which need only simple equipment and often make continuous measurement possible. However, these devices tend to interfere with the flow system being investigated and often require other parameters, such as the solids concentration to be determined simultaneously, thus increasing the complexity and reducing the analysis accuracy of the experimental data (Zhu et al, 2001).

Recently, common cross-correlation method (CCM) has become more and more popular in studying the particle velocity from the solids holdup signals from multi-phase flow systems. CCM is simple and simultaneously carried out with measuring solids holdup, local flux etc. (Zhu et al, 2001). A common measurement technique of solids holdup is

typically to use optical fibre probes containing light-emitting and light-receiving fibres to detect reflected light from particles in their vicinity. The intensity of the reflected light is mainly a function of concentration, size and material properties of the particles. If there are two bundles of emitting and receiving fibres aligned in the direction of the flow, the signals received from a given particle or group of particles will have a time delay between them. This time delay is a direct function of the particle velocity and can be determined by cross-correlating the pairs of signals. There are built-in and off-line coded CCM to obtain the time delay from optical measurement signals. The build-in CCM directly provides particle velocity with the solids holdup together through the measurement instrument, such as PV6 (Xu, 2010). To increase flexibility, off-line CCM was widely used according to the operation conditions and investigation purposes to analyze particle velocity from the concentration signals afterwards (Nieuwland et al, 1996; Li, 2010; Zhu and Zhu, 2008).

However, Zhu et al (2001) considered that a significant disadvantage of the CCM is the preferential detection of the velocity of particle clusters over individually flowing particles, especially when the gas–solid flow suspension is not very dilute. For the light reflection signals, the passage of particles closely grouped together in the form of clusters or agglomerates tends to cause much larger peaks than individual particles. During cross-correlation, it is the large peaks in the signals which dominate in determining the maximum of the cross-correlation function so that the particle velocities thus obtained are over-weighted to those of the clusters rather than particles travelling individually. On the other hand, individual particles tend to travel at higher velocities in most gas–solid

upflow given their reduced slip velocities. As a result, CCM tends to underestimate the actual particle velocity in upflow, while overestimating the magnitude of the velocity in downflow systems or regions. Computing average particle velocities over extended periods is another disadvantage of the cross-correlation method. It provides no information on the distribution of velocities or the instantaneous velocity. This, for example, makes it difficult to synchronize the velocity data with any measured solids concentration. Zhu et al (2001) developed a new five-fibre optical probe to obtain the particle velocities directly from the peak times so that the disadvantages of CCM were eliminated. Such an optical fibre probe directly measuring particle velocity was regarded as hardware solution to the disadvantages of CCM.

Recently, Zhu and Zhu (2008 a and b) proposed a new circulating turbulent fluidized bed (CTFB) reactor, integrating solids circulation and conventional turbulent fluidized beds into a unique high-density fluidization system to simultaneously gain efficient gas-solid contact and low solids back-mixing. The results demonstrated that CTFB is independent of bubbling, circulating and high density circulating fluidized beds (Qi and Zhu, 2009, 196; Zhu, 2010). While our earlier investigations (Zhu et al, 2012, Chapter 4; Qi et al, 2012, Chapter 5) have confirmed that CTFB and conventional TFB are in the same regime and that CTFB comprises TFB with obvious similarities and dissimilarities, more details of the flow structures in CTFB (particle velocities of the dilute and dense phases, slip velocity and local flux etc.) are yet to be studied. Experiments on CTFB were carried out using FCC particles in this study. A Divided Phase Cross-Correlation Method (DPCCM) on pairs of solids holdup signals was proposed to study the particles

movements with respect to the dilute and dense phases in CTFB, to further assess the new fluidization reactor.

7.2 Experimental setup and methods

7.2.1 Experimental setup

The experimental unit was a cold model circulating turbulent fluidized bed, which consisted of six parts (Fig. 7.1a): (1) a CTFB column, with i.d. of 0.101 m and height of 3.6 m between gas distributor (a perforated-plate with open area ratio 14%) and column top; (2) a quick discharging section at the top of the CTFB column with a diameter of 0.203 m and a total height of 6.4 m; (3) a downcomer (i.d. 0.305 m) with a solids level of 4.95 m when all solids are stored; (4) a solids circulation rate measurement device with two flapper valves in the upper section of the downcomer (Pärssinen and Zhu, 2001a); (5) a recycle loop including a primary inner cyclone, secondary and tertiary standard cyclones, and a bag filter to capture the entrained particles and return them to the downcomer; (6) an inclined solids return pipe at the bottom with a solid circulation rate control device.

After passing the solids control valve in the inclined pipe, the particles coming from the downcomer entered the CTFB bottom at a height of 0.2 m above the gas distributor, and were accelerated by air at ambient conditions. Secondary air supply was distributed via an annular perforated plate with 12.6% free area at the bottom of the upper discharging section to lift the particles upwards and to entrain particles out of the column as quickly as possible to minimize the pressure drop across the upper section. This unique design

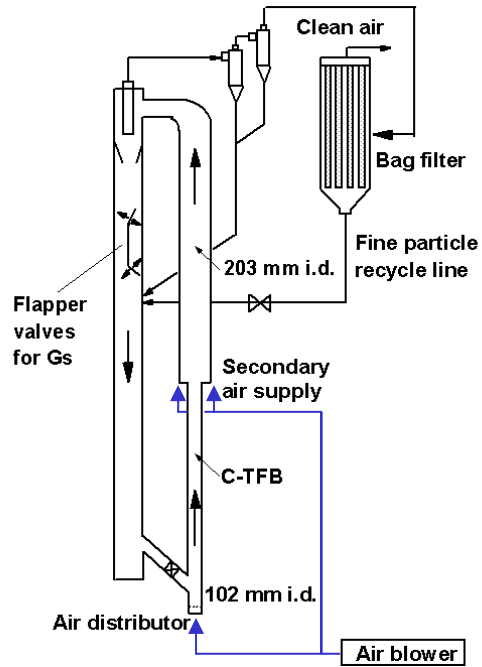
enabled high solids circulation rates and high suspension density in the CTFB at relatively low superficial gas velocities (1–5 m/s). In the present study, the secondary air velocity was kept at 6 m/s. The particles used in this study were FCC catalyst with a Sauter mean diameter of 76 μm and a particle density of 1780 kg/m^3 . The relative humidity was kept between 70 and 80% to minimize the electrostatic effects.

Experimental data were acquired using four multi-fibre optical reflective probes of model PV-6, developed by the Institute of Process Engineering, Chinese Academy of Sciences, Beijing, China. Each of the four probes consists of two fibre bundles located on the same vertical line. Each bundle is composed of both light-emitting and receiving quartz fibres arranged in an alternating array, corresponding to emitting and receiving layers of fibres. The diameter of each fibre was 25 μm . Light from a light emitting diode (LED) transmits through the emitting half of the fibres to the tip, where hitting upon particle(s) in the riser, will be reflected back to the probe. The intensity of the reflected light depends on the concentration, size distribution, composition, and shape of the particles. The received light reflected by the particles was converted by a photo-multiplier into voltage signals. The voltage signals were further amplified and fed into a computer. A special calibration procedure in high particle density environment had been carried out and the calibration curves had been obtained to convert the voltage data to solids holdups, following the procedure proposed by Zhang et al (1998).

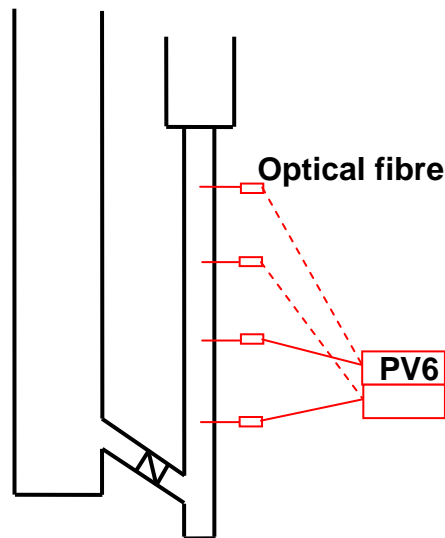
The probes were setup at four separate axial elevations, and traversed horizontally to measure local solids holdup at eleven radial positions (Fig. 7.1b). The 4 axial locations

were chosen in an effort to characterize the acceleration zone (0.8 m) and the fully developed zone (1.5, 2.2 and 3.0 m). Radial positions were chosen at the midpoints of ten equal area circles ($r/R = 0.0, 0.16, 0.38, 0.5, 0.59, 0.67, 0.74, 0.81, 0.87, 0.92, \text{ and } 0.98$) at each axial level within the risers. There were two PV6 units used in the experiments: a master and a slave. A special setup procedure was carried out for the two units to control four probes and a special data processing method was implemented with normalized calibration curves and different unit gains and offsets to obtain consistent experimental results throughout the bed. At one radial location, the units were connected to two adjacent probes and then switched to the other two. To ensure the consistency of the data at one specific operating condition, the data at all locations were collected within one run by the four probes. The sampling rate was 50 kHz and data were collected for 131 sec for each measurement.

Experimental air velocities varied from 0.5 to 5.0 m/s, covering the onset transition air velocity ($u_{bt} = 1.15$ m/s) and ending air velocity ($u_{tc} = 3.0$ m/s at $G_s = 300$ kg/m²s) of CTFB regime, and solids circulation rates from 0 to 420 kg/m²s (Qi et al, 2012, Chapter 5). There were two particle inventory cases to implement the experiments: static downcomer bed height of 3.85m for solids circulation rates of 250 kg/m²s and less, 4.95 m for solids circulation rates of up to 420kg/m²s. The experimental air velocities and corresponding solids circulation rates were obtained through adjusting the opening of the control valves and the pressure of primary air supply, in the condition that there was no apparent dense phase appearing in the delivery section over CTFB.



(a)



(b)

Figure 7.1 Experimental apparatus and optical fibre probe setup

7.2.2 Divided phase cross-correlation method

The measured time series record the instantaneous solids holdups of the dense (peak) and dilute (valley) phases with the relative phase fraction in a gas-solid flow system. A Moment Consistency Data Processing Method (MCDPM) had been proposed to calculate the phase mean solids holdups and the dense phase fraction (Zhu et al, 2012, Chapter 4). Using the dense phase fraction, MCDPM suggested a division procedure of the dilute and dense phases from the measured times series. The division generates two sub series from the measured series representing the dilute and dense phases. For two channel probe measurements, the procedure typically generates the dense phase series pairs and the dilute phase series pairs. Such sub series pairs might be used to calculate phase particle velocities through cross-correlation method.

Unlike the measured series, the two sub series are not continuous over the sampling period, and each of them only consists of the dense peaks (above a division value obtained from the phase fraction) or the dilute valleys (below the division value) discretely distributed along the entire sampling period. Therefore, they cannot be directly used in computing phase particle velocities through cross-correlation method. In other words, the sub series have to be modified to maintain the original time sequence of the peaks and valleys over the sampling period and to eliminate the opposite phase effect on the calculation, as shown in Fig. 7.2. To solve this problem, a new sub series for the dense phase is constructed by substituting dense phase mean value into the dense phase series in the time domains of the valleys (Fig. 7.2b), while a new sub series for the dilute

phase is constructed by substituting dilute phase mean value into the dilute phase sub series in the time domains of the peaks (Fig. 7.2c). With respect to the mean value of the dense phase sub series, cross-correlation method (CCM) is applied to the modified sub series of the dense phase over a period to obtain a delay time and further to compute instantaneous particle velocities of the dense phase. Similarly, with respect to the mean value of the dilute phase sub series, CCM is applied to the modified sub series of the dilute phase over a period to obtain a delay time and further to compute instantaneous particle velocities of the dilute phase. Such an approach in computing phase particle velocities using cross-correlation method on the divided phase sub series pairs of solids holdups is regarded as Divided Phase Cross-Correlation Method (DPCCM).

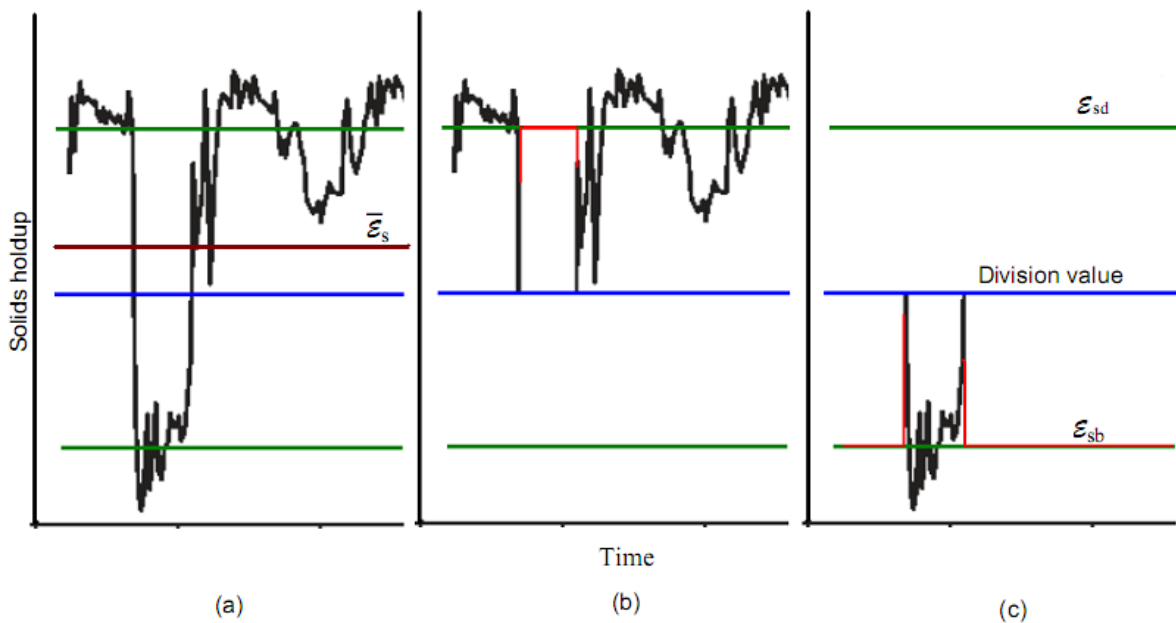


Figure 7.2 Signal decomposition of DPCCM: (a) original signal segment of solids holdup, (b) sub-signals of dense phase substituted dense phase mean value at the dilute phase domain, (c) sub-signals of dilute phase substituted dilute phase mean value at the dense phase domains

The validity of DPCCM may be elucidated by Eqs. 7.1-7.4. A pair of solids holdup series at a measurement have the same population N_i , equal to the population summation of their dilute and dense phase sub series, NC and NB , as shown in Eq. 7.1.

$$N_i = NB + NC \quad (7.1)$$

For a measured solids holdup series pair like in Fig. 7.2a, CCM is capable of generating a set of cross-correlation coefficients for a set of time delay, τ , using an equation like Eq. 7.2 with respect to the overall mean values of the series. Only the time delay corresponding to the maximum coefficients, $\phi(\tau)$, is used in calculating overall mean particle velocity.

$$\phi(\tau) = \frac{\sum_{N_i} [(\varepsilon_{s,1}(n) - \overline{\varepsilon_{s,1}})(\varepsilon_{s,2}(n - \tau) - \overline{\varepsilon_{s,2}})]}{\sqrt{\sum_{N_i} (\varepsilon_{s,1}(n) - \overline{\varepsilon_{s,1}})^2} \sqrt{\sum_{N_i} (\varepsilon_{s,2}(n - \tau) - \overline{\varepsilon_{s,2}})^2}}, \text{ for measured series} \quad (7.2)$$

For the dense phase series pair, substituting the overall mean solids holdups with the dense phase mean solids holdups into Eq. 7.2, Eq. 7.2 is transformed to Eq. 7.3 due to $\varepsilon_s - \overline{\varepsilon_{sc}} = 0$ in the time domains of the dilute phase pair, as seen in Fig. 7.2b. As a result, Eq. 7.3 only processes the sub series of the dense phase with respect to the dense phase mean values over the population of NC , determining a time delay for computing the particle velocity of the dense phase. Similarly, substituting the overall mean solids holdups with the mean solids holdups of the dilute phase pair into Eq. 7.2, Eq. 7.2 is transformed to Eq. 7.4 over the population of NB , determining a time delay for computing the dilute phase particle velocity.

$$\phi_c(\tau) = \frac{\sum_{NC} [(\varepsilon_{s,1}(n) - \overline{\varepsilon_{sc,1}})(\varepsilon_{s,2}(n - \tau) - \overline{\varepsilon_{sc,2}})]}{\sqrt{\sum_{NC} (\varepsilon_{s,1}(n) - \overline{\varepsilon_{sc,1}})^2} \sqrt{\sum_{NC} (\varepsilon_{s,2}(n - \tau) - \overline{\varepsilon_{sc,2}})^2}}, \text{ for the dense phase} \quad (7.3)$$

$$\phi_b(\tau) = \frac{\sum_{NB} [(\varepsilon_{s,1}(n) - \overline{\varepsilon_{sb,1}})(\varepsilon_{s,2}(n - \tau) - \overline{\varepsilon_{sb,2}})]}{\sqrt{\sum_{NB} (\varepsilon_{s,1}(n) - \overline{\varepsilon_{sb,1}})^2} \sqrt{\sum_{NB} (\varepsilon_{s,2}(n - \tau) - \overline{\varepsilon_{sb,2}})^2}}, \text{ for the dilute phase} \quad (7.4)$$

For the time delay, τ , obtained through Eqs, 7.3 and 7.4 over a small given time period in whole sampling time period, instantaneous particle velocity is calculated using Eq. 7.5.

$$v_s = \frac{d}{\tau} \quad (7.5)$$

To obtain the most pertinent instantaneous particle velocity, the series pair require proper sub-grouping with respect to small time period(s). On one hand, each grouped sub series segment should contain sufficient data displaying the characteristic pattern to obtain most pertinent particle velocity. On the other hand, the bigger subgroup size leads to more dissimilarities between the series pair, making particle velocity calculation less accurate (Zhu, 2001). In this study, it was found that 5-cluster grouping (average of 0.02s each group) made the computation most successfully converge to acceptable results. Moreover, for different quality data segments, DPCCM yields different maximum coefficients. Theoretically, the higher the coefficient, the more the series pair is cross-correlated. If the coefficient is too low, the calculation result does not yield an acceptable particle velocity, resulting in a data segment discarding. In this study, the data segment was discarded for coefficient less than 0.6, as proposed by Nieuwland et al (1996)

Although the coefficient sometimes large, the velocity may be too high to be realistic due to the bad quality of the series pair segments, leading to a much higher net cross-sectional average solids flux than the measured solids circulation rate. Such situation may be usually caused by severe static electricity effect and bad probe positioning. To avoid

extremely high particle velocity into calculation, a maximum particle velocity constraint needs to be pre-set to guarantee the calculation to converge. In fact, the computation within the core region easily converges to a realistic particle velocity for the data at high air velocity with little data rejection. But for the computation on series pairs near the wall region and at lower air velocity, more attempts are needed to make the calculation convergent to the measured solids circulation rate through adjusting highest particle velocity constraint, which may result in higher data rejection ratio. For all the experimental conditions, the data rejection ratio was less than 30%. The DPCCM computation was carried out using special codes of Matlab developed in this study.

If Eq. 7.3 or 7.4 does not successfully yield an acceptable result on a series segment, the data segment is discarded. The calculation time of a given phase (dilute phase noted with b and dense phase with c) at a given direction is computed using Eq. 7.6. The total calculation time T from Eq. 7.7 is usually less than the sampling time T_s , corresponding to the measured series population. Using the instantaneous particle velocities and solids holdups, averaged solids flux, net solids flux and particle velocity are computed from Eqs. 7.8-7.10 respectively, while the computation accuracy and convergent condition are assessed by the measured solids circulation rate using Eq. 7.11.

$$T_{i,j} = \int_{T_i} dt_{i,j}, \quad (i = b \text{ (dilute)}, c \text{ (dense)} \text{ and } j = \text{up, down}) \quad (7.6)$$

$$T = \sum T_{i,j} \quad (7.7)$$

Corresponding

$$F_{p,i,j} = \frac{\rho_p}{T_{i,j}} \int_{T_i} v_{p,i,j}(t) \varepsilon_{s,i,j}(t) dt, \quad (7.8)$$

$$G_{s,l} = \sum \frac{T_{i,j}}{T} F_{p,i,j} \quad (7.9)$$

$$V_{p,i,j} = \frac{1}{T_{i,j}} \int_{T_i} v_{p,i,j}(t) dt \quad (7.10)$$

$$G_s = \frac{2}{R} \int_{T_i} G_{s,l} dr \quad (7.11)$$

where $\frac{T_{i,j}}{T}$ are defined as upward and downward time fractions of the dilute and dense phases.

7.2.3 Apparent particle velocity and phase slip particle velocity

For the heterogeneous gas-solid flow in a gas-solid system, the dilute phase has lower solids holdup but higher particle velocity, while the dense phase has higher solids holdup but lower particle velocity. Therefore, the arithmetic average of the particle velocities of the two phases does not produce the overall mean particle velocity of the flow. In comparison with the superficial air velocity, apparent local particle velocity is defined by Eq. 7.12, with the cross-sectional average net solids flux over local mean solids holdup.

$$\bar{V}_{p,j} = \frac{G_{s,l}}{\varepsilon_s} \quad (7.12)$$

Conventionally, slip velocity is mostly defined as the difference between the local average particle velocity and the superficial air velocity (Chan, 2010) or between local time-average particle velocity and local average air velocity (Yang et al, 1993). In this study, the difference between the upward average particle velocities of the dilute and dense phases determined by DPCCM is defined as phase slip particle velocity, as represented by Eq. 7.13, considering the much higher percentages of upward time

fractions than the ones of the downward.

$$V_{p,slip} = V_{p,b,up} - V_{p,c,up} \quad (7.13)$$

7.3 Results and discussion

Particle movements play very important roles in gas-solid contacting and mixing, heat/mass transfers as well as erosion in fluidized beds. Particle velocity distributions are directly related to the residence time of particles within fluidized bed reactors (Zhu and Zhu, 2008a). Assuming the flow structure (dilute and dense phases) over a small piece of the data (about 0.02s in this study) for vertically moving upward or downward, not both or laterally, there would be four particle velocities to be obtained from Eq. 7.5, upward and downward particle velocities of the dense phase, upward and downward particle velocities of the dilute phase in the condition of vertical probe channel alignment. The results obtained through DPCCM revealed the effects of air velocity and solids circulation rate on the particle movements of the dilute and dense phases in CTFB.

7.3.1 Particle velocities of dilute and dense phases

Fig. 7.3 provides the radial particle velocity profiles of the dilute and dense phases in CTFB in upward direction at similar air velocities and different solids circulation rates. For the dilute phase, the radial particle velocity profiles vary in a parabolic shape, not changing appreciably in the central region but decreasing quickly in the annulus region, while the profiles of the dense phase are not in a parabolic shape, and decrease nearly linearly toward the wall. Comparatively, the particle velocities of the dilute phase are

much greater than the ones of the dense phase in the central region. In the annular region, the particle velocity of the dilute phase decreases more quickly than that of the dense phase to a small value at the wall, both phases having similar non-zero upward particle velocity. At different solids circulation rates, the differences of the particle movements in the dilute and dense phases are significant. In the central region, the particle velocity increases only slightly with increasing solids circulation rate, and it does not vary appreciably near the wall. On the other hand, the particle velocity of the dense phase at low circulation rate is low and uniform across the bed. It increases with increasing solids circulation rate from the centre to the wall. Quantitatively, the velocities of the dense phase are proportional to the increase of the solids circulation rates both at the centre and the wall.

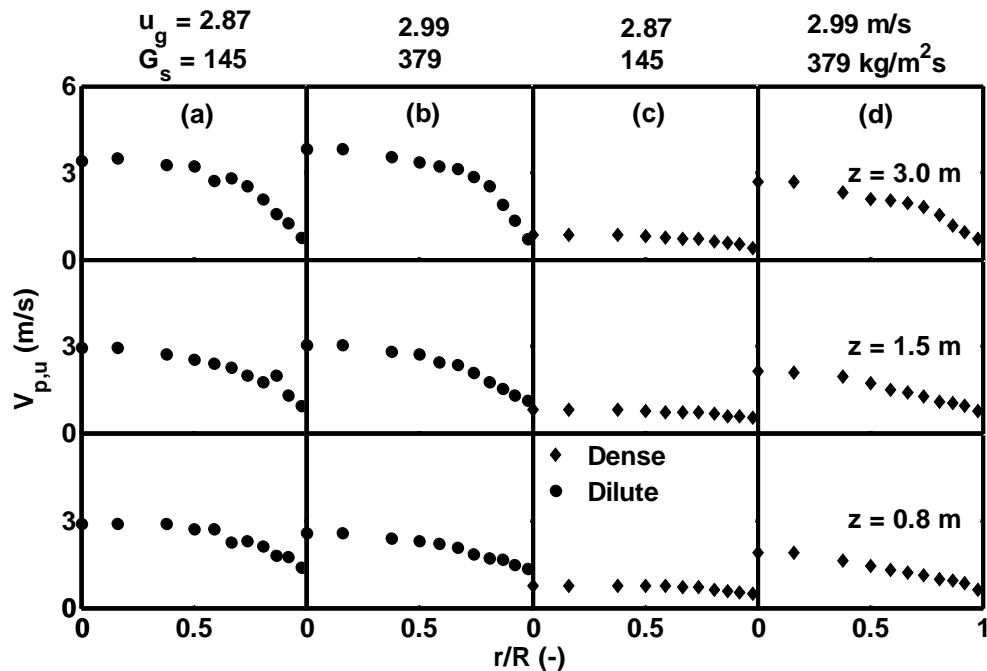


Figure 7.3 Profiles of upward radial particle velocity of dilute and dense phases

The upward particle velocities of the dilute phase are slightly higher than the superficial air velocity in the centre, indirectly suggesting air preferably flows in view of the constant slip velocity between air and the particle of the dilute phase. The particle velocities of the dilute phase are somehow higher in the center of the bed for the higher solids circulation rate of $380 \text{ kg/m}^2\text{s}$, compared to the low flux of $145 \text{ kg/m}^2\text{s}$, different from the results in a high density circulating fluidized bed ($G_s = 489 \text{ kg/m}^2\text{s}$, $u_g = 11 \text{ m/s}$) (Knowlton, 1995). The obvious increase of the particle velocity in the centre of HDCFB with increasing solids circulation rate was attributed to the fact that under a higher solids circulation rate (with a constant u_g) a denser concentration of solids occupies the wall region and restricts the gas flow (Parssinen & Zhu, 2001b; Yang et al, 1993). However, the increase of solids circulation rate in CTFB mainly gives rise to higher particle velocity of the dense phase instead of the one of the dilute phase, suggesting that solids circulation in CTFB does not influence much the air distribution across the bed. Such phenomenon can be elucidated by the facts that solids circulation does not change the radial distribution of the local mean solids holdup (in Chapter 6) and that higher air velocity does not cause the obviously higher particle velocity of the dense phase, as to be discussed later.

On the other hand, Fig. 7.4 shows difference between the dilute and dense phases for downward particle movements. The magnitudes of particle velocities of the dilute phase are largest at the centre and decrease toward the wall. They slightly decrease with increasing solids circulation rate. All these phenomena suggest the downward particle movement of the dilute phase predominates in the central region over near the wall and

solids circulation reduces this kind of downward particle movement. On the contrary, the magnitudes of the particle velocity of the dense phase are uniform across the bed and increase with increasing solids circulation rate, echoing the results of the constant downward particle velocity reported by Zhu and Zhu (2008a). Quantitatively, the magnitudes of the particle velocity of the dense phase smaller than that of the dilute phase suggest the larger inertia and not easily changed the state of the dense phase, while their increase with increasing solids circulation rate suggest that higher upward particle velocity of the dense phase gave rise to a higher downward particle velocity.

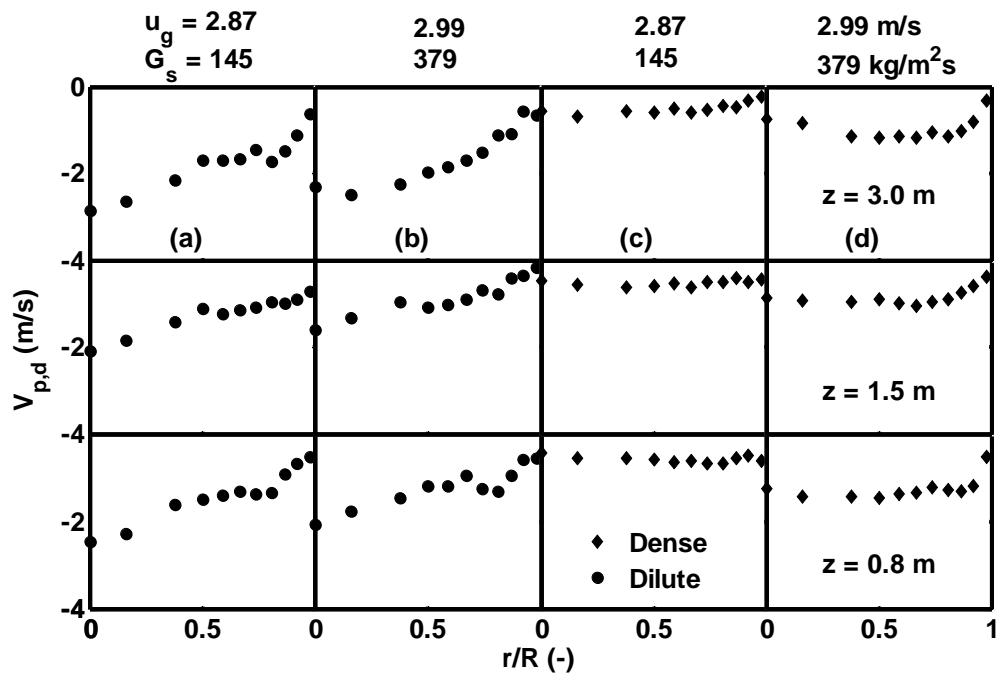


Figure 7.4 Profiles of downward radial particle velocity of dilute and dense phases

The variations of annular average particle velocities with respect to the air velocity and the solids circulation rate further display the particle movement variation with the flow

transition in CTFB, as shown in Figs. 7.5 and 7.6. For the dilute phase, the average upward particle velocity in the central region increases nearly linearly with increasing air velocity. In the middle and wall annular regions, it increases in a parabolic shape. In other words, the upward particle velocity changes similarly across the bed at low air velocity but it varies in different way between the central and annular regions with increasing air velocity, possibly suggesting the variation of the particle movement pattern from BFB to CFB. For the dense phase, the particle velocity increases with increasing air velocity in a small rate than that of the dilute phase. Relatively, the particle velocity increasing quicker near the wall than in the other two regions suggests that the vigorous core flow gives rise to strengthening the dense phase movement near the wall.

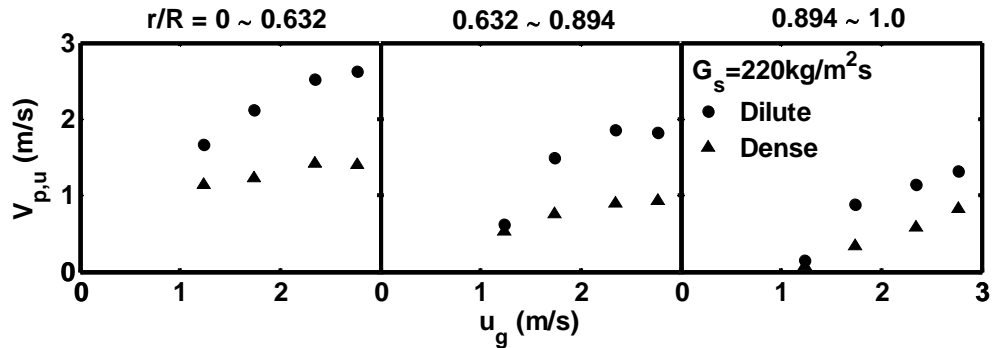


Figure 7.5 Annular average of upward particle velocities of dilute and dense phases with respect to air velocity, $z = 1.5\text{m}$

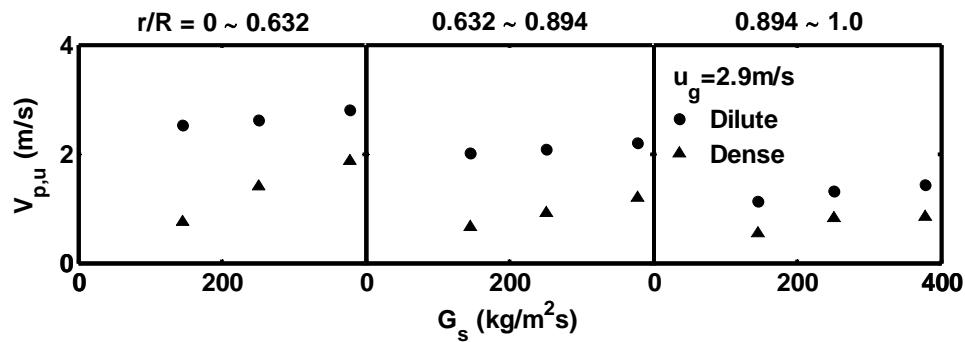


Figure 7.6 Annular average of upward particle velocities of dilute and dense phases with respect to solids circulation rate, $z = 1.5$ m

On the contrary, the dilute and dense phases behave in different ways with respect to the solids circulation rate. The particle velocity of the dense phase increases with increasing solids circulation rate quickly in the centre and slightly near the wall, suggesting that high solids circulation rate would lead to pushing dense phase moving upward faster than low circulation rate. On the other hand, the particle velocity of the dilute phase only slightly increases with increasing solids circulation rate across the bed, echoing the solids circulation does not influence significantly air distribution across the bed in view of a constant slip velocity between air and the particles in the dilute phase. Such slight increase of the particle velocity of the dilute phase implies that the high solids circulation rate also influenced small cluster movements in the dilute phase. On average, Zhu and Zhu (2008a) found that solids circulation rate had less effect on upward particle velocity than air velocity but increasing air velocity led to an increase of upward particle velocity at all radial positions, corresponding to higher degree of increase in the central region. They considered that particle movement was strongly correlated to the overall solids flow structure in flow with the very high solids holdup of CTFB.

Compared to Fig. 7.3, Fig. 7.4 shows that the downward particle velocities have the same order as the upward particle velocity of the dilute and dense phases. In fact, those results are the average values of each item over its corresponding calculation period instead of the overall calculation period using Eq. 7.10. In other words, the effects of the dilute and dense phases on the flow depend on their corresponding time fractions, as shown in Fig. 7.7. The upward movement fraction of the dilute phase decreases toward the wall in a parabolic shape, while the one of the dense phase increases toward the wall linearly. Comparatively, the downward movement fractions of the dilute and dense phases are negligible in the central region, while they increase near the wall to values much lower than the one of the upward movement of the dense phase. Although the fraction profiles in the acceleration zone are different from the ones in the upper part of the bed, the predominant relationships between these 4 items remain the same throughout the bed. These results are consistent with the data of Zhu and Zhu (2008a). They considered that upward particle movement took more than 50% time fraction across the entire section but decreased gradually towards the wall and that the upward movements of solids dominated the net solids flow direction across the bed. Based on the above reasons, one might postulate that the upward movements of the dilute and dense phases predominate in the core region and the annulus region respectively over the downward particle movements, in view of the upward particle velocities larger than the magnitudes of the downward particle velocities.

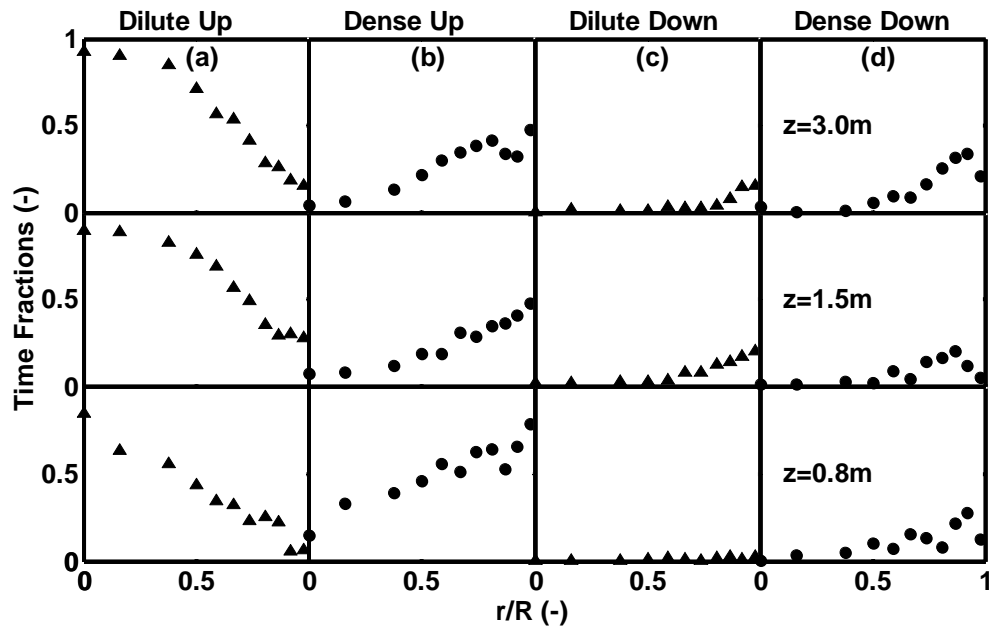


Figure 7.7 Profiles of upward and downward time fractions of dilute and dense phases, $u_g = 2.90$ m/s, $G_s = 145$ kg/m²s

7.3.2 Phase slip particle velocity

From the point of the mass and heat transfer, slip particle velocity is a measure of gas-solid contact. On the other hand, the difference of the particle velocities between the dilute and dense phases or phase slip particle velocity indirectly reflects the relative movements between gas and solids in view of the constant slip velocity between gas and dilute phase particles. After knowing the predominance of the upward particle movement of the dilute and dense phases, the phase slip particle velocity might be defined as the difference of upward particle velocities between the dilute and dense phases by Eq. 7.13, as shown in Figs. 7.8 and 7.9. Similar to the upward particle velocity profiles of the dilute phase, the phase slip particle velocity does not appreciably change in the central region and decreases quickly near the wall in a parabolic shape. The slip velocity decreases in

the central region and becomes more uniform across the bed with an enlarged core region with increasing solids circulation rates (Fig. 7.8). Such slip velocity profile implies that the gas uniformly distributes in the central region and quickly decreases in the annulus in view of the constant slip velocity between air and the particles of the dilute phase. Such air distribution across the bed is totally different from the steep parabolic distribution obtained in CFB (Yang et al, 1993) and the triangle distribution (Song et al, 2005; Nieuwland et al, 1996), suggesting preferable gas-solids mixing with increasing solids circulation rate.

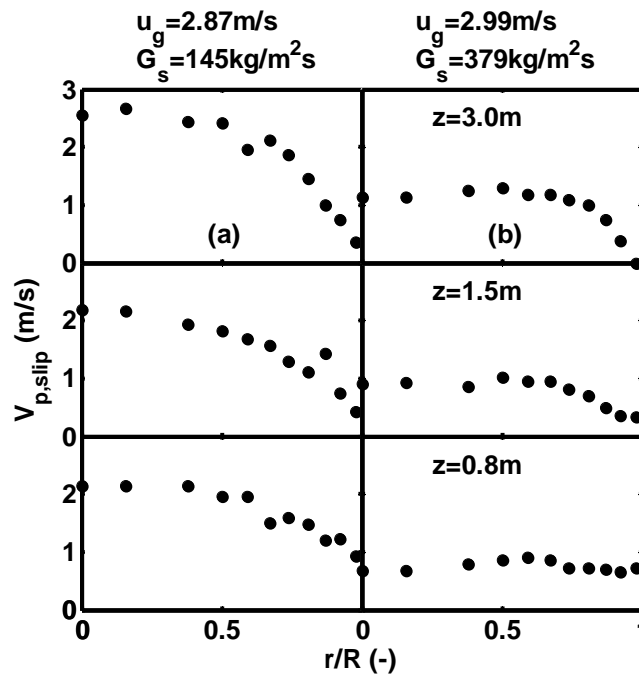


Figure 7.8 Profiles of phase slip particle velocity between dilute and dense phases

To further study the phase slip particle velocity, the annulus average values have been obtained against air velocity and solids circulation rate, varying in a parabolic shape, as

shown in Fig. 7.9. In the core region, the average slip velocity increases with increasing air velocity, suggesting the gas-solids flow tends to change its phase slip particle velocity from a minimum value in bubbling fluidized bed (BFB) to a maximum value at the end of CTFB regime or at the beginning of high density circulating fluidized bed (HDCFB). Slightly different from the central region, the average slip velocities in the middle and the wall annular regions also increase with increasing air velocity at low air velocity from very small slip velocity to a maximum value. Such slip velocities decrease slowly to the minimum value appearing in the core region at higher air velocity, echoing the start of the core-annular structure prevailing in HDCFB. In other words, the increase of the slip velocity corresponds to the core dilute flow structure evading to the wall region, while the decreasing of the slip velocity corresponds to vigorous core flow pushing more particles to the wall region and reducing the dilute phase effect. For increasing solids circulation rate, on the other hand, the phase slip particle velocities in the central and the middle annulus decrease quickly at low solids circulation rates and then decrease slowly at higher solids circulation rates. It might suggest that the dilute phase at low solids circulation rates pull the dense phase up, leading to high phase slip velocity, while the dense phase at higher solids circulation rate is pushed by the high back-pressure of the downcomer, giving rise to lower phase slip velocity.

Obviously, phase slip particle velocity corresponds to gas-solids contact time. For mass transfer between gas and solids, gas-solids reaction and cracking catalyst reaction, the flow structure in CTFB suggests that gas-solids contact increases with increasing solids circulation rate (corresponding to phase slip velocity decrease) and slightly decreases

with increasing air velocity. Such gas-solids contact is more uniform across the bed than other fluidization reactors.

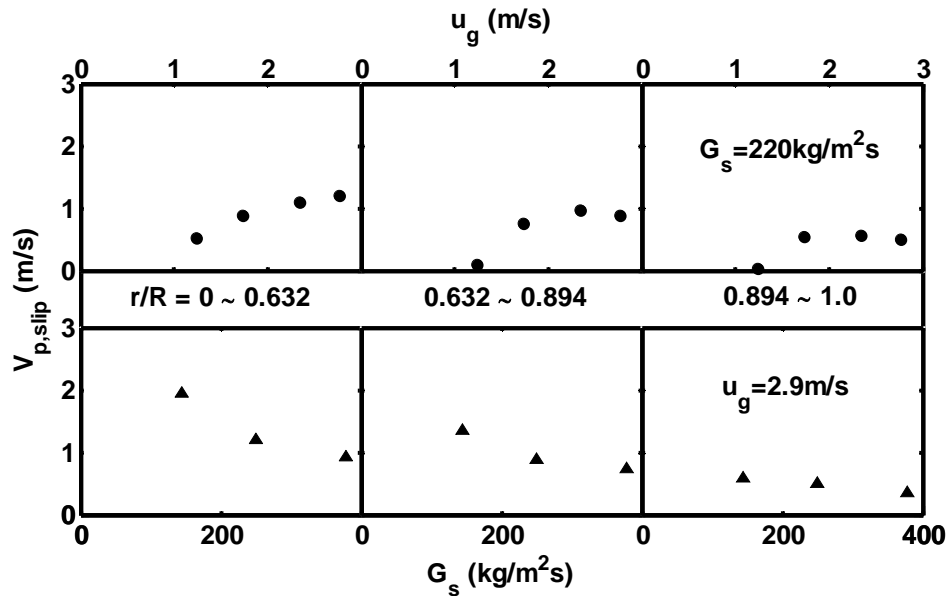


Figure 7.9 Phase slip particle velocity between dilute and dense phases at $z = 1.5 \text{ m}$

7.3.3 Solids flux of dilute and dense phases

To study the flow structure in CTFB by combining the solids holdup effect with the particle velocity, local upward and downward solids fluxes of the dilute and dense phases have been obtained, as shown in 7.10 and 7.11. Like the average particle velocity profiles, they are the phase average at the specific direction using Eq. 7.8, instead of overall time average. For the upward solids flux, the profiles of the dilute and dense phases are characterized in core-annular regions (Fig. 7.10). The solids flux of the dilute phase in the central region slowly increases towards the wall, and then increases somehow quicker

and reaches a maximum at the edge of the core region, and then dramatically decreases in the annulus region in a saddle shape across the bed. Such local upward flux slightly increases with increasing solids circulation rate. Relatively, local solids flux of the dense phase does not change appreciably within the core region and decreases drastically in the annular region in a trapezoid shape. Noticeably, it is proportional to the increase of the solids circulation rate. For the downward solids flux (Fig. 7.11), the profiles of the dilute and dense phases vary in a complicated way. Generally speaking, the flux of the dilute phase hardly changes with increasing solids circulation rate, while the one of the dense phase proportionally increases with increasing solids circulation rate.

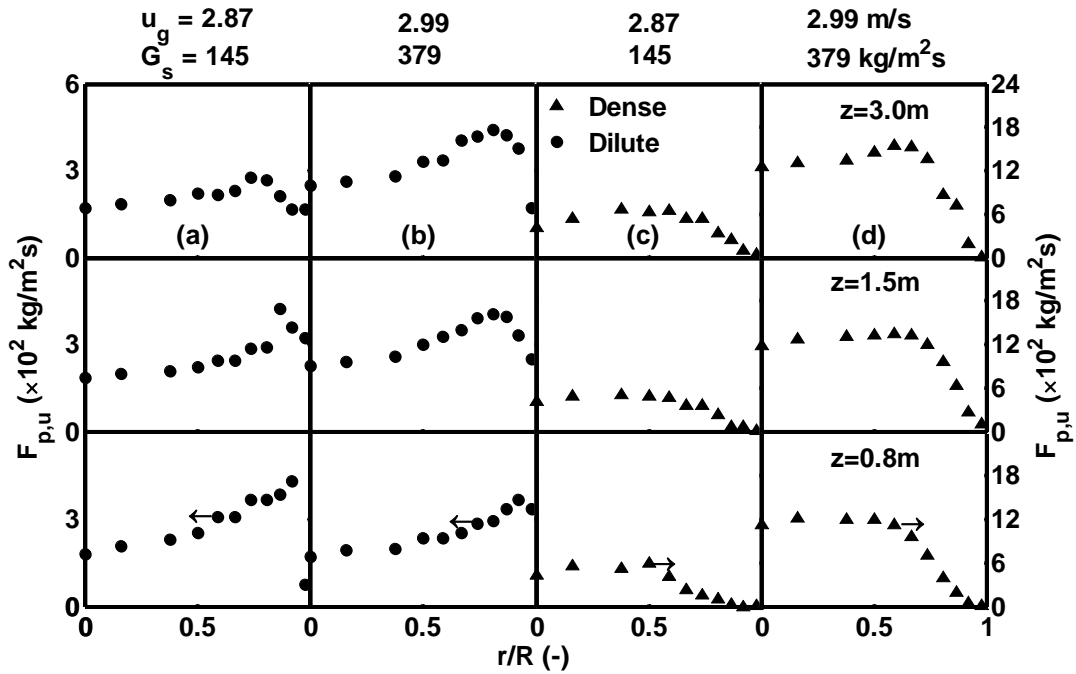


Figure 7.10 Profiles of upward solids flux of dilute and dense phases

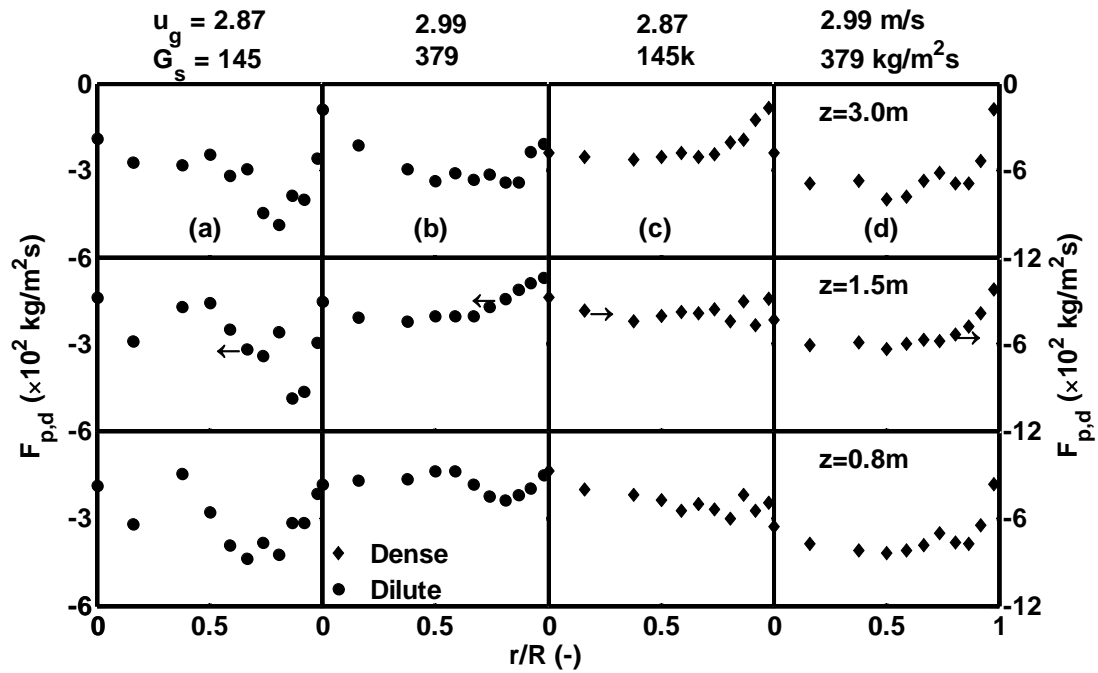


Figure 7.11 Profiles of downward solids flux of dilute and dense phases

Comparing these four local solids flux profiles between the dense and dilute phases in Figs. 7.10 and 7.11, the detail variation of local solids fluxes in the centre of CTFB can be observed. The upward flux of the dilute phase is slightly less than one quarter of that of the dense phase at lower circulation rate of $145 \text{ kg/m}^2\text{s}$, while the upward flux of the dilute phase is somewhat greater than one quarter of that of the dense phase at higher circulation rate of $379 \text{ kg/m}^2\text{s}$. Such ratio of the local solids fluxes between the dense and the dilute phases seems also to happen in downward direction, occasionally equivalent to the cross-sectional average solids holdup of around 0.25 (Chapter 6). The underlying reason of such relationship requires to be further studied.

The dilute phase has similar upward local solids fluxes to downward solids fluxes across the bed at lower solids circulation rate, and it has slightly higher local upward solids fluxes than the downward fluxes at higher solids circulation rate. It means that the magnitudes of the local solids flux of the dilute phase are nearly the same in upward and downward directions at similar air velocities and they are a little affected by the solids circulation rate. In other words, solids circulation does not influence much the dilute phase behavior. On the other hand, the local upward fluxes of the dense phase in the centre of the bed are the same as the downward magnitudes at lower solids circulation rate of $145 \text{ kg/m}^2\text{s}$, while they are about twice as much as the downward ones at higher rate of $379 \text{ kg/m}^2\text{s}$. Such results reveal that gas-particle interaction dominates in the dilute phase, as the particle velocity and local solids flux in the dilute phase are mainly affected by air flow rate (Figs. 7.5, 7.10 and 7.11). They also demonstrate that particle-particle and back-pressure interactions dominate in the dense phase. On one hand, the particle velocity of the dense phase increases mainly with increasing solids circulation rate (Fig. 7.6) and the local upward solids fluxes are equal in the downward and upward directions at lower solids circulation rate of $145 \text{ kg/m}^2\text{s}$, suggesting particle-particle interaction. The higher upward local solids flux than the downward one at higher solids circulation rate of $379 \text{ kg/m}^2\text{s}$ might imply the higher bottom pressure than the top one over pieces of dense phase to slow down the downward particle movement of the dense phase, in addition to the similar particle-particle interaction in both directions.

Therefore, one can postulate that the higher solids circulation rate might result in dense phase moving faster (somehow including small clusters in dilute phase) and higher dense

phase solids flux. High G_s might provide some momentum to support the particles moving upwards and the high particle concentration resulted in a higher effective viscosity of the rising suspension, thereby imposing more shears on the descending particles in HDCFB (Grace et al, 1999). High solids concentration in CTFB would also increase the inter-particle collision, which could reduce the tendency for the solids downflow. The lack of net solids back-mixing was one of the main advantages of the CTFB, which may lead to a reduction in the extent of axial dispersion of gas carried by the downflow particles (Liu et al, 1999). Generally, the solids fluxes in the central region were relatively high. Moving outward towards the wall, they appeared to decrease due to the higher local solids concentrations and lower local gas velocities than those in the central region, resulting in more frequent formation and break-up of clusters, as well as stronger particle-particle collisions (Qi and Zhu, 2009).

All those local solids flux profiles can be examined together through local apparent net solids flux, as shown in Fig. 7.12. Comprehensively taking into account the effects of the dense and dilute phases in flow, local net solids flux is the integration of instantaneous solids holdup and particle velocity in upward and downward directions. Correspondingly, the reduced net solids flux is defined as the local net solids flux over the measured solids circulation rate. All reduced flux profiles have similar trapezoid shapes, uniform in core region and quick decrease in annular region. At a given solids circulation rate, the reduced local net solids flux profile does not change apparently but has the maximum point varying from the centre to $r/R = 0.7$ and shows some particle back-mixing near the wall at higher air velocity, corresponding to more dilute flow in the central region. At a

given air velocity, the reduced local net solids flux at high solids circulation rate are similar to the one at low solids circulation rate, but the backmixing happening near the wall is apparently reduced. In other words, increasing solids circulation rate is able to reduce the solids backmixing and proportionally increase solids throughput. Similarly, with increasing solids circulation rate, the local net solids flux near the wall was able to change from negative value to a sharp increase to meet the measured solids circulation rate (Maclus et al, 2002). Similar profile obtained in more dilute flow using cross-correlation methods from solids holdup signals was claimed to be agreeable with the directly measured results and suggested the profile shape relatively unaffected by a change in the solids circulation rate (Herbert et al, 1994). The reduced net solids flux profile in CFB was insensitive to changing solids circulation rate over a wide range at a given air velocity (Rhode et al, 1992). In other words, the local net flux in CTFB is similar to the most cases of other fluidization regimes but with much less backmixing.

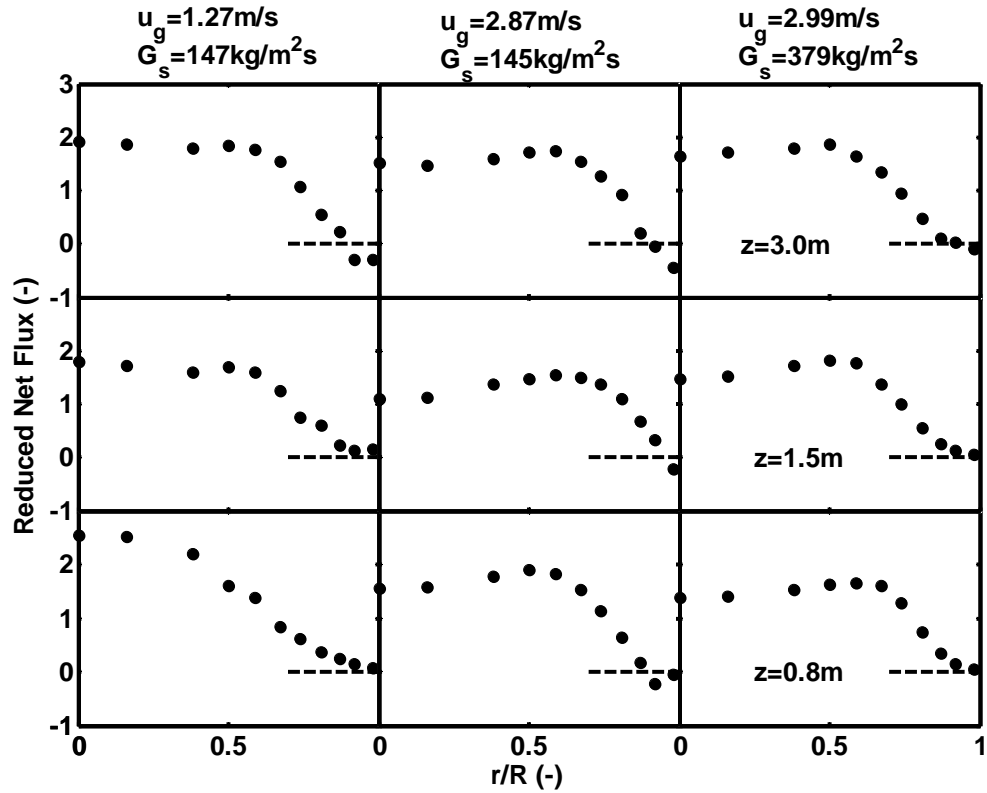


Figure 7.12 Profiles of apparent particle velocity at different air velocities and solids circulation rates

7.3.4 Apparent particle velocity and cross-correlation methods

Using Eq. 7.13, the apparent particle velocity can be obtained from the four local solids fluxes, as shown in Fig. 7.13. The radial profile shows a flat center region, then turning smoothly downward towards the wall, and having a fairly wide wall region, on average, without downward particle movement across the bed. Such an apparent particle velocity profile is very similar to the profile obtained in a similar experiment in CTFB by Zhu and Zhu (2008a; Zhou et al, 1995) and other prior results. Using LDV probe which is capable of measuring apparent particle velocity, Wei et al (1998) obtained similar particle velocity profiles as was divided into uniform region ($r/R < 0.4$), steep velocity region ($0.4 < r/R <$

0.85) and constant velocity annular region ($r/R > 0.85$). At the bottom dense section of a high flux CFB, Pärssinen and Zhu (2001) measured a horizontal "S" shape profile of a fairly wide wall region with a velocity value of less than 2 m/s (upwards). Malcus et al (2002), however, reported local net solids flux profiles in hook shape with a sharp increase near the wall because the axial solids holdup distribution was much less uniform than this work. Comparatively, the solids flow direction in the wall region of a low-flux riser is often reported to be downwards under fluxes of less than 200 kg/m²s and superficial gas velocities of less than 6.5 m/s (Bader et al, 1988; Glicksman et al, 1988; Hartge et al, 1988; Nowak et al, 1991), in contrast to high-flux and/or high-density applications where the flow direction is nearly always upwards (Grace et al, 1999).

For comparison, the upward particle velocity profiles of the dilute and dense phases obtained using DPCCM are also plotted in Fig. 7.13. The apparent particle velocity profile slightly differs from the other profiles near the wall as the computation comprises effects of the downward flow. Its values are the lowest of the three profiles in the annular region and slightly higher than the particle velocity of the dense phase in the core region, indicating that dense phase overweighting the computation of average particle velocity. Across the bed, the upward particle velocity profile of the dilute phase is higher than that of the dense phase. Relatively, the upward particle velocity profile obtained by CCM varies in a complicated way, its values being between the upward dilute and dense particle velocities and close to the upward particle velocity of the dilute phase within the core region. It means that particle velocity computation of CCM method over-weights the dilute phase across the bed, which confirms the prior analysis results that large peaks of

the signals determine the maximum of the cross-correlation function (Zhu et al, 2001). Comparing the profile of the apparent particle velocity and the one obtained with CCM, one can see that CCM would produce the higher average particle velocity from the original solids holdup signals due to the negligible time fraction of downward particle flow.

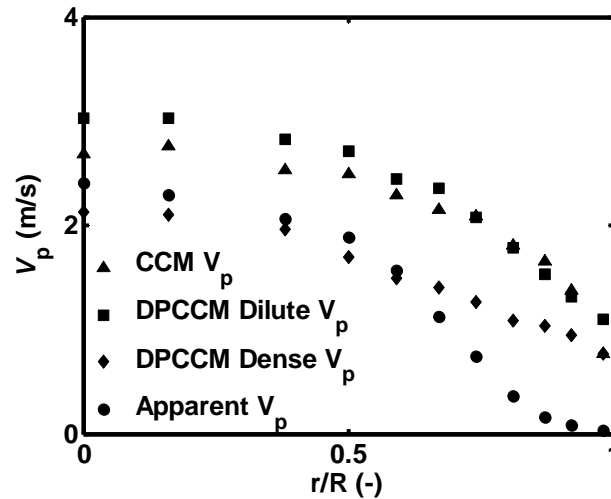


Figure 7.13 Apparent particle velocity and comparison between CCM and DPCCM, $u_g = 2.99$ m/s, $G_s = 379$ kg/m²s, $z = 1.5$ m

Conclusion

Experiments were carried out using FCC particles at different air velocities and solids circulation rates in a circulation turbulent fluidized bed (CTFB). The distribution of solids holdup was taken by dual channel optical fibre probes. To investigate the particle movements of the dilute and dense phases from the pairs of solids concentration signals, a Divided Phase Cross-Correlation Method (DPCCM) was proposed, which was capable

of predicting the particle velocities of the dilute and dense phases. The results demonstrated that the upward particle velocity of the dilute phase increased with increasing air velocity and did not change significantly with solids circulation rate, while the particle velocity of the dense phase increased proportionally with increasing solids circulation rate and hardly changed with increasing air velocity. The results also revealed that the core-annulus distribution of the local solids flux in CTFB, i.e. the net solids holdup flux in the core region was uniform and quickly decreased in the annular region. The particle velocity of the dense phase and the net solids flux, which was increasing with solids circulation rate, suggested higher solids circulation rate helped to reduce the solids backmixing and to raise solids throughput in CTFB. In detail, the results revealed gas-particle interaction dominated in the dilute phase, and particle-particle interaction dominated in the dense phases at low solids circulation rate, while particle-particle and back-pressure interactions dominated in the dense phase at high solids circulation rate.

Acknowledgement

The authors are grateful to the Natural Sciences and Engineering Research Council of Canada for supporting this work.

Nomenclature

d , distance between the emitting and receiving optical fibre bundles of the probe, m

F_p , phase solids flux, kg/m²s

G_s , cross-sectional average net solids flux or solids circulation rate, kg/m²s

G_{sl} , local net solids flux, kg/m²s

K , standard kurtosis of local solids holdup fluctuations

N , population of a time series

R , radius of the column, m

S , skewness of local solids holdup fluctuations

T , time, s

V , local average particle velocity, m/s

\overline{V}_s , apparent particle velocity, m/s

r , radial position, m

u_g , superficial air velocity, m/s

u_c , onset transition air velocity of CTFB, m/s

u_k , onset air velocity of CTFB, m/s

u_{tr} , ending air velocity of CTFB, m/s

v_s , instantaneous particle velocity, m/s

Z , elevation from the air distributor, m

ρ_p , particle density, kg/m³

ϵ_s , local time-averaged solids holdup

τ , delay time, s

σ , standard deviation of local solids holdup fluctuations

σ_p , standard deviation of differential pressure drop

subscript

b, dilute phase

c, dense phase

d, downward

g, air

l, local

s, solids

u, upward

Abbreviation

CCM, Cross-correlation method

DPCCM, divided phase cross-correlation method

References

Adrian R.J., (1991), *Rev. Fluid Mech.*, 23, 261

Bachalo W.D., (1994), *Int. J. Multiphase Flow* 20, 261, (suppl.)

Bader R., Findlay J. and Knowlton T. M. (1988), Gas-solid flow patterns in a 30.5 cm-diameter circulating fluidized bed. In P. Basu, & J. F. Large (Eds.), *Circulating fluidized bed technology II* (pp. 123-137), Oxford, Pergamon Press

Bi H. T., Ellis N., Abba I. A. and Grace J. R., (2000), Review: A state-of-the-art review of gas-solid turbulent fluidization, *Chemical Engineering Science*, 55, 4789-4825

Bi H. T. and Su P., (2001), Local Phase Holdups in Gas-Solids fluidization and Transport, *AIChE Journal*, Vol. 47(9), 2025

Cheremisinoff N.P., (1986), *Ind. Eng. Chem. Process Des. Dev.* 25, 329

Chian W. Chan, Jonathan P.K., Seville, David J., Parker and Jan Baeyens, (2010), Particle velocities and their residence time distribution in the riser of a CFB, *Powder Technology*, (November 2010), 203 (2), pg. 187-197

Clift R. and J.R. Grace, (1985), *Fluidization*, 2nd edn., Academic Press, London

Glicksman L. R., (1988), Circulating fluidized bed heat transfer. In P. Basu, & J. F. Large (Eds.), *Circulating fluidized bed technology II* (pp. 13-29) Oxford: Pergamon Press

Grace J. R. (1986b). Contacting modes and behaviour classification of gas-solid and other two-phase suspensions, *Canadian Journal of Chemical Engineering*, 64, 353-363

Grace JR, Issangya AS, Bai DR, Bi HT and Zhu, JX, (1999), Situating the high density circulating fluidized bed, *AIChE J.*, 45, 2108-2116.

Hartge E. U., Rensner D. and Werther J., (1988), Solids concentration and velocity patterns in circulating fluidized beds. In P. Basu, & J. F. Large (Eds.), *Circulating fluidized bed technology II* (pp. 165-180). Oxford: Pergamon Press.

Herberta P. M., Gauthierb T. A., Briema C. L. and Bergougnou M. A., (1994), Application of fiber optic reflection probes to the measurement of local particle velocity and concentration in gas-solid flow, *Powder Technology*, 80, 243-252

Knowlton T., (1995), Interaction of pressure and diameter on CFB pressure drop and holdup, Paper for workshop: Modeling and control of fluidized bed systems, Hamburg, May 22-23

Li D., Ph. D., (2010), Thesis: Investigation of CFB Riser and Downer Reactor Performance for Catalytic Ozone Decomposition, Western University

Liu JZ, Grace JR, Bi HT, Morikawa H ND Zhu JX, (1999), Gas dispersion in fast fluidization and dense suspension upflow, 54, 5441–5449

Malcus S., E. Cruz, C. Rowe, T.S. Pugsley, (2002), Radial solid mass flux profiles in a high-suspension density circulating fluidized bed, Powder Technology, (May 2002), 125 (1), pg. 5-9

Nieuwland J. J. etc., (1996), Measurement of solid concentration and axial solids velocity in gas-solid two phase flow, Powder Technology, 87, 127 - 139

Nowak W., Minco H., Yamazaki R. and Yoshida K., (1991), Behavior of particles in a circulating fluidized bed of a mixture of two different sized particles, In P. Basu, M. Horio, & M. Hasatani (Eds.), *Circulating fluidized bed technology III* (pp. 219-224). Oxford: Pergamon Press.

Pärssinen J. H and Zhu J. X., (2001a), Axial and radial solids distribution in a long and high-flux CFB riser, AIChE J. 47, 2197–2205

Pärssinen J.H. and J.-X. Zhu, (2001b), Particle velocity and flow development in a long and high-flux circulating fluidized bed riser, Chemical Engineering Science (September 2001), 56 (18), pg. 5295-5303

Qi M., Zhu J. and Baighi, S., (2012), Transition characteristics of gas-solid flow in circulating turbulent fluidized beds, Powder Technology, submitted, Chapter 5 in this thesis

Rhodes M., Mineo H. and Hiramata T., (1992), Particle motion at the wall of a circulating fluidized bed, Powder Technology, 70 207-214

Song X., et al, (2005), Gas Mixing in the Reactor Section of Fluid Cokers, Ind. Eng. Chem. Res., 44, 6067-6074

Wei Fei, Lin Hongfei, Cheng Yi, Wang Zhanwen and Jin Yong, (1998), Profiles of particle velocity and solids fraction in a high-density riser, Powder Technology (December 1998), 100 (2-3), pg. 183-189

Xu Jing, (2010), Ph. D. Thesis: Hydrodynamics Studies on Macro- and Micro-Flow Structure with Effects of Particle Properties in a Circulating Fluidized Bed, Western University, 2010

Yang Y. L. et al, (1993), Local slip behaviors in the Circulating fluidized Bed, AIChE Symposium Series, Vol 89, (296), 82

Yates J. G. and S.J.R. Simons, (1994), Int. J. Multiphase Flow, 20, 297, (suppl.)

Zhou J., J. R. Grace, C. J. Lim and C. M. H. Brereton, (1995), Particle velocity profiles in a circulating fluidized bed riser of square cross-section, Chemical Engineering Science (January 1995), 50 (2), pg. 237-244

Zhang H. and Zhu J.-X, (1998), A novel calibration procedure for a fiber optic solids concentration probe, Powder Technology, 100, 260-272

Zhu J. et al, (2001), Direct measurements of particle velocities in gas - solids suspension flow using a novel five-fiber optical probe, Powder Technology, 115, 184 - 192

Zhu J. (2010), Circulating turbulent fluidization—A new fluidization regime or just a transitional phenomenon, *Particuology*, 8, Pages 640-644

Zhu J, Qi M., Baighi S., (2012), Identification of Micro Flow Structures and Regime Transition in Gas-Solid Fluidized Beds through Moment Analysis, AIChE Journal, Submitted, Chapter 4 in this thesis

Zhu H. and Zhu J.-X, (2008a), Gas-Solids flow Structures in a Novel Circulating Turbulent fluidized Bed, AIChE Journal, Vol. 54 (5), 1213

Zhu H. and Zhu J.-X, (2008b), Comparative study of flow structures in a circulating turbulent fluidized bed, Chemical Engineering Science, 63, 2920-2927

8 Conclusions and recommendations

8.1 Conclusions

Circulating Turbulent Fluidized Bed (CTFB) refers to a fluidized bed that integrates the traditional turbulent fluidized bed and circulating fluidized bed into a high density circulating system, so as to simultaneously achieve highly efficient gas-solid interaction that exists in the turbulent fluidized beds and significantly low solids backmixing featured by circulating fluidized beds. Hydrodynamics and micro flow structure were experimentally studied. Based on statistical parameters, such as mean, standard deviation, skewness and kurtosis, a Moment Consistency Data Processing Method (MCDPM) was proposed. Compared to other investigation methods on flow structures in gas-solid systems, MCDPM was successfully used in directly estimating the average solids holdups of the dense and dilute phases and the dense phase volume fraction from the measured solids holdup signal series, without additional information. MCDPM also includes a procedure to divide the solids holdup signal into sub-signals of the dense and dilute phases. A Divided Phase Cross-Correlation Method (DPCCM) was then also adopted in cross-correlating the sub solids holdup signals of the dense and dilute phases to obtain the phase particle velocities.

Using MCDPM, solids holdups of the dense and dilute phases and the phase fractions were obtained over 5 fluidization regimes, bubbling (BFB), turbulent (FTB), circulating turbulent (CTFB), high-density circulating (HDCFB) and circulating (CFB) fluidized bed

systems. In low air velocity, the dense phase fraction of the BFB, TFB and CTFB regimes decreased with increasing air velocity, while the transition from HDCFB to CFB in the high-velocity regime experienced appreciable change in solids holdup of the dense phase. From the CTFB/TFB to HDCFB/CFB regimes across the low- to high-velocity regime boundary, both the solids holdup and the fraction of the dense phase experienced a drastic decrease, suggesting that this transition corresponded to a more profound change in flow structure and further suggesting that CTFB is in reality still a turbulent fluidized bed. Of the five fluidization regimes, CTFB was further studied with respect to its transition characteristics, flow structure and particle movements.

From the unique transition characteristics, it was postulated that the onset transition air velocity from bubbling to (circulating) turbulent fluidization regime took place at the phase inversion point, where the regime transited from the dense phase dominating flow in bubbling fluidization regime to the dilute phase dominating flow in the central region of the turbulent fluidization regime. It was also observed that the ending transition air velocity from turbulent to circulating fluidization regimes occurred at the transition point, where the dense phase started to expand, corresponding to the transition from bi-peak PDF to the triangular PDF. The experimental results demonstrated that the onset transition velocity hardly changed, while the ending transition velocity increased with increasing solids circulation rate, implying that the operation range of the air velocity for the CTFB regime can significantly extend with increasing solids circulation rate.

In CTFB, the cross-sectional average solids holdup of higher than 0.25 was distributed along the majority of the bed, more uniformly than any other regimes. Local average solids holdup varied radially in a parabolic shape ranging from 0.15 to 0.50.

Microscopically, CTFB was characterized by dilute dominating flow in the centre and dense phase dominating flow in the annular region, different from either the dense phase dominating flow of bubbling fluidized bed or the dilute phase dominating flow of circulating fluidized bed. Furthermore, the dense phase solids holdup in CTFB remained fairly constant with changing operation conditions and bed positions, while the dilute phase solids holdup increased along the radial direction and decreased slightly with increasing gas velocity.

The experimental results further revealed that the upward particle velocity of the dilute phase inside CTFB increased with increasing air velocity and did not change significantly with solids circulation rate, while the particle velocity of the dense phase increased proportionally with increasing solids circulation rate but hardly changed with increasing air velocity. Radially, the dilute phase velocity had a parabolic shape, while the dense phase velocity was more uniform with some decrease towards the wall. In term of the phase division, the dilute phase fraction was high in the centre and the dense phase fraction was high in the annular region.

8.2 Assessment on CTFB

Combining with earlier studies (Qi and Zhu, 2009, 196; Zhu and Zhu, 2008, 180; Zhu, 2010), the results obtained so far demonstrated that CTFB runs in a novel gas-solid flow regime, which differed from BFB, HDCFB and CFB in many aspects. The typical characteristics of CTFB can be summarized with respect to flow structure and applications. For flow structure, CTFB has:

(1) Homogeneous axial flow structure with high solids concentration. Under a wide range of air velocities of 1.0 ~ 3.0 m/s and solids circulation rates of 0 ~ 420 kg/m²s, CTFB has the homogeneous axial solids holdup distribution of 0.25 ~ 0.35 observed within the majority part of the bed. Such high solids concentration varies neither with solids circulation rates nor with air velocities. Although CTFB and TFB are classified into the same regime, the axial profile of CTFB is different from that of TFB but is similar to HDCFB.

(2) Optimal radial flow structure. CTFB has quite different radial profile of solids holdup from BFB, TFB, HDCFB and CFB, which varies from about 0.15 to 0.5, much higher than the highest value among TFB, HDCFB and CFB regimes. The results also exhibit that there exists an optimal air velocity, where the difference of the solids distribution between the centre and the wall is least. Moreover, such a radial solids distribution is independent of solids circulation rate and reproducible to a maximum extent over the CTFB operation air velocity range, as regarded as the steady state of CTFB, further suggesting the fully developed state of CTFB.

(3) Excellent micro flow structure. CTFB is quite attributed to two-phase flow. Over the entire operation air velocity range of CTFB, the dilute phase contains the solids holdup, about 0.08 in the centre, 0.10 in the middle annular region, and 0.15 in the wall annular region, while the dense phase has constant solids holdup of 0.40. These solids holdups are quite uniform and high, compared to those of HDCFB and CFB. From the variation of dense phase fraction, on the other hand, CTFB is of a dilute phase dominating flow in

the centre and dense phase dominating flow in the annular region, totally different from the dense phase dominating flow in BFB and dilute phase dominating flow in HDCFB and CFB.

(4) No net downward solids flux. The fairly uniform radial solids flux across the bed in the CTFB increases with solids circulation rate, which makes CTFB distinguished by the lack of significant backmixing of solids from the “regular” TFB and circulating fluidization regimes, proportional to the solids circulation rate like a plug flow.

(5) Intensive particle–particle interaction. High solids holdup at relatively low air velocity and high solids circulation rate leads to intensive particle-particle interaction. Such particle-particle interaction is energized by the high back-pressure from downcomer and the pressure of the primary air supply.

(6) Quite wide operation range of air velocity and solids circulation rate. The starting air velocity, (u_{bt}), of CTFB is similar to ‘regular’ TFB, while the ending velocity is proportional to the solids circulation rate. In other words, the higher the circulation rate, the wider the range of operating air velocity in CTFB. TFB is a special case of CTFB.

(7) Extremely large solid-to-gas loading ratio, $G_s/(\rho_g u_g)$. Operating at $u_{tc} = 3.0$ m/s at $\alpha = 0 \sim 380$ kg/m²s, the solid-to-gas loading ratio reaches $0 \sim 350$ under the all experimental operating conditions, in comparison of 10–80 for most CFB operations of Geldart’s Group A particles.

For the industrial applications, CTFB is capable of (1) recycling a large amount of particles, while maintaining a high solids concentration and therefore high gas–solid reaction intensity; (2) having a flexible capacity dealing with solids circulation and gas throughput due to a wide range of operation gas velocities and solids circulation rates with little change of axial and radial solids holdup profiles; (3) having better solids selection due to no net downflow solids flux over the entire reactor; (4) operating at good mass and heat transfer efficiencies because of high average solids holdup over the entire reactor, and of high average solids holdup in the dilute phase; (5) Buffering fluctuation of loading and temperature during production to a maximum extent; (6) easily predicting the performance of a CTFB reactor and being simply modeled on hydrodynamics, mass and heat transfer in the reactor in view of the constant solids holdups of the dense and dilute phases across the bed;

In essence, CTFB can maintain a high solids concentration to intensify gas–solids contact efficiency and to enhance chemical reactions while suppress axial solids backmixing in order to accommodate reactions where a narrow solids residence time distribution is required for high reaction selectivity. Thus, CTFB is suitable for such processes as FCC process, where the catalyst deactivates quickly and therefore requires continuous regeneration, and the reaction time is short, while the solids backmixing is impeded in favour of high reaction selectivity. However, the construction and operation of CTFB is much simpler than those of CFB

8.3 Recommendations

Compared with BFB, HDCFB and CFB, CTFB and TFB appeared to be similar, but the solids circulation makes CTFB rather different from TFB. Further study on such differences need to be done with respect to the column geometry and diameter, particle density, particle size and shape, particle distribution, etc.

Furthermore, the results in this study demonstrated that the onset air velocity of CTFB does not vary with solids circulation rate, but the ending air velocity increases with increasing air velocity. However, axial profile and PDF of the solids holdup of TFB are obviously different from those of CTFB. On the other hand, the onset air velocity of CTFB determined in this study seems to be higher than that of TFB at similar experimental conditions. It is worth studying whether solids circulation delays the starting of CTFB regimes.

Solids circulation rate played an important role in demarcating CTFB as it can operate at low air velocity and very high solids circulation rates. This raises a question on how CTFB is located in the regime diagraph. That may require studying the solids circulation effects on low-velocity fluidization regimes, and redrawing or modifying the regime diagraphs.

There is an optimal air velocity for CTFB regime. How does the reaction activity vary throughout the bed at such conditions? Combining the group studies on ‘ozone reaction in fluidized beds’ under similar conditions to this (and earlier) study, one could analyze the similarities and dissimilarities between TFB and CTFB to further determine the regime classification.

How do the reactions proceed corresponding to the core-annular distribution of the local solids fluxes proposed in this study? Modeling CTFB with the results from earlier study and this work, the further assessment might be done on the new regime to promote its applications in industry.

Appendix A.1 Derivation of MCDPM (Chapter 4)

The structural component parameters of modelled signal are related to the statistic results of the original signal by the following

$$\bar{\varepsilon}_s = f_d \varepsilon_{sd} + (1 - f_d) \varepsilon_{sb} \quad (4.7)$$

$$\sigma = \sqrt{(\varepsilon_{sd} - \bar{\varepsilon}_s)^2 f_d + (\varepsilon_{sb} - \bar{\varepsilon}_s)^2 (1 - f_d)} \quad (4.8)$$

$$S = \frac{1}{\sigma^3} [(\varepsilon_{sd} - \bar{\varepsilon}_s)^3 f_d + (\varepsilon_{sb} - \bar{\varepsilon}_s)^3 (1 - f_d)] \quad (4.9)$$

$$K = \frac{1}{\sigma^4} [(\varepsilon_{sd} - \bar{\varepsilon}_s)^4 f_d + (\varepsilon_{sb} - \bar{\varepsilon}_s)^4 (1 - f_d)] \quad (4.10)$$

The three structural component parameters can be solved with any three of the above formula. Three combinations will be established.

Let

$$D = \varepsilon_{sd} - \bar{\varepsilon}_s \quad (A-1)$$

$$B = \bar{\varepsilon}_s - \varepsilon_{sb} \quad (A-2)$$

Derivation of Method One (M1)

Substitute (A-1) and (A-2) into (4.7)-(4.9) and obtain

$$f_d = \frac{B}{D + B} \quad (A-3)$$

$$\sigma = \sqrt{D^2 f_d + B^2 (1 - f_d)} \quad (A-4)$$

$$S = \frac{1}{\sigma^3} [D^3 f_d - B^3 (1 - f_d)] \quad (\text{A-5})$$

Reorganize (A-3) and (A-4)

$$B = \frac{f_d D}{1 - f_d} \quad (\text{A-6})$$

From (A-5) and (A-6)

$$S = \frac{f_d D}{\sigma^3} [D^2 - B^2] = \frac{f_d D}{\sigma^3} (D + B)(D - B) \quad (\text{A-7})$$

$$\sigma^2 - D^2 f_d = B^2 (1 - f_d)$$

$$\sigma^2 = D f_d (D + B)$$

$$S \sigma = (D - B) \quad (\text{A-8})$$

Substitute (A-6) into (A-7)

$$\sigma^2 - D^2 f_d = \frac{f_d^2 D^2}{1 - f_d}$$

$$D = \sigma \sqrt{\frac{1 - f_d}{f_d}} \quad (\text{A-9})$$

From (A-6), (A-8) and (A-9)

$$f_d = \frac{1}{2} (1 \pm S \sqrt{\frac{1}{4 + S^2}})$$

For bubbling fluidized beds and low velocity turbulent fluidized beds, $S < 0$ and $f_d > 0.5$, while $S > 0$ and $f_d < 0.5$ for fast fluidized bed, which need to be met, so the reasonable solution is

$$f_d = \frac{1}{2} (1 - S \sqrt{\frac{1}{4 + S^2}}) \quad (4.11)$$

Substitute (A-9) with (15a)

$$\varepsilon_{sd} = \varepsilon_s + \frac{\sigma}{2}[\sqrt{4 + S^2} + S] \quad (4.12)$$

Substitute (A-8) with (16a)

$$\varepsilon_{sb} = \varepsilon_s - \frac{\sigma}{2}[\sqrt{4 + S^2} - S] \quad (4.13)$$

Derivation of Method Two (M2)

Similarly, consider equation (4.7), (4.8) and (4.10)

$$f_d = \frac{B}{D + B} \quad (A-3)$$

$$\sigma = \sqrt{D^2 f_d + B^2(1 - f_d)} \quad (A-4)$$

$$\sigma^2 = D^2 f_d + B^2(1 - f_d) \quad (A-10)$$

$$K\sigma^4 = D^4 f_d + B^4(1 - f_d) \quad (A-11)$$

(A-3) gives

$$D = \frac{B(1 - f_d)}{f_d} \quad (A-12)$$

$$D^2 f_d = \frac{B^2(1 - f_d)^2}{f_d} \quad (A-13)$$

$$D^4 f_d = \frac{B^4(1 - f_d)^4}{f_d^3} \quad (A-14)$$

Substitute (A-10) with (A-13)

$$\sigma^2 = \frac{B^2(1 - f_d)^2}{f_d} + B^2(1 - f_d)$$

and

$$\sigma^2 \frac{f_d}{(1 - f_d)} = B^2 \quad (A-15)$$

$$\sigma^4 \frac{f_d^2}{(1-f_d)} = B^4(1-f_d) \quad (\text{A-16})$$

Substitute (A-11) with (A-14)

$$K\sigma^4 = \left[\frac{(1-f_d)^3}{f_d^3} + 1 \right] B^4(1-f_d) \quad (\text{A-17})$$

Substitute (A-17) with (A-16)

$$K = \frac{(1-f_d)^3 + f_d^3}{f_d} \frac{1}{1-f_d}$$

$$\frac{1}{3+K} - f_d + f_d^2 = 0$$

$$f_d = \frac{1}{2} \left(1 \pm \sqrt{\frac{K-1}{3+K}} \right) \quad (4.14)$$

Substitute (A-15) with (14) and (A-2), and consider $B > 0$

$$\varepsilon_{sb} = \bar{\varepsilon}_s - \frac{\sigma}{2} (\sqrt{K+3} \pm \sqrt{K-1}) \quad (4.15)$$

Substitute (A-15) with (14) and (A-2), and consider $B > 0$

$$\varepsilon_{sd} = \bar{\varepsilon}_s + \frac{\sigma}{2} (\sqrt{K+3} \mp \sqrt{K-1}) \quad (4.16)$$

**Appendix A.2 Calculation of coefficient of determination
in Chapter 3**

$$SS_{\text{tot}} = \sum_i (y_i - \bar{y})^2,$$

$$SS_{\text{err}} = \sum_i (y_i - f_i)^2$$

$$\bar{y} = \frac{1}{n} \sum_i^n y_i$$

$$R^2 \equiv 1 - \frac{SS_{\text{err}}}{SS_{\text{tot}}}.$$

where, y_i is observed value, f_i is predicted value

Appendix A.3 List of equations in Chapter 4

$$\{\varepsilon_i\}, i \in N \quad (4.1)$$

$$\bar{\varepsilon}_s = \frac{1}{N} \sum_{i=1}^N \varepsilon_i \quad (4.2)$$

$$\sigma = \left[\frac{1}{N-1} \sum_{i=1}^N (\varepsilon_i - \bar{\varepsilon}_s)^2 \right]^{1/2} \quad (4.3)$$

$$S = \frac{\sum_{i=1}^N (\varepsilon_i - \bar{\varepsilon}_s)^3}{(N-1)\sigma^3} \quad (4.4)$$

$$K = \frac{\sum_{i=1}^N (\varepsilon_i - \bar{\varepsilon}_s)^4}{(N-1)\sigma^4} \quad (4.5)$$

$$\{\varepsilon_{id} = \varepsilon_{sd}, \varepsilon_{ib} = \varepsilon_{sb}\}, id \in N \text{ and } ib \in N \quad (4.6)$$

$$\bar{\varepsilon}_s = f_d \varepsilon_{sd} + (1-f_d) \varepsilon_{sb} \quad (4.7)$$

$$\sigma = \sqrt{(\varepsilon_{sd} - \bar{\varepsilon}_s)^2 f_d + (\varepsilon_{sb} - \bar{\varepsilon}_s)^2 (1-f_d)} \quad (4.8)$$

$$S = \frac{1}{\sigma^3} [(\varepsilon_{sd} - \bar{\varepsilon}_s)^3 f_d + (\varepsilon_{sb} - \bar{\varepsilon}_s)^3 (1-f_d)] \quad (4.9)$$

$$K = \frac{1}{\sigma^4} [(\varepsilon_{sd} - \bar{\varepsilon}_s)^4 f_d + (\varepsilon_{sb} - \bar{\varepsilon}_s)^4 (1-f_d)] \quad (4.10)$$

$$f_d = \frac{1}{2} \left(1 - S \sqrt{\frac{1}{4+S^2}} \right) \quad (4.11)$$

$$\varepsilon_{sd} = \bar{\varepsilon}_s + \frac{\sigma}{2}[\sqrt{4+S^2} + S] \quad (4.12)$$

$$\varepsilon_{sb} = \bar{\varepsilon}_s - \frac{\sigma}{2}[\sqrt{4+S^2} - S] \quad (4.13)$$

$$f_d = \frac{1}{2}(1 \pm \sqrt{\frac{K-1}{3+K}}) \quad (4.14)$$

$$\bar{\varepsilon}_{sd} = \bar{\varepsilon}_s + \frac{\sigma}{2}(\sqrt{K+3} \mp \sqrt{K-1}) \quad (4.15)$$

$$\bar{\varepsilon}_{sb} = \bar{\varepsilon}_s - \frac{\sigma}{2}(\sqrt{K+3} \pm \sqrt{K-1}) \quad (4.16)$$

$$E_K = \frac{|K^{1/4} - K_{th}^{1/4}|}{K^{1/4}}, \quad (M1) \quad (4.17)$$

$$E_S = \frac{|S^{1/3} - S_{th}^{1/3}|}{S^{1/3}}, \quad (M2) \quad (4.18)$$

$$\text{Method 1 for } |S| < 1.5 \text{ or } K < 4.5 \quad (4.19a)$$

and

$$\text{Method 2 for } |S| > 1.5 \text{ or } K > 4.5 \quad (4.19b)$$

$$n = f_d N \quad (4.20)$$

Appendix A.4 List of equations in Chapter 5

$$S = \frac{\sum_{i=1}^N (\varepsilon_{si} - \bar{\varepsilon}_s)^3}{(N-1)\sigma^3} \quad (5.1)$$

$$K = \frac{\sum_{i=1}^N (\varepsilon_{si} - \bar{\varepsilon}_s)^4}{(N-1)\sigma^4} \quad (5.2)$$

$$\beta = K - S^{4/3} \quad (5.3)$$

$$u_{tc} = 0.0041G_s + 1.78 \quad (5.4)$$

Appendix A.5 List of equations in Chapter 7

$$N_t = NB + NC \quad (7.1)$$

$$\phi(\tau) = \frac{\sum_{N_t} [(\varepsilon_{s,1}(n) - \overline{\varepsilon_{s,1}})(\varepsilon_{s,2}(n-\tau) - \overline{\varepsilon_{s,2}})]}{\sqrt{\sum_{N_t} (\varepsilon_{s,1}(n) - \overline{\varepsilon_{s,1}})^2} \sqrt{\sum_{N_t} (\varepsilon_{s,2}(n-\tau) - \overline{\varepsilon_{s,2}})^2}}, \text{ for measured series} \quad (7.2)$$

$$\phi_c(\tau) = \frac{\sum_{NC} [(\varepsilon_{s,1}(n) - \overline{\varepsilon_{sc,1}})(\varepsilon_{s,2}(n-\tau) - \overline{\varepsilon_{sc,2}})]}{\sqrt{\sum_{NC} (\varepsilon_{s,1}(n) - \overline{\varepsilon_{sc,1}})^2} \sqrt{\sum_{NC} (\varepsilon_{s,2}(n-\tau) - \overline{\varepsilon_{sc,2}})^2}}, \text{ for the dense phase} \quad (7.3)$$

$$\phi_b(\tau) = \frac{\sum_{NB} [(\varepsilon_{s,1}(n) - \overline{\varepsilon_{sb,1}})(\varepsilon_{s,2}(n-\tau) - \overline{\varepsilon_{sb,2}})]}{\sqrt{\sum_{NB} (\varepsilon_{s,1}(n) - \overline{\varepsilon_{sb,1}})^2} \sqrt{\sum_{NB} (\varepsilon_{s,2}(n-\tau) - \overline{\varepsilon_{sb,2}})^2}}, \text{ for the dilute phase} \quad (7.4)$$

$$v_s = \frac{d}{\tau} \quad (7.5)$$

$$T_{i,j} = \int_{T_i} dt_{i,j}, \quad (i = b \text{ (dilute)}, c \text{ (dense)} \text{ and } j = \text{up, down}) \quad (7.6)$$

$$T = \sum T_{i,j} \quad (7.7)$$

Corresponding

$$F_{p,i,j} = \frac{\rho_p}{T_{i,j}} \int_{T_i} v_{p,i,j}(t) \varepsilon_{s,i,j}(t) dt, \quad (7.8)$$

$$G_{s,l} = \sum \frac{T_{i,j}}{T} F_{p,i,j} \quad (7.9)$$

$$V_{p,i,j} = \frac{1}{T_{i,j}} \int_{T_i} v_{p,i,j}(t) dt \quad (7.10)$$

$$G_s = \frac{2}{R} \int_{T_i} G_{s,l} dr \quad (7.11)$$

$$\bar{V}_{p,j} = \frac{G_{s,l}}{\varepsilon_s} \quad (7.12)$$

$$V_{p,slip} = V_{p,b,up} - V_{p,c,up} \quad (7.13)$$

Appendix B.1 Matlab code for MCDPM and phase division

```
clear all
close all
clc

% to approximately retrieve working directory by select any .pma data
file
p = uigetdir;
cd(p)

%offsets and gains of two channel probes
probe={'z1','z2','z3','z4'};
radial={'rc','r1','r2','r3','r4','r5','r6','r7',
'r8','r9','r10'};

%search for experiments and data files
testfiles = dir('.\Date*');
testname = {testfiles.name};
testNum=length(testname);
testname{:}
for testloop=1:testNum % different tests
testname{testloop}
  for probelooop=1:4 % different heights
    for rloop=1:11 %radial positions
      clear filedir datafiles filename

subdir=strcat('.\',testname{testloop},'\',probe{probelooop},'\',radial{r
loop},'\');
filedir=strcat(subdir,'*.pma');
datafiles=dir(filedir); %retrieve data files
filename={datafiles.name};
dnc=length(filename);
clear Es essort
for j=2:dnc % data files
  clear volt1 volt2 ch1 ch2 indices
  [ch1,ch2] = textread([subdir,filename{j}], '%d %d',
'delimiter',' ','headerlines', 6);
  volt1=(ch1-offset1(probelooop))*5/netgains1(probelooop);
  indices=find(volt1<0);
  volt1(indices)=0;
  clear indices ch1
  indices=find(volt1>5);
  volt1(indices)=5;
  clear indices
```

```

volt2=(ch2-offset2(probeloop))*5/netgains2(probeloop);
indices=find(volt2<0);
volt2(indices)=0;
clear indices ch2
indices=find(volt2>5);
volt2(indices)=5;
clear indices volt

volt=(volt1+volt2)/2;

clear B AC4 solut volt1 volt2
B=-(2*b(probeloop).*volt+a(probeloop)^2);
A2=b(probeloop)^2*2;
AC4=4*b(probeloop)^2.*volt.^2;
solut=(-B-(B.^2-AC4).^0.5)/A2;
if j==2
    Es=solut;
else
    Es=[Es;solut];    %put 20 files together
end
end %files
meanEs(rloop)=mean(Es)*Esmf;
stddev(rloop)=std(Es*Esmf);
skewn(rloop)=skewness(Es*Esmf);
kurto(rloop)=kurtosis(Es*Esmf);
eb(rloop)=meanEs(rloop)-stddev(rloop)/2*(sqrt(4+skewn(rloop)^2)-
skewn(rloop));
ed(rloop)=stddev(rloop)*skewn(rloop)+2*meanEs(rloop)-eb(rloop);
deltad(rloop)=(meanEs(rloop)-eb(rloop))/(ed(rloop)-eb(rloop));
%phase division
essort=sort(Es*Esmf, 'descend');
body=length(Es);
high=round(body*deltad(rloop));
delimer(rloop)=essort(high);
edexp(rloop)=mean(essort(1:high));
ebexp(rloop)=mean(essort(high+1:body));
kdev(rloop)=(meanEs(rloop)-delimer(rloop))/stddev(rloop);
clear essort
end %radial loop
cell=strcat('A',num2str(probeloop));
xlsfile= strcat('.',testname{testloop}, '\M2ofMCDPM.xls');
xlswrite(xlsfile,ed, ' Solids Holdup of Dense phase',cell)
xlswrite(xlsfile,eb, ' Solids Holdup of Dilute phase',cell)
xlswrite(xlsfile,deltad, 'Dense Phase Fraction',cell)
end %axial positions
end %experiments

```

Appendix B.2 MatLab code for DPCCM

```
function [upvp downvp, minLe flag upxcf downxcf upend downend
totaltime,uptime, downtime]= DPCCM(signal1, ...
signal2, upend, downend, b, group, minLe, rloop, le, totaltime,
deltatime, clustertime)

%compute positive cluster velocity and negative cluster
%velocity
clear indices vlt1 vlt2
frequency=50000;
vplimit=60;
shift=[];
code=0;
flag=0;
upvp=[]; %means computation invalid
downvp=[];
upxcf=[];
downxcf=[];
minLe=minLe;
uptime=[];
downtime=[];

grouppoints=length(signal1)/group;
vlt1 = reshape(signal1,grouppoints,group);
vlt2 = reshape(signal2,grouppoints,group);
%length(vlt1)
clear ind s1 s2 xcf index lags bounds
for igrup=1:group %group=1
if isempty(vlt1) || isempty(vlt2)
lags(ind)=[];
xcf(ind)=[];
flag=1; %invalid calculation, very rarely
else
s1=(vlt1(:,igrup)-
mean(vlt1(:,igrup)))/std(vlt1(:,igrup)); %normalization of signals
s2=(vlt2(:,igrup)-mean(vlt2(:,igrup)))/std(vlt2(:,igrup));
[xcf, lags, bounds] = crosscorr(s1, s2, grouppoints-1);
%xcf---correlation coefficient, lags---time lapse
ind=find(xcf<=0.5); %remove negative correlative data
lags(ind)=[];
xcf(ind)=[];
end
%}
clear ind s1 s2
ind=find(lags==0);
lags(ind)=[]; %invalid cross-correlation
xcf(ind)=[];
if isempty(xcf) %invalid computation
flag=1;
rloop=4;
```

```

code=0;
end
clear ind
%xcoef = (xcf_max-mean(s1)*mean(s2))/(std(s1)*std(s2));
if rloop<2 %within the core region
clear index
[xcf_max index] = max(xcf); %IMPORTANT: index
if isempty(index)
code=0; %invalid
else
if abs(lags(index))<minLe %find maximum particle velocity bounds
minLe=abs(lags(index));
if minLe>vplimit
code=1; % goto particle velocity computation
else
minLe=vplimit; %invalid due to very high particle velocity
code=0;
end
else
code=1; % >minLe and goto particle velocity computation
end
end
else %remove extra large particle velocity data
ind=find(abs(lags)<minLe); %remove odd data of positive particle
velocity
lags(ind)=[];
xcf(ind)=[];
clear ind index
[xcf_max index] = max(xcf); %IMPORTANT: index
if isempty(index)
code=0; %invalid and quit
else
%[rloop j]; %invalid data group
code=1; % goto next step
end
end
if code ==1 %next step: particle velocity
totaltime=totaltime+clustertime;
shift=lags(index);
if shift>0 %ascend particles
upvp=clustertime*le*frequency/shift; %put 49 files together
vp=vp*time
%downvp=0;
%downxcf=0;
upxcf=xcf_max;
upend=[upend b];
uptime=clustertime;
else %descend particles
downvp=clustertime*le*frequency/shift;
%upvp=0;
%upxcf=0;
downxcf=xcf_max;
downend=[downend b];
downtime=clustertime;
end
end
end
%[rloop upvp downvp]

```

```
end %group
end %end of function
```

Appendix C.1 Velocity chart for the primary air supply

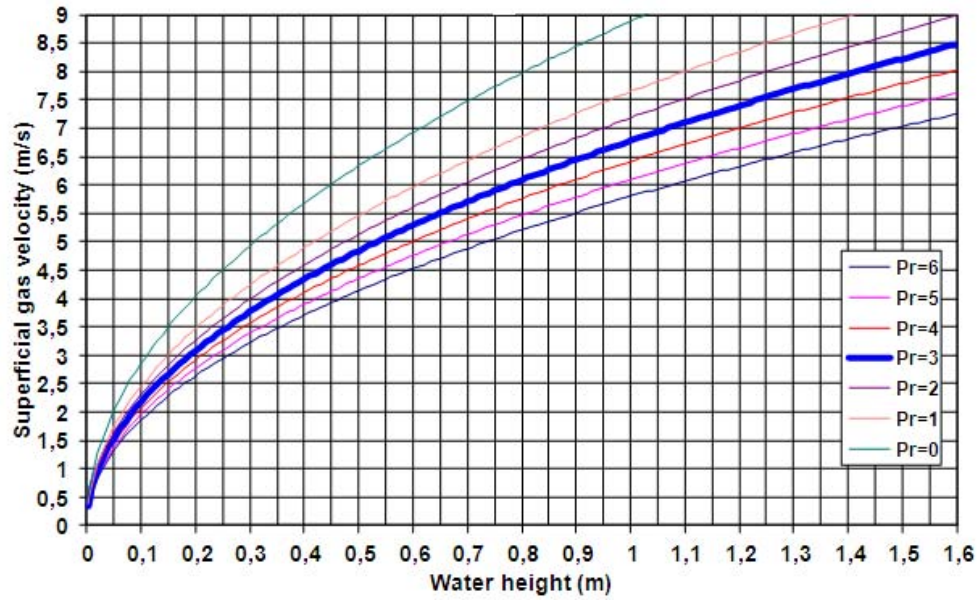


Figure A 6 Velocity chart for the primary air supply

Appendix C.1 Velocity chart for the secondary air supply

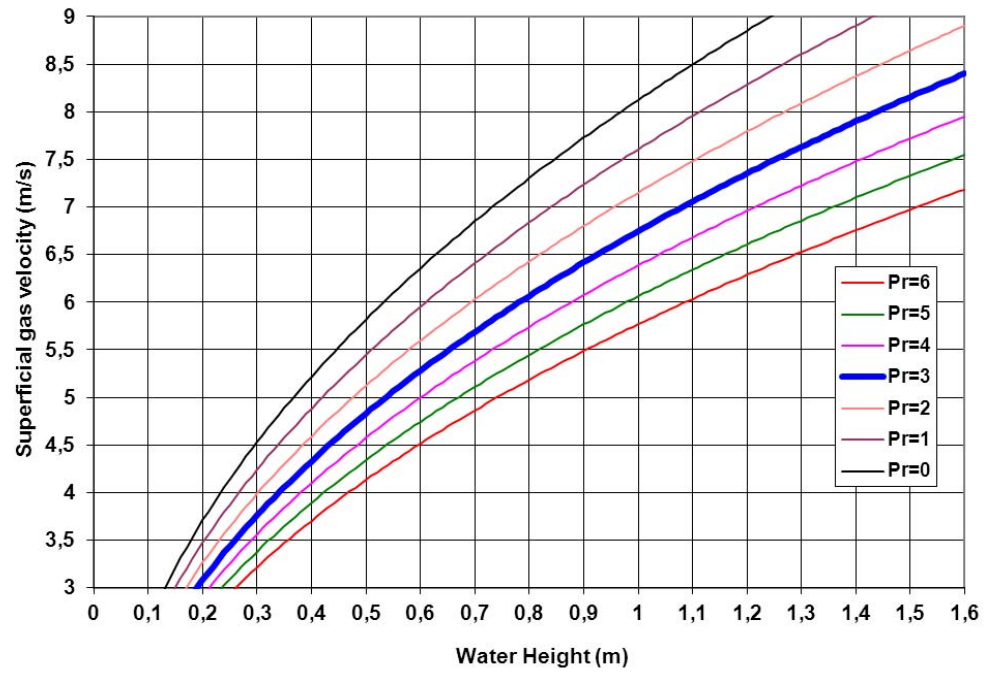


Figure A 7 Velocity chart for the secondary air supply

Appendix D.1 Pressure chart for transducer

(PX163-120D5V)

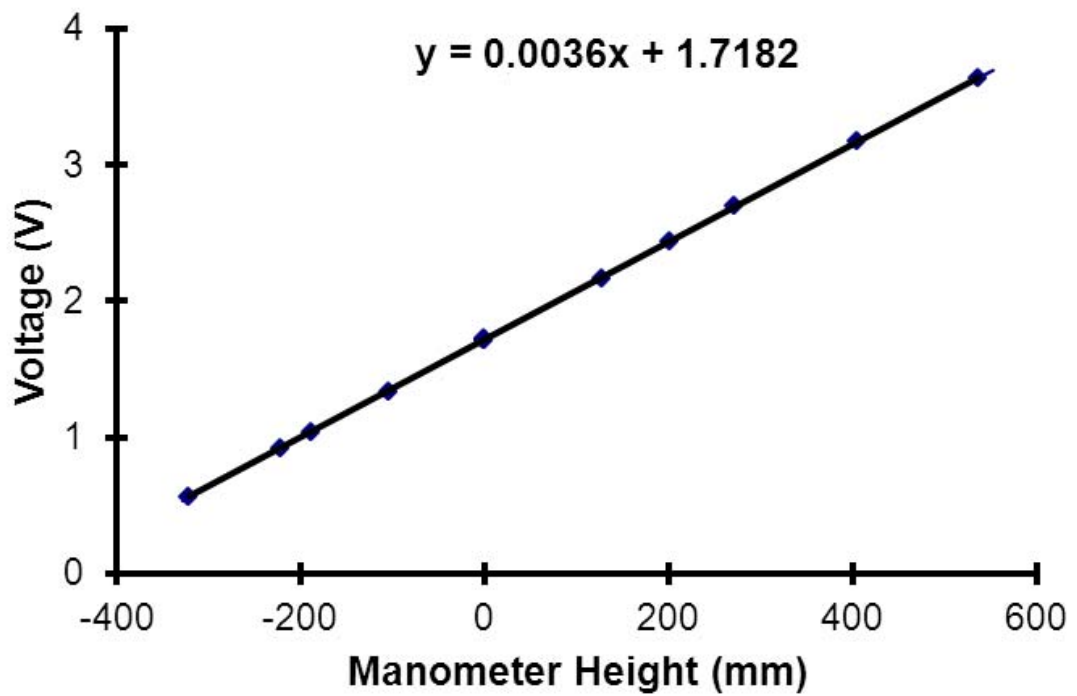


Figure A8 Pressure chart for transducer of PX163-120D5V

Appendix D.2 Pressure chart for transducer

(PX162-027D5V)

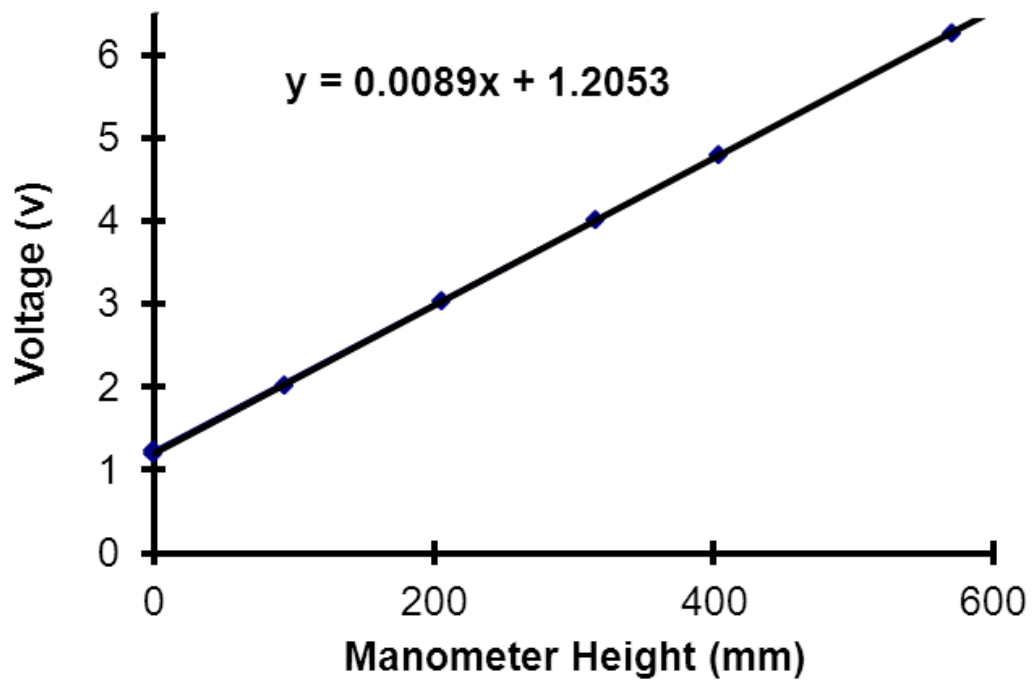


Figure A9 Pressure chart for transducer of PX162-027D5V

Appendix D.3 Error analysis of solids holdup measurements using optical fibre probes

In order to ensure the accuracy of solids holdup measurements using 4 optical fibre probes, preliminary measurements were carried out at 2 operating conditions ($U_g = 0.53$ m/s, $G_s = 0$ kg/m²s; $U_g = 1.95$ m/s, $G_s = 220$ kg/m²s) at 4 elevations along the bed. For each elevation, 10 measurements were taken for every one of 11 radial positions at sampling frequency $50 \text{ kHz} \times 26.2 \text{ s} \times 10$. Using the experimental data, statistical errors were analyzed, as shown in Tables A.1-4. The figure A.5 shows the radial profiles of mean solids holdup with corresponding error bars, corresponding mean absolute error of 0.0128 (mean relative error of 4%) over these two operating conditions. As a result, it was postulated that the optical fibre probes calibrated in this study had quite high measurement accuracy to obtain the consistency outputs of local mean solids holdups over all experimental conditions. This postulate was also extended to the particle velocity measurements.

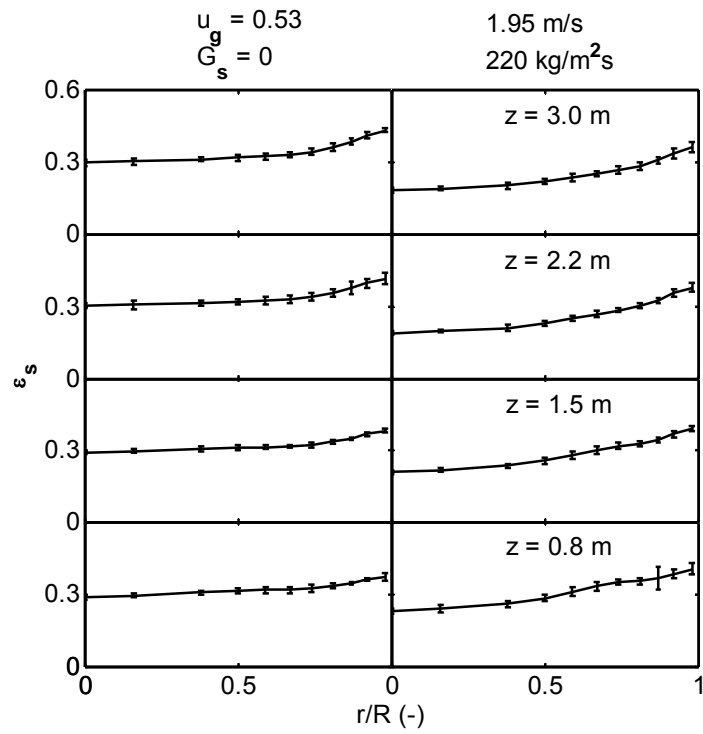


Figure A10 Solids holdup profiles and error bars of optical fibre probe data

Table A.1 Error Analysis of probe #1 (at z = 0.8 m)

Operating conditions	r/R	0	0.16	0.38	0.5	0.59	0.67	0.74	0.81	0.87	0.92	0.98	
0.53 m/s 0 kg/m ² s	ϵ_s	1	0.274	0.287	0.303	0.299	0.314	0.32	0.331	0.326	0.34	0.348	0.35
		2	0.261	0.293	0.297	0.313	0.32	0.321	0.316	0.33	0.342	0.342	0.354
		3	0.267	0.282	0.304	0.319	0.312	0.312	0.327	0.329	0.345	0.342	0.354
		4	0.284	0.288	0.297	0.31	0.319	0.312	0.326	0.335	0.34	0.348	0.359
		5	0.27	0.285	0.296	0.307	0.323	0.32	0.328	0.327	0.343	0.345	0.357
		6	0.267	0.275	0.299	0.319	0.302	0.298	0.292	0.309	0.328	0.333	0.386
		7	0.258	0.273	0.298	0.298	0.296	0.289	0.301	0.321	0.326	0.341	0.384
		8	0.259	0.269	0.295	0.305	0.299	0.303	0.298	0.325	0.33	0.338	0.379
		9	0.273	0.263	0.277	0.312	0.298	0.292	0.302	0.3	0.336	0.343	0.386
		10	0.273	0.287	0.291	0.294	0.285	0.291	0.291	0.315	0.333	0.337	0.388
	σ_s	0.016	0.008	0.01	0.008	0.008	0.012	0.013	0.016	0.011	0.007	0.005	
1.95 m/s 220 kg/m ² s	ϵ_s	1	0.225	0.262	0.302	0.312	0.332	0.373	0.355	0.384	0.313	0.342	0.397
		2	0.236	0.231	0.275	0.28	0.344	0.377	0.366	0.4	0.306	0.361	0.38
		3	0.256	0.262	0.289	0.305	0.346	0.354	0.366	0.359	0.318	0.362	0.402
		4	0.253	0.257	0.29	0.312	0.327	0.376	0.35	0.403	0.306	0.355	0.385
		5	0.229	0.235	0.266	0.305	0.316	0.39	0.37	0.383	0.328	0.352	0.393
		6	0.243	0.251	0.254	0.296	0.325	0.342	0.382	0.387	0.389	0.395	0.434
		7	0.227	0.258	0.263	0.282	0.334	0.333	0.368	0.376	0.393	0.395	0.44
		8	0.222	0.24	0.275	0.317	0.31	0.338	0.358	0.377	0.408	0.386	0.443
		9	0.238	0.228	0.264	0.289	0.289	0.336	0.367	0.382	0.415	0.387	0.436
		10	0.235	0.269	0.286	0.287	0.342	0.364	0.339	0.375	0.39	0.395	0.439
	σ_s	0.011	0.011	0.015	0.015	0.013	0.018	0.02	0.012	0.013	0.046	0.021	

Table A.2 Error Analysis of probe #2 (at z = 1.5 m)

Operating conditions	r/R	0	0.16	0.38	0.5	0.59	0.67	0.74	0.81	0.87	0.92	0.98	
0.53 m/s 0 kg/m ² s	ϵ_s	1	0.321	0.315	0.348	0.338	0.325	0.344	0.339	0.358	0.369	0.39	0.404
		2	0.309	0.328	0.338	0.319	0.328	0.338	0.343	0.358	0.373	0.389	0.397
		3	0.319	0.327	0.341	0.333	0.331	0.326	0.344	0.357	0.371	0.389	0.397
		4	0.314	0.316	0.336	0.342	0.323	0.341	0.349	0.356	0.364	0.399	0.396
		5	0.32	0.318	0.337	0.339	0.345	0.35	0.359	0.362	0.377	0.384	0.399
		6	0.311	0.316	0.321	0.337	0.337	0.341	0.32	0.357	0.371	0.382	0.413
		7	0.309	0.309	0.321	0.322	0.327	0.334	0.334	0.355	0.366	0.39	0.408
		8	0.308	0.321	0.339	0.325	0.34	0.348	0.332	0.361	0.372	0.37	0.415
		9	0.314	0.307	0.32	0.341	0.333	0.33	0.34	0.342	0.357	0.389	0.413
		10	0.314	0.31	0.318	0.343	0.315	0.338	0.338	0.351	0.365	0.383	0.414
	σ_s	0.016	0.005	0.007	0.011	0.009	0.009	0.008	0.01	0.006	0.006	0.008	
1.95 m/s 220 kg/m ² s	ϵ_s	1	0.196	0.206	0.228	0.249	0.293	0.316	0.322	0.342	0.36	0.382	0.427
		2	0.207	0.194	0.231	0.233	0.253	0.299	0.306	0.331	0.366	0.377	0.427
		3	0.192	0.209	0.229	0.255	0.298	0.326	0.319	0.304	0.344	0.41	0.422
		4	0.192	0.205	0.245	0.254	0.271	0.284	0.303	0.329	0.363	0.399	0.417
		5	0.221	0.205	0.235	0.231	0.252	0.301	0.321	0.336	0.364	0.37	0.412
		6	0.196	0.196	0.223	0.242	0.283	0.286	0.291	0.31	0.332	0.385	0.438
		7	0.195	0.201	0.234	0.222	0.275	0.282	0.333	0.321	0.351	0.379	0.43
		8	0.204	0.215	0.226	0.255	0.292	0.296	0.319	0.322	0.362	0.367	0.441
		9	0.203	0.199	0.207	0.265	0.275	0.306	0.307	0.327	0.349	0.378	0.424
		10	0.208	0.197	0.228	0.233	0.289	0.323	0.308	0.323	0.342	0.388	0.439
	σ_s	0.011	0.009	0.006	0.01	0.014	0.016	0.016	0.012	0.012	0.011	0.013	

Table A.3 Error Analysis of probe #3 (at z = 2.2 m)

Operating conditions	r/R	0	0.16	0.38	0.5	0.59	0.67	0.74	0.81	0.87	0.92	0.98
0.53 m/s 0 kg/m ² s	1	0.29	0.314	0.29	0.291	0.31	0.309	0.324	0.338	0.368	0.385	0.41
	2	0.277	0.307	0.289	0.3	0.318	0.303	0.325	0.343	0.366	0.391	0.421
	3	0.295	0.294	0.291	0.31	0.319	0.329	0.331	0.332	0.358	0.382	0.409
	4	0.277	0.291	0.294	0.306	0.304	0.297	0.33	0.348	0.361	0.382	0.406
	5	0.292	0.302	0.317	0.32	0.297	0.308	0.309	0.333	0.364	0.391	0.415
	6	0.271	0.282	0.288	0.283	0.288	0.273	0.298	0.333	0.314	0.355	0.376
	7	0.287	0.285	0.28	0.301	0.273	0.291	0.308	0.303	0.324	0.35	0.362
	8	0.267	0.258	0.283	0.284	0.28	0.297	0.318	0.308	0.325	0.36	0.35
	9	0.276	0.268	0.285	0.292	0.292	0.282	0.275	0.303	0.32	0.344	0.392
	10	0.271	0.277	0.279	0.295	0.306	0.289	0.305	0.329	0.295	0.356	0.388
	σ_s	0.016	0.01	0.017	0.011	0.011	0.015	0.016	0.017	0.016	0.027	0.018
1.95 m/s 220 kg/m ² s	1	0.177	0.183	0.209	0.225	0.239	0.247	0.26	0.297	0.293	0.314	0.388
	2	0.179	0.192	0.198	0.222	0.235	0.271	0.259	0.28	0.305	0.339	0.41
	3	0.181	0.173	0.189	0.207	0.236	0.258	0.288	0.29	0.286	0.33	0.389
	4	0.19	0.193	0.205	0.206	0.216	0.243	0.268	0.269	0.296	0.333	0.389
	5	0.168	0.188	0.195	0.21	0.239	0.266	0.264	0.296	0.298	0.329	0.379
	6	0.173	0.183	0.189	0.223	0.24	0.271	0.269	0.285	0.31	0.317	0.357
	7	0.185	0.196	0.206	0.231	0.232	0.262	0.274	0.298	0.292	0.332	0.355
	8	0.172	0.189	0.22	0.218	0.223	0.237	0.271	0.28	0.303	0.346	0.354
	9	0.17	0.181	0.189	0.22	0.214	0.239	0.271	0.284	0.32	0.353	0.362
	10	0.18	0.184	0.19	0.246	0.225	0.266	0.266	0.305	0.313	0.308	0.369
	σ_s	0.011	0.007	0.007	0.011	0.012	0.01	0.013	0.008	0.011	0.011	0.014

Table A.4 Error Analysis of probe #4 (at z = 3.0 m)

Operating conditions	r/R	0	0.16	0.38	0.5	0.59	0.67	0.74	0.81	0.87	0.92	0.98
0.53 m/s 0 kg/m ² s	1	0.313	0.301	0.33	0.31	0.325	0.348	0.364	0.363	0.408	0.441	0.466
	2	0.327	0.335	0.312	0.317	0.343	0.321	0.366	0.399	0.416	0.449	0.457
	3	0.303	0.317	0.312	0.351	0.317	0.361	0.376	0.385	0.417	0.457	0.457
	4	0.308	0.328	0.314	0.323	0.334	0.345	0.367	0.396	0.414	0.449	0.459
	5	0.299	0.324	0.327	0.335	0.352	0.346	0.36	0.383	0.426	0.447	0.461
	6	0.283	0.322	0.326	0.321	0.345	0.345	0.351	0.383	0.394	0.436	0.464
	7	0.273	0.291	0.328	0.338	0.367	0.341	0.349	0.351	0.394	0.419	0.471
	8	0.291	0.306	0.321	0.322	0.345	0.352	0.353	0.378	0.396	0.429	0.482
	9	0.303	0.326	0.33	0.345	0.337	0.343	0.368	0.383	0.399	0.437	0.472
	10	0.287	0.325	0.334	0.33	0.328	0.359	0.33	0.372	0.408	0.426	0.472
	σ_s	0.016	0.014	0.008	0.013	0.014	0.011	0.013	0.014	0.011	0.012	0.008
1.95 m/s 220 kg/m ² s	1	0.167	0.188	0.238	0.207	0.234	0.244	0.258	0.292	0.314	0.324	0.393
	2	0.191	0.184	0.205	0.224	0.214	0.268	0.232	0.284	0.305	0.314	0.414
	3	0.174	0.202	0.202	0.209	0.254	0.253	0.278	0.296	0.308	0.317	0.389
	4	0.205	0.189	0.215	0.211	0.227	0.246	0.268	0.307	0.291	0.321	0.389
	5	0.182	0.196	0.208	0.218	0.257	0.248	0.244	0.308	0.307	0.367	0.404
	6	0.173	0.177	0.192	0.204	0.243	0.258	0.272	0.267	0.312	0.312	0.363
	7	0.168	0.179	0.205	0.227	0.227	0.269	0.264	0.261	0.324	0.367	0.356
	8	0.182	0.193	0.198	0.222	0.251	0.261	0.252	0.297	0.312	0.329	0.372
	9	0.177	0.191	0.212	0.213	0.242	0.266	0.256	0.284	0.295	0.344	0.377
	10	0.179	0.186	0.203	0.231	0.25	0.245	0.262	0.268	0.324	0.31	0.347
	σ_s	0.011	0.008	0.012	0.009	0.014	0.01	0.014	0.017	0.011	0.021	0.021

Curriculum vitae

Name: Maozhan Qi

Place of Birth Hebei, China

Post-secondary Education: Chemical Engineering, University of Western Ontario, London, Ontario, Canada, 2008-2012, Ph D

Mechanical Engineering, Univ. of Sc. & Tech. Beijing, China, 1992-1995, Ph D

Hydraulic Engineering, Huabei Institute of Water Conservancy and Hydro-electricity, China, 1987-1990, M. E. Sc.; 1977-1981, B.E. Sc.

Work Experience: Graduate Research Assistant, Teaching Assistant, Editor Assistant of 'Powder Technology' and 'Particuology', University of Western Ontario London, Ontario, Canada, 2008-2012

Research Fellow, University of Western Ontario London, Ontario, Canada, 2001-2002

Associate professor, Tsinghua University, Beijing China, 1995-2000

Assistant professor, Huabei Institute of Water Conservancy and Hydro-electricity, China, 1982-1990,

Honors & Awards: Graduate Student Fellowship Fund, University of Western Ontario, 2008-2012

Graduate Thesis Research Award, University of Western Ontario, 2012